Synthesis and Characterization of Tri- and Tetravalent Actinide Amidinates

DISSERTATION

Zur Erlangung des akademischen Grades

Doctor rerum naturalium

(Dr. rer. nat.)

vorgelegt

dem Bereich Mathematik und Naturwissenschaften

der Technischen Universität Dresden

von

M.Sc. Sebastian Fichter (geb. Schöne)

geboren am 07.06.1992 in Dresden

Tag der Einreichung: 24.06.2020
Tag der Verteidigung: 15.10.2020

Gutachter:

Prof. Dr. phil.-nat. habil. Thorsten Stumpf

Prof. Dr. rer. nat. habil. Peter W. Roesky

Die Dissertation wurde in der Zeit von November 2016 bis April 2020 am Institut für Ressourcenökologie des Helmholtz-Zentrums Dresden-Rossendorf angefertigt.

Betreuer:

Prof. Dr. phil.-nat. habil. Thorsten Stumpf
Dr. rer. nat. Juliane März

MEINEM GROßVATER

Dass ich erkenne, was die Welt im Innersten zusammenhält.
Johann Wolfgang von Goethe, Faust I

DANKSAGUNG

ein offenes Ohr, wenn die wissenschaftlichen Fragestellungen wieder einmal philosophisch wurden. Außerdem möchte ich mich im Speziellen bei Roger für die vielen quantenchemischen Rechnungen bedanken, auch wenn die Größe meiner Actinidkomplexe die Grenze des Möglichen ausreizte.

Außerdem bedanke ich mich bei meinen weiteren, teils ehemaligen, Bürokolleginnen Astrid Jäschke, Anne Bauer, Sarah Fischer, Ariette Schierz, Jenny Jessat und Luisa Köhler für die stets angenehme Büroatmosphäre und die gesprächsintensiven Mittagspausen. Besonders bei Astrid möchte ich mich für die Unterstützung beim Verfassen wissenschaftlicher Artikel und die Einführung in die Calixaren-Chemie bedanken.

Ich bedanke mich außerdem bei allen Mitarbeitern des Instituts für Ressourcenökologie für die Unterstützung während meiner Promotion.

Zu guter Letzt danke ich meiner Familie und meinen Freunden für ihre Unterstützung und Nachsicht, wenn die Promotion doch wieder einen großen Teil meiner Zeit in Anspruch genommen hat.

Zum Schluss möchte ich mich bei meiner Frau Sabrina für ihre immerwährende Unterstützung in allen Lebenslagen bedanken. Ohne dich wäre ich nicht der, der ich heute bin.

PUBLIKATIONSLISTE

Im Rahmen der Promotion wurden folgende Publikationen in wissenschaftlichen Zeitschriften veröffentlicht:

S. Schöne, T. Radoske, J. März, T. Stumpf, M. Patzschke, A. Ikeda-Ohno: *[UO$_2$Cl$_2$(phen)$_2$], a Simple Uranium(VI) Compound with a Significantly Bent Uranyl Unit (phen=1,10-phenanthroline),* Chem. Eur. J. **2017**, *23*, 13574-13578.

S. Schöne, T. Radoske, J. März, T. Stumpf, A. Ikeda-Ohno: *Synthesis and Characterization of Heterometallic Iron–Uranium Complexes with a Bidentate N-Donor Ligand (2,2'-Bipyridine or 1,10-Phenanthroline),* Inorg. Chem. **2018**, *57*, 13318-13329.

A. Bauer, A. Jäschke, **S. Schöne**, R. Barthen, J. März, K. Schmeide, M. Patzschke, B. Kersting, K. Fahmy, J. Oertel, V. Brendler, T. Stumpf: *Uranium(VI) Complexes with a Calix[4]arene-Based 8-Hydroxyquinoline Ligand: Thermodynamic and Structural Characterization Based on Calorimetry, Spectroscopy, and Liquid–Liquid Extraction,* ChemistryOpen **2018**, *7*, 467-474.

S. Schöne, J. März, T. Stumpf, A. Ikeda-Ohno: *Mixed-valent neptunium oligomer complexes based on cation–cation interactions* Dalton Trans. **2019**, *48*, 6700-6703.

S. Fichter, S. Kaufmann, P. Kaden, T. S. Brunner, T. Stumpf, P. W. Roesky, J. März: *Enantiomeric pure Tetravalent Neptunium Amidinates: Synthesis and Characterization* Chem. Eur. J., **2020**, *26*, 8867-8870.

S. Fichter, R. Kloditz, S. Kaufmann, T. S. Brunner, P. Kaden, M. Patzschke, T. Stumpf, P. W. Roesky, M. Schmidt, J. März: *A Series of Tetravalent Actinide Amidinates: Structure Determination and Bonding Analysis* Inorg. Chem., **2020**, *59*, 15670-15680.

T. Radoske, R. Kloditz, **S. Fichter**, J. März, P. Kaden, M. Patzschke, M. Schmidt, O. Walter, T. Stumpf, A. Ikeda-Ohno: *Systematic comparison of the structure of homoleptic salen-type complexes of tetravalent metals (M(IV) = Zr, Hf, Ce, Th, U, Np, and Pu) in the solid state and solution* Dalton Trans., *submitted.*

T. Radoske, R. Kloditz, **S. Fichter**, P. Kaden, J. März, T. Stumpf, M. Schmidt: *Covalent Trends in the Actinide Series: Bis(chloro)monosalen Complexes with Tetravalent Th, U, Np, and Pu* Inorg. Chem., *to be submitted.*

K. Shimojo, T. Sasanuki, **S. Fichter**, M. Yabe, T. Sugita, M. Ikeda, N. Hirayama, Y. Habata, A. Ikeda-Ohno: *Development of tetradentate diamide-type extractant containing an acidic moiety for selective extraction of scandium from rare-earth elements*, in preparation.

K. Shimojo, T. Sugita, **S. Fichter**, M. Yabe, M. Ikeda, N. Hirayama, Y. Habata, A. Ikeda-Ohno: *Mutual separation of indium and gallium from zinc and aluminium using an acidic diamide-type extractant*, in preparation.

KONFERENZBEITRÄGE

S. Schöne, J. März, P. Kaden, J. J. Weigand, P. W. Roesky, T. Stumpf, A. Ikeda-Ohno: *The First Chiral Benzamidinate Complexes of Tetravalent Actinides (An(IV)) - Synthesis and Characterization*, Actinides 2017, 09.-14.07.2017, Sendai, Japan (Vortrag).

S. Schöne, T. Radoske, J. März, T. Stumpf, A. Ikeda-Ohno: *Synthesis and Structural Characterization of Mixed Iron-Uranium Compounds with Bidentate N-Donor Ligands*, Migration 2017 - 16th International Conference on the Chemistry and Migration Behaviour of Actinides and Fission Products in the Geosphere, 10.-15.09.2017, Barcelona, Spanien (Vortrag).

S. Schöne, J. März, M. Patzschke, R. Kloditz, P. Kaden, P. W. Roesky, T. Stumpf, A. Ikeda-Ohno: *Synthesis and Characterization of the First Chiral Benzamidinate Complexes of Tetravalent Actinides (An(IV))*, ISNSC 2018 - 10th International Symposium on Nano and Supramolecular Chemistry, 09.-12.07.2018, Dresden, Deutschland (Vortrag).

S. Schöne, R. Kloditz, J. März, P. Kaden, M. Patzschke, P. W. Roesky, T. Stumpf, A. Ikeda-Ohno: *Synthesis and Characterization of Tetravalent Actinide Complexes with Nitrogen Donor Ligands*, Plutonium Futures - The Science 2018, 09.-14.09.2018, San Diego, USA (Poster).

S. Schöne, R. Kloditz, J. März, P. Kaden, M. Patzschke, P. W. Roesky, T. Stumpf: *Enantiopure Tetravalent Actinide Amidinates - Synthesis and Reactivity*, JdA 2019 - 49èmes Journées des Actinides, 14.-18.04.2019, Erice, Italien (Vortrag).

S. Schöne, R. Kloditz, J. März, P. Kaden, M. Patzschke, P. W. Roesky, T. Stumpf: *Amidinates - Versatile Ligands for Tetravalent Actinides*, Jahrestagung der GDCh-Fachgruppe Nuklearchemie 2019, 25.-27.09.2019, Dresden, Deutschland (Vortrag).

CONTENTS

SUMMARY

The intriguing chemistry of the actinide elements lacks a fundamental understanding of their inherent properties even more than 80 years after the discovery of the first transuranium element, neptunium. This is for instance reflected in the relatively small number of structurally characterized actinide (8,790 hits) and especially transuranium complexes (537 hits) in the *Cambridge Structural Database* (as of 05/29/2020). The motivation behind this PhD work is thus the investigation of the coordination chemistry of the early actinides (i.e. thorium to plutonium) with organic ligand molecules to narrow this knowledge gap and to deduce their fundamental properties. To this end, this work has synthesized and characterized 36 new compounds, among those the first transuranium amidinate complexes and the first metal-organic neptunium complex possessing a Np–Br bond. These compounds have been characterized not only in the solid state, but wherever possible solution structures have been determined and high-level quantum chemical calculations have been performed to obtain a comprehensive picture of their structures and bonding situation. The thesis covers the most important oxidation states (+III to +VI) of the early actinides but mainly focuses on the tri- and tetravalent oxidation state owing to their accessibility for the early actinides and also for lanthanide and transition metals to compare their properties with. This work aims in particular to elucidate the potential participation of the actinides' valence orbitals in the bonding to medium hard donor atoms like nitrogen in order to compare the actinide–nitrogen bond properties with their lanthanide and transition metal analogues. The degree of covalent interaction in actinide complexes plays an important role in the prediction of their behavior in naturally relevant systems and for separation processes in nuclear industry.

The properties of the An–N bonds are studied by the synthesis of series of actinide complexes using amidinate ligands and are then compared to isostructural lanthanide and transition metal analogues. The analysis of the coordinative bond lengths together with an elucidation of the structures in solution is the key to understand the behavior of the actinide complexes. These investigations are supported by quantum chemical calculations for a detailed analysis of the complexes' electronic structure.

Two different types of amidinate ligands, N,N'-Bis(isopropyl)-benzamidinate (iPr$_2$BA) and (S,S)-N,N'-Bis(1-phenylethyl)-benzamidinate ((S)-PEBA) are used to synthesize series of isostructural bis- and tris(amidinate) complexes. It is shown that the maximum accessible stoichiometry, i.e. the metal-to-ligand ratio, is determined by the ionic radius of the respective metal cation and the steric demand of the ligand itself. Hence, the relatively small tetravalent transition metal analogues titanium and hafnium exclusively form bis(amidinate) complexes with the used benzamidinates whereas tris(amidinate) complexes could be synthesized for the bigger tetravalent cations zirconium and cerium, as well as the actinides thorium, uranium, and neptunium. The difference between the coordination chemistry of the transition metals

zirconium and hafnium with the used amidinate ligands is highly unexpected and could hold implications for future separation technologies.

Two series of tris(amidinate) complexes [$M^{IV}Cl(iPr_2BA)_3$] and [$M^{IV}Cl((S)\text{-}PEBA)_3$] have been synthesized and analyzed regarding their coordinative bond lengths. Single crystal X-ray diffraction (SC-XRD) data indicates a predominantly ionic bonding interaction between the metals and the coordinating atoms, i.e. N and Cl, with the notable exception of the tetravalent cerium complex [$CeCl((S)\text{-}PEBA)_3$] showing noticeably longer bond lengths than the isostructural actinide complex series. This points to a different binding behavior between the $4f$ and $5f$ elements which is investigated using quantum chemical calculations. Quantum theory of atoms in molecules (QTAIM) and natural bond orbital (NBO) analysis of the [$M^{IV}Cl((S)\text{-}PEBA)_3$] complex series indicates a more covalent character of the Ce–N bonds compared to the actinide analogue thorium despite the longer than expected bond lengths. This unforeseen result emphasizes the power of quantum chemical calculations and reveals the strong impact of various crystal packing effects on the elucidation of bond properties. In addition, QTAIM and NBO analyses further reveal an increase of the covalent character when traversing the actinide series from thorium to uranium followed by a plateau from uranium to plutonium, but a different origin. For uranium the major contribution to the covalent character stems from the participation of $6d$ orbitals, whereas for plutonium the $5f$ contribution is dominant. Thus, unless expected otherwise, the prominent role of the $5f$ orbitals in the bonding to nitrogen donor ligands manifests itself only for tetravalent neptunium and plutonium and not for the lighter actinides.

In contrast to the investigations of the [$M^{IV}Cl((S)\text{-}PEBA)_3$] complex series, a detailed analysis of the binding properties of the trivalent actinide complexes of [$M^{III}((S)\text{-}PEBA)_3$] type unequivocally confirms a higher degree of covalent character of the An^{III}–N bonds compared to the lanthanide analogues by both, experimentally determined M^{III}–N bond lengths and quantum chemical calculations using QTAIM and NBO analyses. This difference in covalent character of tri- and tetravalent actinide complexes is expected to stem from the higher LEWIS acidity of the latter, but has been corroborated for the first time within this thesis using the same type of nitrogen donor ligand for both oxidation states. The results indicate a participation of the actinides' valence electrons in the bonding and hence an increased overlap with the ligand orbitals especially for the trivalent actinides.

The tetravalent actinide chloro tris(amidinate) complexes have been further investigated regarding their reactivity using (pseudo)halide exchange reactions yielding the corresponding fluoro, bromo, and azido complexes. It has to be pointed out, that this substitution chemistry is applied for the first time for a transuranium element, yielding unprecedented neptunium (pseudo)halide complexes. Thus, the well-known coordination and substitution chemistry of uranium complexes has been successfully expanded to neptunium which opens new

opportunities to study the fundamental properties of the early actinides with a broader range of accessible compounds.

Within this thesis some of these fundamental properties have been studied for the actinide amidinate complexes by means of nuclear magnetic resonance (NMR) spectroscopy. For the first time the dependence of the paramagnetic hyperfine shift on the number of f electrons has been investigated systematically for tetravalent actinide complexes. Generally, an increase of the hyperfine shift with increasing number of f electrons could be revealed with the remarkable exception of the [UF((S)-PEBA)$_3$] complex. The strongly coordinating fluoride is altering the ligand field of the tetravalent uranium to induce an inverted behavior of the pseudocontact shift. Most remarkably, this behavior is not observed for the isostructural neptunium complex [NpF((S)-PEBA)$_3$], which could be confirmed by multi-configurational quantum chemical calculations. This unexpected behavior of a relatively simple tetravalent uranium complex further underlines the need for a profound analysis of actinides' paramagnetic properties to finally interpret their NMR spectra in more detail.

For the sake of a comprehensive investigation of the early actinide elements also their higher-valent oxidation states (+V and +VI) have been investigated within this thesis using nitrogen donor ligands (i.e. amidinates and diimine ligands). Also here, a rather unexpected behavior of the actinides have been revealed, as it could be shown that these ligands are able to perturb the relatively strong *trans*-dioxo uranyl moiety by the formation of strong intramolecular hydrogen bonding interactions. As a result, the [UO$_2$Cl$_2$(phen)$_2$] complex (phen = 1,10-phenanthroline) shows one of the most strongly bent O–U–O angle (i.e. 161.8(1)°) reported so far, with strong indications for enhanced reactivity of the otherwise relatively inert uranyl moiety.

In summary, during this PhD work it could be shown that nitrogen donor ligands show strong interactions with actinides in all investigated oxidation states. The binding shows varying degrees of covalency, evident in experimental findings and confirmed by computational results, with a general trend towards higher degrees of covalency for the softer actinide/actinyl cations (+III and +V). Nitrogen donor ligands as medium hard donors have shown the potential to investigate the fundamental properties and especially the coordination chemistry of the actinides comprehensively. These investigations should also be taken into account for further studies regarding the complexation of low-valent actinides with ligands bearing nature-derived functional groups to evaluate their influence on the behavior of actinide elements in the environment.

ZUSAMMENFASSUNG

Auch mehr als 80 Jahre nach der Entdeckung des ersten Transuranelements sind die fundamentalen Eigenschaften der Actiniden noch nicht hinreichend untersucht. Dies zeigt sich zum Beispiel in der relativ geringen Anzahl von strukturell charakterisierten Actinid- (8.790 Treffer) und insbesondere Transuran-Komplexen (537 Treffer) in der Cambridge Structural Database (Stand 29.05.20). Die Motivation dieser Doktorarbeit ist es daher, die bestehende Wissenslücke über die grundlegenden Eigenschaften der frühen Actinide, d.h. der Elemente Thorium bis Plutonium, durch die Untersuchung ihrer Koordinationschemie mit organischen Ligandmolekülen zu verringern. Zu diesem Zweck wurden während dieser Arbeit 36 neue Actinidverbindungen synthetisiert und charakterisiert, darunter auch die ersten Transuran-Amidinat-Komplexe und der erste metallorganische Neptuniumkomplex, welcher eine koordinative Np–Br Bindung aufweist. Die Charakterisierung dieser Verbindungen erfolgte nicht nur im festen Zustand, sondern auch in Lösung. Zusätzlich wurden quantenchemische Berechnungen durchgeführt, sodass ein umfassendes Bild der Komplexstrukturen und ihrer Bindungssituation erstellt werden konnte. Diese Arbeit beinhaltet Komplexverbindungen der frühen Actiniden in deren wichtigsten Oxidationsstufen (+III bis +VI), wobei der Hauptschwerpunkt auf der drei- und vierwertigen Oxidationsstufe aufgrund der einfachen Zugänglichkeit und Vergleichbarkeit mit Lanthaniden und Übergangsmetallen liegt. Das Ziel dieser Arbeit ist es zudem, die potentielle Beteiligung der Valenzorbitale der Actiniden an der Bindung zu weniger harten Donoratomen, wie Stickstoff, aufzuklären. Dazu werden die Eigenschaften der Actinid–Stickstoff-Bindungen innerhalb von Serien von Actinid-Amidinat-Komplexen mit ihren Lanthanid- und Übergangsmetall-Analoga verglichen. Diese Untersuchungen werden durch quantenchemische Berechnungen unterstützt, um eine detaillierte Analyse der elektronischen Struktur der Komplexverbindungen zu ermöglichen.

Im Rahmen dieser Arbeit wurden zwei verschiedene Arten von Amidinaten, *N,N′*-Bis(isopropyl)-benzamidinat (*i*Pr$_2$BA) und (*S,S*)-*N,N′*-Bis(1-phenylethyl)-benzamidinat ((*S*)-PEBA), zur Synthese von isostrukturellen Bis- und Tris(amidinat)-Komplexen eingesetzt. Es konnte dabei gezeigt werden, dass die maximal zugängliche Stöchiometrie, d.h. das Metall-zu-Ligand Verhältnis, durch den Ionenradius der jeweiligen Metallkationen und den sterischen Bedarf des Liganden bestimmt wird. So bilden die relativ kleinen vierwertigen Übergangsmetalle Titan und Hafnium ausschließlich Bis(amidinat)-Komplexe mit den verwendeten Benzamidinaten, während Tris(amidinat)-Komplexe für die größeren vierwertigen Kationen Zirkonium und Cer sowie die Actiniden Thorium, Uran, und Neptunium synthetisiert werden konnten. Der Unterschied zwischen der Koordinationschemie der Übergangsmetalle Zirkonium und Hafnium mit den verwendeten Amidinatliganden ist unerwartet und könnte hinweisgebend für zukünftige Trenntechnologien der beiden Elemente sein.

Es wurden zudem zwei Serien von Tris(amidinat)-Komplexen ([M^{IV}Cl(iPr$_2$BA)$_3$] und [M^{IV}Cl((S)-PEBA)$_3$]) synthetisiert und hinsichtlich ihrer koordinativen Bindungslängen analysiert. Einkristall-Röntgenbeugungsdaten (SC-XRD) weisen auf eine vorwiegend ionische Bindung zwischen den Metallen und den koordinierenden Atomen (Stickstoff und Chlor) hin. Eine bemerkenswerte Ausnahme bildet dabei der vierwertige Cerkomplexes [CeCl((S)-PEBA)$_3$], welcher deutlich längere Bindungslängen als die isostrukturelle Actinidenkomplexserie aufweist. Dies deutet auf ein unterschiedliches Bindungsverhalten zwischen den 4f- und 5f-Elementen hin, welches mit quantenchemischen Berechnungen untersucht wurde. Die Analyse mittels *Quantum Theory of Atoms in Molecules* (QTAIM) und *Natural Bond Orbitals* (NBO) weist auf einen kovalenteren Charakter der Ce–N-Bindungen im Vergleich zu den Th–N-Bindungen hin. Dieses unerwartete Ergebnis unterstreicht die Notwendigkeit quantenchemischer Berechnungen und zeigt den starken Einfluss verschiedener Kristallpackungseffekte auf die Aufklärung der Bindungseigenschaften.

Darüber hinaus zeigen QTAIM- und NBO-Analysen eine Zunahme des kovalenten Charakters innerhalb der Actinidenserie von Thorium zu Uran, gefolgt von einem Plateau ähnlicher Kovalenz von Uran zu Plutonium. Die Ursache der kovalenten Wechselwirkung unterscheidet sich jedoch. Bei Uran ergibt sich der Hauptbeitrag zum kovalenten Charakter aus der Beteiligung von 6d-Orbitalen, während bei Plutonium der 5f-Beitrag dominant ist. Die bestimmende Rolle der 5f-Orbitale bei der Bindung zu Stickstoff-Donor-Liganden zeigt sich daher nur für vierwertiges Neptunium und Plutonium und nicht für die leichteren Actiniden.

Im Gegensatz zu den Untersuchungen der [M^{IV}Cl((S)-PEBA)$_3$]-Komplexreihe bestätigt eine detaillierte Analyse der Bindungseigenschaften der dreiwertigen Actinidkomplexe vom Typ [M^{III}((S)-PEBA)$_3$] eindeutig einen höheren kovalenten Anteil der An^{III}–N-Bindungen im Vergleich zu den Lanthanid-Analoga sowohl durch experimentell bestimmte M^{III}–N-Bindungslängen als auch durch quantenchemische Berechnungen mittels QTAIM- und NBO-Analysen. Dieser Unterschied im kovalenten Charakter von drei- und vierwertigen Actinidkomplexen kann auf die höhere LEWIS-Acidität der Letzteren zurückgeführt werden. Dies wurde zum ersten Mal unter Verwendung des gleichen Typs von Stickstoff-Donor-Liganden für beide Oxidationszustände im Rahmen dieser Arbeit bestätigt. Die Ergebnisse deuten weiterhin auf eine Beteiligung der Valenzelektronen der Actiniden an der Bindung und damit auf einen erhöhten Überlapp mit den Ligandorbitalen, insbesondere für die dreiwertigen Actiniden, hin.

Die vierwertigen Actinid-Chloro-Komplexe wurden außerdem hinsichtlich ihrer Reaktivität untersucht, wobei (Pseudo-)Halogenid-Austauschreaktionen durchgeführt wurden. Diese ergaben die entsprechenden Fluoro-, Bromo- und Azidokomplexe. Diese Substitutionschemie wurde dabei erstmals für ein Transuranelement angewandt, wodurch unbekannte Neptunium-

(Pseudo)halogenid-Komplexe hergestellt werden konnten. Somit wurde die bekannte Koordinations- und Substitutionschemie von Urankomplexen erfolgreich auf Neptunium übertragen, was neue Möglichkeiten eröffnet, die grundlegenden Eigenschaften der frühen Actiniden mit einem breiteren Spektrum zugänglicher Verbindungen zu untersuchen.

Im Rahmen dieser Arbeit wurden außerdem einige dieser grundlegenden Eigenschaften der Actinid-Amidinat-Komplexe mit Hilfe der kernmagnetischen Resonanzspektroskopie (NMR) untersucht. Zum ersten Mal wurde dabei die Abhängigkeit der paramagnetischen Hyperfeinverschiebung von der Anzahl der f-Elektronen für vierwertige Actinidkomplexe systematisch untersucht. Generell konnte dabei eine Zunahme der Pseudokontaktverschiebung mit zunehmender Anzahl von f-Elektronen nachgewiesen werden, mit der bemerkenswerten Ausnahme des [UF((S)-PEBA)$_3$]-Komplexes. In diesem Komplex verändert das stark koordinierende Fluorid das Ligandenfeld des vierwertigen Urans, um ein umgekehrtes Verhalten der Pseudokontaktverschiebung zu induzieren. Dabei ist besonders hervorzuheben, dass dieses Verhalten nicht für den isostrukturellen Neptuniumkomplex [NpF((S)-PEBA)$_3$] beobachtet wird, was auch durch quantenchemische Berechnungen bestätigt werden konnte. Dieses unerwartete Verhalten eines relativ einfachen vierwertigen Urankomplexes unterstreicht die Notwendigkeit einer tiefgreifenden Analyse der paramagnetischen Eigenschaften der Actiniden, um letztendlich ihre NMR-Spektren detaillierter interpretieren zu können.

Im Sinne einer umfassenden Untersuchung der frühen Actinidenelemente wurden im Rahmen dieser Arbeit auch deren höherwertige Oxidationsstufen (+V und +VI) mit Stickstoff-Donor-Liganden (Amidinaten und Diiminliganden) untersucht. Auch hier zeigte sich ein eher unerwartetes Verhalten der Liganden, da diese in der Lage sind, die relativ starke *trans*-Uranyleinheit durch die Bildung starker intramolekularer Wasserstoffbrückenbindungen zu beeinflussen. Infolgedessen besitzt die Uranyleinheit des [UO$_2$Cl$_2$(phen)$_2$]-Komplexes (phen = 1,10-Phenanthrolin) einen der kleinsten bisher bekannten O–U–O-Winkel von 161,8(1)°.

Zusammenfassend konnte während dieser Doktorarbeit gezeigt werden, dass Actiniden in allen untersuchten Oxidationszuständen starke Wechselwirkungen mit Stickstoff-Donor-Liganden eingehen, was zur Synthese einer Vielzahl unbekannter Actinidkomplexe führte. Die Bindungsanalyse der An–N-Bindung zeigte dabei unterschiedliche Kovalenzanteile, mit einem allgemeinen Trend zu höheren Anteilen für die weicheren Actinid bzw. Actinyl-Kationen (+III und +V). Mit Hilfe von Stickstoff-Donor-Liganden als weniger harte Donoren konnten somit die grundlegenden Eigenschaften und insbesondere die Koordinationschemie der Actiniden umfassend untersucht werden. Diese Untersuchungen sollten auch für weitere Studien über die Komplexierung von Actiniden mit Liganden in Betracht gezogen werden, welche naturstoffnahe funktionelle Gruppen tragen, um ihren Einfluss auf das Verhalten von Actiniden in der Umwelt detaillierter bewerten zu können.

1 Motivation and Objectives

Ever since the discovery of nuclear fission[1-2] various countries all over the world have used nuclear energy to meet their rising energy needs. Globally the number of nuclear power plants is constantly increasing despite critical accidents in Chernobyl (1986) and Fukushima Daiichi (2011). As a consequence of the latter, Germany decided to shut down their nuclear power plants until 2022.[3] Even after the shutdown of a nuclear power generation program the disposal of spent nuclear fuel remains a challenge for several generations due to the long half-lives of fission products and especially the bred heavy nuclides. Thus, the knowledge about these man-made transuranic elements is crucial, not only for the nuclear fuel cycle but also for the safety assessment of a high-level nuclear waste repository. Due to the relatively short time since their discovery and the handling restrictions based on their radioactivity, investigations of transuranium elements remain scarce even until today. This is for example reflected in the relatively small number of structurally characterized transuranium complexes deposited in the *Cambridge Structural Database* as shown in Figure 1. Even the number of known compounds of the relatively common, naturally occurring elements thorium and uranium is small compared to various transition metals such as iron (55,193 hits) or copper (72,576 hits). This lack of fundamental knowledge about actinide complexes is the general motivation of this thesis. The synthesis and characterization of formerly unknown actinide complexes, especially of transuranium actinides, helps to narrow this knowledge gap as every structure determination is a tremendous achievement to actinide science, especially as a comprehensive approach combining solid and solution state characterization as well as a description by quantum chemical calculations.

The early actinides thorium to plutonium are characterized by a wide variety of oxidation states +II to +VII with +III to +VI being in general the most stable under environmental conditions.[4] The heavier 5f elements, starting from americium, show primarily the trivalent oxidation state like their 4f counterparts, the lanthanides.
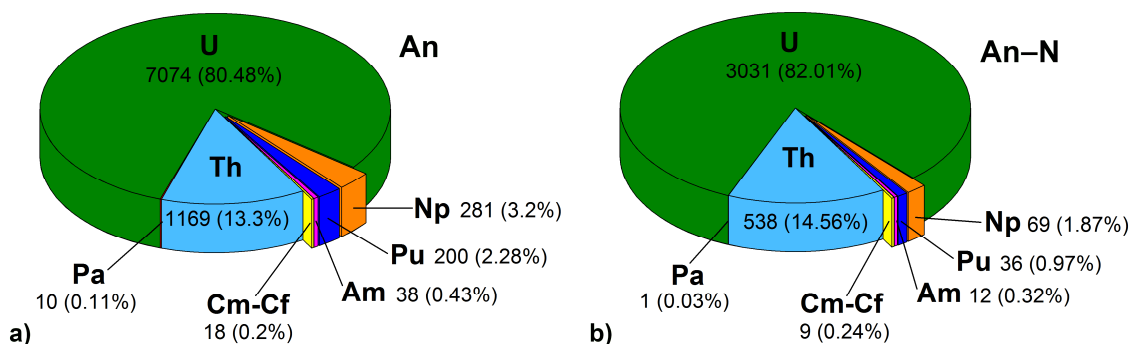

Figure 1. Total amount and fraction of structurally characterized actinide complexes (a) and actinide complexes possessing An–N bonds (b) in *Cambridge Structural Database* (WebCSD, 05/29/2020).

This similarity makes their separation in the reprocessing of spent nuclear fuel a challenge which was eventually overcome by development of ligands possessing specific functionalities, for example nitrogen donor groups.[5] The origin of the selectivity of these ligands has been debated for a long time and could only recently be attributed to an increased covalent interaction of the actinides with the softer donors which is not observed for the lanthanides.[6] This property of actinides to establish covalent interactions with soft donor functionalities can be seen as the starting point for the investigations presented in this work.

The tetravalent oxidation state of the early actinides is the most accessible one for the whole series from thorium to plutonium. Furthermore, most of these elements are expected to exhibit this oxidation state under reducing conditions as they would prevail in a deep geological disposal site.[7] Thus, the fundamental understanding of the early actinides in their tetravalent oxidation state can be seen as equally important as the investigation of the heavier actinides in their trivalent oxidation state.

The assessment of fundamental properties of actinides is often achieved by synthesis of actinide complex series and comparison of their properties to well-studied lanthanide and transition metal analogues.[8-18] The major objective of this work is therefore the synthesis of isostructural complex molecules using nitrogen donor groups, especially amidinate ligands. The amidinate moiety is a well-known ligand motif which has already been widely used in transition metal and lanthanide coordination chemistry with applications in catalysis and chemical vapor deposition methods.[19] Amidinates can be regarded as the nitrogen analogues to carboxylic acids. Their electronic and steric properties can be easily tuned by change of the central and peripheral substituents. In fact, the amidinate ligands have shown the ability to act as a sterically demanding stabilizing ligand similar to the widely used cyclopentadienyl ligands (Cp) in organometallic chemistry.[20] Thus, it is expected that this ligand system will also be suitable for the synthesis and characterization of actinide complexes in different oxidation states. Amidinate complexes of transuranic elements are entirely unknown up to now, which further motivated this study.

This thesis will cover a small but consistent field of actinide chemistry and aims to investigate the complexation behavior of mainly tri- and tetravalent actinides with amidinate ligands in the solid state and in solution. A special focus is given to the analysis of the nuclear magnetic resonance (NMR) spectra which are influenced by the paramagnetism of the actinides originating from their partly filled $5f$ shells (for U, Np, and Pu). This paramagnetic influence has been extensively used in molecular biology to elucidate the tertiary structure of proteins and enzymes using labelling with trivalent paramagnetic lanthanide ions.[21] The fundamental parameters of tri- and tetravalent actinide ions regarding their paramagnetic influence on chemical shifts of coordinated ligand molecules are not known. Thus, the determination of intrinsic parameters like the susceptibility tensor for actinide ions are aimed at.

Finally the question to be answered is, if the tetravalent actinides behave as their trivalent analogues showing an increased degree of covalency in their bonding behavior or if they behave as hard LEWIS acids with mainly ionic bonding interactions. This is achieved by comparison to tetravalent lanthanide and transition metal analogues regarding their structures in the solid state as well as in solution and also the electronic properties of the formed bonds analyzed by quantum chemistry.

In addition to these comprehensive investigations on the behavior of tri- and tetravalent actinides also the chemistry of penta- and hexavalent actinides in the presence of nitrogen donor ligand is of interest due to their appearance or even predominance under aerobic conditions. The presence as dioxo cations makes the chemistry of these high-valent actinides quite different from that of the highly charged low-valent cations. These differences will also be investigated in this thesis by complexation of hexavalent actinides with amidinates and, additionally, diimine ligands. Furthermore, these fundamental investigations will focus on the possibilities to perturb the very stable *trans*-dioxo uranyl(VI) cation by crystal engineering and will additionally reveal the possibility of pentavalent neptunyl cations to act as coordinated metal centers and coordinating ligands by cation-cation interactions simultaneously.

Thus, the coordination chemistry of nitrogen donor ligands with the early actinides in the whole range of environmentally accessible oxidation states (+III to +VI) has been investigated within this PhD thesis with a special focus on transuranium elements. This will increase our fundamental knowledge about the actinides in various oxidation states and finally support potential safety assessments of future nuclear waste disposal sites or studies concerning the behavior of actinides in the environment.

2 FUNDAMENTALS

This thesis focuses on the coordination chemistry of the early actinides in their most accessible oxidation states (+III to +VI) with nitrogen donor ligands. In order to give a brief introduction into the topic, first, the fundamental aspects of actinide chemistry are reviewed. Thereafter the used nitrogen donor ligands will be introduced and finally the fundamental methods used for structure determination in the solid state, in solution and quantum chemical calculation methods are discussed.

2.1 Actinides

This sections aims to highlight the chemical properties of the actinide elements which have been subject to numerous research activities. After a general introduction, the electronic structure of the actinides is discussed, as it is the key to understand their fundamental properties. Thereafter, general aspects of the chemistry of actinides in both, aqueous and organic media are briefly presented.

2.1.1 General aspects

The actinide elements[1] are located at the bottom of the periodic table gradually filling the $5f$ subshell.[4] Historically, the elements thorium and uranium have been known since the end of the 18th (uranium, 1789), respectively, the beginning of the 19th (thorium, 1829) century. At the end of the 19th century Henry BECQUEREL and Pierre and Marie CURIE discovered the inherent radioactivity of both elements, a property the whole actinide series possesses. However, the half-lives of ^{232}Th $(1.405 \cdot 10^{10}$ a$)$ and ^{238}U $(4.468 \cdot 10^{9}$ a$)$ resp. ^{235}U $(7.038 \cdot 10^{8}$ a$)$ are sufficiently long to be accounted as primordial nuclides which still persist on earth since its formation $(4.6 \cdot 10^{9}$ a$)$. It has also been proposed that ^{244}Pu $(t_{1/2} = 8 \cdot 10^{7}$ a$)$ can be found naturally in rare-earth minerals in traces and can hence be regarded as a primordial nuclide, too.[23] However, the results have been questioned recently.[24] The lighter actinide elements actinium and protactinium can also be found in trace amounts in uranium ores as daughter nuclides of ^{238}U or ^{235}U due to their radioactive decay. The transuranic elements neptunium and plutonium have been the first man-made elements in human history, albeit both also appear in nature due to neutron capture of ^{238}U and subsequent β⁻ decay to ^{239}Np and finally ^{239}Pu (see Scheme 1). The neutrons for this reaction may stem from spontaneous fission of ^{238}U or other naturally occurring nuclear reactions producing neutrons.

---

[1] According to the International Union of Pure and Applied Chemistry (IUPAC) the right term would be actinoid as the ending 'ide' indicates a negative ion. Furthermore, actinium should not be included as it is not 'like actinium'. However, due to common usage the IUPAC also accepts to use the term actinides including actinium and the term lanthanide including lanthanum which will be used throughout this thesis.[22]

$$^{238}U(n,\gamma)^{239}U \xrightarrow{\ \beta^-,\ 23.5\ min\ } {}^{239}Np \xrightarrow{\ \beta^-,\ 2.36\ d\ } {}^{239}Pu$$
$$(t_{1/2} = 2.4 \cdot 10^4\ a)$$
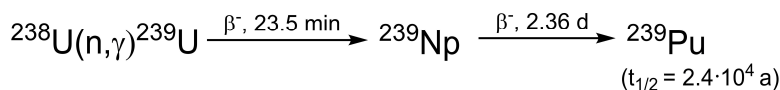
Scheme 1. Nuclear reaction to yield ^{239}Pu from ^{238}U.

Evidence for this reaction has also been given by analysis of naturally pitchblende samples.[25] The same reaction has been performed by MᴄMɪʟʟᴀɴ in 1939 to produce the first transuranic element, neptunium, by neutron capture.[26]

During World War II also the actinides plutonium,[27] americium,[28] and curium[28] have been discovered owing to the enhanced research activities connected with the Manhattan project. These are also the actinide elements which bear the highest potential risk for human kind as they could be used to produce nuclear weapons (^{235}U, ^{239}Pu) and possess the highest radiotoxicity in spent nuclear fuel ($^{238/239/240}$Pu, $^{241/243}$Am) for a long period of time (i.e. 10^2 to 10^6 a) after the decay of the relatively short-lived fission products (e.g. ^{90}Sr, ^{137}Cs).[29] The transcurium elements berkelium to fermium can only be prepared in high neutron flux reactors or in thermonuclear explosions due to multiple neutron capture and are hence not of environmental relevance also due to their relatively short half-lives.

The focus of the next sections is dedicated to the fundamental properties of the early actinide elements, especially thorium to plutonium, as they possess a rich and interesting chemistry due to their ability to exist in multiple oxidation states. This resembles a more transition-metal-like behavior compared to the transplutonium elements which show a lanthanide-like behavior with +III being the most stable oxidation state.

2.1.2 Electronic structure and oxidation states

The peculiarity of the early actinides arises from the orbital expansion of the *d* and *f* orbitals due to the increased shielding of the nucleus by the relativistic orbital contraction of *s* and *p* orbitals. This enables the *5f* and *6d* orbitals to expand into the valence region and to overlap with frontier orbitals of various donor atoms (see Figure 2).
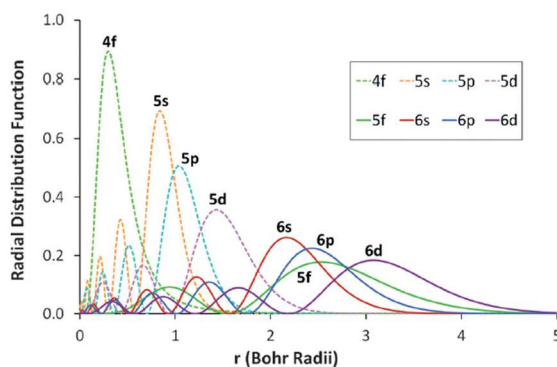

Figure 2. Illustration of radial distribution functions of *5s*, *6s*, *5p*, *6p*, *5d*, *6d*, *4f* and *5f* atomic orbitals.[30]

This is also the starting point for ongoing debates about the amount and the character of covalency in bonds between actinides and various ligand molecules.[9, 31-45] However, when traversing the actinide series from thorium to curium the 6*d* orbitals rise in energy whereas the 5*f* orbitals decline. Depending on the coordination environment around the metal center the orbital population within the early actinides can be changed making the determination of their electronic properties a challenge. The actinides possess a wide variety of oxidation states which arises from the aforementioned orbital expansion of the 5*f* electrons. Table 1 summarizes the possible oxidation states of the early actinides (Ac-Cm).

In general, the early actinides can access the formal oxidation states +II to the highest state which would be reachable by withdrawing all valence electrons (i.e. Ac^{III}, Th^{IV}, Pa^{V}, U^{VI}, and Np^{VII}). The trivalent oxidation state becomes prevalent starting from americium whereas the tetravalent one is easily accessible for the actinides thorium to plutonium. It has to be pointed out, that plutonium can simultaneously exist in four different oxidation states (i.e. +III to +VI) in aqueous solution.[46] Each oxidation state possesses intriguing properties which will be discussed next, first for naturally relevant, i.e. aqueous systems and thereafter for metal-organic complexes in organic solutions.

Table 1. Summary of actinide elements actinium to curium including their accessible oxidation states, valence electrons of metallic state and important isotopes. Oxidation states in bold are the most stable ones, in italic are only accessible in solids or organic solutions, in brackets are claimed but not confirmed independently. The most stable isotope is given for all actinides. Green elements are primordial, orange ones are naturally occurring as decay products and blue elements are mainly man-made. The representation is adapted from MAHER *et al.*[7]

					VII	VII	(VII)	
				VI	VI	VI	VI	
			V	V	**V**	V	V	
Oxidation states:		**IV**	IV	**IV**	IV	**IV**	IV	IV
	III	*III*	*III*	III	III	III	**III**	**III**
		II	*(II)*	*II*	*II*	*II*	*II*	
	89	**90**	**91**	**92**	**93**	**94**	**95**	**96**
	Ac	**Th**	**Pa**	**U**	**Np**	**Pu**	**Am**	**Cm**
Valence electrons:	-	-	5*f*^{2}	5*f*^{3}	5*f*^{4}	5*f*^{6}	5*f*^{7}	5*f*^{7}
	6*d*^{1}	6*d*^{2}	6*d*^{1}	6*d*^{1}	6*d*^{1}	-	-	6*d*^{1}
	7*s*^{2}	7*s*^{2}	7*s*^{2}	7*s*^{2}	7*s*^{2}	7*s*^{2}	7*s*^{2}	7*s*^{2}
Most stable isotope:	^{227}Ac	^{232}Th	^{231}Pa	^{238}U	^{237}Np	^{244}Pu	^{243}Am	^{247}Cm

2.1.3 Aqueous chemistry

Generally, actinides have been stabilized in oxidation states +III to +VII in aqueous solution. The trivalent oxidation state is prevalent for americium, curium and the heavier actinides in aqueous solution. The trivalent neptunium and plutonium cations could also exist under naturally occurring conditions.[7] In contrast, the trivalent oxidation state of uranium cannot be stabilized in water, as it is oxidized under hydrogen evolution due to its low redox potential.

The tetravalent oxidation state is instead prevalent for the early actinides thorium to plutonium under reducing conditions. Thorium is exclusively existing as a tetravalent cation in aqueous solutions whereas the protactinium(IV) cation tends to be easily oxidized to the more stable Pa^V. For uranium and neptunium the tetravalent oxidation state is maintained under mainly reducing conditions, whereas for plutonium the tetravalent oxidation state is only occurring in a narrow range of redox potential and pH values due to the formation and stabilization of trivalent plutonium in aqueous solution.[7] Both, the tri- and the tetravalent actinides exist as highly charged cations in aqueous solutions, having approximately nine water molecules coordinated (see Figure 3a,b). Especially the tetravalent actinides are hard LEWIS acids which tend to form hydrolysis species and precipitate as hydroxides even at low pH values and low concentrations.[47] Thus, they can be regarded as mainly immobile but may be solvated in the presence of organic[48] and inorganic[49] ligands or due to nanoparticle or colloid formation[50-51] and become mobile again. The analysis of the coordination chemistry of the tetravalent actinides with nitrogen donor ligands within this thesis will also help to understand their impact on the solubility in aqueous solutions.

The actinides in higher oxidation states +V and +VI exist as oxo-cations, named "yl" cations in aqueous solution with the dioxo cations of uranium, neptunium and plutonium being the most studied ones due to their prevalence under naturally occurring conditions. The two axial oxygen atoms bind very strongly (formally $An\equiv O$ triple bond) to the actinides and are exclusively forming a linear arrangement in solution, so that the coordination is mainly limited to the equatorial plane.[52] In the case of the uranyl(VI) cation five water molecules can be coordinated (see Figure 3c).

In addition, actinyl cations have the unique possibility to perform cation-cation interactions (CCIs), i.e. interactions between the "yl" oxygens carrying a partial negative charge and another adjacent cationic center. Such interactions have been observed first in aqueous solution between penta- and hexavalent actinyl cations.[53-54] Also in the solid state such interactions have been observed especially for neptunyl(V) compounds.[55] Generally, pentavalent actinyl cations are forming stronger cation-cation interactions than hexavalent actinyl cations due to the higher basicity of the "yl" oxygens in the former. However, also solid-state compounds possessing CCIs with hexavalent uranyl[56-57] and neptunyl[58] are known.
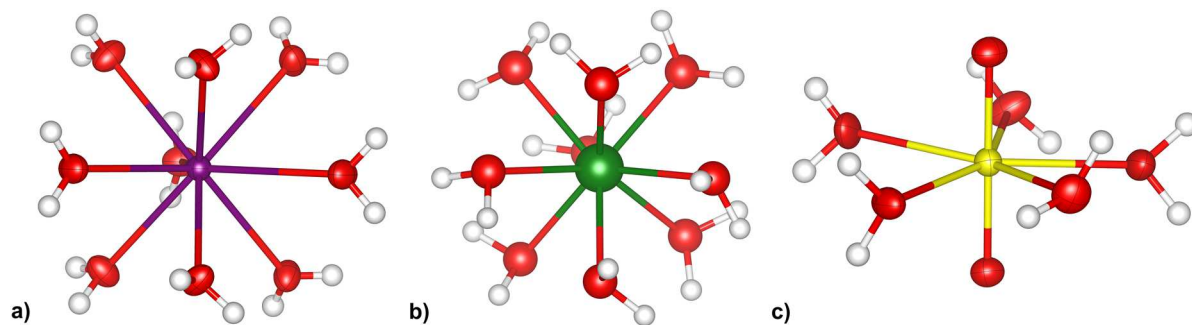
Figure 3. Coordination environment of a) tri-, b) tetra- and c) hexavalent uranium cations in aqueous solution. Structures of tri- and hexavalent uranium have been determined in the solid state by single crystal X-ray diffraction (SC-XRD) of $[U(H_2O)_9(CF_3SO_3)_3]$[59] and $[(UO_2)_2(chdc)_2(C_2O_4)][UO_2(H_2O)_5]$ $\cdot(12C4)\cdot2H_2O$[60].[2] The structure of $[U(H_2O)_9]^{4+}$ has been geometry optimized by quantum chemical calculations.[3]

Especially the hydrolysis tendency of the highly charged tetravalent actinide cations influences their complexation behavior with nitrogen donor ligands due to their basicity. Therefore systematical studies on the coordination chemistry of tri- and tetravalent actinides with amidinate ligands are performed under the exclusion of water and oxygen in organic media. Thus, the fundamental aspects of metal-organic coordination chemistry of actinides are introduced in the following.

2.1.4 Metal-organic coordination chemistry

In organic media a broader range of oxidation states, especially low-valent oxidation states of the actinides could be stabilized in recent years. Starting in 2013 the group of EVANS synthesized the first divalent actinide complexes $[K(crypt)][An(Cp'')_3]$[4] (An = Th,[61] U,[62] Np,[63] Pu[64]). Recently also a non-ionic homoleptic uranium(II) compound ($[U(Cp^R)_2]$)[5] has been reported opening a new field of low-valent actinide chemistry.[65]

Furthermore, the absence of water enables a study of the highly LEWIS-acidic tri- and especially tetravalent actinides in solution without the formation of hydrolyzed species and precipitates. Trivalent uranium complexes are easily accessible in organic solutions and have been extensively used in small-molecule activation,[66] catalysis,[67-68] and magnetic studies.[30] Also the first trivalent thorium complex has been prepared in 1974 ($[ThCp_3]$).[69] Following this pioneering work a number of trivalent thorium complexes have been reported, all with stabilizing soft π donor ligands, i.e. cyclopentadienyl (Cp), cyclooctatetraenyl (COT) and derivatives thereof. However, there is also a heteroleptic thorium(III) complex reported $[ThCp*_2((NiPr_2)_2CMe)]$,[70] where an amidinate ligand is substituting a Cp* ligand,[6] showing

---

[2] chdc: cyclohexyldicarboxylic acid; 12C4: 12-crown-4
[3] Optimization has been performed using Turbomole 7.1 by Roger Kloditz.
[4] crypt: 2.2.2-cryptand; Cp'': η^5-$(C_5H_3(1,3-SiMe_3)_2)$
[5] Cp^R: η^5-(C_5iPr_5)
[6] Cp*: η^5-(C_5Me_5)

the ability of this ligand system to act as a soft and sterically demanding donor to stabilize unusual oxidation states of actinides. Nevertheless, the Cp ligand and its derivatives have played a major role in organoactinide chemistry[71] which has recently also been expanded to transuranium elements.[72-73] In general, the transuranic chemistry has always lagged behind that of uranium and thorium due to the handling restrictions of these radioactive elements. The lack of suitable starting materials hampers the metal-organic coordination chemistry with these elements further. Even until now, there are only two structurally characterized molecular trivalent transuranic precursor compounds known ([NpCl$_3$(py)$_4$][74] and [AmBr$_3$(thf)$_3$][75]) which can be prepared without the need of an actinide in the metallic state, as it is required for a number of other trivalent precursor compounds. Especially the transuranium elements are mostly available as oxides rather than in the metallic state.

For the tetravalent actinides the situation is much more convenient having the precursor compounds [ThCl$_4$(dme)$_2$],[76] UCl$_4$,[77] and [NpCl$_4$(dme)$_2$][78] readily available.[7] Thus, the number of tetravalent metal-organic actinide compounds is increasing with uranium being the most intensively studied element followed by thorium (see Figure 1).[79] For neptunium and plutonium this number is still very small due to the restrictions in handling these highly radioactive materials. A wide variety of tetravalent actinide complexes including chalcogen, pnictogen and carbon donor ligands have been prepared in recent years.[30]

The use of organic solvents and anhydrous conditions further enables the functionalization of the chemically robust "yl" oxygens especially in uranyl(VI) complexes.[80-81] Furthermore, several attempts have been successful to perturb the linear arrangement of the uranyl(VI) cation by sterically demanding ligands[82-83] or via electronic interactions.[84] These examples underline the necessity of investigating the fundamental properties of actinide compounds in non-aqueous systems to decipher formerly unknown reaction pathways. The organometallic chemistry of lanthanides and actinides has been reviewed by EDELMANN and co-workers each year since 2000 indicating the steady increase of research in this field.[85-101] A complete overview of the metal-organic coordination chemistry of the actinides is beyond the scope of this thesis. Hence an overview of the available literature concerning actinide amidinate and diimine complexes will be given at the end of Section 2.2.

---

[7] dme: 1,2-dimethoxyethane

2.2 *N*-donor ligands

Nitrogen donor ligands are an important class of organic ligands possessing medium hard donors according to PEARSON's hard and soft acids and bases (HSAB) concept.[102] Thus, the use of nitrogen donor ligands for the complexation of actinides arises not only from the fundamental interest in their coordination chemistry with 5*f* elements but also due to their softer character compared to hard donors, as oxygen. Hence, a higher orbital overlap between the nitrogen donor atoms and the actinide is expected which corresponds to a more pronounced covalent character. The applicability of nitrogen based ligands for the separation of trivalent actinides from trivalent lanthanides in spent nuclear fuel has been ascribed to these covalent interactions.[6] Thus, nitrogen donor ligands have been used in this thesis to investigate the bonding behavior for the actinides.

Amongst the wide variety of nitrogen donor ligands, this work focuses on polyamide based amidinate ligands which will be introduced in the next section. Furthermore, some studies have been performed on the complexation of hexavalent uranium with pyridine-derived bidentate ligands which will be briefly described in Section 2.2.2. A complete overview about actinide chemistry with nitrogen donor ligands is again beyond the scope of this thesis. Several review articles cover some aspects of this huge field very comprehensively.[79, 103-104]

2.2.1 Amidinates

Amidinates are a well-known class of heteroallylic ligands and can be regarded as the nitrogen analogues to carboxylic acids (see Scheme 2). The additional substituents at the nitrogen donor atoms (R′) make the amidinates a steric equivalent to cyclopentadienyl ligands, whereas the oxygen donor class of ligands remains essentially flat and not sterically demanding.
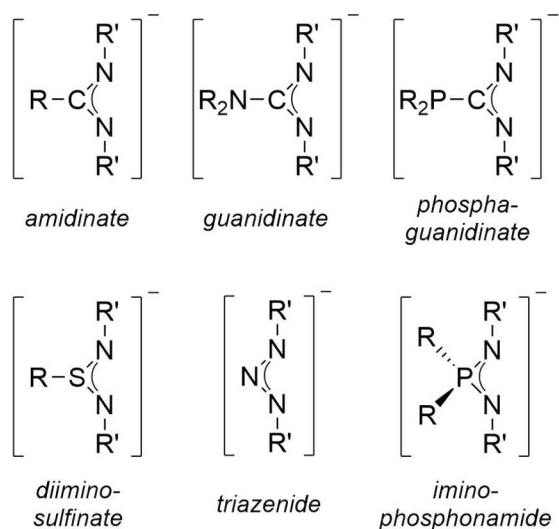
Scheme 2. Structures of amidinate and related ligands.

Although the first amidines have already been prepared during the 19th century[105] the recent literature dates back to 1973 when SANGER *et al.* synthesized and characterized the *N,N,N′*-tris(trimethylsilyl)-benzamidinate.[106] Due to their easy accessibility amidinates have been used for a wide variety of metal complexes. For a comprehensive overview the reader is referred to two excellent review articles by EDELMANN which cover the full range of amidinate chemistry.[20, 107] The amidinates are closely related to a whole class of nitrogen donor ligands which have been substituted either in alpha position to the allylic carbon to yield the guanidinate and phosphaguanidinate ligands or the central carbon atom itself is substituted as shown for the diiminosulfinate, triazenide, and iminophosphonamide ligands (see Scheme 2).

2.2.1.1 Synthesis and overview

Historically, amidines have been synthesized by addition of ammonia, amines or metal amides to nitriles or by chlorination of amides yielding the corresponding imidoylchlorides which react with amines to the corresponding amidines.[108] Today, most commonly either this imidoylchloride route (see Scheme 3a) or the insertion of carbodiimides into metal-carbon bonds (see Scheme 3b) is performed to synthesize the amidines and the metal amidinates.

In this thesis two different benzamidinate ligands, *N,N′*-bis(isopropyl)-benzamidine (H*i*Pr$_2$BA) and the chiral (*S,S*)-*N,N′*-bis-(1-phenylethyl)-benzamidine ((*S*)-HPEBA) have been used to synthesize tetra- and trivalent metal complexes (see Scheme 4). Both ligands will be discussed in detail in the next sections to give an overview of already published metal complexes possessing these ligands. A general overview of different coordination motifs and possible applications for amidine ligands will also be given in the next section for the H*i*Pr$_2$BA ligand.
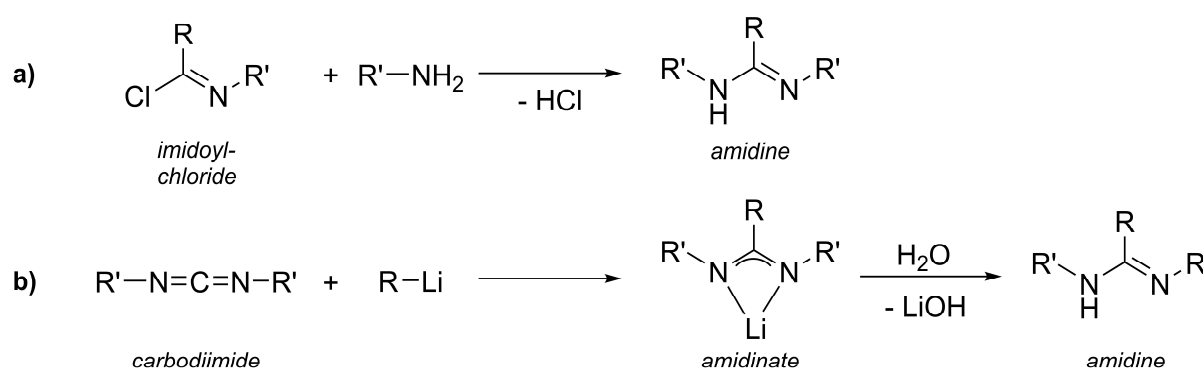
Scheme 3. Common synthesis routes to yield amidines; a) imidoylchloride route, b) carbodiimide insertion.
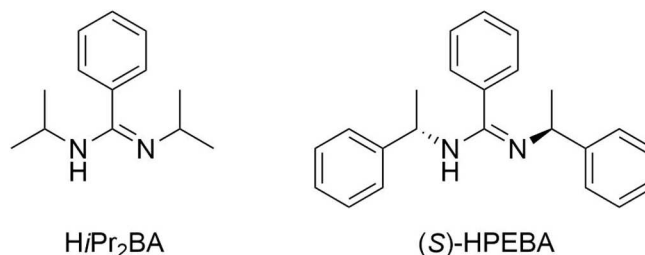
Scheme 4. Amidine ligands used in this thesis.

2.2.1.2 *N,N′*-bis(isopropyl)benzamidine (H*i*Pr₂BA)

The H*i*Pr₂BA ligand and the corresponding lithium amidinate have been first prepared in 1974 by PORNET and MIGINIAC using the already described carbodiimide route.[109] A similar synthetic procedure is used until today by adding phenyllithium to *N,N′*-diisopropylcarbodiimide in etheric solution.[110] A variety of main group,[111-121] transition metal,[122-131] and lanthanide[132] complexes could be prepared with this ligand. In most cases heteroleptic complexes with other organic or inorganic ligands like chloride have been prepared. The cerium(III) complex [Ce(*i*Pr₂BA)₃] is the only reported homoleptic complex with this amidinate.[132] However, actinide complexes of this ligand are not reported, yet. Some of the prepared *i*Pr₂BA complexes have already been used for light emitting applications[128-130] or catalytic processes like photocatalytic water reduction[131] and sulphur oxidation of isonitriles.[126] The possible coordination motifs of amidinates can be described based on two gallium(III) complexes with this ligand (see Figure 4).[120]
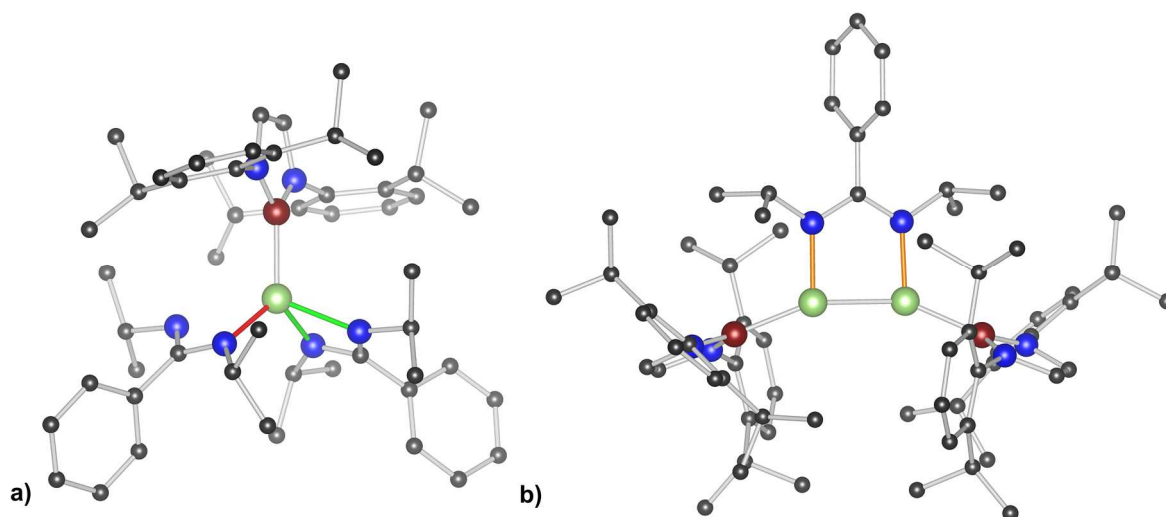
Figure 4. Two reported gallium(III) coordination compounds with the *i*Pr₂BA ligand, a) [Ga(*i*Pr₂BA)₂(B(NDippCH₂)₂)] showing a monodentate (red) and a bidentate (green) coordination motif, b) [Ga₂(B(NDippCH₂)₂)₂(*i*Pr₂BA)][8] showing the bidentate bridging (orange) coordination motif.[120] Hydrogen atoms are omitted for clarity. Color code: gallium (Ga, pale green), boron (B, brown), carbon (C, dark grey), and nitrogen (N, blue).

---

[8] Dipp: 1,5-di*iso*propylphenyl

In most complexes, the amidinates are coordinating bidentately to the metal forming a four-membered metallacycle as shown in green in Figure 4a. In certain circumstances it is also possible to achieve a monodentate coordination, although the negative charge is distributed within the amidinate moiety (see red bond in Figure 4a). Furthermore, the bidentate coordination motif may also stabilize metal-metal bonds as exemplified in orange in Figure 4b. Thus, the iPr$_2$BA ligand has already shown a wide variability in coordination chemistry and is hence used within this thesis to expand this towards the complexation of tetravalent actinides and transition metals. It has to be pointed out, that there are already some examples of tetravalent transition metal complexes in the literature, i.e. [TiCl$_3$(thf)(iPr$_2$BA)][122] and [ZrCl$_2$(iPr$_2$BA)$_2$],[123] which will be compared with the work of this thesis (see Section 3.1.2.1).

2.2.1.3 (*S,S*)-*N,N′*-bis-(1-phenylethyl)-benzamidine (((*S*)-HPEBA)

The first synthesis of the chiral *N,N′*-bis-(1-phenylethyl)-benzamidine (((*R/S*)-PEBA) has been reported by BRUNNER *et. al* in 1980 using the already described imidoylchloride route.[133-134] However, they only obtained an oily compound and used it without further purification for catalytic purposes. In 1983 the crystal structure of (*S*)-HPEBA has been determined using the same synthesis route.[135] Although the synthesis of the chiral carbodiimide (bis-((*R/S*)-1-phenylethyl)-carbodiimide; (*R/S*)-PEC) has been known since 1971[136] and has been repeated using various reaction conditions[137-139] it took until 2006 when HASEGAWA *et al.* published the synthesis of (*R*)-PEBA by the carbodiimide route.[140]

In 2011 ROESKY *et al.* reported an alternative imidoylchloride route starting from benzoylchloride and enantiomeric pure (*R/S*)-1-phenylethylamine (see Scheme 5). They yielded the enantiomeric pure (*R*)- resp. (*S*)-HPEBA in a three-step procedure with moderate yield (28 %) as colorless crystals after recrystallization from ethanol.[141]

Based on this synthesis the corresponding alkali metal salts Li- and KPEBA have been obtained using either *n*-butyllithium or potassium hydride as bases. In this thesis (*S*)-LiPEBA has been obtained by reacting (*S*)-HPEBA with lithium bis(trimethylsilylamide) (LiHMDS) in thf or has been prepared *in situ* (see Section 3.1.1).
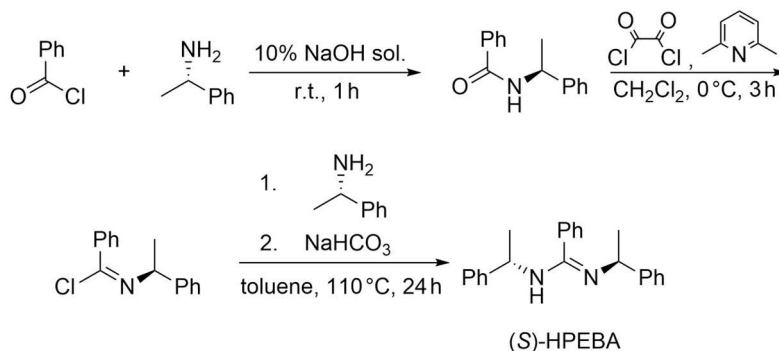
Scheme 5. Synthesis of (*S*)-HPEBA according to ROESKY *et al.*[141]

Starting from the protonated or deprotonated (*R/S*)-PEBA ligand the group of ROESKY could synthesize main group (i.e. Ca, Sr, Ba),[142] transition metal (i.e. Zr, Hf),[143] and a wide variety of lanthanide complexes.[144-145] They used either an amine elimination reaction using the metal amides and the protonated (*R/S*)-HPEBA or a salt-metathesis reaction starting from the deprotonated (*R/S*)-KPEBA and the metal halides. With these approaches mono-, bis- and tris(amidinate) complexes could be prepared depending on the stoichiometry and the metal ionic radius. Also divalent lanthanide ions could be stabilized.[142]

Furthermore, the group of ROESKY could show the ability of the synthesized lanthanide and transition metal complexes for asymmetric catalysis in hydroamination,[144-145] and hydrophosphination reactions[142] as well as ring-opening polymerization of *rac*-lactide.[146] In addition, they increased the family of enantiopure amidinates as ligands for lanthanides and transition metals by substituting the central phenyl substituent by a *tert*-butyl ((*S*)-PETA)[147] or methyl group ((*S*)-PEAA)[148] or by changing the peripheral phenyl rings to naphtyl ((*S*)-NEBA)[149] or cyclohexyl groups ((*S*)-CEBA).[148]

2.2.1.4 Actinide amidinates

The first actinide amidinates were prepared in 1988 by WEDLER *et al.* by reaction of lithium bis(trimethylsilyl)-benzamidinate with uranium tetrachloride in thf yielding a bis- and a tris(amidinate) complex with uranium(IV).[150] During the following years several benzamidinate complexes with Th^{IV} and U^{IV} have been synthesized[151] and further functionalized by methylation.[152] Generally, either a 1:2 (metal:ligand) or a 1:3 stoichiometry has been obtained resulting in a distorted octahedral coordination geometry (CN = 6) for the 1:2 complexes and a monocapped octahedral coordination (CN = 7) for the 1:3 complexes (see Figure 5a).

The first trivalent uranium complex has been prepared in 2004 by reduction of a tetravalent trisamidinate monochloro complex.[153] Shortly thereafter the first uranium guanidinate complex was synthesized by VILLIERS *et al.* in 2007.[154]

Figure 5. Molecular structures of uranium amidinate complexes; a) [U^{IV}Cl((NSiMe$_3$)$_2$CPh)$_3$],[151] b) [U^{VI}O$_2$((NSiMe$_3$)$_2$CPh)$_2$].[155] Hydrogen atoms are omitted for clarity. Color code: uranium (U^{IV}, dark green; U^{VI}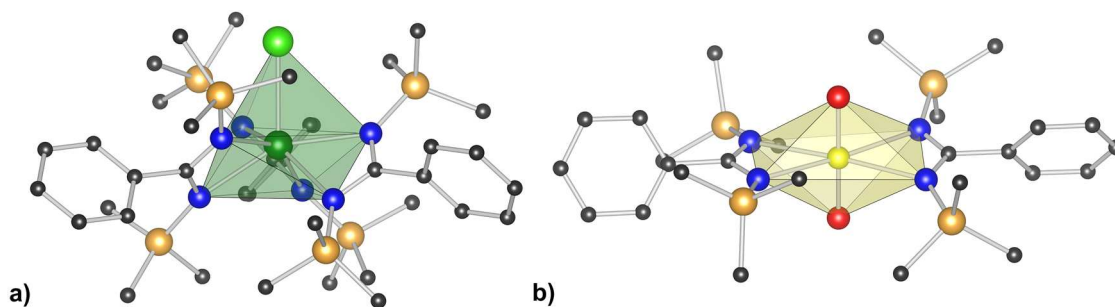, yellow), carbon (C, dark grey), nitrogen (N, blue), oxygen (O, red), silicon (Si, pale orange), and chlorine (Cl, green).

Actinide amidinate complexes have also been prepared by direct insertion of carbodiimides into An–C bonds.[156] Moreover, tetravalent actinide amidinates have already been proven to successfully catalyze ring-opening polymerization reactions.[157-158] The ability of amidinates to stabilize actinide metal centers for further functionalization has also been shown by SARSFIELD *et al.* for some rare examples of hexavalent uranium amidinate complexes (see Figure 5b).[155, 159]

However, up to now there is no transuranic amidinate complex known in the literature and hence no systematic study of the behavior of the actinide amidinates when traversing the 5*f* series. Thus, this PhD work aims to expand the rich amidinate chemistry to these heavy elements and to perform a systematic investigation of their properties in the solid state and in solution.

2.2.2 Diimines

Besides the amidinates as negatively charged nitrogen donor ligands also neutral poly-pyridine based diimine ligands were used during this PhD work. Here the focus is not dedicated to the elucidation of potential bonding contributions when traversing the actinide series. Instead, the structural features of the synthesized complex molecules and their possible environmental relevance are investigated.

The bidentate diimine ligands 2,2′-bipyridine (bipy) and 1,10-phenanthroline (phen) are amongst the most studied ligands in coordination chemistry.[160] Both heteroaromatic ligands are possessing two nitrogen atoms in *juxta* position with a suitable bite angle for bidentate coordination forming five-membered metallacycles with almost all metals. Since the discovery of bipy in 1889 by BLAU[161] both ligands and related substituted ligands have been extensively used in coordination chemistry with applications in catalysis,[162-163] photoelectrochemistry,[164-165] and also biochemistry.[166-167] For an overview about the plethora of studies concerning both ligands, the reader is referred to comprehensive review articles covering possible synthesis strategies[168-169] and the coordination chemistry of both diimine ligands.[170-172]

2,2'-bipyridine   1,10-phenanthroline

bipy   *phen*
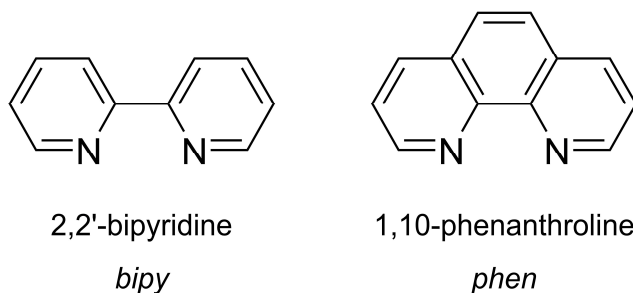
Scheme 6. Diimine ligands used in this thesis.

A total of 126 structurally characterized actinide complexes including bipy and 81 possessing phen molecules are known with those of the hexavalent uranyl(VI) cation having the largest fraction (62 (bipy), resp., 66 (phen).[9] This indicates the importance of these ligands especially for the coordination chemistry of hexavalent actinide cations. In most cases, the diimines act as capping agents in the equatorial plane of $[UO_2]^{2+}$ saturating two of the four to six possible coordination sites to form two-dimensional metal organic frameworks using e.g. polycarboxylates as linker molecules (see Figure 6a).[173-174] Here, especially the rigidity and planarity of the phen ligand favors this coordination motif. Thus, probably this entropic advantage compared to the more flexible bipy ligand enables also unusual coordination geometries of the 1,10-phenanthroline ligand which significantly deviate from equatorial coordination of $[UO_2]^{2+}$ (see Figure 6b).[82, 175] Furthermore, both diimines have been shown to stabilize also cation-cation interactions between adjacent actinyl ions.[176-177]
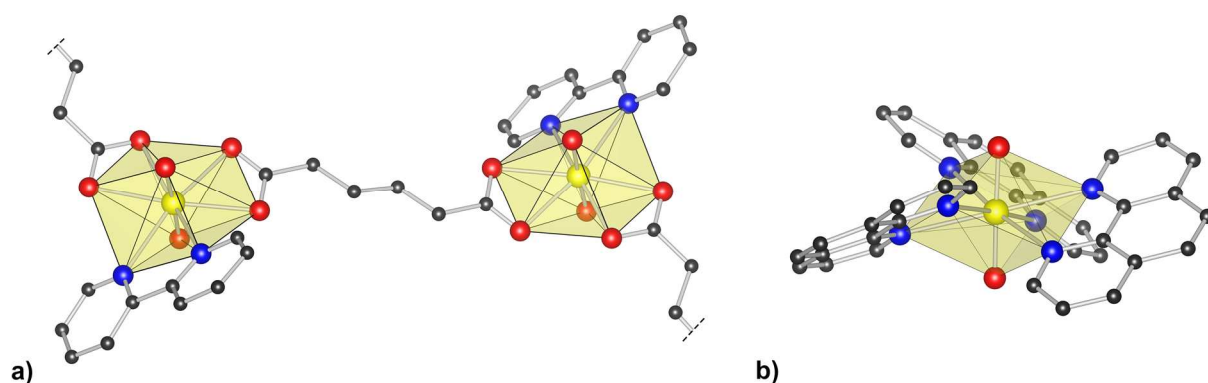
Figure 6. Molecular structures of uranium(VI) diimine complexes; a) $[U^{VI}O_2(bipy)(\mu-\eta^2:\eta^2-C_6H_8O_2)]_n$,[178] b) $[U^{VI}O_2(phen)_3]^{2+}$.[175] Hydrogen atoms, solvent molecules, and counter anions are omitted for clarity. Color code: uranium (U^{VI}, yellow), carbon (C, dark grey), nitrogen (N, blue), and oxygen (O, red).

---

[9] Search in *Cambridge Structural Database* as of 04/07/2020.

2.3   Experimental structure determination

Within this section the major experimental techniques for the structure determination of complex molecules in the solid state (single-crystal X-ray diffraction, SC-XRD) and in solution (nuclear magnetic resonance spectroscopy, NMR) are briefly introduced to give a comprehensive overview.

2.3.1 Solid state – SC-XRD

The solid-state structure of a molecular complex can be determined by the analysis of single-crystals of the respective compound using the diffraction of X-rays. A crystal consist of a periodic arrangement of matter in three dimensions which is described by a crystal lattice. This periodicity can be used to determine the electron density $\rho(\mathbf{r})$[10] of the matter by diffraction of X-rays which have a wavelength λ similar to the distance d of two lattice planes which intersect the crystal. Thus, the X-rays are diffracted at the atoms in a certain lattice plane and constructive interference occurs if the BRAGG equation[179] is fulfilled.

$$n \cdot \lambda = 2d \cdot \sin\theta \qquad \text{[Eq. 1]}$$

Thereby θ denotes the glancing angle between the X-ray beam and the lattice plane. The intensity of the diffracted beam I($\mathbf{h}$) is proportional to the square of the structure amplitude $|F(\mathbf{h})|$.[11]

$$I(\mathbf{h}) \propto |F(\mathbf{h})|^2 \qquad \text{[Eq. 2]}$$

The structure amplitude is the magnitude of the structure factor F($\mathbf{h}$) which corresponds to the FOURIER transform of the electron density and is a complex quantity.

$$F(\mathbf{h}) = \int_V \rho(\mathbf{r})e^{2\pi i(\mathbf{h},\mathbf{r})}dV \qquad \text{[Eq. 3]}$$

The major problem of the diffraction experiment is the proportionality of the intensity of the diffracted beam to the square of the magnitude of the structure factor (Eq. 2). The information about the phase $\varphi(\mathbf{h})$ of the scattered wave is thus not accessible in the diffraction experiment.

$$F(\mathbf{h}) = |F(\mathbf{h})| \cdot e^{i\varphi(\mathbf{h})} \qquad \text{[Eq. 4]}$$

This phase problem is immanent and hampered the development of X-ray diffraction techniques for a long time. Nowadays, several methods are available which circumvent this problem,

---

[10] **r** denotes position vector in real space.
[11] **h** is the reciprocal lattice vector: **h** = h**a***+k**b***+l**c*** with **a***, **b***, and **c*** being the reciprocal lattice constants and h, k, l integer values.

PATTERSON methods,[180] direct methods,[181] and dual space methods like charge flipping[182] and intrinsic phasing.[183] These methods are implemented in modern software packages for single-crystal structure analysis like SHELX[184] or JANA.[185] Thus, solid-state structure determination of molecular compounds having single crystals available is a straightforward task today. Also the determination of the absolute configuration of chiral molecules became possible using anomalous dispersion effects.[186] The presence of resonant scatters in acentric structures breaks FRIEDEL's law[187] (I($\mathbf{h}$) = I($\overline{\mathbf{h}}$)) due to the absorbance of some X-ray photons introducing a phase shift of the scattered wave. This intensity difference can be used to determine the absolute structure of the crystal and hence the absolute configuration.[188] Whether the correct enantiomer has been refined can be finally evaluated using the FLACK parameter x which will be used to establish the enantiopurity of the synthesized chiral complex molecules for the sake of this thesis.[189]

$$|F(\boldsymbol{h}, x)|^2 = (1 - x) \cdot |F(\boldsymbol{h})|^2 - x \cdot \left|F(\overline{\boldsymbol{h}})\right|^2 \qquad \text{[Eq. 5]}$$

Detailed descriptions of the data reduction procedure and refinement techniques can be found elsewhere.[190-191]

2.3.2 Solution – NMR spectroscopy

The fundamental principles of NMR spectroscopy will be covered in this section including the elucidation of dynamic behavior of complex molecules in solution and with a special focus on the effects of paramagnetic ions on the chemical shifts of adjacent nuclei.

2.3.2.1 Diamagnetic NMR spectroscopy

Nuclear magnetic resonance spectroscopy is an analytical technique to elucidate the structure of organic and inorganic molecules in solution and in the solid state. The method is based on the ZEEMANN effect which splits the energy of nuclei with a nuclear spin $I \neq 0$ in the magnetic field B_0. The energy difference between adjacent energy states is defined by the gyromagnetic ratio γ and can be used to study the electronic surrounding of the nuclei of interest.

$$\Delta E = \gamma \cdot \hbar \cdot B_0 \qquad \text{[Eq. 6]}$$

The electron distribution within the observed matter reduces the effective magnetic field B_{eff} at the nuclei which enables a detailed discrimination of these.

$$B_{\text{eff}} = (1 - \sigma) \cdot B_0 \qquad \text{[Eq. 7]}$$

The shielding factor σ is usually very low (e.g. 10^{-5} for ^{1}H) leading to the introduction of the chemical shift δ as the difference between the sample frequency (v_S) and a standard compound (v_R) relative to the spectrometer frequency (v_0) in parts per million (ppm).

$$\delta \, [\text{ppm}] = \frac{v_S - v_R}{v_0}$$ [Eq. 8]

Different functional groups show different chemical shifts based on their electronic surrounding. Nuclei close to electron withdrawing atoms like oxygen or nitrogen usually show an increased deshielding and hence a higher chemical shift. In conjugated π electron systems like benzene or alkynes additional phenomena like ring current and anisotropy effects can be observed which have an additional effect on the chemical shift.

2.3.2.2 Dynamic behavior

Besides the information about the electronic environment of the nuclei NMR spectroscopy also provides information about the dynamic behavior of organic molecules and complexes in solution. The range of observable rate constants for dynamic processes lies between 10 and 10^5 Hz which equals energy barriers between 20 and 100 kJ/mol.[192] Thus, hindered rotations, inversion processes or other conformational changes can be investigated. The rate constant k_c is connected to the GIBBS free enthalpy of the transition state $\Delta G_c^{\ddagger}$ via the EYRING equation.

$$k_c = \frac{k_B * T}{h} e^{-\frac{\Delta G_c^{\ddagger}}{RT}}$$ [Eq. 9]

Depending on the rate constant of the exchange process k_c different signal patterns are observed. If the dynamic process is slow compared to the NMR timescale two separate signals are visible representing the different configurations. Contrary, if a fast exchange process is occurring only one averaged signal is observed. Due to the temperature dependency of the rate constant the transition between both states is observable using temperature dependent NMR spectra. The coalescence temperature T_c is defined as the lowest temperature when only one signal can be observed. The rate constant for the dynamic process can be calculated based on the different chemical shifts of both signals Δδ at low temperatures.

$$k_c = \frac{\pi}{\sqrt{2}} \Delta\delta$$ [Eq. 10]

Thus, the GIBBS free enthalpy of the transition state $\Delta G_c^{\ddagger}$ can be determined and used to investigate the dynamic behavior especially of complexes in solution to gain deeper insight into their structural properties.

2.3.2.3 Paramagnetic NMR spectroscopy

Paramagnetic metals influence the chemical shifts of nuclei in associated ligands which can be used to determine the structure of those paramagnetic complex molecules in solution. Therefore the fundamental properties and equations to interpret these additional shifts are presented in this section. The paramagnetic influence manifests not only by the paramagnetic shift, but other effects like paramagnetic relaxation enhancement (PRE) and residual dipolar coupling (RDC) which are not discussed here.[193-194] In the following, the induced paramagnetic shift due to the coupling of the electron and the nuclear spins will be introduced. In general, the chemical shift of nuclei in paramagnetic complex molecules (δ_{tot}) can be expressed by the sum of a dia- (δ_{dia}) and a paramagnetic contribution, also called the hyperfine contribution (δ_{HF}).

$$\delta_{tot} \approx \delta_{dia} + \delta_{HF} \qquad \text{[Eq. 11]}$$

Thus, the hyperfine contribution of a paramagnetic molecule can be calculated by subtracting the diamagnetic contribution from the measured chemical shift.

$$\delta_{HF} = \delta_{tot} - \delta_{dia} \qquad \text{[Eq. 12]}$$

Usually the best approximation for the diamagnetic contribution is an isostructural complex molecule possessing a diamagnetic metal cation. In the tetravalent actinide series the tetravalent thorium cation is diamagnetic and could serve as such a reference when evaluating tetravalent actinide complexes regarding their paramagnetic shifts. In the trivalent actinide series actinium would be the diamagnetic reference of choice but its usage is limited as all isotopes of actinium have very short half-lives and are thus not available in weighable amounts. Therefore diamagnetic trivalent lanthanides (i.e. La, Lu) are frequently used.

The hyperfine contribution (δ_{HF}) itself consists of two contributions, the FERMI contact (δ_{FCS}) and the pseudocontact (δ_{PCS}) contribution.

$$\delta_{HF} = \delta_{FCS} + \delta_{PCS} \qquad \text{[Eq. 13]}$$

Both hyperfine contributions are different in their origin. The FERMI contact emerges from the unpaired electron spin density located on the nucleus of interest. This requires an *s* orbital type contribution of the related molecular orbital or in other words, a directional chemical bond between the paramagnetic center and the observed nucleus. Thus, a significant FERMI contact contribution can be interpreted as evidence for a covalent bonding character between the paramagnetic metal and the ligands.[6] The FERMI contact contribution is proportional to the electron-nucleus hyperfine coupling constant A which decreases rapidly with increasing distance between the metal and the observed nucleus. Thus, it has been estimated that this term may be neglected if the observed nucleus is more than four bonds away from the metal

center.[195] However, these results rely on the analysis of paramagnetic lanthanide complexes, which are not prone to show intense orbital overlaps between metal and ligand orbitals due to the localized character of the 4*f* orbitals. For the actinides a higher orbital overlap is expected due to the radial extension of the 5*f* electrons which may also influence the FERMI contact contribution. Also, special consideration must be taken with respect to conjugated π systems, which potentially disseminate the FERMI contact contribution further due to the formation of extended molecular orbitals.

The pseudocontact shift, in contrast, is solely dependent on the magnetic susceptibility χ of the metal ion which induces an additional magnetic moment. The anisotropy of this magnetic moment causes a non-vanishing dipolar interaction which is dependent on the spatial arrangement of the nuclei with respect to the metal center. Thus, the pseudocontact shift can be calculated according to:[196]

$$\delta_{\text{PCS}} = \frac{1}{12\pi r^5} \text{Tr}(3\boldsymbol{r} \otimes (\boldsymbol{r} \cdot \boldsymbol{\chi}) - r^2 \boldsymbol{\chi}) \qquad \text{[Eq. 14]}$$

Thereby **r** denotes the vector between the metal center and the observed nucleus and r its magnitude. The symbol $\otimes$ indicates a tensorial product and χ is the magnetic susceptibility tensor. In 1970 KURLAND and MCGARVEY introduced another expression of Eq. 14 only taking the axial ($\Delta\chi_{\text{ax}}$) and rhombic ($\Delta\chi_{\text{rh}}$) anisotropy of the magnetic susceptibility tensor χ into account:[197]

$$\delta_{\text{PCS}} = \frac{1}{12\pi r^3}\left[\Delta\chi_{\text{ax}}(3\cos^2\theta - 1) + \frac{3}{2}\Delta\chi_{\text{rh}}\sin^2\theta\cos(2\varphi)\right] \qquad \text{[Eq. 15]}$$

$$\text{with} \qquad \Delta\chi_{\text{ax}} = \tilde{\chi}_{\text{zz}} - \frac{\tilde{\chi}_{\text{xx}} + \tilde{\chi}_{\text{yy}}}{2} \qquad \text{[Eq. 15a]}$$

$$\Delta\chi_{\text{rh}} = \tilde{\chi}_{\text{xx}} - \tilde{\chi}_{\text{yy}} \qquad \text{[Eq. 15b]}$$

The angles θ and φ denote the polar angles of the nuclei in the reference frame which coincides with the directions of the susceptibility tensor. Furthermore, in a molecular system with an axial symmetry higher than C_2, the rhombic term in Eq. 15 vanishes. Only the axial term of the anisotropy of the magnetic susceptibility $\Delta\chi_{\text{ax}}$ along with the distance r between the metal and the nucleus, as well as the angle θ towards the principal axis is now determining the pseudocontact shift.

$$\delta_{\text{PCS}} = \frac{1}{12\pi r^3}[\Delta\chi_{\text{ax}}(3\cos^2\theta - 1)] \qquad \text{[Eq. 16]}$$

By using this equation structural features of paramagnetic molecules can be deduced in solution assuming that the axial anisotropy of the magnetic susceptibility tensor and the pseudocontact shift are known.

In order to use this equation to gain structural information in solution the pseudocontact shift has to be separated from the FERMI contact contribution. Up to now no suitable separation method is available, especially for actinide complexes. However, BLEANEY proposed a separation method for isostructural lanthanide complex series which is based on the temperature dependence of the paramagnetic hyperfine shift.[198] He assumed that the FERMI contact shift has an inverse dependence of the temperature ($\propto T^{-1}$) whereas the pseudocontact shift is dependent on T^{-2}. Thus, a temperature dependent measurement of the paramagnetic shift would yield both contributions by plotting the product of hyperfine shift and temperature against the inverse temperature ($\delta_{HF} \cdot T$ vs. $1/T$ plot). The axis intercept should hence be proportional to the FERMI contact shift and the slope to the pseudocontact shift. The BLEANEY method makes several assumptions like a low zero-field splitting which is less than $k \cdot T$, a point charge of the paramagnetic metal and instantaneous relaxation.[195] Thus, it is heavily debated in the recent literature.[195, 199-202] However, despite the assumptions made by BLEANEY this theory seems to explain several observations of paramagnetic lanthanide complex series. It will therefore be evaluated for some synthesized actinide complex molecules in this thesis.

The use of paramagnetic metal ions as analytical probes has opened new perspectives in structural biology[21, 203-204] and material science.[205-206] Due to the complexities in working with actinides, the literature dealing with their paramagnetic properties in solution is very scarce. There has been some pioneering work by BERTHON et al. determining the molar magnetic susceptibilities χ_M and the effective magnetic moments μ_B of paramagnetic aqueous actinide cations[207-208] using the EVANS method.[209] The same group investigated the paramagnetic shifts of trivalent lanthanide and actinide complexes in organic solutions and found higher-order temperature dependencies of FERMI and pseudocontact shifts especially for the trivalent actinides.[210] Furthermore, they combined their experiments with quantum chemical calculations and obtained values for the magnetic susceptibility tensor which has been crucial for the determination of structural parameters from paramagnetic shifts (see Eq. 14 ff.). As similar investigations with tetravalent actinides remain elusive, this work also aims to give a fundamental contribution to the understanding of the magnetic properties of tetravalent actinide cations.

2.4 Quantum chemical methods

The interpretation of the experimental findings for actinide complexes is not straightforward and requires in most cases the support by quantum chemical calculations. Especially, the electronic structure of the actinide elements makes their chemistry quite interesting but also non-trivial. Thus, quantum chemical calculations are necessary to reveal and quantify the influence of the electronic structure on the bonding situation in actinide compounds. The evaluation of the covalent character of a chemical bond between the actinides and the donating atoms is a major topic in actinide research which up to now did not yield a conclusive result. Although there is no physical measure for covalency it is well understood from a chemist's viewpoint as a directional sharing of electrons.[42] However, when approaching this term from a quantum chemical perspective two different approaches are currently in use: orbital based and electron density based ones. The orbital based approaches are widely used in the assessment of covalency in actinide complexes. It is believed that the covalency is directly connected to the mixing parameter λ of a metal and a ligand based orbital which increases either if both have a similar energy (i.e. energy near-degeneracy) or have a significant orbital overlap.[9, 31-33, 35-39]

Electron density based methods have the advantage to be based on a physical observable, the electron density, which is more intuitive to evaluate than one-electron wave functions, i.e. orbitals. Amongst the electron density based methods BADER's Quantum Theory of Atoms in Molecules (QTAIM)[211] is one of the most employed theories, especially in actinide chemistry. The QTAIM approach is based on the assignment of electron density in a molecule to an atom or more precisely to a basin. This basin is defined based on the gradient of the electron density. The saddle-point of the electron density between two basins is called a bond-critical point (BCP). This theory is exemplified in Figure 7b for the (S)-PEBA ligand in the N–C–N plane showing the basins as regions within the blue lines and the corresponding bond critical points as blue dots.

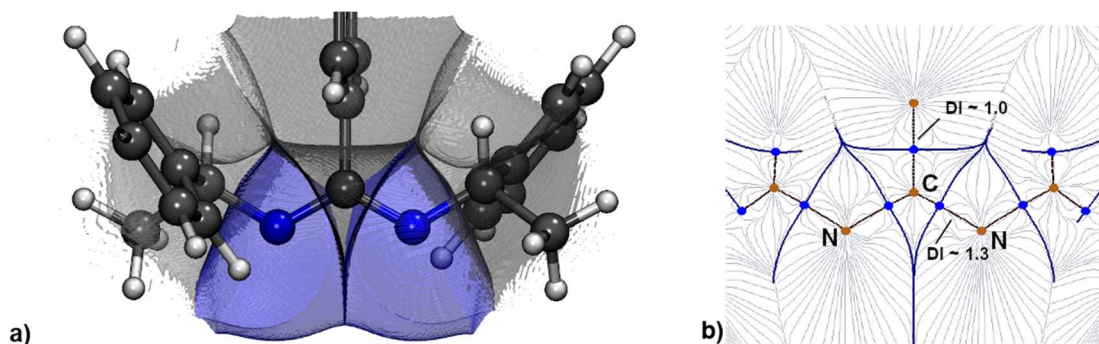
Figure 7. Graphical representation of atomic basins for a part of the (S)-PEBA ligand (a) and map of gradient paths (grey) in N–C–N plane (b). Brown points correspond to the nuclei. Blue points belong to bond critical points.

Based on this unambiguous assignment of atoms within a molecule several parameters can be calculated. The integration over two neighboring atomic basins enables a quantification of the shared electrons between those atoms, i.e. a measure for the bond order, which is called delocalization index (DI) and will be stressed throughout this thesis.[42] The difference between the delocalization index of a C–C single bond and the delocalized C=N bond is exemplified in Figure 7b.

KALTSOYANNIS pointed out in 2013 that different computational tools are yielding different conclusions regarding the trend of covalency within the actinide series.[44] Thus, in order to evaluate the synthesized tri- and tetravalent complex series in more detail a second method, the natural bond orbital analysis (NBO), has been performed.[212] This method is based on the analysis of the wave function Ψ and the resulting electron density matrix **D**.

$$\boldsymbol{D} = \int |\Psi(1,2,\dots N)|^2 d\tau_2 d\tau_3 \dots d\tau_N \qquad \text{[Eq. 17]}$$

Different kinds of orbital representations can be deduced by transformation of this matrix and are converted into chemically meaningful values. For example, in the natural population analysis (NPA)[213] orbital populations and atomic charges can be extracted and compared within the investigated actinide and lanthanide complexes to evaluate the participation of f electrons in the bonding.

Both quantum chemical measures, the delocalization index from the QTAIM analysis and natural population analysis from the NBO approach are used to evaluate the possible trends in the bonding behavior when traversing the actinide series. Furthermore, they will be stressed when comparing the electronic properties of isostructural lanthanide and actinide amidinate complexes to give a conclusive overview of their similarities and differences.

3 RESULTS AND DISCUSSION

The major results of this PhD work are presented in four chapters starting with the discussion of the tetravalent and thereafter the trivalent metal amidinate complexes. Each of the first two chapters is divided into a synthesis section and two sections regarding the structure determination and comparison in the solid state and in solution. These analyses are supported by quantum chemical calculations to investigate the electronic structure of the actinide complexes in detail. The third chapter highlights the investigations of amidinate and diimine complexes of hexavalent uranium and finally in the fourth chapter the synthesis of mixed-valent polynuclear neptunium complexes is discussed.

3.1 Tetravalent metal complexes with amidinates

The synthesized tetravalent neptunium amidinate complexes presented in this section have recently been published by FICHTER *et al*.[214]

The elucidation of the fundamental properties of tetravalent actinides is the major objective of this PhD work. This is achieved by the synthesis and characterization of series of isostructural complexes with tetravalent actinides and nitrogen donor ligands, especially amidinate ligands. Thus, two different benzamidinate ligands, N,N'-bis(isopropyl)-benzamidinate (iPr$_2$BA) and the chiral (S,S)-N,N'-bis(1-phenylethyl)-benzamidinate ((S)-PEBA), have been used to synthesize bis- and tris(amidinate) complexes with tetravalent actinides (Th, U, Np), transition metals (Ti, Zr, Hf) and a tetravalent lanthanide (Ce). The resulting complex series featuring similar coordination environments are investigated regarding their intramolecular distances between the metal center and the coordinating atoms. This leads to a critical evaluation of similarities and differences between tetravalent actinides and their isoelectronic surrogates. Especially the actinide tris(amidinate) complexes [AnCl((S)-PEBA)$_3$] (An = Th, U, Np) are investigated in detail and are further functionalized by anion exchange reactions yielding unprecedented tetravalent actinide (pseudo)halide complexes. Thus, new actinide heteroatom interactions are observed and investigated towards possible systematic trends.

3.1.1 Synthesis

3.1.1.1 Actinide and transition metal chloro complexes

The majority of the tetravalent metal amidinates presented in this work have been synthesized using a salt metathesis approach. A metal chloride or stabilized chloride (like [AnCl$_4$(dme)$_2$]) and the respective deprotonated amidinate ligand have been used as starting materials. Commonly, the synthesis is performed in a two-step reaction procedure, by first synthesizing the respective alkali metal amidinate and a subsequent salt metathesis reaction. This procedure

has been successfully carried out to synthesize the first chiral actinide amidinates [ThCl((*S*)-PEBA)$_3$] and [UCl((*S*)-PEBA)$_3$].[215-216] However, to increase the yield and the purity of the reaction products, a one-pot reaction scheme using the amidine, an amide base and the respective metal chloride was established. Such a one-pot reaction scheme accounts for acidic impurities in the metal chlorides which could be neutralized by a slight excess of the base used (see Scheme 7).

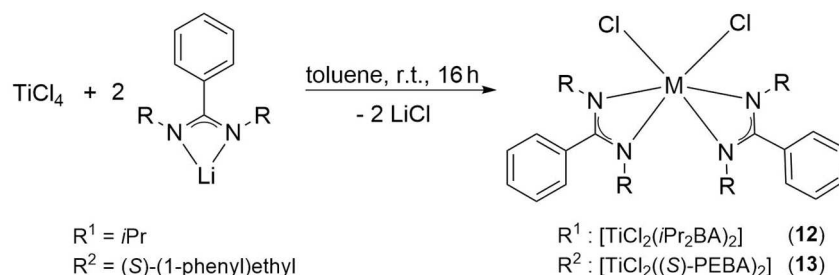| R	M	n	compound	
R^1	Hf	2	[HfCl$_2$(*i*Pr$_2$BA)$_2$]	(**1**)
	Zr	3	[ZrCl(*i*Pr$_2$BA)$_3$]	(**2**)
	Th		[ThCl(*i*Pr$_2$BA)$_3$]	(**3**)
	U		[UCl(*i*Pr$_2$BA)$_3$]	(**4**)
	Np		[NpCl(*i*Pr$_2$BA)$_3$]	(**5**)
R^2	Zr	2	[ZrCl$_2$((*S*)-PEBA)$_2$]	(**6**)
	Hf		[HfCl$_2$((*S*)-PEBA)$_2$]	(**7**)
	U		[UCl$_2$((*S*)-PEBA)$_2$]	(**8**)
	Th	3	[ThCl((*S*)-PEBA)$_3$]	(**9**)
	U		[UCl((*S*)-PEBA)$_3$]	(**10**)
	Np		[NpCl((*S*)-PEBA)$_3$]	(**11**)
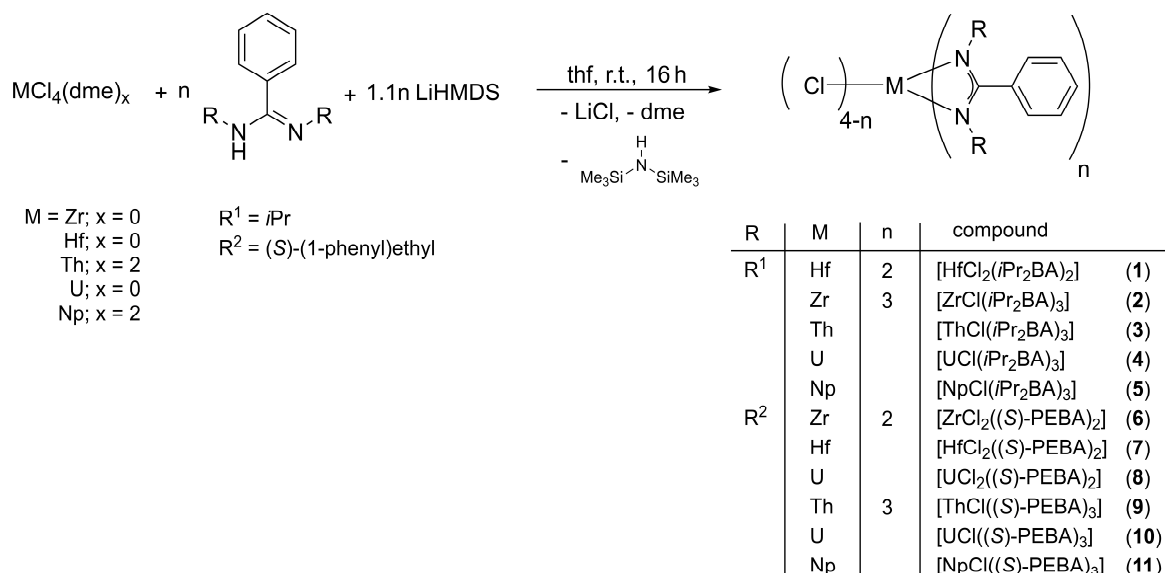
Scheme 7. General reaction scheme for the synthesis of tetravalent metal amidinates **1-11**.

The respective Zr, Hf, Th, U, and Np amidinate complexes **1-11** in 1:2 and 1:3 (metal:ligand) stoichiometry could be obtained after subsequent workup by extraction into toluene to separate from lithium chloride and bis(trimethylsilyl)amine. The compounds crystallize from toluene solution by slow evaporation or diffusion of *n*-pentane (see Experimental Section 5.3.1), incorporating no (**1**, **6-8**), ½ (**2-5**) or one (**9-11**) toluene molecule per complex molecule in the crystal structure (see Appendix for crystallographic details).

A detailed discussion of the dependency of the stoichiometric ratio from the ionic radius of the metal cation will follow in Section 3.1.2. However, in order to complete the group IV metal series, the corresponding titanium complexes were synthesized in toluene starting with the lithium amidinates due to the high reactivity of TiCl$_4$ (see Scheme 8).

R^1 = *i*Pr
R^2 = (*S*)-(1-phenyl)ethyl

R^1 : [TiCl$_2$(*i*Pr$_2$BA)$_2$] (**12**)
R^2 : [TiCl$_2$((*S*)-PEBA)$_2$] (**13**)

Scheme 8. Synthesis of titanium amidinates [TiCl$_2$(*i*Pr$_2$BA)$_2$] (**12**) and [TiCl$_2$((*S*)-PEBA)$_2$] (**13**).

3.1.1.2 Tetravalent cerium complex

Besides those straightforward salt metathesis approaches for the actinide and transition metal complexes, the synthesis of the tetravalent cerium analogues is more challenging, as the neutral cerium tetrachloride is not available as a starting compound. Hence, the synthesis was first tried using an hexachlorocerat(IV) anion (i.e. $[NEt_4]_2[CeCl_6]$) in thf but yielded only a rather unexpected cerium(III) compound $[NEt_4][CeCl_2((S)\text{-}PEBA)_2]$ (**14**) (see Scheme 9).
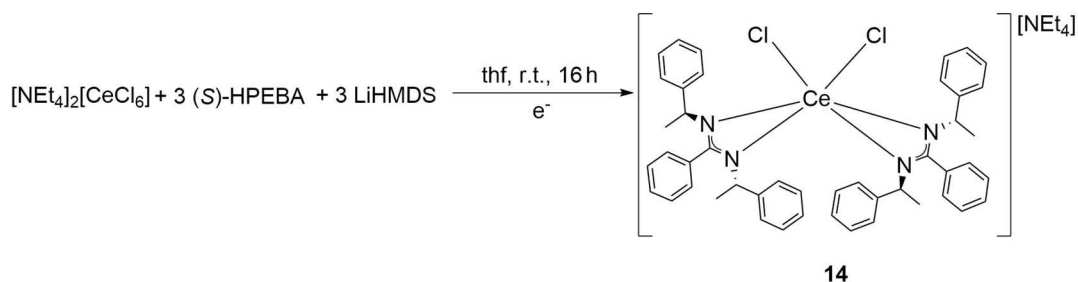
Scheme 9. Synthesis of anionic Ce^{III} amidinate $[NEt_4][CeCl_2((S)\text{-}PEBA)_2]$ (**14**).

Thus, another approach was established to synthesize the tetravalent cerium complex $[CeCl((S)\text{-}PEBA)_3]$ (**16**). This procedure was adopted from the synthesis of the only other tetravalent cerium amidinate complex known so far, $[CeCl((NSiMe_3)_2C(p\text{-}MeOC_6H_4))_3]$, which has been synthesized by oxidizing a homoleptic cerium(III) amidinate ($[Ce((NSiMe_3)_2C(p\text{-}MeOC_6H_4))_3]$) with PhICl$_2$, an iodine(III) reagent.[217] In a first step, the homoleptic cerium(III) complex $[Ce((S)\text{-}PEBA)_3]$ (**15**) has been synthesized by a salt metathesis approach (see Scheme 10). The synthesis of the trivalent cerium complex will be discussed in detail together with other trivalent amidinate complexes in Section 3.2.

Scheme 10. Synthesis of the homoleptic Ce^{III} amidinate $[Ce((S)\text{-}PEBA)_3]$ (**15**).

Subsequently, the cerium(III) compound **15** was oxidized showing an immediate color change from yellow to dark blue. After workup SC-XRD data and NMR spectra proved the successful synthesis of the $[CeCl((S)\text{-}PEBA)_3]$ complex **16** (see Scheme 11). However, this complex is very sensitive towards any kind of moisture or oxygen impurities and temperature sensitive as it has been shown by temperature dependent NMR spectra (see Figure 60 in Appendix). Thus, it was only stable for a short time in solution, whereas the stability in the solid state was sufficient to get structural information by SC-XRD analysis.
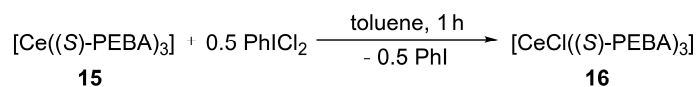

Scheme 11. Oxidation of the trivalent cerium complex $[Ce((S)\text{-}PEBA)_3]$ (**15**) to the tetravalent cerium complex $[CeCl((S)\text{-}PEBA)_3]$ (**16**).

3.1.1.3 Actinide (pseudo)halide amidinate complexes

In addition to the heteroleptic chloro amidinate complexes **1-13** and **16** the chiral tris(amidinate) actinide complexes [AnCl((*S*)-PEBA)$_3$] **9-11** have been further functionalized using (pseudo)halide substitution reactions to elucidate the influence of different (pseudo)halide ligands on the coordination environment of the actinides. Furthermore, this introduces new actinide heteroatom interactions to be studied in the solid state and in solution. Thus, unprecedented fluoro (**17-19**), bromo (**20-22**) and azido (**23-25**) tris(amidinate) complexes of [AnX((*S*)-PEBA)$_3$] type have been synthesized for the investigated tetravalent actinides (An = Th, U, and Np).
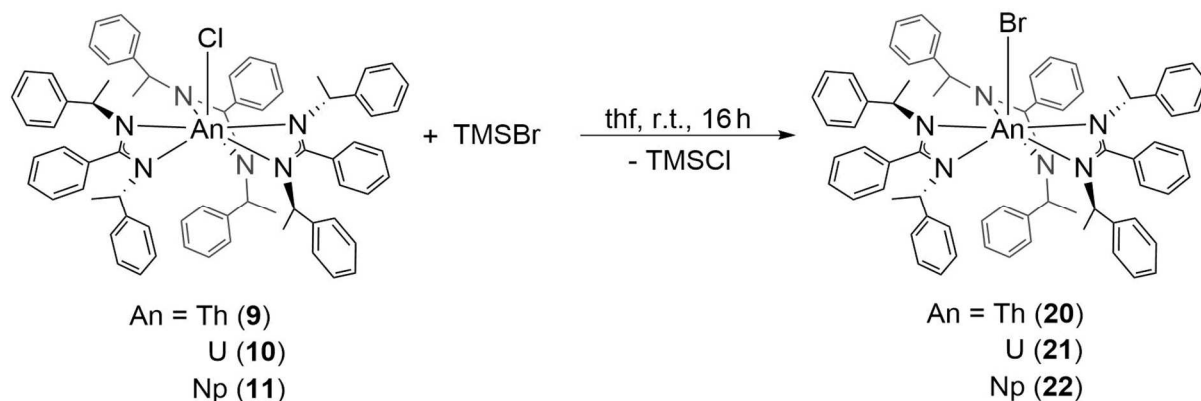
The synthesis of the fluoro tris(amidinate) compounds [AnF((*S*)-PEBA)$_3$] (**17-19**) has been performed by adding AgPF$_6$ to solutions of the respective chloro complexes **9-11** in toluene solution (see Scheme 12).
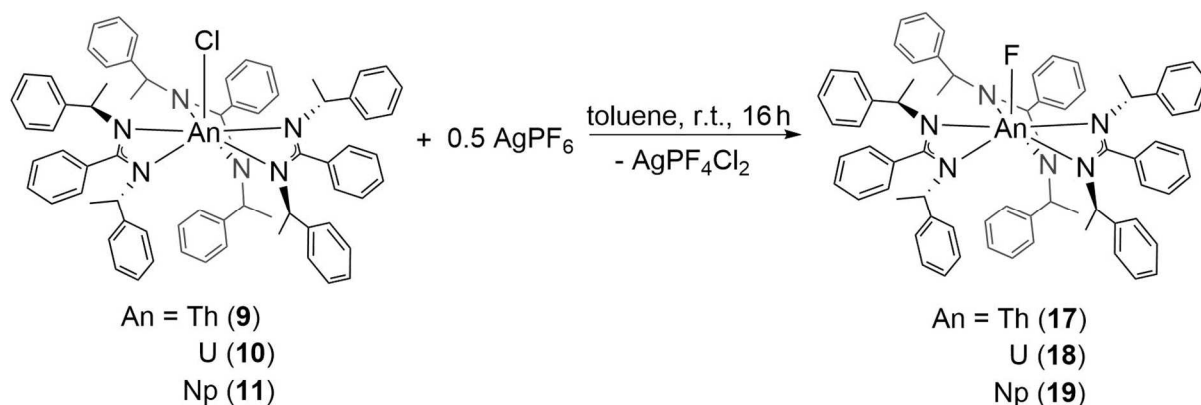
Scheme 12. Synthesis of tetravalent actinide fluoro tris(amidinate) compounds [AnF((*S*)-PEBA)$_3$] **17-19**.

The use of AgPF$_6$ as a fluoride source has already been reported for Zr^{IV},[218] Ta^{V},[219] and Mo^{II}/W^{II} complexes.[220] These investigations all report the formation of PF$_5$ during the reaction. In contrast, a ^{19}F NMR of the reaction mixture of [NpCl((*S*)-PEBA)$_3$] (**11**) with AgPF$_6$ does not show signals for PF$_5$. Instead the signals are in agreement with the formation of the *cis*-[PF$_4$Cl$_2$]$^-$ anion is solution (see Figure 93 in Appendix for ^{19}F NMR spectrum).[221] This implies a two-step reaction sequence with a stepwise substitution of fluoride through chloride at the [PF$_6$]$^-$ anion leading to a halide substitution in two complex molecules per AgPF$_6$. The signal of the fluoro ligand which is directly bound to the metal in complexes **17-19** could not be observed in the ^{19}F NMR spectra although a broad spectral range (-1000 ppm – 1000 ppm) has been investigated. For the paramagnetic uranium and neptunium complexes this behavior can be explained by the paramagnetic relaxation enhancement of the bound metal. However, also for the diamagnetic thorium complex **17** no signal of the fluoro ligand was visible. The formation of the fluoro complexes has been unequivocally proven by SC-XRD and ^{1}H-^{13}C NMR spectra (see Section 8.2.3 in Appendix).

The tetravalent bromo tris(amidinate) compounds **20**-**22** are synthesized by reaction with trimethylsilylbromide in thf solution. This procedure is adapted from a literature procedure.[222]

An = Th (**9**)   An = Th (**20**)
      U (**10**)   U (**21**)
      Np (**11**)   Np (**22**)

Scheme 13. Synthesis of tetravalent actinide bromo tris(amidinate) compounds [AnBr((*S*)-PEBA)$_3$] **20**-**22**.

Furthermore, a salt metathesis using sodium azide yielded the tetravalent actinide azido tris(amidinate) complexes **23**-**25**.

An = Th (**9**)   An = Th (**23**)
      U (**10**)   U (**24**)
      Np (**11**)   Np (**25**)
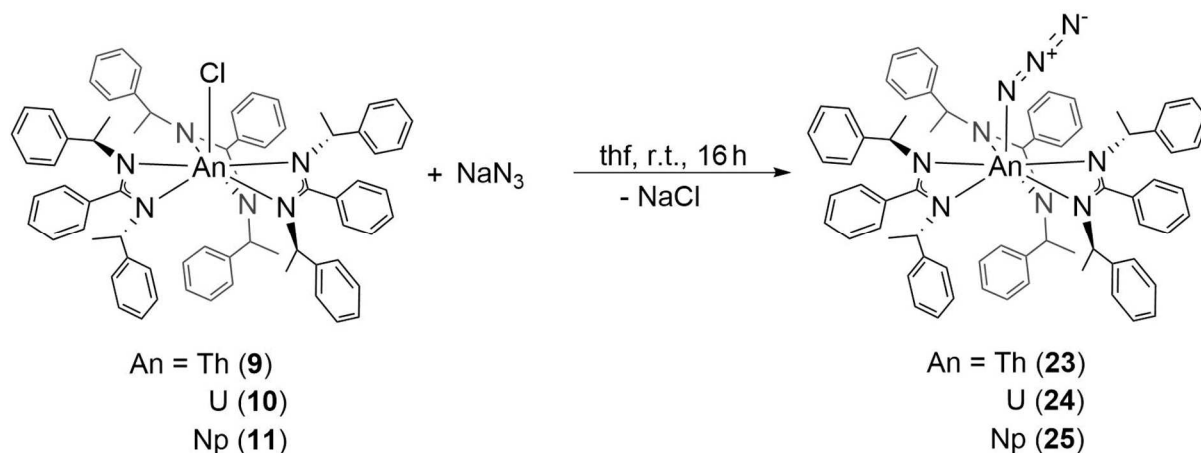
Scheme 14. Synthesis of tetravalent actinide azido tris(amidinate) compounds [AnN$_3$((*S*)-PEBA)$_3$] **23**-**25**.

Similar reaction conditions have already been applied to synthesize tetravalent uranium azido complexes stabilized by amide,[223-225] guanidinate,[226] aryloxide,[224] and SCHIFF base[227] ligands. It has to be pointed out, that the neptunium complexes **19**, **22**, and **25** are unique examples of transuranic metal-organic compounds possessing a fluoro, bromo, or azido ligand.[214]

In the next section, the solid-state structures of the synthesized tetravalent metal amidinate complexes will be discussed and their intramolecular distances will be evaluated to elucidate possible trends which may point to similarities and differences between tetravalent actinides and transition metals, respective, tetravalent lanthanides. Furthermore, quantum chemical calculations have been performed in order to discover the nature of the bonds between the actinides and the coordinating atoms.

3.1.2 Solid-state structures

In total it was possible to isolate four series of isostructural tetravalent metal chloro amidinate complexes possessing either actinide and transition metal cations (for *i*Pr₂BA) or actinide and lanthanide cations (for (*S*)-PEBA). Three additional series of actinide amidinates have been synthesized featuring different (pseudo)halide ligands, i.e. fluoride, bromide and azide. These series will be analyzed in detail in the following section to evaluate the influence of the respective metal ions especially the tetravalent metal ions on the coordination environment and the bond lengths towards the coordinating atoms. The synthesized tetravalent metal chloro amidinates in 1:2 and 1:3 (metal:ligand) stoichiometry are summarized in Table 2 to give a comprehensive overview. From this overview general trends can be deduced which are valid for all investigated complexes.

The relatively small *i*Pr₂BA ligand enables the synthesis of a transition metal tris(amidinate) complex [ZrCl(*i*Pr₂BA)₃] (**2**) which could not be synthesized with the larger (*S*)-PEBA ligand despite several attempts with larger excesses of ligand. Generally, the steric repulsion between the amidinate ligands hampers the complexation of the small transition metals such as titanium and hafnium with three amidinate ligands. Thus, only bis(amidinate) complexes **12**, **13** (Ti) and **1**, **7** (Hf) could be isolated. Isostructural bis(amidinate) complexes with the much larger actinide ions should be possible from a sterical perspective. However, despite the synthesis of the bis(amidinate) uranium complex **8** no other actinide bis(amidinate) has been observed which may point to the increased stability of the tris(amidinate) complexes in solution. The observed difference between zirconium and hafnium is rather unexpected as both metals possess very similar ionic radii (CN = 6: Hf^{IV}: 0.71 Å; Zr^{IV}: 0.72 Å)[228] and chemical properties. This observation is discussed in the next section in more detail.

Table 2. Summary of synthesized tetravalent metal amidinates with *i*Pr₂BA and (*S*)-PEBA in 1:2 and 1:3 (metal:ligand) stoichiometry. Legend: (-) – not possible due to steric reasons, (o) – not observed, SG – space-group type.

metal	*i*Pr₂BA		(*S*)-PEBA	
	1:2	1:3	1:2	1:3
Ti	**12**	-	**13**	-
Zr	[123]	**2**	**6**	-
Hf	**1**	-	**7**	-
Ce	o	o	o	**16**
Th	o	**3**	o	**9**
U	o	**4**	**8**	**10**
Np	o	**5**	o	**11**
SG	*Pbcn*	*Pa*$\overline{3}$ (Zr) / *Pbca*	*P*2₁ (Ti) / *C*₂	*P*2₁2₁2₁

3.1.2.1 Isostructural bis- and tris(amidinates) with iPr₂BA

In order to elucidate possible trends, the synthesized bis- and tris(amidinate) complexes with the *i*Pr₂BA ligand are investigated regarding their solid-state structures in the following. First, the transition metal bis(amidinate) complexes are discussed briefly with a special focus on the elusiveness of tris(amidinate) complexes using the relatively small transition metals titanium and hafnium. Thereafter the isostructural series of tris(amidinate) complexes [MCl(*i*Pr₂BA)₃] (M = Zr (**2**), Th (**3**), U (**4**), Np (**5**)) is investigated regarding the coordinative bond distances to derive the nature of the bonding interactions between the actinides and the coordinating atoms.

Bis(amidinates) [MCl₂(iPr₂BA)₂] (M = Ti, Zr, Hf)

The tetravalent bis(amidinate) complexes using the *i*Pr₂BA ligand have been synthesized only for the transition metals titanium (**12**) and hafnium (**1**) during attempts to synthesize the corresponding tris(amidinate) complexes. The structures of both synthesized transition metal bis(amidinate) complexes [MCl₂(*i*Pr₂BA)₂] (M = Ti (**12**), Hf (**1**)) are in good agreement with the already published zirconium complex [ZrCl₂(*i*Pr₂BA)₂][123] (see Figure 8). The bis(amidinate) complexes [MCl₂(*i*Pr₂BA)₂] (M = Ti, Zr, Hf) isostructurally crystallize in the orthorhombic space-group type *Pbcn* with similar cell parameters (see Table 11 in Appendix). They possess a distorted octahedral coordination geometry around the metal center with a *cis*-arrangement of the amidinate ligands. Thus, an axial chirality is emerging. Although only the Λ-conformers of the complexes are shown in Figure 8, they crystallize as racemates having both diasteromers in the unit cell. This is not surprising as the achiral *i*Pr₂BA ligand cannot have a structure directing effect on the chirality at the metal center.

The amidinates are coordinating asymmetrically towards the metal center (see Table 3) with the slightly longer bond located opposite to the residual chloro ligands. This may be caused by stabilizing intramolecular hydrogen bridges between the chlorides and the adjacent isopropyl groups. In general, the bond lengths between the metal and the coordinating atoms are in accordance with literature data of similar [MCl₂(L)₂] (L = amidinate) compounds (see Table 12 in Appendix) and increase with increasing ionic radii, pointing to a mainly ionic interaction.
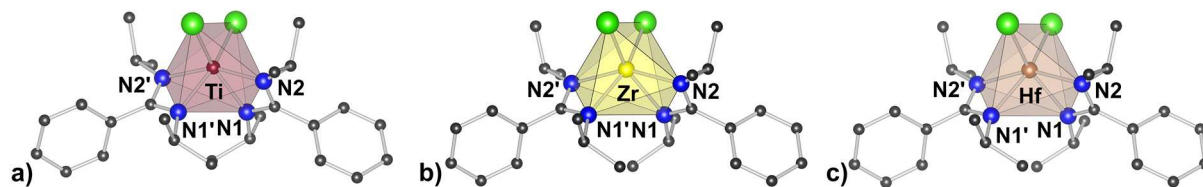

Figure 8. Molecular structures of bis(amidinate) [MCl₂(*i*Pr₂BA)₂] complexes a) [TiCl₂(*i*Pr₂BA)₂] (**12**), b) [ZrCl₂(*i*Pr₂BA)₂],[123] c) [HfCl₂(*i*Pr₂BA)₂] (**1**). Hydrogen atoms are omitted for clarity. Color code: titanium (Ti, purple), zirconium (Zr, yellow), hafnium (Hf, pale brown), carbon (C, dark grey), nitrogen (N, blue), and chlorine (Cl, green).

Table 3. Intramolecular distances between metal center M and coordinating atoms in isostructural bis(amidinate) [MCl$_2$(iPr$_2$BA)$_2$] complexes **1** (M = Hf), **12** (M = Ti), and [ZrCl$_2$(iPr$_2$BA)$_2$][123] together with ionic radius (r$_{ion}$) for coordination number six according to SHANNON.[228]

d(M–X) [Å]	**12** (M = Ti)	(M = Zr)[123]	**1** (M = Hf)
Cl1	2.293(1)	2.416(2)	2.398(1)
N1	2.104(2)	2.207(4)	2.201(2)
N2	2.038(2)	2.197(4)	2.178(2)
r$_{ion}$ (CN = 6)[228]	0.605	0.710	0.720

Interestingly, the difference between the intramolecular M–N distances, i.e. the asymmetry, is also decreasing with increasing ionic radius (i.e. Ti (**12**): 0.066 Å, Hf (**1**): 0.023 Å, Zr[123]: 0.010 Å), another indication for the increased steric repulsion between the amidinate ligands also in the bis(amidinate) complexes [MCl$_2$(iPr$_2$BA)$_2$] possessing small metal cations. This underlines the finding that tris(amidinate) complexes could not be formed using iPr$_2$BA as ligand for titanium and hafnium due to the smaller coordination sphere. No examples of titanium tris(amidinate) complexes of the [TiCl((NR′)$_2$CR)$_3$] type are found in the literature. However, 2-aminopyridine (PyN) complexes of the [TiCl(PyN)$_3$] type could be isolated,[229-230] which show a similar bidentate nitrogen donor coordination motif, but have a smaller bite angle (61.7° for 2-(methylamino)pyridine, 64° for iPr$_2$BA) and are less sterically crowded due to the fixed pyridine unit. Furthermore, tetravalent tris(guanidinate) titanium compounds having two monoanionic and one dianionic ligand could be prepared.[231-232] Here, the absence of an additional chloro ligand enables the synthesis of those compounds due to the less crowded coordination sphere.

In contrast to titanium, the synthesis of hafnium complexes of the [HfCl((NR′)$_2$CR)$_3$] type has already been described using symmetrically[233] and asymmetrically[234-235] substituted amidinates and guanidinates (see also Table 16 in Appendix). The $N,N′$-bis(isopropyl)-benzamidinate (iPr$_2$BA) ligand used in this thesis possesses a larger central substituent (phenyl) compared to the only other symmetric amidinate ($N,N′$-bis(isopropyl)-methylamidinate) used to synthesize tris(amidinate) complexes of hafnium. This additional phenyl moiety could influence the steric demand and hence the formation tendency of these complexes. Thus, the central substituent potentially alters the threshold for the formation of the tris(amidinate) complexes with the iPr$_2$BA ligand exactly between the ionic radius of zirconium and hafnium. This example indicates the possibility of adjusting the sterical and also electronic properties of amidinate ligands by varying the substituents. Smaller amidinate ligands would possibly enable the synthesis of tris(amidinate) hafnium complexes, but not iPr$_2$BA. This is a rare example of different complexation properties for zirconium and hafnium and may point to new separation technologies of both transition metals in the future.

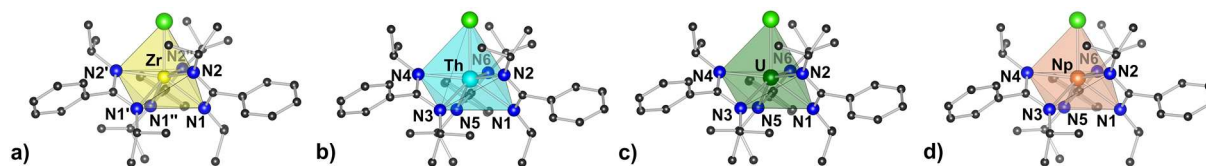*Tris(amidinates) [MCl(iPr₂BA)₃] (M = Zr, Th, U, Np)*

Figure 9. Molecular structure of tris(amidinate) [MCl(*i*Pr₂BA)₃] complexes a) [ZrCl(*i*Pr₂BA)₃] (**2**), b) [ThCl(*i*Pr₂BA)₃] (**3**), c) [UCl(*i*Pr₂BA)₃] (**4**) and d) [NpCl(*i*Pr₂BA)₃] (**5**). Hydrogen atoms and solvent molecules are omitted for clarity. Color code: zirconium (Zr, yellow), thorium (Th, pale blue), uranium (U^IV, dark green), neptunium (Np^IV, orange red), carbon (C, dark grey), nitrogen (N, blue), and chlorine (Cl, green).

A series of tetravalent metal tris(amidinates) [MCl(*i*Pr₂BA)₃] (M = Zr (**2**), Th (**3**), U (**4**), Np (**5**)) has been synthesized. The respective molecular structures of **2-5** are shown in Figure 9. The actinide amidinates [AnCl(*i*Pr₂BA)₃] (An = Th (**3**), U (**4**), Np (**5**)) are crystallizing in the orthorhombic space-group type *Pbca* with similar cell parameters (see Table 14 in Appendix). However, the zirconium complex [ZrCl(*i*Pr₂BA)₃] (**2**) is crystallizing in the highly symmetric cubic space-group type $Pa\overline{3}$. The reason for this behavior is assumed to be the small ionic radius of the zirconium in contrast to the much larger actinide ions.[12] The coordination sphere of the actinide cations is potentially not saturated and hence a symmetric coordination is rather unlikely. In general, the metal cations in **2-5** are coordinated in a monocapped distorted octahedral coordination sphere with the three amidinates helically wound around the metal center introducing an axial chirality. Similar to the bis(amidinate) complexes of the *i*Pr₂BA ligand both diastereomers are present in the unit cell, but only the Λ-conformer is shown in Figure 9. A comparison of the tilting angles of the amidinate units in the complexes reveals the difference between the actinide (**3-5**) and the transition metal complex **2** (see Table 4). The tilting angle is defined as the angle between the plane normal of the amidinate N–C–N plane towards the M–Cl bond. The actinide tris(amidinates) show one smaller (*a*) and two almost identical (*b*, *c*) tilting angles compared to the highly symmetric zirconium complex with only one tilting angle.

Table 4. Tilting angles of different amidinate moieties in tris(amidinate) complexes [MCl(*i*Pr₂BA)₃] (M = Zr (**2**), Th (**3**), U (**4**), Np (**5**)). Inset right shows coordination sphere of [NpCl(*i*Pr₂BA)₃] (**5**) with marked amidinate planes (blue: a, N1–C–N2; green: b, N3–C–N4; red: c, N5–C–N6).

α [°]	**2** (Zr)	**3** (Th)	**4** (U)	**5** (Np)
a	51.7	49.1	49.3	49.5
b	51.7	51.7	51.6	51.5
c	51.7	51.9	51.6	51.7
SG	$Pa\overline{3}$	*Pbca*	*Pbca*	*Pbca*
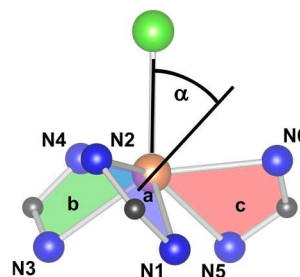
[12] Ionic radii for coordination number seven according to Shannon[228]: Zr^IV: 0.78 Å, Np^IV: 0.93 Å, U^IV: 0.95 Å, Th^IV: 1.00 Å. The values for Th and Np are estimated based on data for coordination number six and eight.

The smaller tilting angle of a is also increasing when traversing the actinide series towards smaller ionic radii (Th > U > Np), another indication of the structural transition from lower (orthorhombic) to higher (cubic) symmetric complexes with decreasing ionic radius of the metal cation.

The tetravalent metal compounds **2-5** are not isomorphous but isostructural, as it is also evident from their nearly identical infrared (IR) spectra (see Figure 41 in Appendix). Thus, the evaluation of the bond lengths within the coordination sphere of the series of tris(amidinate) complexes enables a direct comparison of transition metal and actinide properties. Furthermore, differences between actinides with (U, Np) and without (Th) f electrons are of interest. The intramolecular distances between the metal center and the coordinating atoms have been plotted against the ionic radii of the corresponding metal ions (see Figure 10).

The distances to the nitrogen atoms N1, N3, and N5 (opposite to the chlorine atoms) are averaged to N_{long}, whereas the distances to N2, N4, and N6 are averaged to N_{short} (see Table 15 in Appendix for specific values). The error bars depict the standard deviation σ of these averages. In general, the distances between the metal center and the coordinating atoms are in accordance with available literature data of similar tris(amidinate) complexes (see Table 16 in Appendix). They linearly decrease with the ionic radius of the metal cation as evidenced by the determination coefficients shown in Figure 10.
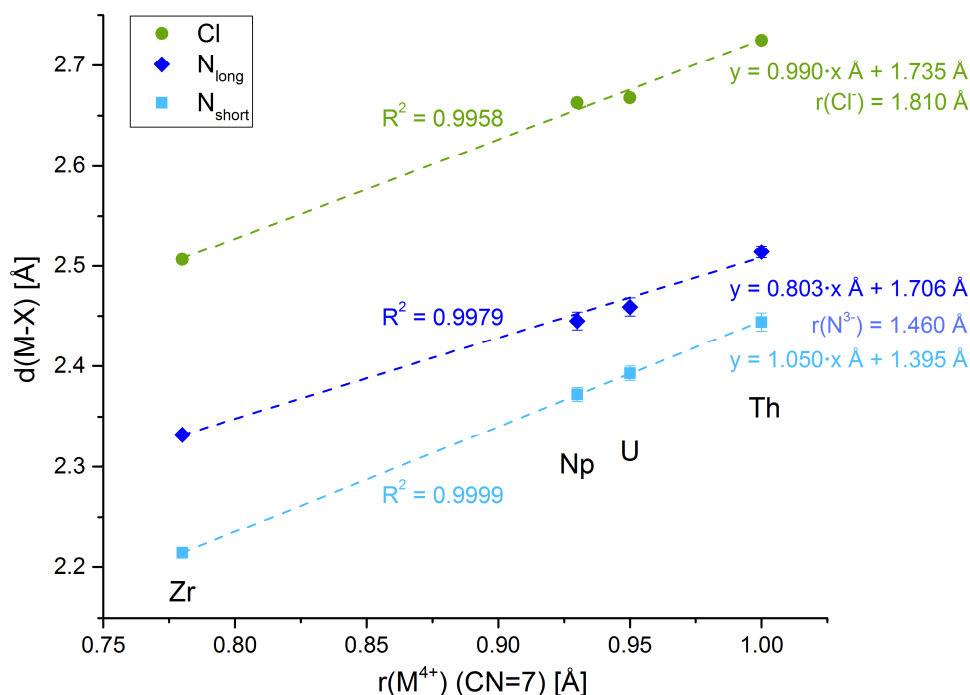
Figure 10. Plot of coordinative intramolecular distances M–X (M = Zr, Np, U, Th ; X = Cl, N) in tris(amidinate) [MCl(iPr$_2$BA)$_3$] complexes **2**, **3**, **4**, **5** against ionic radii (CN = 7)[228]. The error bars correspond to the standard deviation σ of the average. Dashed lines show linear fit with determination coefficients (R^2) and linear regression model. The values for the linear fit have been weighted with $1/\sigma^2$. Ionic radii for coordinating atoms (i.e. Cl$^-$ (CN = 6) and N^{3-} (CN = 4)) are given for comparison.[228]

The slope of the linear fit is close to one especially for the M–Cl and M–N$_{short}$ distances. This is indicative for an ionic interaction between the metal centers and the coordinating atoms. Thus, the axis intercept should in principle equal the ionic radius of chloride (1.81 Å)[228] or nitrogen (1.46 Å)[228]. However, both obtained intercepts for the linear fit of the complex series are 0.075 Å (Cl) resp. 0.065 Å shorter than the ionic radii. At least for the chloride a similar linear decrease has been observed for a series of ionic [PPh$_4$]$_2$[MCl$_6$] (M = Ti, Zr, Hf, Th, U, Np, Pu) complexes (y = 0.98·x Å+1.75 Å).[8] According to RAYMOND and EIGENBROT this behavior corresponds to a purely ionic interaction.[236] The only available systematic investigation of tetravalent actinide complexes possessing An–N bonds, i.e. [M(L^N)$_2$]^{13} (M = Zr, Hf, Ce, Th, U, Pu), shows a similar linear dependence of the An–N distances from the ionic radii of the actinides (y = 0.96·x Å+1.63 Å), but significantly shorter bonds between the nitrogen and the transition metals Zr and Hf.[17] This difference may be related to the different crystal packing comparing the actinide and the transition metal complexes also incorporating different solvent molecules. Thus, also for this example a linear decrease of the An–N distances in the actinide series is observed.

It may be speculated that the smaller axis intercepts of the linear regression for the M–N$_{short}$ and M–Cl distances in the [MCl(iPr$_2$BA)$_3$] complexes of this work originate from an additional bonding contribution. However, this potential bonding contribution is inherent to all investigated metals and thus no difference between the transition metal zirconium and the actinides with and without f electrons is observed. Thus, it can be summarized that an ionic bonding interaction is apparent between the tetravalent metals and the coordinating atoms in the tris(amidinate) complexes [MCl(iPr$_2$BA)$_3$] (M = Zr (**2**), Th (**3**), U (**4**), Np (**5**)). The deviation between the axis intercepts may instead be attributed to the tabulated ionic radii for the coordinating atoms chlorine and nitrogen which are calculated based on solid-state structures with isolated ions in defined coordination environments. This does not reflect the situation of either atom in the investigated complexes causing the observed deviations.

The linear regression model for the nitrogen opposite to the chloride (N$_{long}$) also shows a reasonable correlation, but the slope and intercept do not correspond to the ionic bonding model discussed beforehand. Thus, also here steric effects may play an important role as already reported for the bis(amidinate) series. The difference between the longer (N$_{long}$) and the shorter (N$_{short}$) metal-nitrogen bond lengths is decreasing with increasing ionic radii. This again reflects a higher steric repulsion of the ligands if a smaller metal ion, like zirconium, is present.

---

[13] H$_2$L^N: *N*,*N*′-bis((4,4′-diethylamino)salicylidene)-1,2-phenylenediamine

3.1.2.2 Isostructural bis- and tris(amidinates) with (S)-PEBA

In addition to the *i*Pr$_2$BA ligand, the (*S*)-PEBA ligand has been used to synthesize series of isostructural bis- and tris(amidinate) actinide complexes. In the following, these complex series are investigated regarding their coordinative bonding interactions in the solid state supported by quantum chemical calculations. In addition, the tris(amidinate) complexes [AnCl((*S*)-PEBA)$_3$] are further functionalized using (pseudo)halogen exchange reactions to yield the corresponding fluoro, bromo, and azido complexes which possess new actinide heteroatom interactions to be studied.

In contrast to the achiral *i*Pr$_2$BA ligand, the (*S*)-PEBA ligand possesses two chiral centers in the 1-phenyl(ethyl) substituents next to the donating nitrogen atoms. As already mentioned in Fundamentals Section 2.2 mono-, bis-, and tris(amidinate) complexes of this ligand have already been prepared. Due to the chiral ligand different diastereomers with varying chirality-at-metal can in principle be observed. However, with the used metal salts and the applied stoichiometric ratios only one diastereomer was exclusively observed in the solid state for the tetravalent metal amidinates.

Bis(amidinates) [MCl$_2$((S)-PEBA)$_2$] (M = Ti, Zr, Hf, U)

As already shown in Table 2 complexes of 1:2 (metal:ligand) stoichiometry should be possible for the whole series of tetravalent metals used (i.e. Ti, Zr, Hf, Ce, Th, U, Np) due to steric considerations. However, especially for the larger cations, the tris(amidinate) complexes seem to be favorable because even if only a 1:2 (metal:ligand) ratio was used, for Th and Np the 1:3 complex could be observed exclusively. Only for uranium it was possible to extract the corresponding bis(amidinate) complex, but with impurities of the tris(amidinate) complex already present (see Figure 56 in Appendix). The molecular structures of the synthesized bis(amidinate) complexes [MCl$_2$((*S*)-PEBA)$_2$] (M = Ti (**13**), Zr (**6**), Hf (**7**), U (**8**)) are shown in Figure 11. Interestingly, the chirality-at-metal changes from a Δ-configuration in the smaller transition metal bis(amidinates) [TiCl$_2$((*S*)-PEBA)$_2$] (**13**) and [ZrCl$_2$((*S*)-PEBA)$_2$] (**6**) to the Λ-configuration in [HfCl$_2$((*S*)-PEBA)$_2$] (**7**) and [UCl$_2$((*S*)-PEBA)$_2$] (**8**).
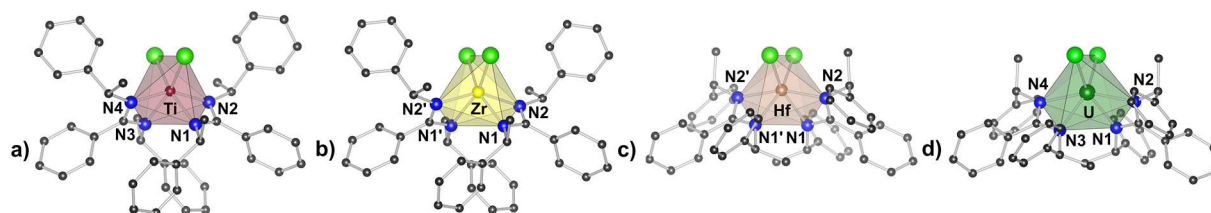
Figure 11. Molecular structures of bis(amidinate) [MCl$_2$((*S*)-PEBA)$_2$] complexes a) Δ-[TiCl$_2$((*S*)-PEBA)$_2$] (**13**), b) Δ-[ZrCl$_2$((*S*)-PEBA)$_2$] (**6**), c) Λ-[HfCl$_2$((*S*)-PEBA)$_2$] (**7**) and d) Λ-[UCl$_2$((*S*)-PEBA)$_2$] (**8**). Hydrogen atoms are omitted for clarity. Color code: titanium (Ti, purple), zirconium (Zr, yellow), hafnium (Hf, pale brown), uranium (U^{IV}, dark green), carbon (C, dark grey), nitrogen (N, blue), and chlorine (Cl, green).

However, even though the chirality-at-metal is the same for the titanium and zirconium (Δ) as well as for the hafnium and uranium (Λ) complexes, the space-group type and lattice parameters differ substantially between these complexes having identical configurations (see Table 19 in Appendix). This is already visible by the different naming schemes for the nitrogen atoms indicating different crystal symmetries.

The diastereomeric purity of the synthesized complexes has been proven by powder X-ray diffraction (PXRD) patterns (see Section 8.2.1 in Appendix). Interestingly, the PXRD pattern of the [ZrCl$_2$((S)-PEBA)$_2$] (**6**) complex rather fits to the simulated diffraction pattern of the titanium complex **13** (see Figure 52 in Appendix). Both possess the same chirality-at-metal but a different molecular packing. Probably, the measured single-crystal of **6** corresponds to a minor polymorph and the majority of the [ZrCl$_2$((S)-PEBA)$_2$] (**6**) complex is crystallizing in the [TiCl$_2$((S)-PEBA)$_2$] (**12**) structure type. The PXRD patterns of [HfCl$_2$((S)-PEBA)$_2$] (**7**) and [UCl$_2$((S)-PEBA)$_2$] (**8**) are quite similar (see Figure 54 in Appendix) making a decision of the corresponding structure type difficult.

The fact that the transition metals zirconium and hafnium possess similar properties and ionic radii but show different chiralities when complexing the chiral (S)-PEBA ligand is noteworthy. In contrast, BRUNNER *et al.* synthesized the corresponding [M(NMe$_2$)$_2$((S)-PEBA)$_2$] (M = Zr, Hf) complexes[143] which both are crystallizing in the Λ-configuration, similar to the hafnium complex **7**. Keeping in mind, that the dimethylamino ligand requires more space than the chlorido ligand in **6** and **7** and the Λ-configuration is favored due to the reduced steric repulsion between the phenyl moieties and the auxiliary ligands (i.e. Cl, NMe$_2$), it may be assumed, that the energy difference between the formation of both diastereomers in **6** is very small. Thus, upon crystallization one diastereomer may be favored due to a small energy gain by crystal packing. Nevertheless, this again shows that the complexation of tetravalent zirconium and hafnium with amidinates could hold potential for the separation of both metals, as already indicated in the previous section 3.1.2.1 for the iPr$_2$BA ligand.

The bond lengths within the bis(amidinate) complexes are shown in Table 20 in the Appendix. Again, they agree well with literature examples of bis(amidinate) complexes (see Table 12 in Appendix) and also with the bis(amidinate) complexes **1** and **12** possessing the iPr$_2$BA ligand reported in this thesis. Due to the change of the chirality-at-metal within the complex series the isostructurality criteria is not fulfilled and hence deriving possible differences between actinides and transition metals from this complex series is not straightforward. Thus, the synthesized tris(amidinate) complexes with the (S)-PEBA ligand will be investigated in detail in the following.

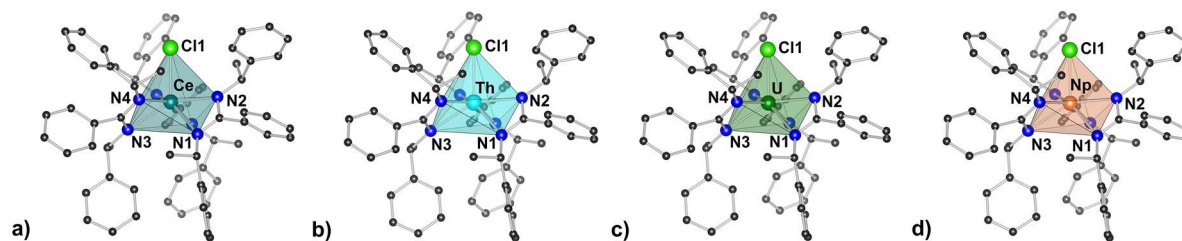*Tris(amidinates) [MCl((S)-PEBA)₃] (M = Ce, Th, U, Np)*

Figure 12. Molecular structure of tris(amidinate) [MCl((*S*)-PEBA)₃] complexes a) Δ-[CeCl((*S*)-PEBA)₃] (**16**), b) Δ-[ThCl((*S*)-PEBA)₃] (**9**), c) Δ-[UCl((*S*)-PEBA)₃] (**10**) and d) Δ-[NpCl((*S*)-PEBA)₃] (**11**). Hydrogen atoms and solvent molecules are omitted for clarity. Color code: cerium (Ce^{IV}, dark blue), thorium (Th, pale blue), uranium (U^{IV}, dark green), neptunium (Np^{IV}, orange red), carbon (C, dark grey), nitrogen (N, blue), and chlorine (Cl, green).

The tris(amidinate) complexes [MCl((*S*)-PEBA)₃] (M = Ce (**16**), Th (**9**), U (**10**), Np (**11**)) are the most extensively studied complexes throughout this work. They are the first examples of actinide amidinates having a chirality at the ligand and, furthermore, include the first structurally characterized transuranic enantiopure complex ([NpCl((*S*)-PEBA)₃] (**11**)).[214] In addition, due to the synthesis of the isostructural tetravalent cerium complex **16** a direct comparison between the properties of tetravalent actinides and lanthanides is possible.

Similar to the already described tris(amidinate) complexes with the *i*Pr₂BA ligand, the three (*S*)-PEBA ligands are coordinating towards the metal ion in a "propeller" type coordination motif having the residual chloro ligand placed on the "propeller" axis. Thus, an axial chirality is induced which could be refined to be solely of Δ-configuration for the whole metal series. The molecular structures of the chiral tris(amidinate) complexes are shown in Figure 12.

Complexes **9**-**11** and **16** crystallize in the chiral space-group type *P*2₁2₁2₁ with reasonably low FLACK parameters (see Table 22 in Appendix), indicating their enantiopurity. PXRD patterns of the thorium and uranium complexes **9** and **10** (see Figure 62 and Figure 71 in Appendix) and IR spectra of all isostructural compounds (see Figure 89 in Appendix) support these findings. The monocapped distorted octahedral coordination polyhedron is characterized by distinct tilting angles of the amidinate units towards the metal–chlorine axis similar to the already shown tris(amidinates) with the *i*Pr₂BA ligand. In contrast to the *i*Pr₂BA ligand series, three distinct tilting angles are observed for the tris(amidinate) complexes with (*S*)-PEBA (see Table 24 in Appendix). However, the tilting angles do not vary substantially within the complex series, again reflecting the isostructurality.

The intramolecular distances between the metal center and the coordinating atoms are plotted against the ionic radii of the respective metal cation (see Figure 13) to get further insight into the bonding behavior between the metal and the coordinating atoms. The ionic radius of Ce^{IV} for coordination number seven was estimated to be 0.92 Å based on data for coordination number six and eight.[228]
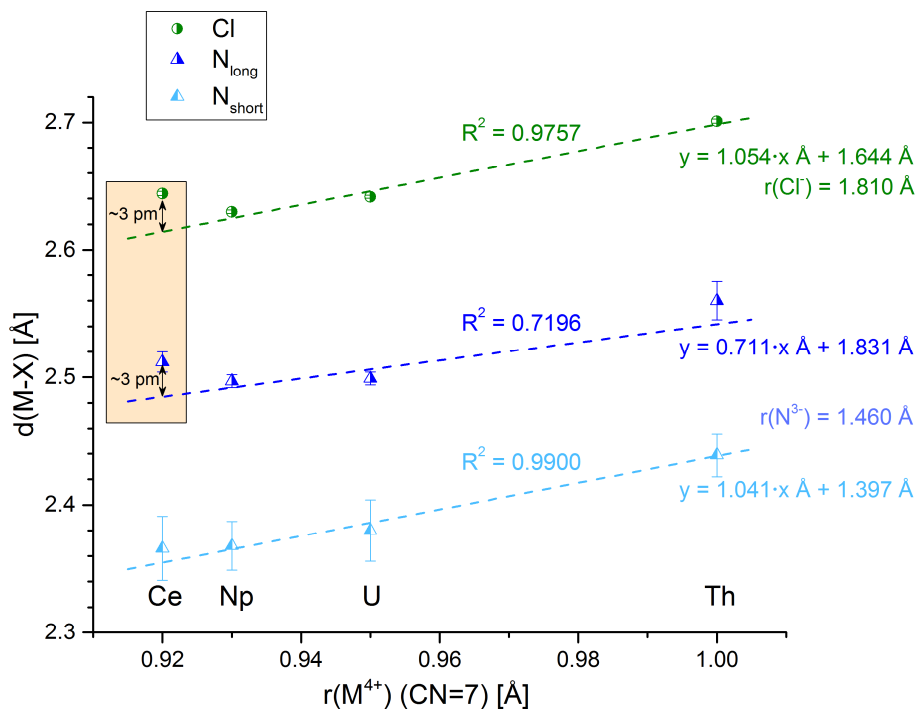
Figure 13. Plot of coordinative intramolecular distances M–X (M = Ce, Np, U, Th ; X = Cl, N) in tris(amidinate) [MCl((S)-PEBA)$_3$] complexes **9-11**, **16** against ionic radii (CN = 7).[228] The error bars correspond to the standard deviation σ of the average for N$_{short}$ and N$_{long}$. Dashed lines show linear fit only for actinide complexes **9**, **10** and **11** with determination coefficient (R^2) and linear regression model. The values for the linear fit have been weighted with 1/σ^2. Ionic radii for coordinating atoms (i.e. Cl$^-$ (CN = 6) and N^{3-} (CN = 4)) are given for comparison.[228]

Again, the M–N bonds opposite to the chloride (i.e. N1, N3, and N5) have been averaged to M–N$_{long}$ and the bonds to N2, N4, and N6 to M–N$_{short}$ (see Table 23 in Appendix for specific values). The error bars correspond to the standard deviation σ of these averages. Compared to the tris(amidinates) with the iPr$_2$BA ligand, higher standard deviations are observed, as a consequence of the three distinct tilting angles of the amidinate moieties.

In general, the observed trend of decreasing M–X intramolecular distances within the actinide complexes **9-11** seems to be similar to that of the corresponding tris(amidinate) complexes **3-5** with the iPr$_2$BA ligand. The slopes and axis intercepts for the M–Cl and M–N$_{short}$ are similar to what has been reported in the previous section, but the M–N$_{long}$ distances deviate significantly from the expected linear regression due to the increased steric repulsion between the bulky 1-phenylethyl substituents. This behavior is further evidenced by the comparison between the solid-state structures of both synthesized tetravalent actinide tris(amidinate) complex series (see next Section 3.1.2.3). However, it has to be pointed out that the linear fit has only been performed for the actinide complexes **9-11**, as the cerium complex **16** clearly deviates from this linear trend especially for the M–Cl and the M–N$_{long}$ distances. The 4f element cerium clearly shows longer bond lengths (~ 3 pm) than the actinides which is an indication for a difference in the bonding properties when comparing 4f and 5f elements. This behavior is noteworthy as a similar deviation is observed for the Ce–N distances in homoleptic bissalophen complexes

presented in the previous section but not for the Ce–O bonds.[17] This can be an indication, that the tetravalent 5*f* elements show an additional bonding contribution to the nitrogen which may originate from the participation of the more diffuse 5*f* orbitals compared to the 4*f* orbitals in the lanthanides.

To gain more insight in the bonding behavior of the [MCl((*S*)-PEBA)$_3$] complexes and the differences between the tetravalent actinides and cerium, quantum chemical calculations have been performed which will support the experimental findings based on the analysis of the intramolecular bond lengths and the paramagnetic shifts. Thus, the molecular structures of the tetravalent chloro amidinates [MCl((*S*)-PEBA)$_3$] (M = Ce (**16**), Th (**9**), Pa, U (**10**), Np (**11**), Pu) including the experimentally not accessible protactinium and plutonium complexes have been optimized using the PBE functional including the COSMO model. The dielectricity constant ε was set to infinity to implicitly simulate solid-state structures. Further details are given in the Experimental Section 5.1.6. A frequency analysis of the optimized structures (see Table 53 in Appendix) revealed only marginal imaginary wavenumbers indicating a reasonable convergence. The experimentally determined solid-state structures of the tetravalent actinide complexes are similar to the geometry optimized structures. A comparison of the [MCl((*S*)-PEBA)$_3$] (M = Ce (**16**), Th (**9**), Pa, U (**10**), Np (**11**), Pu) complex structures can be found in Section 8.6 in the Appendix.

The geometry optimized structures have been used to gain more insight into the bonding between the actinides and the coordinating atoms in the amidinate complexes, especially the nitrogen atoms. The electronic structure of the synthesized and optimized complex molecules has been investigated using two different approaches, BADER's Quantum Theory of Atoms in Molecules (QTAIM)[211] and the Natural Bond Orbital (NBO) analysis.[212] Two different comparisons will be evaluated: First, the actinide complexes will be compared within the actinide series to estimate the influence of the 5*f* electrons on the bonding situation. Secondly, the properties of the 5*f* elements (i.e. actinides) will be compared to the 4*f* elements (i.e. lanthanides) in order to evaluate differences and similarities.

The QTAIM method defines the atoms within a molecule on the basis of a topological analysis of the electron density. Moreover, using QTAIM charges for the thus defined atoms (q) as well as delocalization indices (DI) for the interaction between those can be calculated (see Fundamentals Section 2.4). The delocalization index can be interpreted as a measure for the bond order, i.e. the number of electron pairs shared between both atoms. A delocalization index of approximately one corresponds to a single bond. The results of the QTAIM analysis are summarized in Table 5 for [MCl((*S*)-PEBA)$_3$] complexes.

Table 5. Summary of values obtained from QTAIM analysis. Charge (q) and delocalization index (DI) for tetravalent chloro tris(amidinate) compounds [MCl(L)$_3$] (M = Ce, Th, Pa, U, Np, Pu; L = (S)-PEBA). Delocalization indices for M–N$_{short}$ and M–N$_{long}$ are added up (Σ DI). Solid arrows indicate increasing, dashed arrows decreasing values.

	q(M)	q(N$_{long}$)	q(N$_{short}$)	q(Cl)	Σ DI (M–N)	DI (M–Cl)
[CeCl(L)$_3$]	+2.44	-1.21	-1.21	-0.69	0.88	0.54
[ThCl(L)$_3$]	+2.76	-1.23	-1.24	-0.73	0.79	0.52
[PaCl(L)$_3$]	+2.67	-1.23	-1.23	-0.70	0.86	0.55
[UCl(L)$_3$]	+2.59	-1.21	-1.22	-0.70	0.90	0.57
[NpCl(L)$_3$]	+2.53	-1.22	-1.22	-0.70	0.90	0.58
[PuCl(L)$_3$]	+2.47	-1.21	-1.22	-0.70	0.92	0.52

In contrast, the NBO analysis is based on the density matrix **D** and defines an atom based on its natural atomic orbitals which are deduced from the molecular orbitals of the system. The natural population analysis (NPA) allows a calculation of the charge of each atom within the molecular framework. The values of the NBO analysis are summarized in Table 6. The f excess corresponds to the number of f electrons in addition to the expected value.[14] In the following both quantum chemical analysis methods are compared with regard to the two already mentioned comparisons within the 5f series and between the 5f and the 4f series.

Table 6. Summary of values obtained from NBO analysis. Charges (q) and natural population analysis (d population and excess of f electrons) are given for tetravalent chloro tris(amidinate) compounds [MCl(L)$_3$] (M = Ce, Th, Pa, U, Np, Pu; L = (S)-PEBA). Solid arrows indicate increasing, dashed arrows decreasing values.

	q(M)	q(N$_{long}$)	q(N$_{short}$)	q(Cl)	population	
					d	f excess
[CeCl(L)$_3$]	+1.80	-0.61	-0.61	-0.56	1.20 (5d)	0.81 (4f)
[ThCl(L)$_3$]	+1.80	-0.65	-0.68	-0.44	1.09 (6d)	0.81 (5f)
[PaCl(L)$_3$]	+1.65	-0.61	-0.63	-0.44	1.11 (6d)	0.73 (5f)
[UCl(L)$_3$]	+1.58	-0.60	-0.61	-0.46	1.16 (6d)	0.81 (5f)
[NpCl(L)$_3$]	+1.61	-0.60	-0.61	-0.49	1.13 (6d)	0.87 (5f)
[PuCl(L)$_3$]	+1.72	-0.59	-0.64	-0.56	1.05 (6d)	0.92 (5f)

The comparison of the obtained values from QTAIM and NBO analysis for the [AnCl((S)-PEBA)$_3$] (An = Th, Pa, U, Np, Pu) complexes reveals a complex picture at the electronic level. According to the QTAIM analysis the charge of the actinide center is decreasing from thorium to plutonium. The charge of the metal cation can be regarded as a measure of the ionic behavior, with a high charge corresponding to charge separation between

---

[14] Th^{IV} (5f^0); Pa^{IV} (5f^1), U^{IV} (5f^2), Np^{IV} (5f^3), Pu^{IV} (5f^4)

the metal center and ligand, and thus more ionic behavior. The decreasing charge of the actinide corresponds to an increase of electron exchange between the metal and the ligands when traversing the series. However, the charges of the coordinating atoms are not decreasing in a similar manner which can be understood as the electronic exchange is distributed over all coordinating ligands and hence the change for one coordinating atom is small. The largest difference is observed for the charge of the chloride in the thorium complex pointing to the most pronounced ionic interaction in this complex.

This observation is further underlined by the analysis of the delocalization indices for the M–N and M–Cl bonds which are generally increasing when traversing the series from thorium to plutonium. This again indicates an increasing covalent character especially when comparing thorium with the later members of the actinide series. The delocalization indices for both An–N bonds sum up to ~0.8 for the thorium complex and remain constant at ~0.9 for the uranium, neptunium, and plutonium complexes. A similar behavior has been found in a series of dithiocarbamate complexes $[M(S_2CNiPr_2)_4]$ (M = Ti, Zr, Hf, Th, U, Np) where the DI increases from 0.42 for the M–S bond in the thorium complex to around 0.48 for the uranium and neptunium complexes.[15] Also KERRIDGE observed a plateau of similar delocalization indices for Pa to Pu in a series of $[An(COT)_2]$ (An = Th, Pa, U, Np, Pu, Am, Cm) complexes, but again a decreasing covalent character towards the middle of the actinide series.[43] Thus, from the analysis of QTAIM it can be assured that the actinides uranium to plutonium are possessing a higher degree of covalency than thorium. Interestingly, such a difference has not been observed by the analysis of the intramolecular bond lengths of $[AnCl((S)-PEBA)_3]$ complexes **9** (Th), **10** (U), and **11** (Np) showing a linear dependence on the ionic radius of the actinide cation with the slope of one. Thus, it can be concluded that the difference between the covalent character of thorium and the later actinides can be revealed by quantum chemical calculations but its magnitude is, however, relatively small and the effect easily becomes overcompensated in the solid state, e.g. by packing effects or intermolecular interactions.

The analysis of the NBO data (see Table 6) shows similar and deviating trends compared to the QTAIM analysis. The NBO charges show a minimum value for the uranium complex. In contrast, the charges of the coordinating atoms behave differently, with the expected decrease of the charge of the nitrogen atoms but an increase for the chloride when traversing the actinide series.

The core of the NBO concept is the ability to analyze populations of "natural orbitals" in a compound. For the actinides, the analysis of the 5*f* and 6*d* orbitals is of highest interest. Here, two values are of importance which is the population of the 6*d* orbitals and the excess of electrons located in the 5*f* orbitals. The 6*d* population increases from thorium to uranium and decreases again to plutonium. Interestingly, this is in accordance with the trend of the NBO charge of the metal cation. On the other hand the 5*f* excess drops from thorium to protactinium

and then rises consistently to plutonium. Thus, possibly both $6d$ and $5f$ orbitals participate in the bonding to a different degree. This is potentially correlated to the energetic differences between both orbitals. However, these results are in contrast to a common concept in actinide chemistry which is FEUDAL (f orbitals essentially unaffected, d orbitals accommodate ligands) by BURSTEN.[237] Instead of unaffected $5f$ orbitals, their participation is increasing when traversing the actinide series whereas the $6d$ covalency seems to have a maximum at uranium. This could possibly also explain the similar results for the M–N delocalization indices for the uranium, neptunium, and plutonium complexes.

In addition to the evaluation of the effects within the $5f$ series, also a comparison between the $4f$ and the $5f$ series is appropriate due to the deviation of the intramolecular bond lengths of the cerium complex **16** from the behavior of the actinide complexes **9-11** (see Figure 13). Although the NBO charge is identical for the tetravalent thorium and the isostructural cerium complex, the charges of the coordinating atoms as well as the QTAIM charges of the metal indicate an increased charge separation, i.e. a more ionic character for the thorium complex. In addition, the higher delocalization index for the M–N and M–Cl bonds is in accordance with the higher occupation of the $5d$ orbitals for the cerium compared to the $6d$ occupation of the thorium complex and also point to a higher covalency in the case of the cerium complex which is similar to that of the protactinium complex. The difference between Ce^{IV} and the tetravalent actinides Th^{IV} and U^{IV} has already been investigated for isostructural compounds possessing M–Cl,[238] M–C,[14] M–O,[18] and M–N[239] bonds yielding similar computational results. In all cases the covalency of the tetravalent cerium complex is similar or only slightly smaller than for the tetravalent uranium complex due to the participation of $4f$ and $5d$ orbitals in the bonding.

In summary, the results from QTAIM and NBO analysis indicate that especially from thorium to uranium an increase of covalent character of the An–N and An–Cl bonds can be observed which can be attributed to a participation of the $6d$ orbitals. This contribution declines when moving from uranium to plutonium, whereas the $5f$ orbitals now accommodate the ligands. Whether this trend holds for the following actinides or if the participation of the $5f$ orbitals drops again after plutonium as they get more shielded is part of ongoing calculations and will be revealed in future work.[240-242] Despite these findings the An–N and An–Cl bonds in the tris(amidinate) complexes can be characterized as being of mainly ionic bonding character as evidenced by the analysis of the intramolecular bond lengths. However, there is a certain degree of covalent character which changes when traversing the actinide series. The covalent character of the tetravalent cerium complex is significantly higher than for the isostructural thorium complex which underlines the exceptionally high ionicity of the tetravalent thorium compared to the heavier actinides.

The heteroleptic chloro tris(amidinate) complexes **9-11** have been further functionalized by (pseudo)halide exchange reactions yielding unprecedented tetravalent actinide complexes which will be analyzed in the following section.

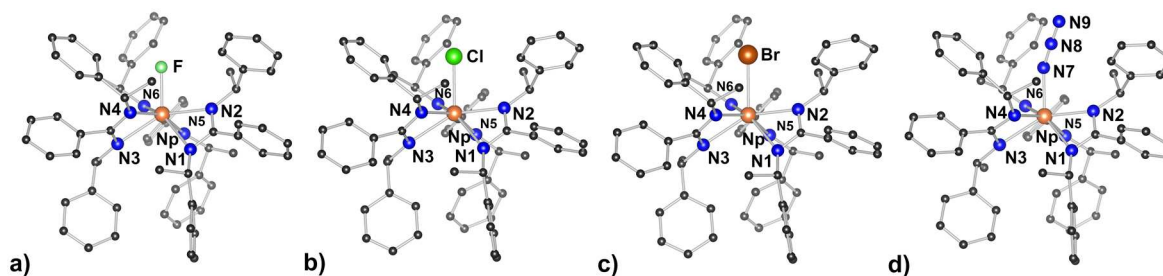*Tris(amidinates) [AnX((S)-PEBA)₃] (An = Th, U, Np; X = F, Cl, Br, N₃)*

Figure 14. Molecular structures of [NpX((*S*)-PEBA)₃] (X = F (**19**, a), Cl (**11**, b), Br (**22**, c), N₃ (**25**, d)). Hydrogen atoms and solvent molecules are omitted for clarity. Color code: neptunium (Np^{IV}, orange red), carbon (C, dark grey), nitrogen (N, blue), fluorine (F, pale green), chlorine (Cl, green), and bromine (Br, brown).

In order to characterize the influence of the (pseudo)halide ligand on the coordination behavior of the amidinate ligands and the observed trends of changing covalent character, three additional series of isostructural actinide complexes [AnX((*S*)-PEBA)₃] have been prepared. The molecular structures of the (pseudo)halide tris(amidinate) complexes [NpX((*S*)-PEBA)₃] (X = Cl (**11**), F (**19**), Br (**22**), N₃ (**25**)) are shown in Figure 14 as representatives for the isostructural thorium and uranium complexes **9**, **10** (X = Cl); **17**, **18** (X = F); **20**, **21** (X = Br) and **23**, **24** (X = N₃). All synthesized (pseudo)halide compounds **9**-**11** and **17**-**25** crystallize in the same chiral space-group type $P2_12_12_1$ with similar cell parameters, indicating their isostructurality (see Appendix).

A comparison of the intramolecular distances revealed (see Table 27 in Appendix), that although the differences between the M–N distances of the (pseudo)halide tris(amidinate) complexes are very small (< 0.05 Å), the fluoro compounds possess the largest M–N bond lengths compared to the chloro-, bromo- and azido complexes. This is not surprising, as the distance to the fluoride is very short and thus, the (*S*)-PEBA ligands have to move away from the metal center. The intramolecular distances between thorium, uranium and the (pseudo)halides are in accordance with literature data for thorium and uranium (pseudo)halides (see Table 32-34 and Table 37-39 in Appendix). The neptunium fluoro (**19**), bromo (**22**), and azido (**25**) complexes are the first members of metal-organic neptunium complexes possessing Np^{IV}–F, Np–Br, and Np^{IV}–N₃ bonds.[214] Thus, the distances could only be compared to inorganic Np halide compounds and are in accordance with those (see Table 42 in Appendix).

In order to elucidate structural trends, the intramolecular distances from the metal center to the coordinating atoms of all chiral tetravalent actinide tris(amidinate) complexes [AnX((*S*)-PEBA)₃] (X = F, Cl, Br, N₃) are plotted against the ionic radius of the relevant actinide (see Figure 15). The M–N$_{short}$ and M–N$_{long}$ distances have been averaged over all complex molecules of the respective actinide (i.e. N1, N3, N5 to N$_{long}$ and N2, N4, N6 to N$_{short}$). The error bars correspond to the standard deviation of these averages.
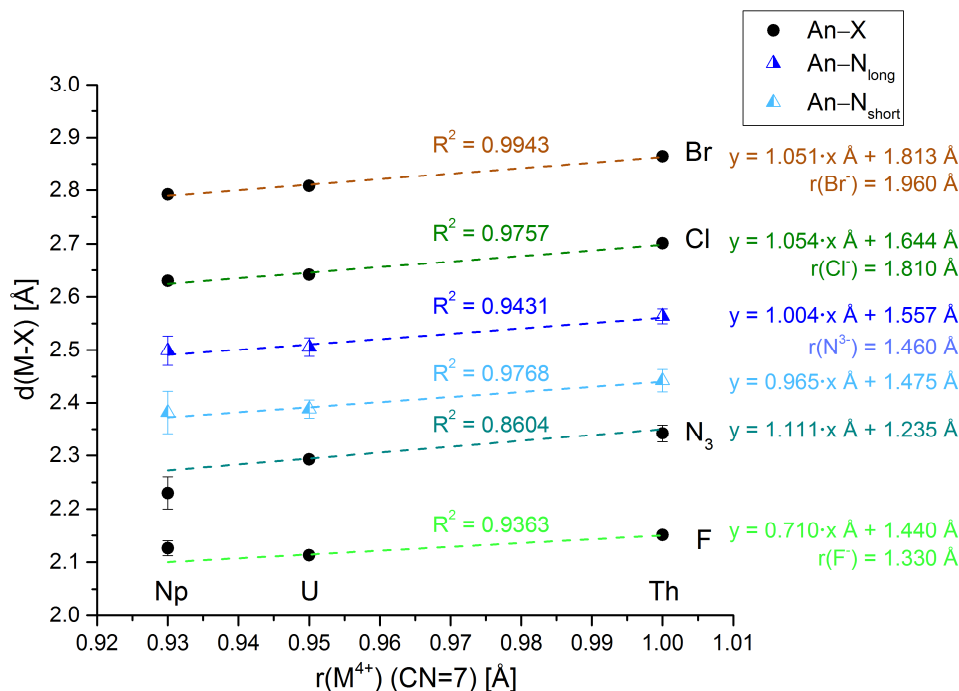
Figure 15. Plot of intramolecular distances An–X (M = Th, U, Np; X = Br, Cl, N, F) in tris(amidinate) [AnX((*S*)-PEBA)$_3$] complexes **9**-**11**, **17**-**27** against ionic radii (CN = 7). Values for N$_{long}$ and N$_{short}$ have been averaged over all tris(amidinate) compounds for a specific actinide. The error bars correspond to the standard deviation σ of the averages. The dashed lines represent the linear fit with determination coefficients (R²) and linear regression models for the An–Br (brown), An–Cl (dark green), An–N$_{long}$ (blue), An–N$_{short}$ (pale blue), An–N$_{azide}$ (petrol green), and An–F (green) bond lengths. The values for the linear fit have been weighted with $1/\sigma^2$. Ionic radii for coordinating atoms (i.e. F$^-$ (CN = 6), Cl$^-$ (CN = 6), Br$^-$ (CN = 6), and N^{3-} (CN = 4)) are given for comparison.[228]

According to these values a linear regression model with a slope close to one can be found for the An–Br, An–Cl as well as An–N$_{short}$ and An–N$_{long}$ distances, thus indicating an ionic bonding interaction as already discussed for the chloro compounds [AnCl((*S*)-PEBA)$_3$] **9**-**11**. Thus, the (pseudo)halide ligand do not largely affect the properties of the tetravalent actinide complexes in the solid state.

However, especially the Np–F and Np–N$_3$ distances do not exactly follow the linear trend which emerges from the uranium and thorium fluoro and azido complexes, respectively. In both neptunium fluoro and azido complexes **19** and **25** crystallographic peculiarities cause the mismatch of the intramolecular bond lengths. The crystals of the neptunium fluoride could only be refined as a non-merohedral twin with a small fraction (~ 10 %) of a fluoride-chloride disorder (see 8.2.3.11 in Appendix). This causes the Np–F distances to be significantly elongated. The very small crystal size of all measured crystals of the neptunium azido complex **25** causes the low resolution and hence the high standard uncertainty. Therefore the values of the linear fits are weighted with $1/\sigma^2$ to account for this uncertainties.

In contrast to the halide ligands, the triatomic azide functionality in complexes **23**-**25** possesses an additional measure to investigate the changes within the actinides series by their infrared activity (see Figure 90 in Appendix for IR spectra). The asymmetric stretching vibration of the

azide $\nu_{as}(N_3)$ is summarized in Table 7 together with the attachment angle (i.e. An–N7–N8 in **23**-**25**) and compared to the only available literature examples of isostructural actinide azido complexes. Generally, a decrease of the An–N–N attachment angle from thorium to uranium can be found in complexes **23**-**25** and in the available literature examples (see also Table 34 and Table 39 in Appendix). However, the differences are small and sparsely above statistical significance. Thus, this counterintuitive result may be obtained by intermolecular packing effects influencing the An–N–N attachment angle.

The measured stretching frequencies of the azido complexes **23**-**25** are similar to other tetravalent actinide azido complexes.[243-245] However, no defined trend can be deduced and potentially correlated to the electronic structure of the actinide when comparing the thorium with the uranium complexes (see Table 7). This is also in accordance with recent theoretical investigations on the limited utilizability of azide stretching frequencies for geometry determinations.[246]

In summary, the influence of the (pseudo)halide ligands on the coordination behavior of the amidinate ligands is negligible despite the strongly coordinating fluoro ligand. This peculiar behavior of the actinide fluoro complexes is also strongly evidenced in solution by the analysis of the paramagnetically shifted NMR signals which will be discussed in detail in the next section 3.1.3. Beforehand, both synthesized series of tetravalent tris(amidinate) complexes possessing the iPr$_2$BA and the (S)-PEBA ligand are compared in the following section.

Table 7. IR stretching frequencies $\nu_{as}(N_3)$ and An–N–N angles (β) of [AnN$_3$((S)-PEBA)$_3$] complexes together with literature values for isostructural thorium and uranium azido complexes.

An	[AnN$_3$((S)-PEBA)$_3$]		[An(N$_3$)(Cp*)$_2$(N(SiMe$_3$)$_2$]^{15}		[An(N$_3$)$_2$(L^{21})$_2$]^{16}	
	$\nu_{as}(N_3)$ [cm^{-1}]	β [°]	$\nu_{as}(N_3)$ [cm^{-1}]	β [°]	$\nu_{as}(N_3)$ [cm^{-1}]	β [°]
Th	2099	160(1)	2081 [243]	166	2065 [244]	146
U	2093	156(1)	2090 [245]	164	2063 [244]	143
Np	2092	153(3)	-	-	-	-

---

[15] Cp*: η^5-C$_5$Me$_5$
[16] L^{21}: ((NC$_9$H$_6$)N=C(H)C$_6$H$_2$^{t}Bu$_2$O-κ^3(O,N,N'))

3.1.2.3 Comparison between chloro tris(amidinates) with i*Pr*$_2$*BA* and *(S)*-PEBA

The molecular structures of the synthesized tetravalent actinide tris(amidinates) are compared for the *i*Pr$_2$BA and the (*S*)-PEBA ligand in order to evaluate the influence of the peripheral substituents next to the nitrogen atoms of the amidinates on the coordination sphere of the actinide. The molecular structures of the respective neptunium tris(amidinates) **5** (*i*Pr$_2$BA) and **11** ((*S*)-PEBA) are shown in Figure 16. The Δ-conformer is shown for **5** to have a better comparison to Δ-**11**.

The coordination around the metal center looks very similar for both amidinate complexes. However, as already evidenced by the different tilting angles for the tris(amidinate) complexes, the detailed coordination differs from each other. This is further investigated by a comparison of the bond lengths between the actinide and the respective coordinating atoms in **3**-**5** (*i*Pr$_2$BA) and **9**-**11** ((*S*)-PEBA) (see Figure 17). Interestingly the bond lengths to the nitrogen atoms on the same side as the chloride (N$_{short}$) are identical for both complex series within the error range. On the contrary, the distance to the chloride is decreased in the chiral (*S*)-PEBA complexes **9**-**11** whereas the distance to the nitrogen atoms opposite to the chloride increases (N$_{long}$) compared to the *i*Pr$_2$BA complexes **3**-**5**. Thus, the bulky (1-phenyl)ethyl substituents in **9**-**11** are moving away from each other. In turn, the distance of the metal to the nitrogen atom opposite to the chlorine increases. This rearrangement opens some additional space on the other side, whereas the chloride could move closer to the actinide. Hence, it can be concluded, that the steric demand of the ligands significantly influences the bond distances not only of the ligand itself, but all coordinating atoms in the complex and that this factor may also be considered when drawing conclusions regarding the bonding analysis of the [MCl((*S*)-PEBA)$_3$] complexes. In both cases, the tris(amidinate) complexes possessing the *i*Pr$_2$BA and the (*S*)-PEBA ligand, the analysis of the trend of the intramolecular coordinative bond lengths with the ionic radii revealed a mainly ionic bonding interaction for the actinide tris(amidinate) complexes.
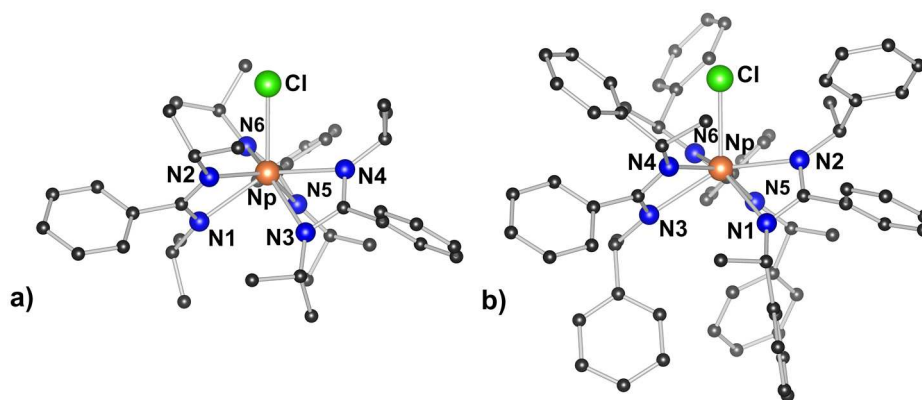

Figure 16. Molecular structures of a) [NpCl(*i*Pr$_2$BA)$_3$] (**5**) and b) [NpCl((*S*)-PEBA)$_3$] (**11**). Hydrogen atoms and solvent molecules are omitted for clarity. Color code: neptunium (Np^{IV}, orange red), carbon (C, dark grey), nitrogen (N, blue), and chlorine (Cl, green).
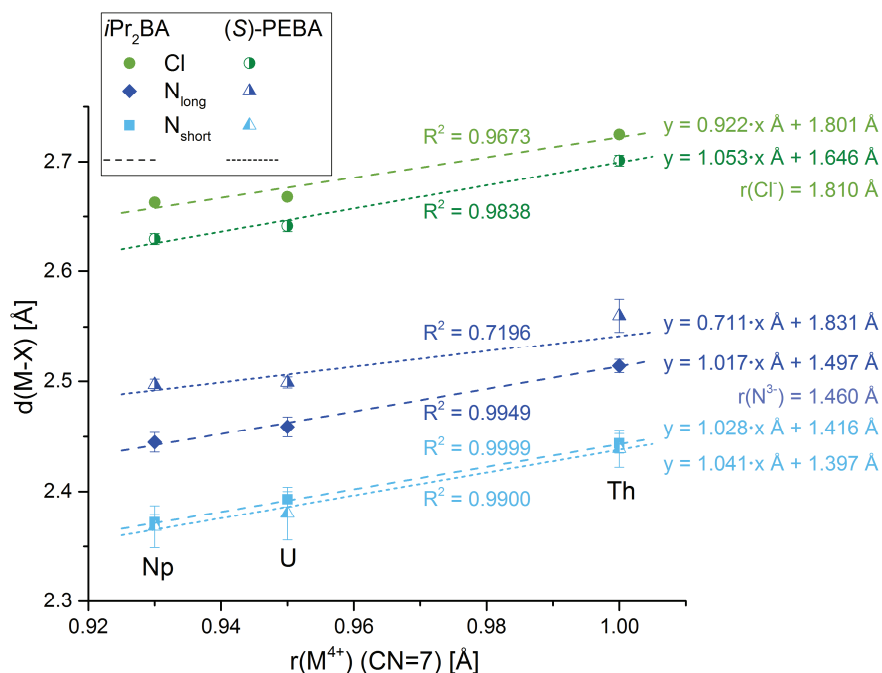
Figure 17. Comparison of coordinative intramolecular bond lengths (An–X; An = Th, U, Np, X = Cl, N) of tetravalent actinide tris(amidinate) complexes [AnClL$_3$] (L = iPr$_2$BA: **3** (An = Th), **4** (An = U), **5** (An = Np); L = (S)-PEBA: **9** (An = Th), **10** (An = U), **11** (An = Np)) against ionic radii. Dashed lines show linear fit with determination coefficient (R^2) and linear regression model. The values for the linear fit have been weighted with $1/\sigma^2$. Ionic radii for coordinating atoms (i.e. Cl$^-$ (CN = 6) and N^{3-} (CN = 4)) are given for comparison.[228]

The essential results of this comprehensive investigation of the tetravalent metal complexes with amidinates in the solid state are shortly summarized in the following to highlight the most important findings.

- Mainly ionic bonding interaction between tetravalent actinides and coordinating N-donor and halide ligands

- Small, but increasing covalent character of coordinative bonds following the order Th^{IV} < Pa^{IV}~Ce^{IV} < U^{IV}~Np^{IV}~Pu^{IV}

- Changing origin of covalency from mainly 6d (U) to 5f (Pu) participation

- Successful synthesis and characterization of the first chiral actinide amidinate complexes including the first transuranic amidinates possessing unprecedented Np–F, Np–Br, and Np–N$_3$ functionalities in metal-organic complexes

- Different complexation behavior of amidinate ligands towards tetravalent zirconium and hafnium

3.1.3 Complex structure in solution

In addition to the solid-state structures, the behavior of the synthesized tetravalent metal amidinates has been investigated in solution by multinuclear NMR spectroscopy. Based on the chemical shifts of ^{1}H and ^{13}C nuclei, the complex geometries in solution are deduced and potential dynamic exchange processes will be discussed. The influence of the tetravalent metal cation on the chemical shifts of the amidinate ligands is highlighted. Thereby, special attention has been paid to the paramagnetic shifts which are introduced by paramagnetic U^{IV} and Np^{IV} metal centers. The angular and distance dependency of this additional contribution to the chemical shift enables a detailed analysis of the complex structure in solution (see Fundamentals Section 2.3). Similar to the aforementioned solid-state investigations, first, the spectra of the bis(amidinate) complexes are discussed briefly and, secondly, the tris(amidinate) complexes with iPr$_2$BA and (S)-PEBA are investigated in detail.

3.1.3.1 Bis(amidinate) complexes

Both transition metal bis(amidinate) complex series with the iPr$_2$BA (Ti (**12**); Hf (**1**)) and the (S)-PEBA (Ti (**13**), Zr (**6**), Hf (**7**)) ligand show similar chemical shifts in ^{1}H and ^{13}C NMR (see Table 13 in Appendix), as would be expected for these diamagnetic metal complexes possessing similar binding patterns. The ^{1}H NMR spectra of the transition metal bis(amidinate) complexes [MCl$_2$((S)-PEBA)$_2$] (M = Ti (**13**), Zr (**6**), Hf (**7**)) are shown in Figure 18.

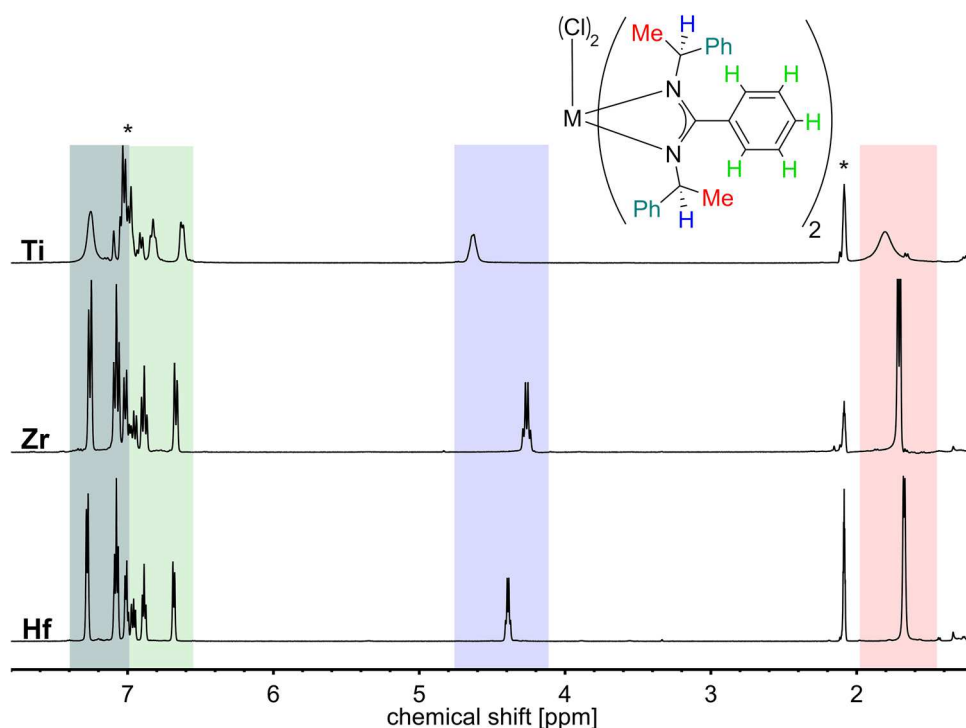**Figure 18.** ^{1}H-NMR spectra of [TiCl$_2$((S)-PEBA)$_2$] (**13**, top), [ZrCl$_2$((S)-PEBA)$_2$] (**6**, middle) and [HfCl$_2$((S)-PEBA)$_2$] (**7**, bottom) at 298 K in toluene-d$_8$. Signals are marked with colors: blue (NCH), red (Me), green (Ph^{NCN}) and petrol green (Ph). Asterisks indicate solvent signals (i.e. toluene).

The signal pattern is similar to the [MCl$_2$(iPr$_2$BA)$_2$] (M = Ti (**12**); Hf (**1**)) complexes (see Figure 36 in Appendix) and in accordance with a D_2 symmetry of the complex molecules in solution, implying a fast dynamic exchange of the ligands (i.e. chloride and/or iPr$_2$BA) on the NMR time scale.

The significant line broadening of the titanium complex potentially results from an increasing steric hindrance between the bulky (*S*)-PEBA ligands and hence a hindered rotation of the ligands due to the small metal cation. The largest influence of the diamagnetic metals on the chemical shift can be observed for the NC*H* protons (marked in blue in Figure 18). Several effects may influence the chemical shift of these protons located close to the metal center. For the 3*d* metal titanium the lack of primogenic repulsion[247] may result in a higher charge density than for the larger zirconium and hafnium cations. Hafnium on the other hand may be already affected by spin orbit coupling effects which could also have an impact on the chemical shift of the coordinated ligand molecules. This may be the reason that no defined trend of the chemical shifts can be deduced when traversing the group IV metals (see also Table 21 in Appendix for ^{13}C signals).

The ^{1}H NMR spectra of the bis(amidinate) [UCl$_2$((*S*)-PEBA)$_2$] (**8**) complex shows paramagnetically shifted signals compared to the analogous diamagnetic hafnium complex **7** (see Figure 19). A detailed analysis of this paramagnetic influence was hampered by the already mentioned impurity of the tris(amidinate) complex [UCl((*S*)-PEBA)$_3$] (**10**) which causes multiple signal overlaps, especially at lower and higher temperatures (see Figure 57 in Appendix for temperature dependent ^{1}H NMR spectra).
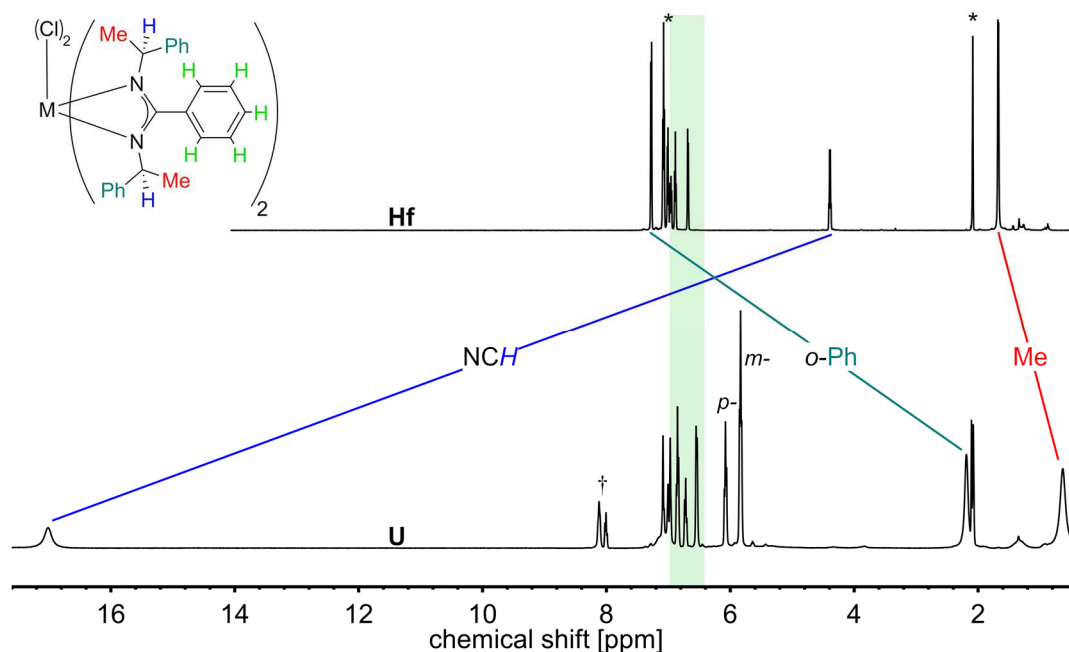

Figure 19. ^{1}H-NMR spectra of [HfCl$_2$((*S*)-PEBA)$_2$] (**7**, top) and [UCl$_2$((*S*)-PEBA)$_2$] (**8**, bottom) at 298 K in toluene-d$_8$. Paramagnetic shifts for the tetravalent uranium complex **8** are indicated for NC*H* (blue), methyl (red), and phenyl protons (petrol green). Signals of central phenyl group (green) do not shift drastically. Asterisks indicate solvent signals (i.e. toluene) and dagger impurity of [UCl((*S*)-PEBA)$_3$] (**10**).

Due to a dynamic exchange behavior of the tris(amidinate) complex **10** in solution, only the signals of the bis(amidinate) uranium complex **8** are visible at room temperature and could be unambiguously assigned. This dynamic exchange process will be discussed in detail in the next section in order to elucidate the complex structure of the tris(amidinate) complexes in solution more comprehensively.

3.1.3.2   Tris(amidinate) complexes

The solution structure of two different tris(amidinate) complex series possessing the iPr$_2$BA ([MCl(iPr$_2$BA)$_3$], M = Zr, Th, U, Np) and the (S)-PEBA ([MCl((S)-PEBA)$_3$], M = Ce, Th, U, Np)) ligand are investigated using NMR spectroscopy. Again, the deduction of the influence of the metal cation on the chemical shifts is the major objective of this section. Therefore, the diamagnetic complexes are firstly discussed together with a more detailed analysis of the dynamic behavior of the tris(amidinate) complexes in solution. The analysis of the dependence of the dynamic exchange rate on the metal cation and the (pseudo)halide substituent enables an estimation of the potential dynamic exchange processes happening in solution. Thereafter, the paramagnetic influence for the uranium and neptunium cations on the chemical shifts of the ligands will be discussed and investigated resulting in a comprehensive overview of the complex structure in solution.

Diamagnetic complexes

The chemical shifts of the protons in the diamagnetic tris(amidinate) complexes [ZrCl(iPr$_2$BA)$_3$] (**2**) and [ThCl(iPr$_2$BA)$_3$] (**3**) are similar to the already reported bis(amidinate) complexes **1** and **12** indicating a similar coordination motif. However, a comparison between the ^{1}H NMR spectra of the bis- and tris(amidinate) complexes (see Figure 36 in Appendix) revealed that there are subtle differences again depending on the complex stoichiometry. For the bis(amidinate) complexes only one signal for all phenyl protons is observed, whereas in the tris(amidinate) complexes three separate signals for *ortho*-, *meta*-, and *para*-positions are visible. This coincides with a more rigid coordination environment around the metal center in the tris(amidinate) complexes compared to the more flexible bis(amidinates).

The ^{1}H NMR spectra of the diamagnetic chiral tris(amidinate) compounds [ThCl((S)-PEBA)$_3$] (**9**) and [CeCl((S)-PEBA)$_3$] (**16**) are shown in Figure 20. Similar to the comparison of the transition metal bis(amidinate) complexes (see Figure 18) the nuclei located next to the metal center (i.e. NC*H*) experience the largest influence of the metal cation on the chemical shifts. This is also valid for the ^{13}C NMR signals of NC*N* and NC*H* showing a difference of 4 ppm resp. 3 ppm between both complexes (see Table 25 in Appendix).
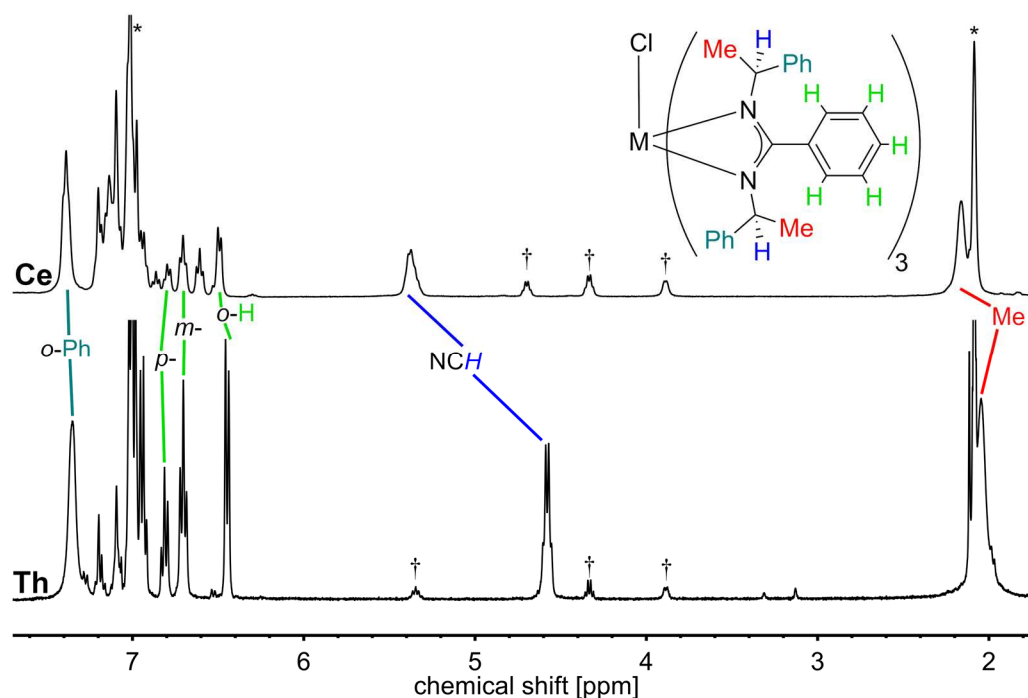
Figure 20. ^{1}H NMR spectra of [CeCl((*S*)-PEBA)$_3$] (**16**, top) and [ThCl((*S*)-PEBA)$_3$] (**9**, bottom) at 298 K in toluene-d$_8$. Signals are marked with colors according to the schematic drawing of the complex molecules. Signals of *m*- and *p*-Ph are not indicated for clarity. Asterisks indicate solvent signals (i.e. toluene) and dagger impurities of (*S*)-HPEBA and (*S*)-LiPEBA.

Similar to the difference between the transition metals zirconium and hafnium to titanium, the lack of primogenic repulsion[247] for the 4*f* orbitals of Ce^{IV} may be the reason for the different chemical shifts compared to the 5*f* element thorium. The increased charge density at the cerium is withdrawing more electrons from the ligand which results in a deshielding and hence a downfield shift especially of the NC*H* signals. This behavior is also evidenced by the calculated charge of the metal cation by QTAIM analysis as shown in the previous section (q(Ce) = +2.44; q(Th) = +2.76; see Table 5).

The ^{1}H and ^{13}C chemical shifts of the substituted [ThX((*S*)-PEBA)$_3$] (X = F , Br, N$_3$) are nearly identical to the chemical shifts of the chloro complex **9** (see Table 35 in Appendix). Thus, the (pseudo)halide ligands only have a minor effect on the electron density of the amidinate ligands. In contrast, they do have a major influence on the dynamic behavior of the complex molecules in solution which will be discussed in the following.

Dynamic behavior

The temperature dependent ^{1}H NMR spectra of all synthesized tris(amidinate) complexes reveal an dynamic exchange process which manifests by a signal splitting of various signals when decreasing the temperature. Below a certain temperature, the coalescence temperature, two separate signals are observed for nuclei which cannot be transferred into each other by a dynamic exchange process anymore as this process is now too slow on the NMR timescale. Thus, the purpose of this section is to deduce potential dynamic exchange mechanisms in

solution and to correlate the observed coalescence temperatures with structural properties of the complexes like the size of the metal cation and the (pseudo)halide ligand. The fundamental understanding of the processes happening in solution helps to gain a comprehensive overview of the complex structure. This understanding is crucial for the detailed analysis of the paramagnetic influence of the tetravalent actinides presented in the next section.

The spectra of all diamagnetic tris(amidinate) complexes **2**, **3**, **9**, **17**, **20** and **23** are consistent with a D_3 symmetry of the complex molecules in solution at high temperatures and with a C_3 symmetry at low temperatures. This behavior is exemplified for [ThCl((*S*)-PEBA)$_3$] (**9**) in Figure 21. The temperature dependent ^{1}H NMR spectrum of complex **9** revealed two different coalescence temperatures, the first at 263 K for the NC*H* and *meta*-Ph^{NCN} protons which is assigned in Figure 21 and the second at 283 K for the methyl and *ortho*-phenyl protons. This implies, that two different dynamic exchange mechanisms should be involved.

The first coalescence temperature can be assigned to the rotation of the central phenyl moiety which is hindered in the complex molecules due to the peripheral substituent attached to the nitrogen atoms. This should result in a signal splitting of *ortho*- and *meta*-protons as it is also observed by WEDLER *et al.* for the phenyl group in benzamidinates of [UCl((NSiMe$_3$)$_2$CPh)$_3$] type.[152]
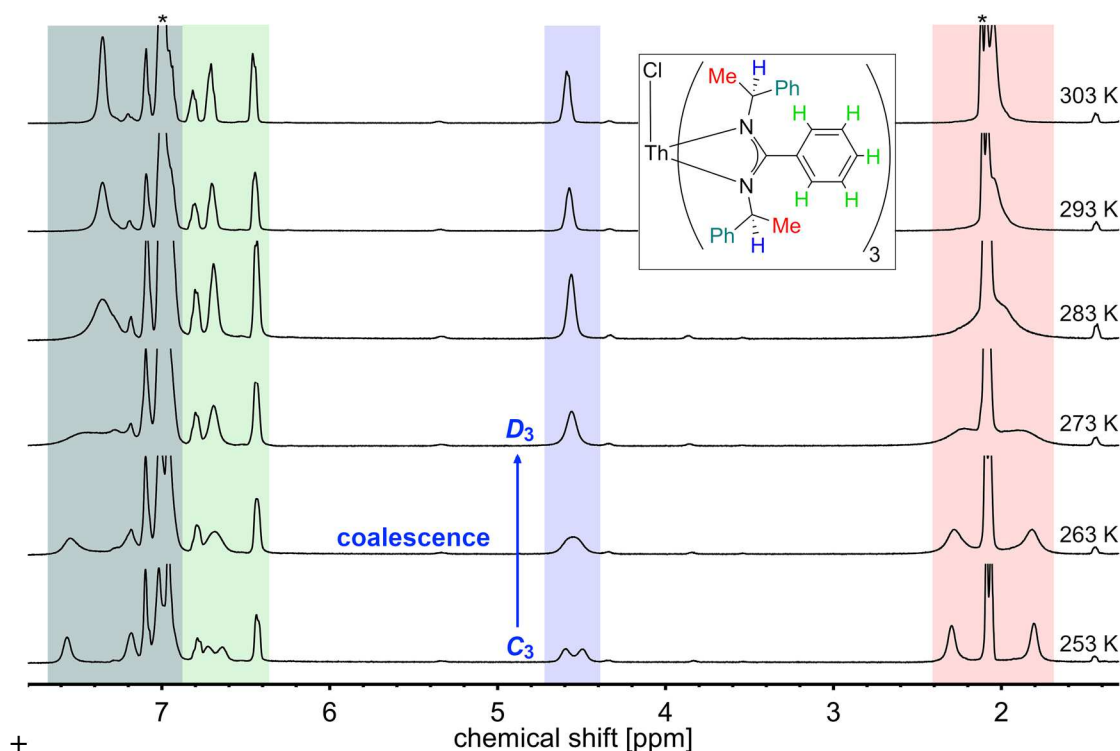

Figure 21. Variable temperature ^{1}H-NMR spectrum of [ThCl((*S*)-PEBA)$_3$] (**9**) in a temperature range from 253 K to 303 K. Signals are marked with colors: blue (NC*H*), red (Me), green (Ph^{NCN}) and petrol green (Ph). Transition between C_3 and D_3 symmetry is exemplified by the NC*H* signal (blue). Asterisks indicate solvent signals (i.e. toluene).

Interestingly, the *ortho*-protons of the central phenyl ring do not split into two signals in **9** at low temperatures as it would be anticipated by a hindered rotation of the central phenyl ring. However, two separate ^{13}C signals for the carbons in *ortho* position are observed (see Figure 67 in Appendix), which underlines the rotation of the central phenyl group as the first dynamic exchange process happening in solution. The similar coalescence temperature of the NC*H* and *meta*-Ph^{NCN} protons may be assigned to ring current effects of the central phenyl ring which are not averaged anymore due to the hindered rotation.

The second dynamic exchange process, i.e. the coalescence of the ^{1}H signals of groups attached to the amidinate nitrogen atoms, is investigated in more detail, as it is at first glance not obvious how this isomerization occurs. Therefore four potential isomerization mechanism are depicted in Figure 22 and discussed in the following.

Mechanism A involves the isomerization between the Δ- and Λ-diastereomers of the tris(amidinate) complexes via a trigonal prismatic transition state. This mechanism has been proposed by COOK *et al*. for zirconium and hafnium tris(amidinate) complexes of [MCl((N*i*Pr)$_2$CMe)$_3$] type only very recently.[233] They also observed similar coalescence temperatures for the ^{1}H signals of the isopropyl groups (i.e. 283 K) as for the methyl groups in complex **9**. However, a simple isomerization between the Δ- and Λ-diastereomers of the tris(amidinate) complexes is not sufficient to explain the observed dynamic exchange process, as it lacks a complex structure possessing a D_3 symmetry as observed in the ^{1}H NMR. The anisotropy is preserved due to the axial chlorine which is also present in the trigonal prismatic transition state. Thus, this mechanism cannot explain the observation from ^{1}H NMR spectroscopy.

Instead, three different isomerization mechanisms (B-D) are proposed in this work to explain the dynamic behavior of the tris(amidinate) complexes in solution. All mechanism are possessing a D_3 symmetric transition state by time average. Furthermore, they enable a change of the position of the nitrogen donors with respect to the halide ligands as indicated with colored atoms in Figure 22.

The dissociative mechanism (B) includes a heterolytic M–Cl bond cleavage yielding a proposed contact ion pair [M(L)$_3$]$^+$Cl$^-$ which in turn would show a D_3 symmetry around the metal center. The chloride may be stabilized outside the complex. Thus, it was attempted to isolate the potential cationic intermediate. To this end a sodium salt with a non-coordinating anion (i.e. NaBPh$_4$) has been added to a thf solution of [UCl((*S*)-PEBA)$_3$] (**10**). If the chloride is stabilized in solution it should be precipitated as NaCl and a cationic complex [U((*S*)-PEBA)$_3$][BPh$_4$] may be yielded. However, no reaction has been observed, i.e. no NaCl precipitated and also no change in the ^{1}H NMR has been observed (see Figure 73 in Appendix). So there is no evidence for this dissociative mechanism.
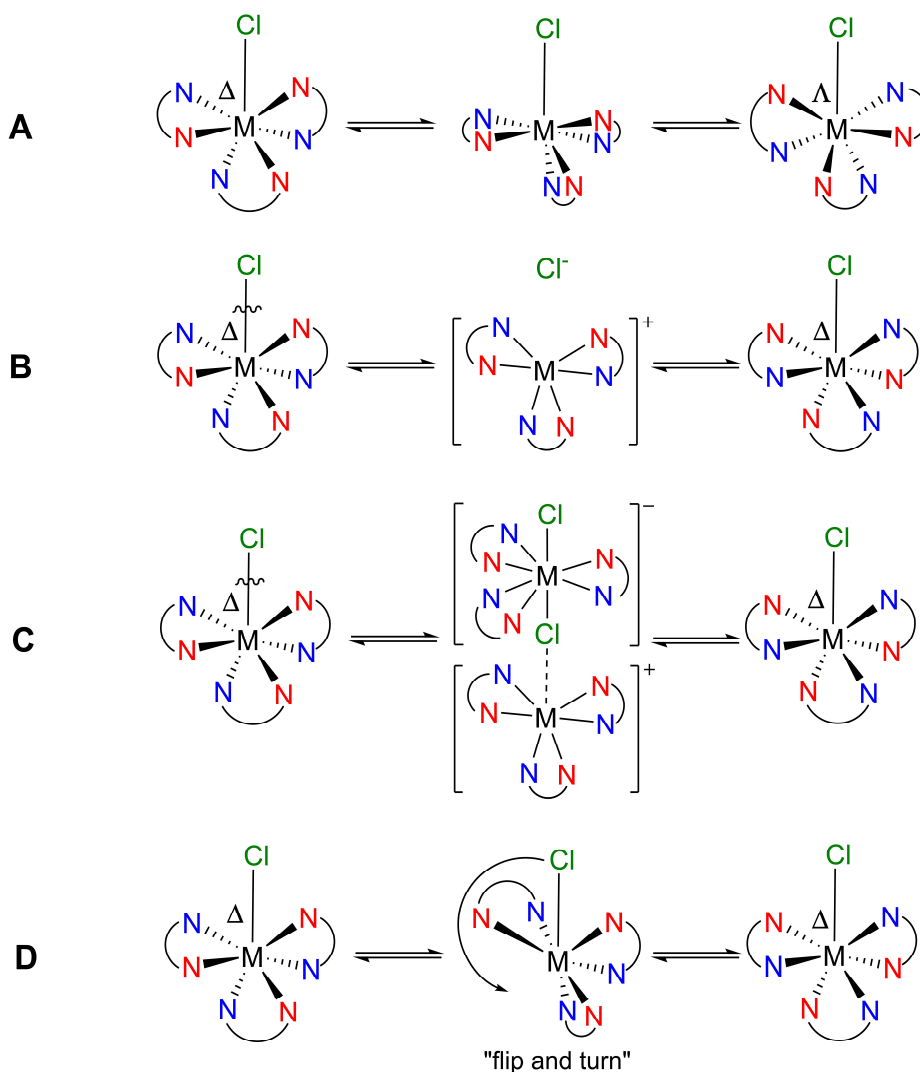
Figure 22. Proposed mechanisms of isomerization between tris(amidinate) complexes. A – isomerization *via* trigonal prismatic transition state;[233] B – dissociative mechanism; C – dissociative mechanism *via* contact-ion pair; D – non-dissociative mechanism. Stereodescriptors indicate chirality-at-metal.

Ruling out mechanisms A and B leaves two alternative options for the dynamic exchange process, a dissociative mechanism involving the formation of a contact-ion pair (C) and a non-dissociative mechanism (D) with a "flip and turn" process. To elucidate the most probable exchange mechanism, the dependency of the coalescence temperatures and hence the isomerization enthalpies on the size of the metal cation and the (pseudo)halide substituent will be evaluated.

In general, the coalescence temperatures are increasing for all signals as the radius of the metal cation is decreasing (see Table 17 and Table 29 in Appendix). This is not surprising as a smaller metal cation increases the sterical crowdedness in the coordination sphere and hence higher energies are needed to overcome the rotational barriers of the ligands. However, this behavior would be expected for both mechanisms C and D and thus, does not enable a discrimination between both.

Therefore, the influence of the (pseudo)halide ligand on the dynamic behavior of the tris(amidinate) complexes in solution is investigated in the diamagnetic (pseudo)halide complexes [ThX((S)-PEBA)$_3$] (X = F (**17**), Cl (**9**), Br (**20**), N$_3$ (**23**)). All of these complexes show the already observed symmetry change from a C_3 symmetry at low temperatures to a D_3 symmetry at high temperatures. Based on the coalescence temperature (T_c, see Table 29 in Appendix) and the distance of the separated signals ($\Delta\delta$) at low temperatures the rate constant of isomerization k_c and the GIBBS free enthalpy of the isomerization $\Delta G_c^{\ddagger}$ has been calculated using the EYRING equation (see Eq. 9 in Fundamentals Section 2.3.2.2). For the chlorido, bromo, and azido complexes almost identical values are obtained for all observed isomerization processes (see Table 8 and Table 30 in Appendix). However, in the fluoro complex **17** significantly larger $\Delta G_c^{\ddagger}$ values are observed which can be explained with the aforementioned dissociative mechanism C. The fluoride is bound much stronger to the actinide than the other halides which causes a higher dissociation energy and hence a higher energy for the isomerization. On the other hand the fluoride is much smaller than the chloride or bromide and should hence show a smaller free GIBBS energy of isomerization expecting the non-dissociative mechanism D with the (pseudo)halide flipping around the metal complex.

In addition, the calculated values of k$_c$ and $\Delta G_c^{\ddagger}$ for the azide compound **23** are smaller than in the fluoro compound **17**, which is also unexpected for a flipping mechanism, as the triatomic azide would be expected to have a higher energy barrier especially compared to the fluoride.

In summary, the tris(amidinate) complexes are prone to two different dynamic exchange processes which can be observed by a symmetry decrease from D_3 at high temperatures to C_3 at low temperatures. The first process can be assigned to the rotation of the central phenyl group which is hindered at low temperatures causing a signal splitting of all nuclei in *ortho-* and *meta-*position. The second process is most likely a dissociative mechanism *via* the formation of a contact-ion pair which enables an exchange of the substituents facing towards and opposite to the (pseudo)halide substituents (see Figure 22-C). This knowledge about the behavior of the tetravalent actinide amidinate complex in solution is crucial for the detailed analysis of the paramagnetic influence of the actinide cations on the chemical shifts of the coordinated ligands which will be presented in the following.

Table 8. Calculated GIBBS free enthalpy of isomerization $\Delta G_c^{\ddagger}$ for dynamic processes of selected protons in diamagnetic tris(amidinate) compounds [ThX((S)-PEBA)$_3$] (X = F (**17**), Cl (**9**), Br (**20**), N$_3$ (**23**)). Error in brackets is calculated by error propagation using $\Delta T = \pm 10K$ and $\Delta\Delta\delta_{1H} = \pm 0.01$ ppm.

$\Delta G_c^{\ddagger}$ [kJ/mol]	F (**17**)	Cl (**9**)	Br (**20**)	N$_3$ (**23**)
Me	58.1(6)	54.8(6)	52.6(6)	54.0(6)
NC*H*	59.2(7)	54.3(8)	54.7(12)	53.6(7)
m-H^{NCN}	61.3(9)	54.6(8)	53.6(10)	54.6(8)
o-H	58.5(6)	55.4(6)	53.3(6)	53.8(7)

Paramagnetic influence

Based on the investigations of the dynamic properties of the tris(amidinate) complex in solution, this section is dedicated to perform a more precise structure determination of these complexes using the paramagnetic shifts induced by the U^{IV} and Np^{IV} cations. Furthermore, the fundamental properties of the paramagnetic influence of tetravalent actinides on ^{1}H and ^{13}C chemical shifts of bound ligands are studied. Again a special focus is given to the influence of the (pseudo)halide ligand on the chemical shifts of the amidinate ligands. Due to the strong dependence of the solution structure on the temperature the following investigations have been performed at low temperature (i.e. 243 K) where a C_3 symmetry of the complex molecules is observed in solution and may be correlated to the solid-state structure.

The observed chemical shift (δ_{tot}) of the nuclei in the complexes including a paramagnetic cation (i.e. U or Np) can be expressed as the sum of a diamagnetic (δ_{dia}) and a paramagnetic contribution, called the hyperfine shift δ_{HF} (see Fundamentals Section 2.3.2.3). In order to calculate the pure hyperfine shift, the diamagnetic contribution has to be subtracted from the observed chemical shift for paramagnetic complexes in solution. The diamagnetic contribution can be described best by an isostructural complex molecule possessing a diamagnetic cation. This is readily available in the tetravalent actinide series by the synthesized thorium complexes as evidenced by SC-XRD analysis (see Section 3.1.2.2). In the following, the extracted hyperfine shifts of the different tris(amidinate) complexes are used to determine the spatial orientation of the paramagnetically shifted nuclei.

The paramagnetic hyperfine shift of the chloro tris(amidinate) complexes [AnCl((*S*)-PEBA)$_3$] (An = U (**10**), Np (**11**)) has been extracted for all protons at low temperature using the chemical shifts of the thorium complex **9** as diamagnetic reference (see Figure 23). Several two-dimensional NMR spectra have been used in order to assign the signals to the protons in the assumed C_3 symmetric molecular structure (see Section 8.2.2.3 in Appendix). Thus, the procedure of the signal assignment will be discussed stepwise in the following.

The calculated hyperfine shift consists of two major contributions, the FERMI contact and the pseudocontact contribution. Based on several structural investigations from lanthanide systems it is expected that the FERMI contact term can be neglected for nuclei in a distance more than four bonds away from the metal center.[195] Corresponding data for the actinides are not available. Consequently, such a contribution is expected for NC*H* protons (i.e. H1, H16) and the methyl groups (i.e. H2, H17). For H1 and H16 the FERMI contact contribution is clearly visible by the increased hyperfine shift of more than 15 and up to ~45 ppm (see Figure 23). This is a direct confirmation of the covalent character of the An–N bonds in the tetravalent actinide complexes **10** and **11**, as the FERMI contact contribution is propagated via chemical bonds. The methyl groups, on the other hand, show a rather small hyperfine shift which may indicate an interplay of both FERMI and pseudocontact contribution.
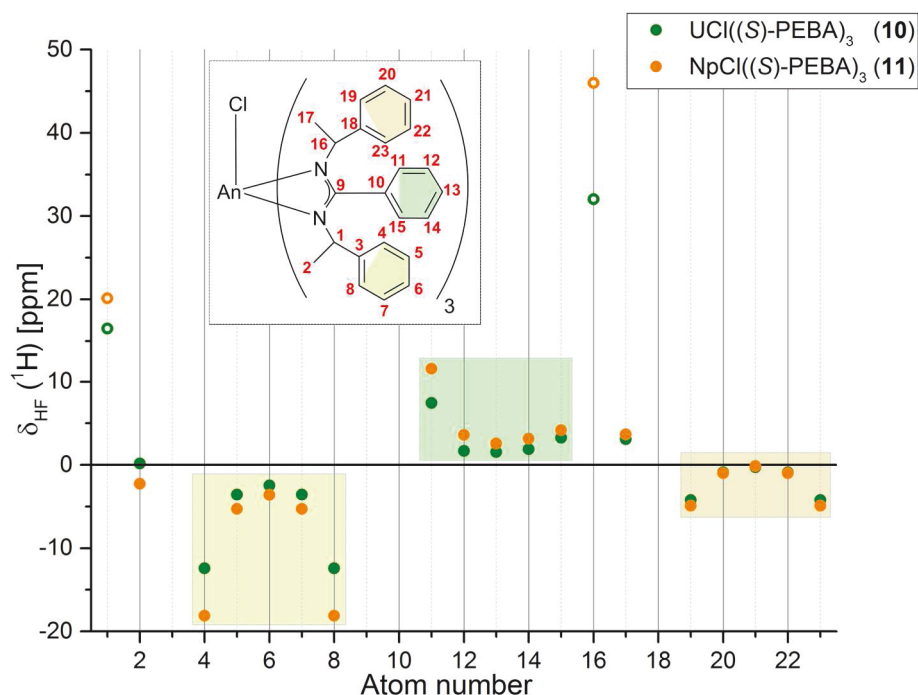
Figure 23. Plot of the ^{1}H hyperfine shift for [AnCl((S)-PEBA)$_3$] (An = U (**10**), Np (**11**)) in toluene-d$_8$ at 243 K. Open symbols indicate significant FERMI contact contribution.

Generally, the amount of the observed hyperfine shift is higher for the tetravalent neptunium complex **11** (5f^3) than for the tetravalent uranium complex **10** (5f^2) indicating an increase with the number of f electrons. By assuming a negligible FERMI contact contribution for protons with a larger distance from the metal center, it can further be proposed that the crucial value of the pseudocontact contribution, the anisotropy of the magnetic susceptibility tensor $\Delta\chi_{ax}$, is higher for neptunium(IV) than uranium(IV). This is in contrast to the trivalent lanthanides, showing smaller values for the trivalent neodymium (4f^3, $\Delta\chi_{ax}=1.7\times10^{-32}$ m^3) than the trivalent praseodymium (4f^2, $\Delta\chi_{ax}=3.4\times10^{-32}$ m^3).[204]

In order to compare the expected pseudocontact shift with the observed hyperfine shift, the spatial orientation of all protons in the [UCl((S)-PEBA)$_3$] complex **10** has been determined for the single-crystal structure and for the quantum-chemically geometry optimized structure (see Figure 24).

This representation assumes the observed C_3 symmetry of the complex molecules at low temperature meaning that only one signal is visible for any distinct proton (H1-H23) although each of them exist three times per complex molecule. The distance from the metal center to the respective protons r as well as the Cl–U–^{1}H angle θ have been determined from both available structures. These spherical coordinates have than been converted into Cartesian coordinates having the metal located at the origin and the U–Cl bond on the z-axis. Based on the knowledge about the involved dynamic processes in solution, it is assumed that the central phenyl moiety (i.e. o, m, p-Ph^{NCN}) is hindered in its rotation and hence each proton is plotted separately in Figure 24.
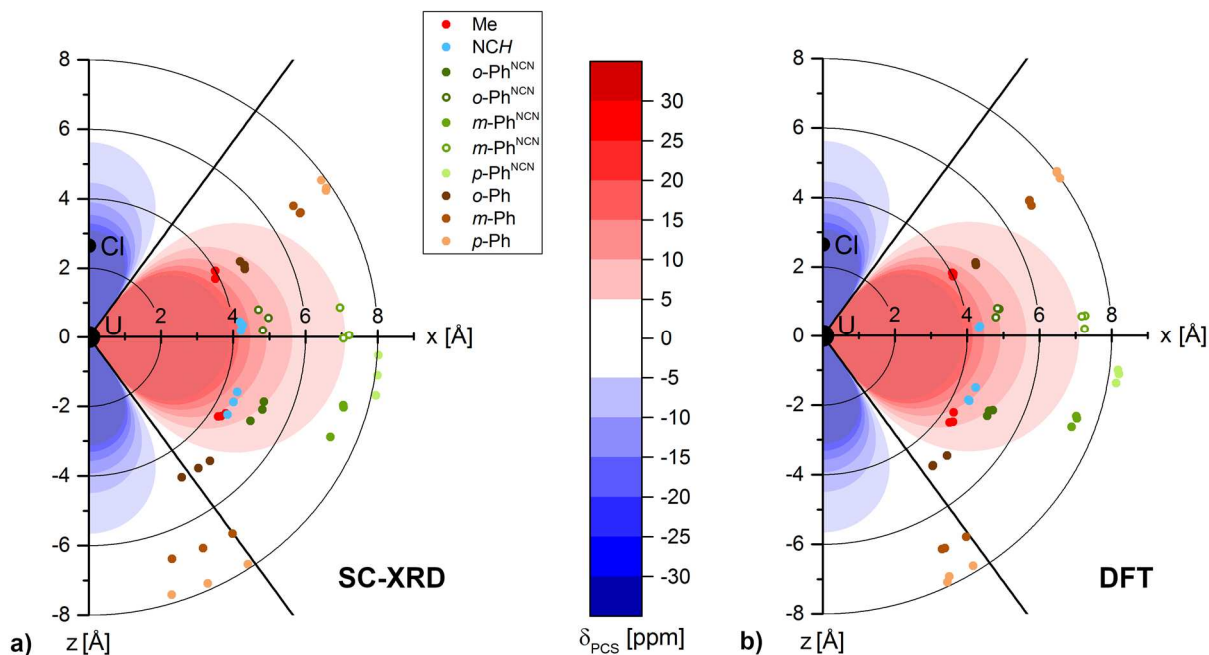
Figure 24. Two-dimensional representation of spatial arrangement of protons in [UCl((*S*)-PEBA)$_3$] (**10**) based on SC-XRD data (a) and on geometry optimization by DFT (b). Proton positions at rotating groups (i.e. methyl and peripheral phenyl groups) have been averaged. The z axis is aligned with the chiral U–Cl axis in the complex molecules. Bold black lines at ± 54.74° indicate a change of the pseudocontact contribution from positive (red) to negative (blue). Thin black lines indicate regions of identical distance to the metal center. The pseudocontact contribution has been calculated based on the KURLAND-MCGARVEY equation (Eq. 15 in Section 2.3.2.3) and a value for the magnetic anisotropy of the susceptibility tensor of $\Delta\chi_{ax} = 3.4 \cdot 10^{-32}$ m^3.

For the peripheral phenyl rings (i.e. *o*-, *m*-, *p*-Ph) in total six signals are observed which points to a free rotation of the phenyl rings but a different spatial orientation of both rings. Thus, the distances and angles have been averaged for *ortho*- and *meta*-protons located at one phenyl ring. Similarly, the distances and angles towards the methyl protons have been averaged for each methyl group separately, resulting in six individual points (red). Finally, the expected pseudocontact shift which originates from the paramagnetic tetravalent metal center has been calculated using the KURLAND-MCGARVEY equation (Eq. 15 in Section 2.3.2.3). As a value for the anisotropy of the magnetic susceptibility tensor $\Delta\chi_{ax}$ is not determined yet for tetravalent uranium cations, the value of $\Delta\chi_{ax} = 3.4 \cdot 10^{-32}$ m^3 for the isoelectronic Pr^{III} (4f^2) cation has been used to calculate the spherical lobes of emerging pseudocontact shifts.[204]

From the spatial orientation of the protons it becomes obvious that neither the SC-XRD nor the geometry optimized structure possesses an inherent C_3 symmetry. A comparison of both structures can be found in Figure 121 in the Appendix. However, it may be expected that the optimized structure represents the solution structure more closely as it is not influenced by solid-state packing effects. From the comparison of the extracted hyperfine shifts (Figure 23) with the spatial orientation and the estimated pseudocontact shifts (Figure 24), it can be concluded that the solution structure fits fairly well with the geometry optimized structure. The central phenyl ring (i.e. H11-H15) shows a positive hyperfine shift which is in accordance with the

spatial orientation in the positive PCS lobe. Also the peripheral phenyl ring located opposite to the chlorine (i.e. H4-H6) is at least partly located in the negative region of the pseudocontact shift as estimated by the derived hyperfine shift. The second peripheral phenyl ring located in proximity to the chlorine (i.e. H19-H23) show negative hyperfine shifts but is located in the positive lobe of the pseudocontact shift. Thus, neither structure fully represents the actual solution structure of the complex.

However, the difference of the hyperfine shifts for the peripheral phenyl rings is reflected by their spatial orientation with respect to the uranium–chlorine axis which accounts for the usability of the pseudocontact contribution to determine structural parameters from paramagnetic complexes in solution.

It has to be pointed out again, that these structural investigations are based on the assumption that the FERMI contact contribution can be neglected for all protons but the NC*H* protons, an assumption based solely on NMR data of lanthanide complexes. This is clearly not the case for ^{13}C NMR (see Figure 25). For example, the ^{13}C nuclei of the central phenyl ring (i.e. C11-C15) show an alternating behavior of the hyperfine shift which may point to a significant FERMI contact contribution. It is unclear how this affects the ^{1}H hyperfine shifts, but it seems unlikely that the FERMI contact contribution is as negligible as assumed.

However, the ^{13}C hyperfine shift for the carbon atoms of the peripheral phenyl rings (i.e. C4-C8 and C19-C23) is in accordance with the behavior of the adjacent protons (see Figure 23). The hyperfine shift of the carbon atoms positioned opposite the chlorine (C4-C8) is higher than for the carbon atoms of the phenyl ring facing towards the chlorine (C19-C23).
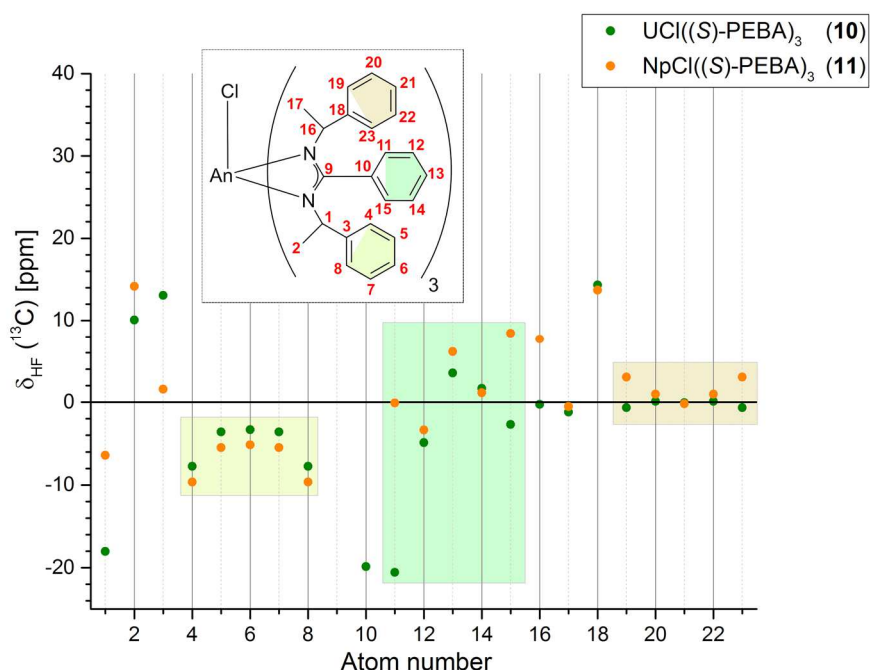

Figure 25. Plot of the ^{13}C hyperfine shift for [AnCl((*S*)-PEBA)$_3$] (An = U (**10**), Np(**11**)) in toluene-d$_8$ at 243 K.

For the neptunium complex **11** even a change of the sign of the hyperfine shift for both peripheral phenyl rings is observed as it would be expected based on the spatial arrangement of the protons presented in Figure 24.

In summary, the evaluation of the hyperfine shifts revealed differences between ^{1}H and ^{13}C nuclei which have to be investigated in more detail. Therefore it is crucial to develop suitable methods to separate FERMI and pseudocontact contributions for actinide compounds to really estimate their influences on certain nuclei.

In the next step, the hyperfine shifts of all synthesized (pseudo)halide tris(amidinate) complexes [AnX((*S*)-PEBA)$_3$] **10**, **11** (X = Cl); **18**, **19** (X = F); **21**, **22** (X = Br); **24**, **25** (X = N$_3$) have been extracted at 243 K based on the diamagnetic thorium reference compounds **9**, **17**, **20**, **23** (see Figure 26). In general, the (pseudo)halide compounds behave similar to the already discussed chloro tris(amidinate) complexes **10** and **11** (see Figure 23 and descriptions thereafter). The influence of the (pseudo)halide on the ^{1}H hyperfine shift of the amidinate ligands is small with the notable exception of the [UF((*S*)-PEBA)$_3$] complex **18**. For this fluorine compound the ^{1}H hyperfine shifts show an opposite sign for protons which are mainly affected by pseudocontact contribution compared to the chloro-, bromo-, and azido complexes, respectively.

No such behavior is observed for the corresponding neptunium fluoro complex **19**. Assuming their solution structures are similar, as DFT optimizations suggest and the solid-state structures are as well, this is a clear indication that the fluoro ligand in the uranium(IV) complex **18** has a different effect on the electronic properties of U^{IV} than Np^{IV}, which influences the spatial electron distribution, i.e. the origin of the pseudocontact shift. A similar behavior can be found in the ^{13}C signals for the respective (pseudo)halide compounds (see Figure 76 in Appendix).

In order to gain more insight into the observed difference between the paramagnetic hyperfine shift of the fluoro tris(amidinate) complexes of uranium (**18**) and neptunium (**19**), the magnetic susceptibility tensor χ has been calculated. A spin-orbit coupled complete active space calculation (SOCAS) has been performed by using the geometry optimized structures obtained by DFT calculation (see Section 5.1.6 for more details). The results of the uranium and neptunium fluoro complexes **18** and **19** are depicted in Figure 27 in comparison to the calculated spatial orientations of the pseudocontact contributions for the corresponding chloro complexes **10** and **11**.

Most remarkably, the observation of a "mirroring" of the pseudocontact contribution for the uranium fluoro complex **18** can be confirmed by the quantum chemical calculations. As already shown in Figure 24 in two dimensions, the pseudocontact contribution in complexes **10**, **11** and **19** possesses a negative lobe in the axial direction, i.e. in direction of the actinide–halide bond, whereas the equatorial region experiences a positive pseudocontact contribution.
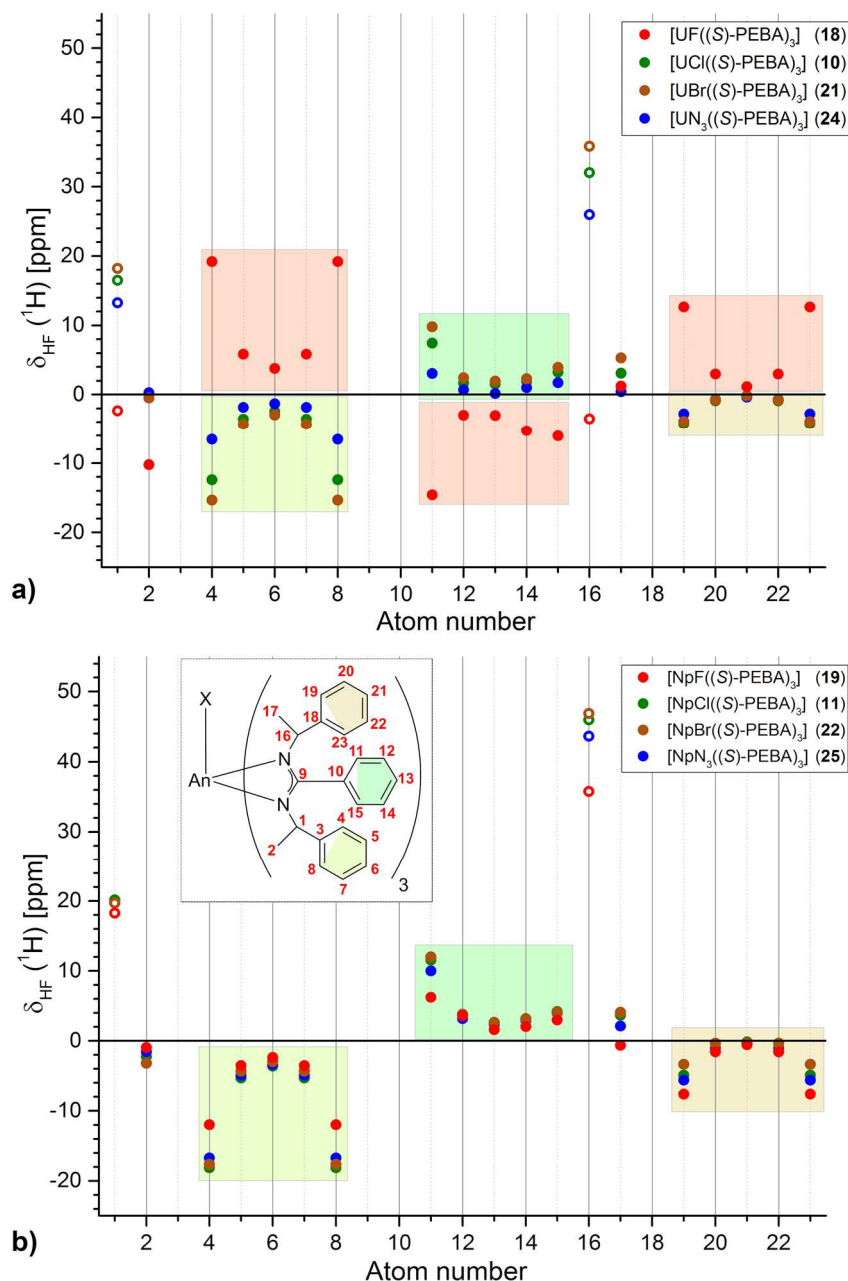
Figure 26. Plot of the ^{1}H hyperfine shifts in toluene-d$_8$ at 243 K for a) [UX((S)-PEBA)$_3$] (X = F (**18**), Cl (**10**), Br (**21**), N$_3$ (**24**)) and b) [NpX((S)-PEBA)$_3$] (X = F (**19**), Cl (**11**), Br (**22**), N$_3$ (**25**)). Open symbols indicate significant FERMI contact contribution.

Instead, the pseudocontact contribution for the uranium fluoro complex **18** shows opposite signs for both spatial lobes. Furthermore, the principal axis is not aligned with the symmetrical rotation axis anymore, which is not in accordance with the observed C_3 symmetry of all complex molecules in solution. The reason for this unexpected behavior is assumed to be the starting point of the CAS calculation which is the geometry optimized structure of **18**. This structure only possesses a C_1 symmetry (see Figure 27) which resulted in non-negative values for the non-diagonal elements of the magnetic susceptibility tensor. Similarly, also the pseudocontact lobes of compounds **10**, **11**, and **19** are not fully aligned with the rotation axis and, furthermore, show also a rhombic contribution in the equatorial region.
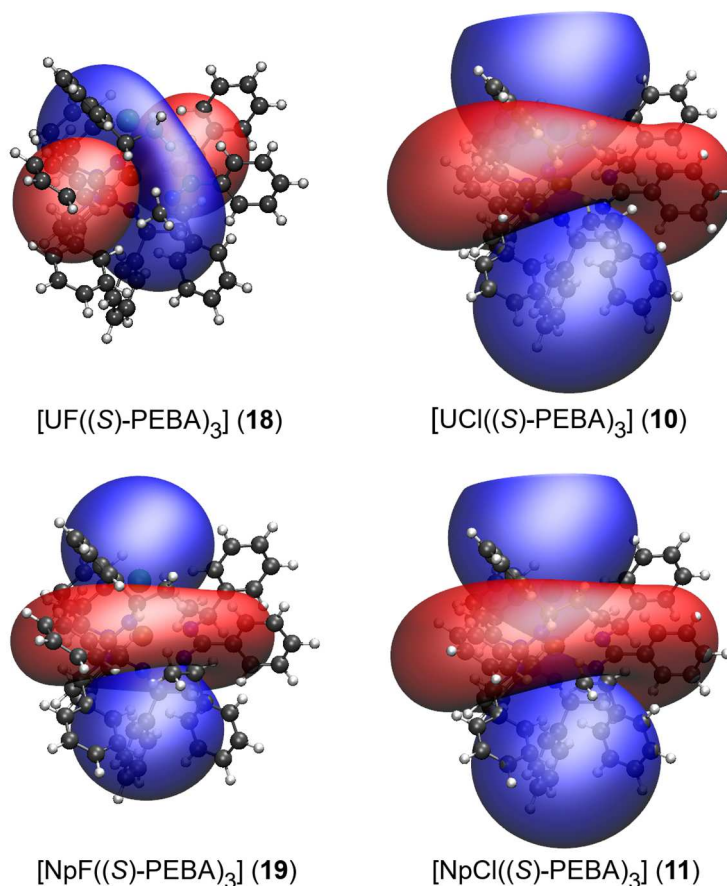
[UF((S)-PEBA)₃] (**18**)   [UCl((S)-PEBA)₃] (**10**)

[NpF((S)-PEBA)₃] (**19**)   [NpCl((S)-PEBA)₃] (**11**)

Figure 27. Graphical representation of calculated pseudocontact contributions to the chemical shift of paramagnetic [AnX((S)-PEBA)₃] (An = U, X = F **18**, X = Cl **10**; An = Np, X = F **19**, X = Cl **11**) complexes. Isosurfaces are set to the same isovalue. Blue regions represent a negative shift, red regions a positive shift.

The influence of a fluoro ligand on the magnetic susceptibility tensor and hence the emergence of the pseudocontact shift has already been reported in the literature for a number of trivalent lanthanide complexes.[248-250] However, in the reported complexes this change of the magnetic susceptibility tensor was observed comparing the binding of a water molecule vs. the binding of a very strong fluoride anion in aqueous solutions. The observed difference in the paramagnetic shift of a uranium fluoro complex (**18**) to the isostructural uranium chloro (**10**) and neptunium fluoro (**19**) complexes as shown here is unique. Currently additional quantum chemical calculations are performed in order to understand, how exactly the fluorine alters the magnetic susceptibility tensor.

In summary, the detailed analysis of the paramagnetic hyperfine shift enabled a correlation to structural parameters of the complexes in solution although a direct deduction of the spatial orientation of the nuclei was not possible as there is potentially a non-negligible FERMI contact contribution even at larger distances (> four bonds away) from the paramagnetic center. Thus, the separation of both contributions has been attempted for both tris(amidinate) complexes series using the BLEANEY method (see Fundamentals Section 2.3.2.3) yielding ambiguous results (see Table 18 and Table 26 in Appendix). Especially the alternating sign of the deduced

pseudocontact shift for both uranium tris(amidinate) complexes **4** and **10** is not expected and underlines the findings by AUTSCHBACH *et. al* who derived expressions for FERMI contact and pseudocontact shielding tensors for different spins depending on the **g**- and **A**-tensors.[200] For all systems with S > ½, higher order temperature dependencies (i.e. $1/T^3$) are deduced which is the case for the U^{IV} (S = 1) and Np^{IV} (S = 3/2) cations investigated in this thesis. The BLEANEY method is thus not working for the actinide complexes investigated in this thesis as well as for certain cases of lanthanide complexes.[195, 199, 210] To get more insight especially into the differences between the tetravalent actinide complexes and their influence on the paramagnetic hyperfine shifts of different nuclei, quantum chemical calculations have to be performed to potentially calculate the **g**- and **A**-tensors. The **g** tensor can also be extracted from electron paramagnetic resonance (EPR) spectra which would be essential to enable a detailed analysis of the paramagnetic shifts to finally obtain structural data of complex molecules in solution. Such a structure determination by paramagnetic resonance spectroscopy would be a major accomplishment as the number of analytical techniques for this purpose is limited.

The major outcomes of the comprehensive analysis of the behavior of the tetravalent actinide amidinate complexes in solution by multinuclear NMR spectroscopy are summarized to highlight their fundamental contribution to a detailed understanding of actinide complexes:

- Confirmation of covalent character of An–N bonds by significant FERMI contact contribution for closest nuclei

- Strong influence of coordinating fluoro ligand on pseudocontact shift in tetravalent uranium complex [UF((S)-PEBA)$_3$]

- Increase of pseudocontact shift with the number of f electrons from U ($5f^2$) to Np ($5f^3$) ($|\Delta\chi_{ax}|$ (U^{IV}) < $|\Delta\chi_{ax}|$ (Np^{IV}))

- Different manifestation of FERMI contact contribution depending on observed nucleus (i.e. ^{1}H or ^{13}C)

- Different solution structure of [AnX((S)-PEBA)$_3$] than in the solid state, but possible derivation of structural parameters by careful analysis of paramagnetic shifts

3.2 Trivalent actinide and lanthanide complexes with amidinates

In addition to the comprehensive analysis of tetravalent actinide complexes in the solid state and in solution presented in the previous section, also trivalent actinide compounds with the chiral (*S*)-PEBA ligand have been prepared. Their properties will be evaluated in the following and compared to their tetravalent analogues, as well as to isostructural trivalent lanthanide complexes. Again, first the synthesis of these complexes is described and thereafter their structure in the solid state and in solution. The elucidation of possible trends by comparing the trivalent actinide and lanthanide complexes is aided by quantum chemical calculations.
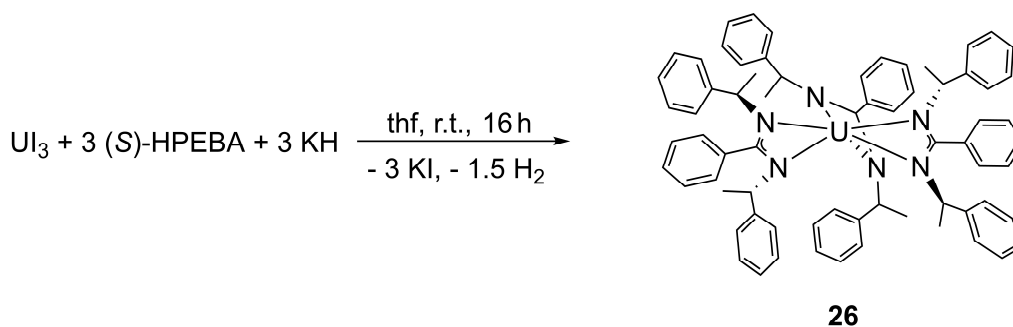
3.2.1 Synthesis

Trivalent homoleptic tris(amidinate) complexes [U((*S*)-PEBA)₃] (**26**) and [Np((*S*)-PEBA)₃] (**27**) have been prepared by reduction of the corresponding tetravalent actinide chloro tris(amidinate) complexes [AnCl((*S*)-PEBA)₃] (An = U(**10**), Np(**11**)) (see Scheme 15).
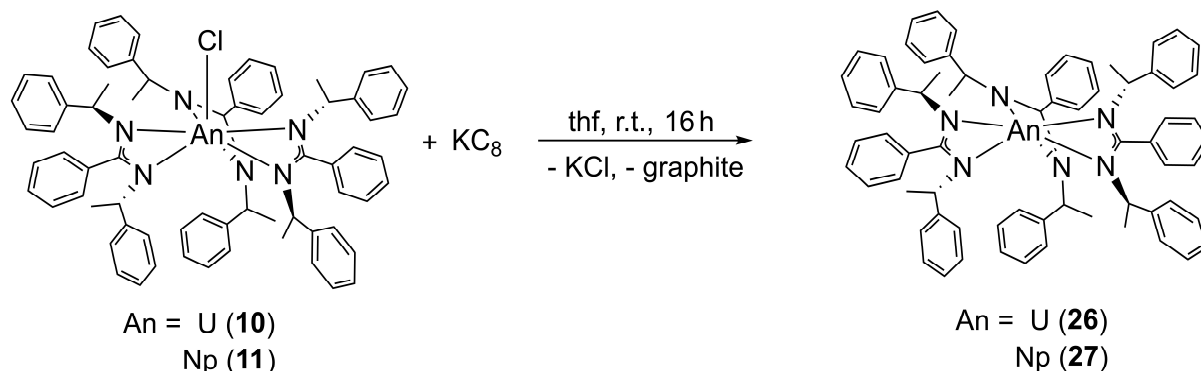
Scheme 15. Synthesis of trivalent actinide complexes [An((*S*)-PEBA)₃] (An = U (**26**), Np (**27**)) via reductive route.

Similar reduction of amido stabilized tetravalent actinide complexes to trivalent complex molecules has already been successful also for neptunium and plutonium.[251] The trivalent uranium complex **26** is also accessible starting from uranium triiodide (see Scheme 16). However, due to the limited availability of trivalent neptunium starting materials[74] synthesis attempts to yield complex **27** in a non-reductive way could not be performed.

Scheme 16. Synthesis of trivalent uranium complex **26** starting from UI₃.

The trivalent actinide complexes **26** and **27** are highly soluble in non-polar solvents like *n*-pentane and are hence not easy to crystallize. Thus, only the solid-state structure of the trivalent uranium complex could be analyzed yet. According to the NMR studies (see Section 3.2.3) the structure of both trivalent actinide complexes is very similar in solution. Thus, it can be anticipated that the neptunium complex **27** should also show a similar behavior as the uranium complex **26** in the solid state. The synthesis of the trivalent cerium complex **15** has already been introduced in Section 3.1.1.2 (see Scheme 10). It was prepared by a salt metathesis reaction starting from thf stabilized cerium(III) chloride. In contrast, the already reported homoleptic samarium complex [Sm((*S*)-PEBA)₃][145] has been accessible using an amine elimination reaction. Thus, a similar reaction has been used to synthesize the trivalent lanthanum complex [La((*S*)-PEBA)₃] (**28**) (see Scheme 17) which is used as diamagnetic reference for the analysis of the paramagnetic NMR spectra (see Section 3.2.3).

$$[La(N(SiMe_3)_2)_3] + 3\ (S)\text{-HPEBA} \xrightarrow[-\ 3\ HN(SiMe_3)_2]{thf,\ r.t.,\ 16\,h}$$

28
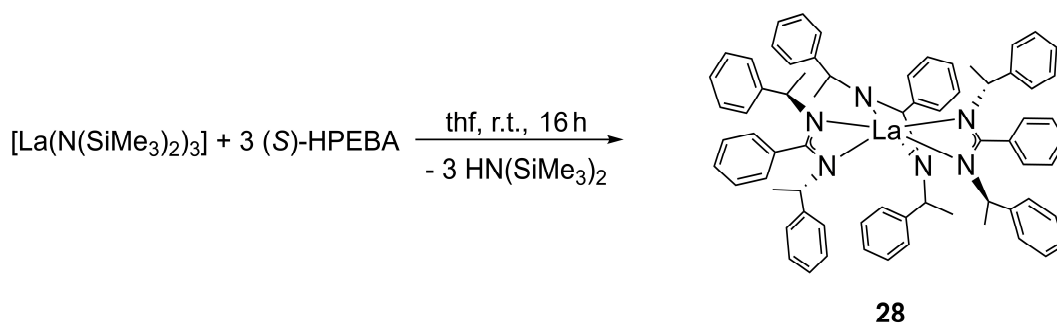
Scheme 17. Synthesis of [La((*S*)-PEBA)₃] (**28**) using an amine elimination reaction.

In total four homoleptic tris(amidinate) complexes **15** and **26**-**28** have been prepared which are investigated regarding their structural properties and potential systematic trends in the following.

3.2.2 Solid-state structures

The trivalent *f*-element complexes [M((*S*)-PEBA)₃] (M = La (**28**), Ce (**15**), Sm,[144] U (**26**)) are isostructurally crystallizing in the chiral space-group type *P*2₁3. The chiral (*S*)-PEBA ligands are again inducing an axial chirality to the complex molecules. The Λ-configuration is observed in the solid state, with an angle of the amidinate units towards the C_3 axis close to 70° (see Table 9). The molecular structures of the trivalent *f* element tris(amidinate) complexes with the (*S*)-PEBA ligand are shown in Figure 28.

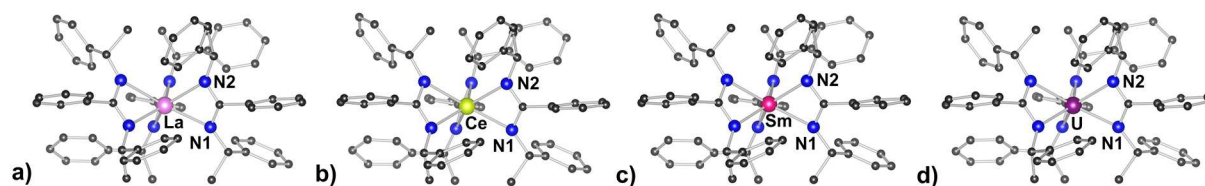**Figure 28.** Molecular structures of [M((*S*)-PEBA)₃] (M = La (a, **28**), Ce (b, **15**), Sm (c, [144]), U (d, **26**)). Hydrogen atoms are omitted for clarity. Color code: lanthanum (La, rose), cerium (Ce^{III}, yellow green), samarium (Sm, pink), uranium (U^{III}, purple), carbon (C, dark grey), and nitrogen (N, blue).

Table 9. Intramolecular distances between metal center M and coordinating atoms and angle α of plane normal of N1–M–N2 against C_3 axis in isostructural tris(amidinate) [M((*S*)-PEBA)₃] complexes **15**, **26**, **28** and [Sm((*S*)-PEBA)₃].[145]

	28 (M = La)	**15** (M = Ce)	(M = Sm)[145]	**26** (M = U)
d(M–N1) [Å]	2.591(12)	2.520(4)	2.440(4)	2.532(16)
d(M–N2) [Å]	2.503(14)	2.505(4)	2.437(4)	2.465(17)
α [°]	71.4(6)	72.5(2)	71.8(2)	73(1)

Interestingly, the trivalent tris(amidinate) complexes **15**, **26**, and **28** also possess two different M–N bond lengths (see Table 9) similar to the reported tetravalent tris(amidinate) complexes **9**-**11**, although they lack an additional halide ligand in the coordination sphere. This potentially reflects the unsaturated coordination sphere of the larger cations La³⁺ and U³⁺ with a coordination number of only six. The difference between both M–N distances is less for Ce^III and they are identical within error for Sm^III indicating the proposed dependence on the ionic radius.

To further evaluate the intramolecular coordinative bond lengths the averaged M–N distances (N_av) have been plotted against the metal ionic radii for coordination number six[228] (see Figure 29). In order to have a better comparison between the trivalent lanthanide and trivalent actinide complexes, their structures have been geometry optimized using the PBE functional including the COSMO model ($\varepsilon = \infty$) (see Section 5.1.6 for computational details). The respective intramolecular M–N distances are shown in Figure 29 as open circles. The geometry optimized structures show shorter intramolecular bond lengths than experimentally determined. This behavior may be related to packing effects which affect the crystallographically determined intramolecular distances. Such intermolecular interactions are incorporated into the geometry optimization using COSMO with an infinite dielectricity constant. However, this simplification potentially causes the observed discrepancy. Furthermore, the DFT optimized structures of [M((*S*)-PEBA)₃] (M = Sm, Ce, Np, U) show a different conformation compared to the crystal structure. The peripheral phenyl rings are located in an axial position whereas in the solid state structure the 1-phenylethyl groups are rotated so that the methyl groups are pointing in the axial direction (see Figure 122 in Appendix).

Generally, the intramolecular M–N distances are linearly increasing with the ionic radius for both, the geometry optimized and the crystallographically determined complex structures. The averaged An–N distances in the geometry optimized structures are around 2.5 pm shorter than in their isostructural lanthanide counterparts. The experimental value for the uranium complex is around 4 pm below that expected for a lanthanide of the same ionic radius. This bond shortening corresponds to an increased attraction between the actinide and the amidinate ligands which points to an increased covalent character of the actinide nitrogen bond.
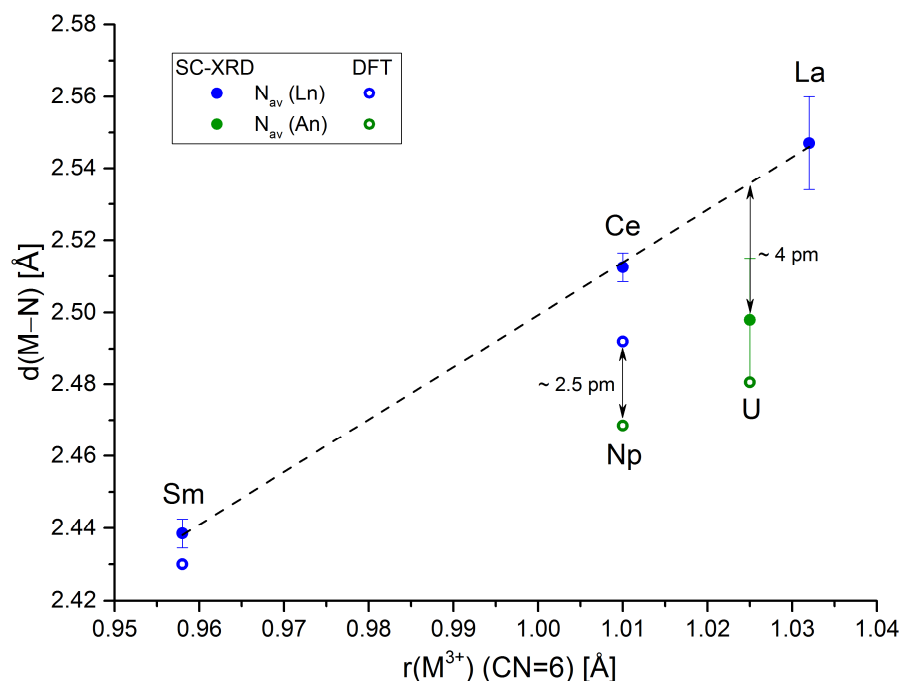
Figure 29. Plot of intramolecular distances M–N in tris(amidinate) [M((*S*)-PEBA)$_3$] (M = Sm, Ce (**15**), U (**26**), La (**28**)) complexes against ionic radii (CN = 6).[228]

A similar behavior of isostructural trivalent actinide complexes showing significantly shorter bond lengths than their lanthanide analogues have already been obtained for different ligand types,[210, 252-255] including amidinate complexes.[153] Interestingly, such a difference between the 4*f* and 5*f* M–N bonds lengths has also been observed for the tetravalent [MCl((*S*)-PEBA)$_3$] (M = Ce (**16**), Th (**9**), U (**10**), Np (**11**)) complexes (see Section 3.1.2.2). Thus, also for the trivalent actinide complexes quantum chemical calculations have been performed in order to evaluate the findings from the analysis of the intramolecular bond lengths. Natural Bond Orbital (NBO) analysis supports the experimental findings (see Table 10).

Table 10. Summary of values obtained from NBO analysis. Charges (q) and natural population analysis (*d* population and excess of *f* electrons in addition to expected value: Ce^{III} (4*f* ^{1}), Sm^{III} (4*f* ^{5}), U^{III} (5*f* ^{3}), Np^{III} (5*f* ^{4})) are given for trivalent tris(amidinate) complexes [M(L)$_3$] (M = Ce, Sm, U, Np; L = (*S*)-PEBA).

	q(M)	q(N$_{long}$)	q(N$_{short}$)	population	
				d	*f* excess
[Ce(L)$_3$]	+2.00	-0.78	-0.78	0.70 (5*d*)	0.15 (4*f*)
[Sm(L)$_3$]	+2.02	-0.78	-0.78	0.72 (5*d*)	0.12 (4*f*)
[U(L)$_3$]	+1.75	-0.76	-0.76	0.68 (6*d*)	0.28 (5*f*)
[Np(L)$_3$]	+1.79	-0.77	-0.77	0.66 (6*d*)	0.33 (5*f*)

The charge (q) of the trivalent actinide cations is smaller than the trivalent lanthanide congeners, indicating a higher degree of covalency which is also evidenced by the increased $5f$ excess. The $5d$, respectively, $6d$ population is similar for the trivalent lanthanide and actinide complexes indicating the prominent role of the $5f$ orbitals in the trivalent actinide complexes. This is in contrast to the findings of the tetravalent actinide complexes where both, $6d$ and $5f$ orbitals have been shown to accommodate the ligands. Although for both, tri- and tetravalent actinide amidinates, significantly shorter An–N bonds compared to the Ln–N bonds have been observed in the solid state, the degree of covalent interaction is not comparable. This becomes evident when comparing the synthesized cerium complexes to the uranium analogues. The trivalent cerium in **15** possesses significantly less covalent interaction with the nitrogen donor ligands than the trivalent uranium in **26**, whereas the covalent contribution is almost similar for the tetravalent cerium and uranium complexes **16** and **10**. This lead to the conclusion that the overall degree of covalency is higher for the trivalent actinides compared to the tetravalent analogues as the differences to the lanthanide ions are more pronounced. This resembles the significantly higher LEWIS acidity of the tetravalent actinides compared to the trivalent analogues.

3.2.3 Complex structure in solution

Apart from the comprehensive investigations of the structure of the trivalent actinide and lanthanide complexes in solution also their behavior in solution is of interest especially for the investigation of the paramagnetic influence of the trivalent actinides. The NMR spectra of the trivalent f-element tris(amidinate) complexes **15**, **26**-**28** are in accordance with a D_3 symmetry throughout the whole accessible temperature range (243 K to 373 K) (see Section 8.3.2 in Appendix). Thus, the deviations from D_3 symmetry in the solid state, i.e. slightly different M–N bond lengths, are averaged in solution. In order to also investigate the paramagnetic influence of the trivalent lanthanide and actinide cations, the paramagnetic ^1H hyperfine shift has been extracted for all paramagnetic metal complexes using the lanthanum complex **28** as diamagnetic reference (see Figure 30).

The derived paramagnetic hyperfine shifts for all protons except the methyl groups show a positive sign. The difference between the actinide and lanthanide complexes is small for most protons but again the NCH protons (i.e. H1 and H16) are most strongly affected by the paramagnetic metal. This again points to an increased FERMI contact contribution for these protons, which are closest to the paramagnetic center. The FERMI contact contribution is directly related to the orbital overlap of metal and ligand orbitals and can thus be also related to the covalent interaction. Assuming that the FERMI contact contribution is dominant for the NCH protons (i.e. H1 and H16), the increased hyperfine shift of the trivalent actinides compared to the paramagnetic cerium does undoubtedly reflect the findings from SC-XRD and quantum chemical calculations of a higher degree of covalent character for the actinides.
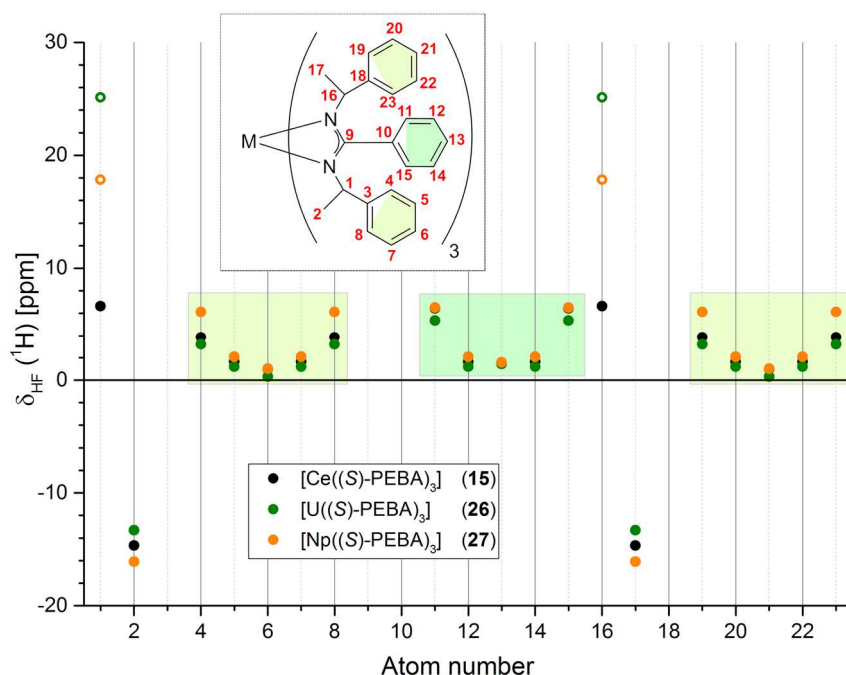
Figure 30. Plot of the ^{1}H hyperfine shift of trivalent tris(amidinates) [M((S)-PEBA)$_3$] (M = Ce (**15**), U (**26**) and Np (**27**)) in toluene-d$_8$ at 243 K. Open symbols indicate significant FERMI contact contribution.

This independent justification of the results from the quantum chemical calculations underlines the importance of a fundamental understanding of the paramagnetic properties of actinides and the need for the development of suitable separation methods of FERMI and pseudocontact contributions.

However, the very similar hyperfine shifts for all other protons indicate a similar order of the pseudocontact contribution for both, the trivalent actinide and lanthanide cations. It is hence expected, that the axial term of the anisotropy of the magnetic susceptibility tensor $\Delta\chi_{ax}$ for U^{III} (5f^3) and Np^{III} (5f^4) is of similar magnitude and sign as the known value of Ce^{III} (i.e. $2.1\cdot10^{-32}$ m^3).[204] Furthermore, the calculated hyperfine shifts are again higher for the neptunium complex than the uranium complex, despite for the NCH protons which are affected by the FERMI contact contribution. Here, the trivalent uranium complex (5f^3) shows a higher hyperfine shift than the trivalent neptunium complex (5f^4). Thus, from the evaluation of both, tri- and tetravalent actinide complexes, it can be deduced that the measure for the pseudocontact contribution, i.e. the axial term of the anisotropy of the magnetic susceptibility tensor $\Delta\chi_{ax}$, increases with the number of f electrons from 5f^2 to 5f^4 whereas the FERMI contact contribution seems to have a maximum at 5f^3 (i.e. U^{III} or Np^{IV}) electronic configuration.

In addition, by assuming a rapidly declining FERMI contact contribution with increasing distance from the metal, the calculated hyperfine shifts can be correlated to the spatial orientation of the protons with respect to the principal axis of the magnetic susceptibility tensor (see Figure 31). It is again assumed that the symmetry axis of the complex molecules coincides with the magnetic axis.
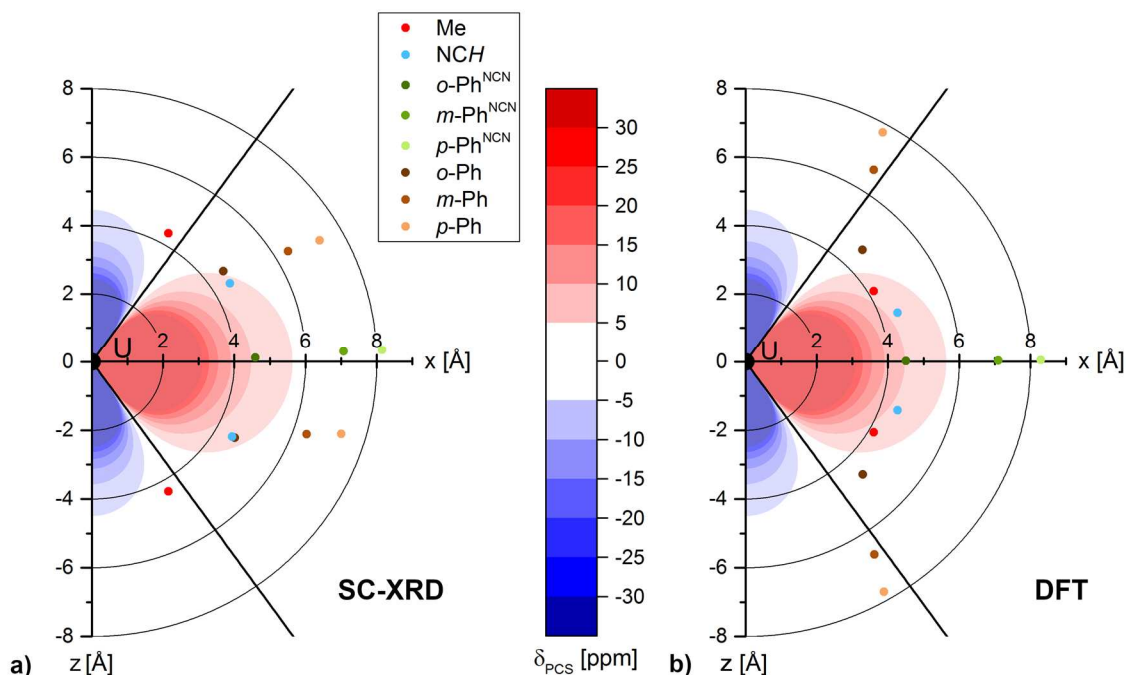
Figure 31. Two-dimensional representation of spatial arrangement of protons in [U((*S*)-PEBA)$_3$] (**26**) based on SC-XRD data (a, left) and DFT optimization (b, right). Proton positions at rotating groups (i.e. methyl and peripheral phenyl groups have been averaged. The y-axis is aligned with the proposed principal axis in the complex molecules. Bold black lines at ± 54.74° indicates a change of the pseudocontact contribution from positive (red) to negative (blue). Thin black lines indicate regions of identical distance to the metal center. The pseudocontact contribution has been calculated based on the KURLAND-MCGARVEY equation and a value for the magnetic anisotropy of the susceptibility tensor $\Delta\chi_{ax} = 1.7 \cdot 10^{-32}$ m^3.

Interestingly, the observed sign of the hyperfine shifts (see Figure 30) coincides with the SC-XRD structure (see Figure 31a) but not with the DFT optimized structure (see Figure 31b). This is easily visible by comparing the observed negative hyperfine shift of the methyl groups (H2, H17 in Figure 30) with the calculated spatial orientation (red symbols in Figure 31) which only matches for the SC-XRD structure. This observation is quite unexpected, as the DFT optimized structure of [U((*S*)-PEBA)$_3$] (**26**) has been calculated to be 25.7 kJ/mol lower in energy than the structure which has been constrained to reflect the SC-XRD structure more closely. Thus, the simple picture of the emergent pseudocontact contribution as drawn in Figure 31 may not hold for the synthesized trivalent actinide complexes. This deviation may also be caused by a different orientation of the magnetic and the symmetry axis of the complex molecules.

Additionally, the hyperfine shift of the ^{13}C nuclei shows a different behavior having mostly a negative sign (see Figure 101 in Appendix). Thus, the ^{13}C nuclei also exhibit a significant FERMI contact contribution, which is not significant for the protons. This behavior has already been observed for the tetravalent actinide complexes and again underlines the necessity of a profound understanding of the underlying mechanisms to gain more insight into the paramagnetic properties of actinides.

RESULTS AND DISCUSSION

The comprehensive analysis of trivalent actinide and lanthanide complexes with amidinate ligands in the solid state and in solution revealed several results of a broader scope which are shortly summarized in the following.

- Increased covalent character for trivalent actinides compared to trivalent lanthanides

- Overall higher degree of covalent character for trivalent actinides compared to tetravalent actinides

- Similar amount of paramagentic pseudocontact contribution for Ce^{III}, U^{III}, and Np^{III}, but slight increase from U^{III} to Np^{III}

- Different behavior of FERMI contact contribution with maximum value at $5f^3$ configuration (i.e. U^{III} resp. Np^{IV})

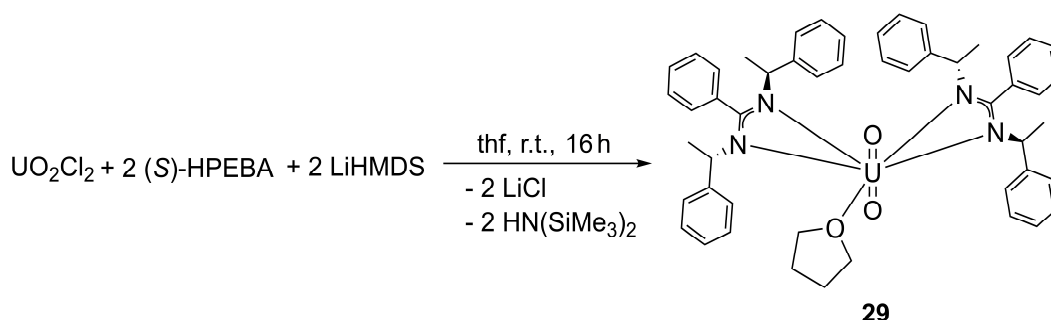# 3.3 Hexavalent uranium complexes with amidinates and diimines

The syntheses and solid-state structures of the hexavalent uranium diimine complexes presented in this chapter have been published in two publications by SCHÖNE *et al.*[49, 82]

After these comprehensive analysis of isostructural tri- and tetravalent amidinate complexes including their properties in the solid state and in solution the next two sections focus on some additional topics of the PhD work which are closely related to the aforementioned topics. In this section the complexation of hexavalent uranium with nitrogen donor ligands will be investigated. As already introduced in the Fundamentals Section 2.1, the hexavalent oxidation state is the most stable oxidation state for uranium, as uranyl(VI) (UO_2^{2+}), under aerobic conditions in aqueous solutions. Therefore it has been widely investigated in solution by numerous spectroscopic techniques[256-257] and also in the solid state.[258] The robust nature of the uranyl moiety having formally two U≡O triple bonds is limiting the coordination in most cases to the equatorial plane.[52] However, the metal-organic coordination chemistry of uranyl complexes flourished within the last years due to new synthesis strategies to functionalize the uranyl entity.[80, 259]

During this PhD thesis several investigations regarding the complexation behavior of hexavalent uranium with nitrogen donors have been performed.[49, 82] First, the series of tri- and tetravalent actinide complexes with (*S*)-PEBA will be expanded with a uranyl(VI) complex of the same ligand. Subsequently, this compound will be compared to U^{VI} complexes with ligands possessing neutral *N*-donor atoms 2,2′-bipyridine (bipy) and 1,10-phenanthroline (phen). Similar to the previous sections, first, the synthesis of the complex molecules will be discussed and thereafter their solid-state structures. Detailed studies about their solution behavior have not been performed, mainly due to the low solubility of some of the formed complex molecules.

3.3.1 Synthesis

A salt metathesis approach has been used to synthesize a hexavalent uranium amidinate complex [UO_2((*S*)-PEBA)$_2$(thf)] (**29**) similar to the already discussed tri- and tetravalent actinide complexes in the previous sections (see Scheme 18).

Scheme 18. Synthesis of hexavalent uranium amidinate [UO_2((*S*)-PEBA)$_2$(thf)] (**29**).

75
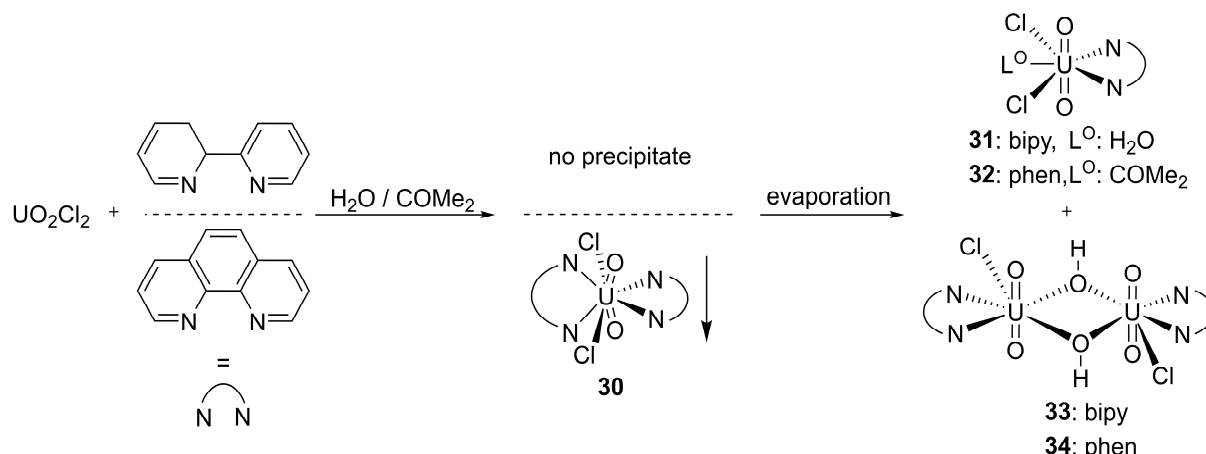
Scheme 19. Synthesis scheme for uranyl diimine complexes **30**-**34**.

In contrast to the amidinate ligand (*S*)-PEBA, the used diimine ligands bipy and phen are neutral nitrogen donor ligands. Thus, their complexation behavior with uranyl(VI) has been studied without the addition of a base in aqueous solutions. The results of this investigation are summarized in Scheme 19.

The often stressed similarity between bipy and phen regarding their complexation behavior does not apply for uranyl chloride in aqueous solutions. Whilst the combination of different metal-to-ligand ratios (1:1 to 1:3, metal:ligand) for the bipy ligand results in clear solutions, a yellow precipitate is formed when the same metal-to-ligand ratios are applied with the phen ligand. This precipitate has been identified as [UO$_2$Cl$_2$(phen)$_2$] (**30**), an unique phen complex of uranyl(VI) in 1:2 stoichiometry.[82] The evaporation of the bipy solutions and the supernatant after the precipitation of **30** yielded mono- and dinuclear uranyl diimine complexes **31**-**34**. Thereby a higher metal to ligand ratio favors the formation of the hydroxyl bridged dimeric complexes **33** and **34** due to the basicity of the diimine ligands.[49] However, in all synthesized uranyl complexes the uranium is coordinated by the nitrogen donor ligands, chloride and oxygen.

3.3.2 Solid-state structures

The complex structures of the hexavalent uranium amidinate and diimine complexes are discussed in the following. In contrast to the aforementioned synthesis of isostructural series of tri- and tetravalent metal amidinates, the focus of this section is dedicated to the coordination chemistry of the uranyl cation, especially the possibility to distort the *trans*-uranyl moiety by special ligand arrangements in the solid state. As it will be evidenced, both, amidinate and diimine ligands could be used for this approach. This fundamental knowledge further helps to increase the number of structurally characterized actinide complexes by crystal engineering.
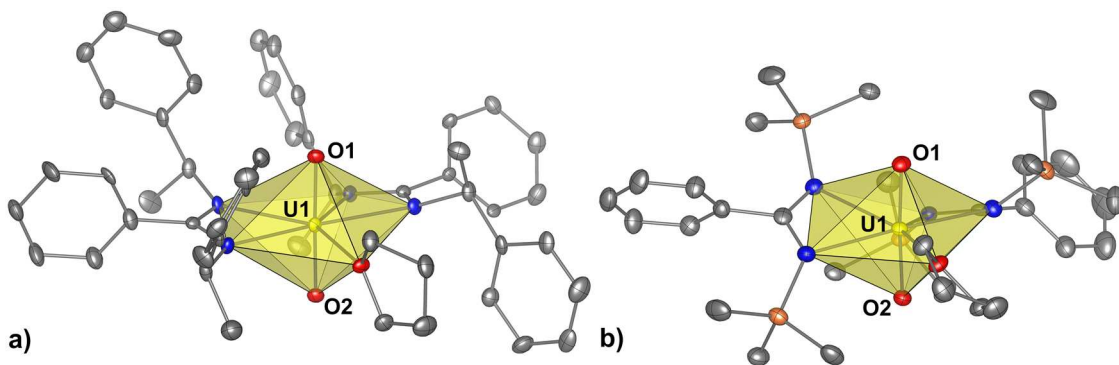
Figure 32. Molecular structures of hexavalent uranium bis(amidinate) complexes a) [UO$_2$((S)-PEBA)$_2$(thf)] (**29**) and b) [UO$_2$((SiMe$_3$)$_2$NCPh)$_2$(thf)].[159] Ellipsoids are drawn at 50 % probability level. Hydrogen atoms are omitted for clarity. Color code: uranium (U^{VI}, yellow), carbon (C, dark gray), nitrogen (N, blue), oxygen (O, red), and silicon (Si, pale orange).

The hexavalent uranium amidinate complex [UO$_2$((S)-PEBA)$_2$(thf)] (**29**) is crystallizing in the chiral space-group type $P2_12_12_1$ indicating the enantiopurity of the complex (see Table 45 in Appendix). The uranium is coordinated by two amidinates and one thf molecule in the equatorial plane and two "yl" oxygens forming an only slightly distorted pentagonal bipyrimidal coordination polyhedron. This is in contrast to the reported [UO$_2$(N(SiMe$_3$)$_2$CPh)$_2$(thf)] complex of similar type, which shows higher deviations of the coordination of the amidinate ligands from the equatorial plane (see Figure 32).[159] This is caused by intramolecular hydrogen bridges between the trimethylsilyl substituents and the "yl" oxygens also causing the uranyl unit (i.e. O–U–O) to bend to an angle of 169.7(2)°. Instead, no such deviations are observed in the (S)-PEBA complex **29**, as the 1-(phenyl)ethyl substituents are rotated around the N–C bonds to avoid steric interactions (see Table 46 in Appendix) and hence the number of hydrogen donor atoms in proximity to uranyl is limited. Thus, in **29**, in one ligand the two peripheral phenyl rings are in *cis* position whereas in the other amidinate ligand they possess a *trans* arrangement.

A similar effect of the bending of the uranyl unit is observed in the diimine complex [UO$_2$Cl$_2$(phen)$_2$] (**30**). This type of diimine uranyl complex was unprecedented at the time of publication,[82] and has since already been used as a template to synthesize similar complexes by substituting the chloro ligands with halogenated benzoates.[83] In the following, the origin of this unexpected behavior of 1,10-phenanthroline is discussed and compared to other attempts to influence the strong *trans* arrangement of the uranyl oxygen atoms.

The uranyl complex **30** is crystallizing in triclinic space-group type $P\bar{1}$. The uranium center is eightfold coordinated by the two "yl" oxygens, two chlorides and four nitrogen atoms of two phen molecules (see Figure 33). Instead of the often observed bipyrimidal coordination environment around the uranyl a dodecadeltahedral coordination sphere is forming. This is unique for uranyl complexes and resembles the ability of the phen ligand to form unusual coordination environments with uranyl cations.[175]
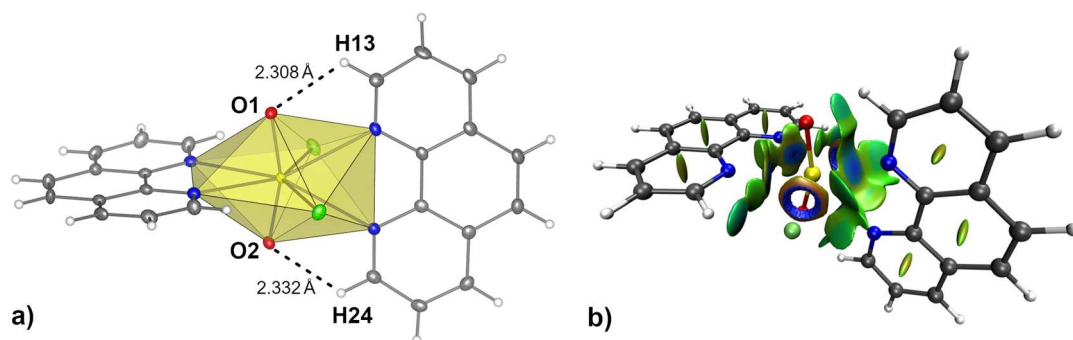
Figure 33. Molecular structure of [UO$_2$Cl$_2$(phen)$_2$] (**30**) (a, left) and plot of weak interactions of DFT optimized structure (b, right, reprinted with permission from Wiley-VCH[82]). Ellipsoids are drawn at 50 % probability level. The degree of the interactions is illustrated by the color gradation from blue (strong non-covalent interaction), through green (very weak interactions), to red (strong non-bonded orbital overlapping). Color code: uranium (U^{VI}, yellow), hydrogen (H, white), carbon (C, dark gray), nitrogen (N, blue), oxygen (O, red), and chlorine (Cl, green).

Furthermore, complex **30** has been the first uranyl phen complex possessing a 1:2 stoichiometry in the solid state. Besides the out-of-plane coordination of one phen ligand the uranyl unit deviates significantly from its ideal linear geometry. The O–U–O angle of 161.8(1)° is identical within the error tolerance to the lowest reported uranyl angle thus far, i.e. 161.7(5)° in [UO$_2$(OTf)(thf)(^{Me}N$_4$)][OTf]**[17]**.[260]

The origin of the bending of the uranyl moiety in **30** has been investigated by quantum chemical calculations. These indicate a weak but distinct interaction between the "yl" oxygens and the adjacent hydrogens (i.e. O1$\cdots$H13 and O2$\cdots$H24) of the phen ligands (see Figure 33). Furthermore, extended π stacking networks between the phen ligands are stabilizing the complex in the solid state. Thus, both the intramolecular interactions between the "yl" oxygens and the adjacent hydrogen atoms of the phen ligands, and the ability to establish extended π stacking networks are the reason for the unexpected coordination of 1,10-phenanthroline to uranyl(VI) in [UO$_2$Cl$_2$(phen)$_2$] (**30**).[82]

In contrast, CARTER and coworkers assume an electrostatic repulsion between the non-planar nitrogens of one phen ligand and the charge in the U–O bond as the reason for the bending of the uranyl moiety in similar complexes of [UO$_2$X$_2$(phen)$_2$] type.[83] Due to the coordination of the non-planar nitrogens the charge and hence the electrons within the U–O bond are rearranged to the far side of the uranyl indicated by the bending in this direction. They could show by quantum chemical calculations that an angle around 162° seems to be the minimal value which can be achieved using this sterical repulsion approach.

As already pointed out in the synthesis section, the unique behavior of the phen ligand is in contrast to that of bipy which does not show the formation of an analogous 1:2 compound. It can be assumed that the higher stiffness of the phen ligand is the cause for this different behavior as it enables the formation of extended π stacking networks in the solid state.

---

[17] OTf = O$_3$SCF$_3$; ^{Me}N$_4$=*N*,*N*′-dimethyl-2,11-diaza[3,3](2,6)pyridinophane
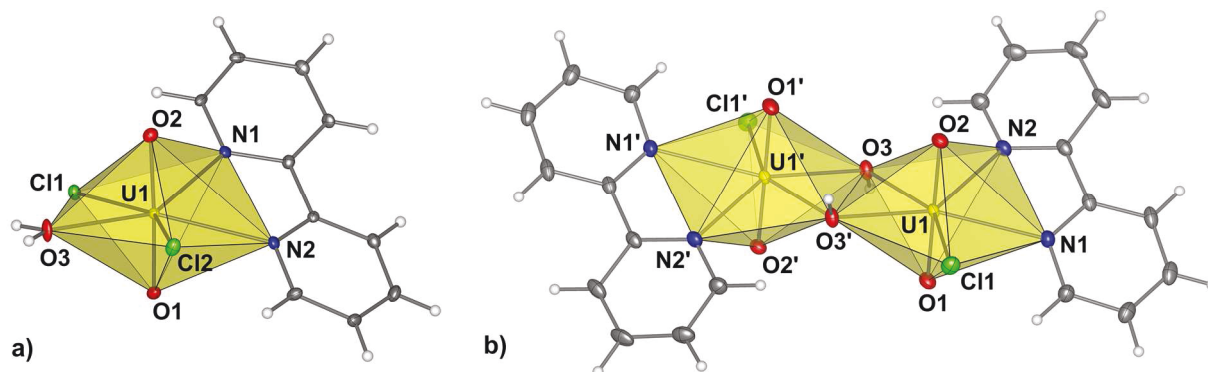
Figure 34. Molecular structure of [UO$_2$Cl$_2$(bipy)(H$_2$O)] (**31**) (a, left) and [(UO$_2$Cl(bipy))$_2$(μ_2-OH)$_2$] (**33**) (b, left). Ellipsoids are drawn at 50 % probability level. Color code: uranium (U^{VI}, yellow), hydrogen (H, white), carbon (C, dark gray), nitrogen (N, blue), oxygen (O, red), and chlorine (Cl, green).

However, by crystallization from the supernatants mono- and dinuclear uranyl complexes having either bipy or phen coordinated could be yielded which are similar to already reported complexes (see Table 48 in Appendix). The molecular structure of the bipy complexes **31** and **33** are shown in Figure 34 as representatives. In all uranyl diimine complexes **31**-**34** the uranyl cation is coordinated by five atoms in the equatorial plane forming the already introduced pentagonal bipyrimidal coordination environment around the metal. In contrast to **30**, no bending of the uranyl moiety is observed in complexes **31**-**34** whereas the U–O and U–N distances are similar (see Table 49 in Appendix). Interestingly, the deviation of the N1–U–N2 plane of the diimine ligands from the equatorial uranyl plane is higher in the monomeric complexes **31** and **32** than in the hydroxo-bridged complexes **33** and **34** (see Table 50 in Appendix). Similar observations have been made in substituted pyridine complexes of uranyl chloride.[261]

The presented investigations on hexavalent uranium complexes with amidinates and diimines led to new insights into the chemistry of high-valent uranyl cations which may potentially be expanded also to the transuranic "yl" cations.

- Great impact of intramolecular hydrogen bonding interactions on the coordination environment of "yl" cations in the solid state

- Synthesis of formerly unknown actinide complexes by selective ligand design (i.e. sterical crowdedness, stiffness, donor/acceptor functionalities) with distinct properties *via* crystal engineering

3.4 Mixed-valent polynuclear neptunium complexes

The syntheses and solid-state structures of the mixed-valent polynuclear neptunium complexes presented in this chapter have been published recently by SCHÖNE *et al.*[262]

One major achievement of this PhD work has been the synthesis and characterization of tri-(**27**) and tetravalent (**5**, **11**, **17**, **20**, **23**) neptunium amidinate complexes. In order to perform these syntheses, the use of an appropriate starting material is crucial. To enable such systematic studies, first several investigations have been performed to increase the knowledge about the fundamental chemistry of tetravalent neptunium in organic media. Throughout these investigations, mixed-valent polynuclear neptunium complexes $[(Np^{IV}Cl_4)(Np^VO_2(thf)_3)_2(\mu_2\text{-Cl})_2]$ (**35**) and $[(Np^{IV}Cl_3)(Np^VO_2(thf)_2)_3(\mu_2\text{-Cl})_3(\mu_3\text{-Cl})]$ (**36**) were obtained.[262] The polynuclear cores of these complexes are held together by cation-cation interactions (CCIs) which are observed for several actinyl compounds in the solid state and also in solution (see Fundamentals Section 2.1.3). In the following, the solid-state structure of both complexes is discussed briefly with special focus on the CCIs.

The trinuclear neptunium complex **35** consists of two neptunyl(V) units (i.e. Np2, Np3) which are coordinating to the tetravalent neptunium cation (i.e. Np1) via CCIs (see Figure 35). This is evidenced by the significantly longer Np^V–O distances towards the Np^{IV} center (1.918 Å vs. 1.793 Å for Np2, see also Table 52 in Appendix). The Np^{IV} center is coordinated by two "yl" oxygens and four additional chloro ligands for charge compensation causing a distorted octahedral coordination sphere. For the pentavalent neptunyl(V) units a pentagonal bipyramidal coordination sphere similar to the uranyl(VI) complexes is formed by two "yl" oxygens, three thf molecules, and two μ_2-bridging chloro ligands. Interestingly, an isostructural $Np^{V/VI}$ complex (i.e. $[(Np^{VI}O_2Cl_2)(Np^VO_2(thf)_3)_2(\mu_2\text{-Cl})_2]$) has been reported[263] offering the unique opportunity to compare the ability of Np^{IV} and Np^{VI} to accept CCIs from Np^V.
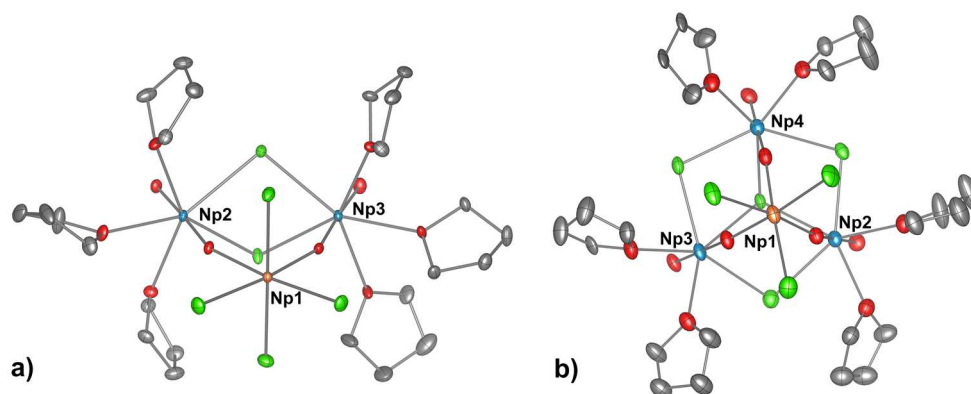
Figure 35. Molecular structure of $[(NpCl_4)(NpO_2(thf)_3)_2(\mu_2\text{-Cl})_2]$ (**35**) (a, left) and $[(NpCl_3)(NpO_2(thf)_2)_3(\mu_2\text{-Cl})_3(\mu_3\text{-Cl})]$ (**36**) (b, right). Ellipsoids are drawn at 50 % probability level. Hydrogen atoms and solvent molecules are omitted for clarity. Color code: neptunium (Np^{IV}, orange red; Np^V, pale blue), carbon (C, dark gray), oxygen (O, red), and chlorine (Cl, green).

81

A comparison of the respective intramolecular distances revealed a stronger CCI from Np^V to Np^{IV}, i.e. a shorter distance between both neptunium centers, due to the higher effective charge of Np^{IV} compared to Np^{VI}.[262]

The neptunium centers in the tetranuclear neptunium complex **36** are arranged in a pseudo-tetrahedral arrangement which is unique for complex molecules made of CCIs. The respective coordination polyhedra are similar to the trinuclear complex **35** with a distorted octahedron for Np^{IV} and a pentagonal bipyramid for Np^V. In contrast, three Np^V centers are connected *via* one μ_3-bridging chloride and three μ_2-bridging chlorides which connect adjacent Np^V units. A calculation of the Bond Valence Sum (BVS) values for both complexes indicate a potential charge delocalization for the tetravalent neptunium cations having higher than expected charges (4.14 in **35**, 4.30 in **36**).[262]

In summary, both synthesized mixed-valent polynuclear neptunium complexes show the ability of neptunyl(V) to coordinate to other cations via cation-cation interactions. These interactions have also been observed in solution studies[53-54] indicating the relevance of these investigations also for environmentally relevant systems, where "yl" cations of the actinides may be present.

These investigations underline the overall motivation of this thesis, which is the lack of knowledge especially for the transuranium elements also in terms of structurally characterized complex molecules. Thus, the successful synthesis and characterization of both mixed-valent polynuclear neptunium complexes narrows this knowledge gap even further and can finally help to understand the properties of actinide elements in-depth.

4 CONCLUSIONS AND OUTLOOK

The complexation behavior of the early actinides thorium, uranium, and neptunium in various oxidation states (+III to +VI) with nitrogen donor ligands has been studied thoroughly in the solid state and in solution to investigate the fundamental properties of these heavy elements and to improve the limited database with respect to these compounds. A total of four isostructural series of bis- and tris(amidinate) complexes using tetravalent actinides, lanthanides, and transition metals have been synthesized including the first examples of transuranic amidinate complexes, i.e. [NpCl(iPr$_2$BA)$_3$] (**5**) and [NpCl((S)-PEBA)$_3$] (**11**). Furthermore all actinide complexes possessing the chiral (S)-PEBA ligand are the first members of enantiomerically pure actinide amidinate complexes. In addition to these isostructural chloro substituted complex series, the reactivity of the tetravalent actinide complexes **9**-**11** has been successfully shown by synthesis of the corresponding fluoro (**17**-**19**), bromo (**20**-**22**), and azido (**23**-**25**) complexes. Thus, the well-known coordination chemistry of uranium could be expanded to neptunium reflecting the similarities of their tetravalent oxidation states. Hence, the first examples of metal-organic neptunium fluoro, bromo, and azido complexes have been prepared during this work.[214]

The major objective of this work was the elucidation of covalent contributions to actinide–nitrogen bonding. The influence of 5f electrons on this covalency as well as the comparison of actinides in different oxidation states (III, IV) and of actinides and transition metals or lanthanide analogues were of special interest in this context. In the series of tris(amidinate) complexes [M^{IV}Cl(iPr$_2$BA)$_3$] (M = Zr (**2**), Th (**3**), U (**4**), Np (**5**)) a linear dependence of the intramolecular metal-to-ligand bond lengths on the ionic radii with a slope of one has been observed for the actinides and the transition metal zirconium. This reflects a mainly ionic bonding interaction for all investigated metals and indicates no differences between the actinides and the transition metals. Similarly, a linear decrease of the actinide-to-ligand bond lengths for the complex series using the chiral (S)-PEBA ligand (i.e. [An^{IV}X((S)-PEBA)$_3$] (An = Th, U, Np; X = F, Cl, Br, N$_3$) was revealed. Also the complex geometry does not change when traversing the actinide series. This indicates a negligible influence of 5f electrons on the complex structure for the investigated tetravalent actinide tris(amidinate) complexes.

In contrast to the experimental findings, quantum chemical calculations using QTAIM and NBO analysis are able to reveal an increase of covalent character of the An–N and An–Cl bonds for [An^{IV}Cl((S)-PEBA)$_3$] complexes when traversing the actinide series from thorium to uranium. The degree of covalent character remains roughly constant from uranium to plutonium, although the origin changes from mainly 6d participation for uranium to mainly 5f character in plutonium, also reflecting an interplay between orbital overlap and energy-degeneracy driven

covalency. For the heavier actinides the $6d$ covalent contribution should diminish based on the trends observed here, while the $5f$ orbitals become increasingly core-like. It can then be expected that a reversed trend of covalent interaction may be observed when traversing the actinide series even further to americium and curium as shown previously.[42, 44] Interestingly, the increased covalent character of the uranium and neptunium complexes is not reflected in the intramolecular bond lengths as those show a linear increase relative to the thorium complex. Thus, there is a clear indication for covalency in the actinide-ligand bonds, but the degree of covalent character is small compared to the mainly ionic bonding interaction between the tetravalent actinides and the nitrogen and chloride donors, respectively.

This is also reflected by the analysis of the difference between the Ce(IV) amidinate complex and the actinide series. Although the cerium complexes shows longer coordinative bond lengths as expected by the linear trend within the actinide series, its covalent character is higher than that of the thorium complex and similar to the protactinium complex as evidenced by quantum chemical calculations. The reason is an increased participation of $5d$ orbitals in the bonding. Again, this underlines the finding that the overall covalent character of the tetravalent f elements is small and that the analysis of the experimentally determined intramolecular bond lengths is hence of limited suitability as these small effects are easily overcompensated by various effects like intramolecular interactions or packing effects. Thus, a profound investigation of the covalent character of actinide complexes compared to lanthanide and transition metal analogues is only possible with the help of accurate quantum chemical calculations. The sole analysis of the change of the intramolecular bond lengths with the ionic radii of the central metal cation is not sufficient to decipher small differences between the investigated elements.

In contrast, the analysis of the intramolecular bond lengths in the trivalent actinide and lanthanide series of isostructural complexes (i.e. [M^{III}((S)-PEBA)$_3$] (M = Ce (**15**), La (**28**), U (**26**), Np (**27**))) revealed significantly shorter bond lengths for the actinides compared to the lanthanides. QTAIM and NBO analyses confirm that the origin of this observable deviation lies in increased covalent interactions in the actinide complexes. The $5f$ orbitals play the prominent role in the bonding throughout the whole actinide series. This clearly points to an overall higher degree of covalent interaction in the trivalent actinides compared to the tetravalent actinides due to their softer character which results in a less contracted set of $5f$ orbitals compared to the much harder tetravalent actinides and thus, better orbital overlap with the medium-hard N-donor ligands.

Thus, in this PhD thesis the nature of intramolecular actinide–nitrogen bonds has been studied by systematic analysis of the solid-state structures of series of isostructural compounds and with the help of quantum chemistry. Based on these analyses it can be concluded that the covalent character of the actinide elements is strongly dependent on the oxidation state. Lower oxidations states favor the formation of more covalent interactions with softer donors whereas for the

highly charged tetravalent actinides a mainly ionic interaction is observed. Nevertheless, with the help of quantum chemical calculations subtle changes of the covalent character can also be revealed for the tetravalent actinides. From an academic perspective it would therefore be attractive to compare f element systems in even lower oxidation states like +II to further verify this assumption. Furthermore, recent studies[223, 239, 264] gave evidence that multiple bonded donor functionalities possess an increased sensitivity for covalent interactions due to enhanced orbital overlap which should hence be a focus of future systematic investigations of actinide and lanthanide complexes.

The second major objective of this PhD work has been the elucidation of structural parameters of actinide complexes in solution using paramagnetic NMR spectroscopy and the structural comparison to the solid-state structures. Both contributions of the derived hyperfine shift, the FERMI contact and the pseudocontact shift contain valuable information about the amount of orbital overlap (the former) and the spatial orientation of the observed nuclei with respect to the magnetic axis (the latter). Unfortunately, a reliable separation method for both contributions is not available. Our attempts confirm that the separation of both contributions by the BLEANEY method[198] is not appropriate for paramagnetic actinide complexes and should hence be replaced by modern quantum chemical methods to explain the observed paramagnetically shifted NMR signals. It is commonly assumed that the FERMI contact contribution can be neglected for any nuclei separated by more than four bonds from the paramagnetic ion. This assumption seems to be appropriate only for protons indicated by a significant FERMI contact contribution only for the closest protons. This FERMI contact contribution reflects the orbital overlap and hence independently confirms the findings of a partial covalent bonding character in the paramagnetic uranium and neptunium complexes. However, in the case of ^{13}C nuclei, the FERMI contact contribution is disseminated much further into the coordinating ligands, casting doubt on the assumption's general validity. This again underlines the necessity for the development of suitable separation methods of FERMI and pseudocontact contribution depending on the observed nuclei to finally understand the fundamental aspects of paramagnetic NMR spectroscopy of actinide complexes, and thus facilitate their structural characterization in solution.

Furthermore, it could be shown that not only the actinide but also the ligands have an immense influence on the paramagnetic shift as evidenced by the hyperfine shift analysis of the fluoro complexes [AnF((S)-PEBA)₃] (An = U (**18**), Np (**19**)). Quantum chemical calculations could relate the experimentally observed "flipping" of the hyperfine shift to changes in the anisotropy of the magnetic susceptibility due to complexation of the fluoride in the uranium complex **18**, but not in the neptunium complex **19**. Thus, the very hard and strongly complexing fluoro ligand alters the ligand field of the uranium complex **18** causing a change of the magnetic susceptibility tensor in comparison to the investigated [UCl((S)-PEBA)₃] (**10**) and [NpX((S)-PEBA)₃] (X = F (**19**), Cl (**11**)) complexes. Such a specific influence of the fluoride on the paramagnetic

properties of tetravalent actinides has not been observed before and must be investigated in more detail to fully understand the changes in the electronic structure. Especially the investigation of these complexes with EPR spectroscopy to directly determine the **g** tensors would be of utmost importance to validate the findings by theory.

In the sense of a comprehensive analysis of the fundamental properties of the early actinides as presented in this thesis including thorium, uranium, and neptunium complexes, the synthesis of the corresponding plutonium complexes would be a great opportunity to evaluate the emerging trends also from an experimental perspective. It should be the goal for future studies to investigate the complexation of actinides in different oxidation states with small ligand systems possessing different donor functionalities in the solid state and in solution. Especially the trivalent oxidation state seems promising as it has been shown to be more sensitive towards covalency effects than the harder tetravalent oxidation state. Furthermore, the established reactivity of the synthesized actinide complexes should be further explored to potentially yield new, unprecedented transuranic complexes bearing e.g. An–C or An–P bonds. This bottom-up approach could raise the number of available actinide and especially transuranic complexes which will at the end help to understand the chemical behavior of the actinides in more detail.

In summary, this PhD study has comprehensively investigated the interaction of the early actinides thorium to neptunium with nitrogen donor ligands, significantly expanding the scarce knowledge base in this field. The detailed analysis of structures and bond properties has improved our understanding of covalency in actinide metal-organic compounds, its atomic orbital contributions, and its influence on their structures. The studies also reveal how the use of specialized ligands in a crystal engineering approach can be used to increase or control the reactivity of the actinides in various oxidation states, leading to a number of unprecedented compounds and opening pathways to even more compounds with hitherto unknown properties. The NMR studies on the other hand, have uncovered a distinct lack of fundamental understanding of actinide paramagnetic NMR spectroscopy, the resolution of which will be a challenge for future studies in experimental as well as quantum chemistry. The improved understanding of actinide chemistry generated by this work will finally help to predict their properties in various applications and environmentally relevant scenarios.

5 EXPERIMENTAL

5.1 Analytical methods

The used actinides (thorium, uranium and neptunium) are consisting of radioactive nuclides including long-lived α-emitters (^{232}Th, $T_{1/2} = 1.41 \times 10^{10}$ a; ^{235}U, $T_{1/2} = 7.04 \times 10^{8}$ a; ^{238}U, $T_{1/2} = 4.47 \times 10^{9}$ a; and ^{237}Np, $T_{1/2} = 2.14 \times 10^{6}$ a). Special precautions as well as appropriate equipment and facilities for radiation protection are required for handling these materials, especially ^{237}Np. All the experiments were carried out in a controlled laboratory at the Institute of Resource Ecology, Helmholtz-Zentrum Dresden-Rossendorf.

5.1.1 Single-crystal XRD

Crystals of all compounds were analyzed on a Bruker D8 Venture single-crystal X-ray diffractometer with micro-focused Mo Kα radiation ($\lambda = 0.71073$ Å) and a PHOTON 100 CMOS detector. All data were collected at 100 K. Single crystals appropriate for the measurement were selected on an optical microscope equipped with a polarization filter, and mounted on a MicroMount^{TM} supplied by MiTeGen, USA, with mineral oil. Generic φ- and ω-scans were performed to collect several sets of narrow data frames. Data treatment was performed with the Bruker APEX 3 program suite including the Bruker SAINT software package for integration.[265] Empirical absorption correction using the Multi-Scan method (SADABS)[266] was applied to the collected data. The structure was solved and refined with full-matrix least-squares data on F^2 using the Bruker SHELXTL[183] software package and the program ShelXle.[267] All non-hydrogen atoms were refined anisotropically. Hydrogen atoms of the phenyl rings were placed at calculated positions and allowed to ride on their parent atoms. The FLACK parameter (x) of chiral compounds with (*S*)-PEBA ligand exceeds 3σ for compounds **7-11**, **16**, **18**, **20, 21, 26, 29** but is close to 0 (<0.075) and was hence not refined as an inversion twin. Only for complex **23** with FLACK (x) = 0.11(2) a two component twin refinement was performed. The solvent molecule in compound **17** could not be refined properly, hence the *Squeeze* algorithm[268] was used indicating one molecule of toluene per formula unit by electron count. The crystals of the neptunium amidinate **19** have all shown signs of non-merohedral twinning. Thus, the crystal used for the structure determination has been integrated as a two component twin. The absorption correction was performed using TWINABS.[269] The structure was solved using the HKLF4 file and finally refined against the HKLF5 file. However, despite the twin refinement the FLACK x parameter is too high (0.37(9)) so that an isomerization of the complex molecules could not been ruled out.

5.1.2 Powder XRD

The purity of the obtained compounds was confirmed by PXRD. The data were collected at ambient temperature on a Rigaku MiniFlex 600 equipped with Cu Kα radiation ($\lambda = 1.54184$ Å) and a D/Tex Ultra Si strip detector in the Bragg−Brentano geometry (θ−2θ mode).

5.1.3 NMR Spectroscopy

NMR spectra were recorded on a Varian Inova 400 spectrometer with a ^{1}H frequency of 399.89 MHz, a ^{13}C frequency of 100.56 MHz, a ^{15}N frequency of 40.55 MHz, and a ^{19}F frequency of 376.18 MHz. All spectra were recorded on a Varian AutoX ID probe head with z gradient. Deuterated solvents were purchased at Deutero GmbH and dried over potassium mirror prior to use.

^{1}H, ^{13}C and ^{19}F NMR spectra were recorded directly, ^{15}N signals for diamagnetic complexes were recorded using ^{1}H-^{15}N-HMBC spectra without ^{15}N enrichment. Signals of ^{1}H and ^{13}C were correlated for all complexes using two-dimensional ^{1}H-^{13}C-HSQC, ^{1}H-^{13}C-HMBC and ^{1}H-^{1}H-COSY spectra. This is exemplified for [ThCl((S)-PEBA)₃] (**9**) in Section 8.2.2.3 in the Appendix. Two-dimensional spectra for all other complexes are not shown in this thesis due to space limitations.

5.1.4 IR Spectroscopy

IR spectra were measured on an Agilent Cary 630 FT-IR spectrometer equipped with a single-reflection attenuated total reflection (ATR) accessory made of diamond. The measurements were performed in an inert glove box with N_2 atmosphere. The spectra were recorded between 4000 and 650 cm^{-1} with a resolution of 1 cm^{-1}.

5.1.5 Elemental analysis

Elemental analysis for H, C, and N was performed on a vario MICRO cube (Elementar) with a helium gas flow. No elemental analysis was performed for neptunium complexes **5**, **11**, **19**, **22**, **25**, **27**, **37**, and **38** due to radiological safety issues.

5.1.6 Quantum chemical calculations

The quantum chemical calculations in this work have been kindly performed by Roger Kloditz and Dr. Michael Patzschke.

Quantum chemical calculations were performed with the Turbomole suite, version 7.1,[270] for the structure optimizations and the Orca package, version 4.1.2,[271] in combination with the AIMAll package, version 17.11.14,[272] for the QTAIM[211] analysis.

The SC-XRD structures of [AnCl((*S*)-PEBA)₃] (An = Ce, Th, U, Np) were used as starting points for the structure optimization of these complexes. The protactinium complexes were optimized using the respective uranium structures as starting point. For the plutonium complexes the corresponding neptunium structures have been used. The trivalent *f* element complexes [M((*S*)-PEBA)₃] (M = Sm, Ce, U) have been optimized using the SC-XRD structures as starting point. The isostructural neptunium complex has been geometry optimized using the uranium complex as starting structure. The calculations were performed using DFT with the PBE exchange-correlation functional[273] and the def2-TZVPP basis sets[274] for the H, C, N, and Cl atoms, respectively. For Sm, Ce, Th, Pa, U, Np, and Pu the def-TZVPP basis sets[275] were used. The 28 (for Sm, Ce)[276] or 60 (for Th, Pa, U, Np, Pu)[277-278] inner core electrons were implicitly incorporated by a scalar-relativistic effective core potential and only the valence electrons are treated. Further speed-up could be obtained by using the RI-J approximation.[279] Since it is necessary to incorporate the influence of the chemical vicinity of the complexes to obtain realistic bond lengths, the conductor-like screening model (COSMO)[280] as implemented in Turbomole was used. To simulate the crystal-packing in the solid phase, the dielectric constant was set to infinity. Other parameters like the element-specific radii of the cavities were not altered. Furthermore, it is to be expected that the intramolecular dispersion interactions of the ligands heavily affect the molecular structure. Consequently, dispersion was included by using the empirical approximation (version 3) developed by GRIMME.[281] By using the harmonic approximation it was tried to confirm the optimized structures to minimize the molecular potential hyper-surface, but this did not succeed for all complexes even after several attempts (see further details in Section 8.6 in Appendix).

The optimized structures were then used to perform the QTAIM analysis. For this purpose, the Orca package was used to perform higher level single-point DFT calculations. The PBE0 exchange-correlation functional[282] was used in combination with the DKH-def2-TZVPP basis sets[283] for H, C, N, and Cl, respectively. The all-electron SARC-DKH-TZVPP basis sets[284-285] were used for Sm, Ce, Th, Pa, U, Np, and Pu. To include scalar-relativistic effects the DOUGLAS-KROLL-HESS (DKH) approach was used.[286] For considerable speed-up the RIJCOSX approximation[287] in conjunction with the automatic generation of respective auxiliary basis sets (AUTOAUX)[288] was used. Tight SCF convergence criteria were imposed to produce a high-quality wave function.

The QTAIM analysis was performed using the AIMAll professional package.[272] In order to correctly recover the high electron density oscillations at the metal positions, a *very fine* integration mesh was used.

The magnetic susceptibility tensors for [AnX((*S*)-PEBA)₃] (An = U, Np; X = F, Cl) have been calculated using the Orca package, version 4.2.0.[271] CAS calculations with the *f* orbitals of the actinide as the active space were performed. For uranium these two electrons in seven orbitals

lead to 21 triplet and 28 singlet states. These states were then spin-orbit coupled and the susceptibility tensor was calculated. For Np a similar approach was used with three electrons in seven orbitals resulting in 35 quartets and 112 doublets. Scalar relativistic effects were included by the use of the DKH method.[286] For the actinides the SARC-def2-TZVPP basis sets were used,[284-285] all other elements were described by the DKH-def2-SVP basis sets.[289] The pseudocontact shift has been calculated using the *spinach* library, version 1.4.5157, in Matlab.[290]

5.2 Chemicals

The transition metal chlorides $TiCl_4$, $ZrCl_4$, and $HfCl_4$ as well as $LaN(SiMe_3)_2$ were used as purchased (Sigma Aldrich). $CeCl_3 \cdot 2\,thf$ (thf = tetrahydrofuran) was prepared by evaporation of a saturated solution of anhydrous $CeCl_3$ (Sigma Aldrich) in thf. $[NEt_4][CeCl_6]$ was prepared according to a modified literature procedure.[291] All actinide starting materials $[ThCl_4(dme)_2]$,[76] UO_2Cl_2,[292] UCl_4,[77] UI_3,[293] $NpCl_4$,[294] and $[NpCl_4(dme)_2]$[78] were prepared according to literature procedures. The amidine ligands (*S*)-HPEBA[141] and H*i*Pr$_2$BA were prepared by Sebastian Kaufmann (Institute of Inorganic Chemistry, Karlsruhe Institute of Technology) according to literature procedures. The respective lithium salts (*S*)-LiPEBA and Li*i*Pr$_2$BA were synthesized by a modified literature procedure.[145] $PhICl_2$ was prepared from PhI according to a modified literature procedure.[295] $AgPF_6$ and NaN_3 were dried *in vacuo* at 80°C prior to use. KC_8 was also prepared by a literature procedure.[296] All other chemicals were used as received without further purification.

5.3 Procedures

All preparations except those for the hexavalent uranium complexes were performed under the exclusion of oxygen and moisture in nitrogen filled glove boxes or using SCHLENK techniques. All solvents except water and acetone were pre-dried over $CaCl_2$ and distilled from Na/K alloy or potassium hydride dispersion. They were stored over molecular sieve 3 Å prior to use.

5.3.1 Synthesis of tetravalent metal amidinates

The tetravalent metal amidinate complexes were prepared using an *in situ* salt metathesis approach. The appropriate starting materials were dissolved in thf and reacted with the protonated ligands H*i*Pr$_2$BA or (*S*)-HPEBA and LiHMDS as a base. The combined solutions were stirred for 16 h at room temperature. The solvent was subsequently removed *in vacuo* and the residue was extracted into toluene. The solution was decanted after centrifugation and the solvent was removed *in vacuo* yielding the tetravalent actinide complexes in good yield after washing with *n*-pentane.

[HfCl₂(iPr₂BA)₂] (**1**) A 32.5 mg (0.101 mmol, 1 eq) HfCl$_4$ was dissolved in 1 mL thf and a solution of 62.9 mg (0.308 mmol, 3.1 eq) H*i*Pr$_2$BA and 56.1 mg (0.335 mmol, 3.32 eq) LiHMDS in 1 mL thf was slowly added resulting in a color change to pale yellow. The solution was stirred for 16 h and the solvent subsequently removed *in vacuo*. The yellow residue was extracted into 1 mL toluene and separated from insoluble substances by centrifugation. The solvent was slowly evaporated and the crystalline residue was washed with *n*-pentane and dried to yield 17.0 mg (0.026 mmol, 26 %) of [HfCl$_2$(*i*Pr$_2$BA)$_2$] (**1**). ^{1}H NMR: (400 MHz, toluene-d$_8$, 298 K) δ[ppm]: 7.07 (br s, 5H, PhH^{NCN}), 3.45 (hept, 2H, $^3J_{H-H}$ = 6.4 Hz, NC*H*), 1.34 (d, 12H, $^3J_{H-H}$ = 6.5 Hz, Me). ^{13}C{^{1}H} NMR: (100.58 MHz, toluene-d$_8$, 298 K): 179.2 (N*C*N), 131.6 (*i*-Ph^{NCN}), 129.4 (*p*-Ph^{NCN}), 129.0 (*m*-Ph^{NCN}), 126.2 (*o*-Ph^{NCN}), 49.7 (N*C*H), 24.9 (Me). ^{15}N{^{1}H} NMR: (40.55 MHz, toluene-d$_8$, 298 K): 200.9 (*NCN*). IR (ATR): ν [cm^{-1}] 702 (s), 730 (m), 739 (m), 777 (s), 1005 (m), 1017 (m), 1075 (m), 1139 (m), 1171 (m), 1231 (m), 1344 (s), 1383 (m), 1415 (s), 1453 (m), 1472 (m), 1508 (w), 2964 (w). EA: (C$_{26}$H$_{38}$N$_4$Cl$_2$Hf, 655.99 g/mol) Calc.: C, 47.6; H, 5.8; N, 8.5; Found: C, 48.0; H, 5.9 N, 8.6.

[ZrCl(iPr₂BA)₃]·0.5C₇H₈ (**2**) A 23.9 mg (0.103 mmol, 1 eq) ZrCl$_4$ was dissolved in 1 mL thf. A solution of 62.1 mg (0.304 mmol, 3.0 eq) H*i*Pr$_2$BA and 55.5 mg (0.332 mmol, 3.2 eq) LiHMDS in 1 mL thf was slowly added resulting in a color change to yellow. The solution was stirred for 16 h and the solvent subsequently removed *in vacuo*. The residue was extracted into 1 mL toluene and separated from insoluble substances by centrifugation. The solvent was slowly evaporated yielding [ZrCl(*i*Pr$_2$BA)$_3$]·0.5C$_7$H$_8$ (**2**) as crystalline material. After washing with *n*-pentane and drying 41.7 mg (0.053 mmol, 53 %) were yielded. Single crystals could be grown by slow evaporation of a saturated solution in toluene. ^{1}H NMR: (400 MHz, toluene-d$_8$, 243 K) δ[ppm]: 7.41 (d, 1H, $^3J_{H-H}$ = 7.2 Hz, *o*-PhH^{NCN}), 7.25 (d, 1H, $^3J_{H-H}$ = 7.4 Hz, *o*-PhH^{NCN}), 7.06 (m, 3H, *m*-PhH^{NCN} + *p*-PhH^{NCN}), 3.81 (br s, 1H, NC*H*), 3.47 (br s, 1H, NC*H*), 1.81 (s, 3H, Me), 1.50 (s, 3H, Me), 1.24 (s, 6H, Me). ^{13}C{^{1}H} NMR: (100.58 MHz, toluene-d$_8$, 243 K): 176.6 (N*C*N), 134.2 (*i*-Ph^{NCN}), 128.3 (*m*-Ph^{NCN}), 128.3 (*p*-Ph^{NCN}), 127.7 (*o*-Ph^{NCN}), 126.2 (*o*-Ph^{NCN}), 49.3 (N*C*H), 25.7 (Me), 24.2 (Me), 23.9 (Me), 23.6 (Me). IR (ATR): ν [cm^{-1}] 703 (vs), 729 (s), 740 (m), 779 (s), 841 (m), 864 (m), 888 (m), 938 (m), 1015 (s), 1075 (m), 1141 (s), 1171 (s), 1215 (s), 1338 (vs), 1376 (s), 1416 (s), 1439 (s), 1450 (s), 1467 (s), 2964 (w). EA: (C$_{42.5}$H$_{61}$N$_6$ClZr, 782.64 g/mol) Calc.: C, 64.9; H, 7.7; N, 10.7; Found: C, 64.6; H, 8.3; N, 11.3.

[ThCl(iPr₂BA)₃]·0.5C₇H₈ (**3**) A 56.3 mg (0.102 mmol, 1 eq) [ThCl$_4$(dme)$_2$] was suspended in 1 mL thf. A solution of 58.3 mg (0.285 mmol, 3.0 eq) H*i*Pr$_2$BA and 57.0 mg (0.341 mmol, 3.3 eq) LiHMDS in 1 mL thf was slowly added resulting in a color change from orange to dark red. The solution was stirred for 16 h and the solvent subsequently removed *in vacuo*. The yellow residue was extracted into 3 mL toluene and separated from insoluble substances by centrifugation. The toluene solution was slowly evaporated to yield [ThCl(*i*Pr$_2$BA)$_3$]·0.5C$_7$H$_8$ (**3**) as colorless blocks. After washing with *n*-pentane 48.0 mg (0.052 mmol, 52 %) were yielded. ^{1}H NMR: (400 MHz, toluene-d$_8$, 298 K) δ[ppm]: 7.25 (d, 2H, $^3J_{H-H}$ = 6.8 Hz, *o*-PhH^{NCN}), 7.14 (t, 2H, $^3J_{H-H}$ = 7.4 Hz, *m*-PhH^{NCN}), 7.07 (t, 1H, $^3J_{H-H}$ = 7.4 Hz, *p*-PhH^{NCN}),

3.62 (hept, 2H, $^3J_{\text{H-H}}$ = 6.5 Hz, NCH), 1.43 (d, 12H, $^3J_{\text{H-H}}$ = 6.5 Hz, Me). ^{13}C{^{1}H} NMR: (100.58 MHz, toluene-d$_8$, 298 K): 176.1 (NCN), 135.4 (i-Ph$^{\text{NCN}}$), 128.5 (m-Ph$^{\text{NCN}}$), 128.3 (p-Ph$^{\text{NCN}}$), 126.8 (o-Ph$^{\text{NCN}}$), 49.8 (NCH), 25.2 (Me). IR (ATR): ν [cm^{-1}] 707 (s), 729 (m), 738 (m), 781 (s), 1010 (s), 1077 (m), 1125 (m), 1138 (m), 1170 (m), 1205 (m), 1334 (s), 1376 (m), 1423 (s), 1445 (m), 1459 (m), 2959 (w). EA: (C$_{42.5}$H$_{61}$N$_6$ClTh, 923.46 g/mol) Calc.: C, 55.2; H, 6.6; N, 9.1; Found: C, 56.0; H, 6.7; N, 9.2.

[UCl(iPr$_2$BA)$_3$]·0.5C$_7$H$_8$ (**4**) A 39.5 mg (0.103 mmol, 1 eq) UCl$_4$ was dissolved in 1 mL thf yielding a greyish green solution. Upon adding a solution of 64.1 mg (0.314 mmol, 3.1 eq) H*i*Pr$_2$BA and 56.5 mg (0.338 mmol, 3.3eq) LiHMDS in 1 mL thf the color changes to a yellowish green. The solution was stirred for 16 h and the solvent subsequently removed *in vacuo*. The dark brown residue was extracted into 5 mL toluene to yield a dark brown solution. The solution was slowly evaporated after centrifugation yielding green block shaped crystals of [UCl(*i*Pr$_2$BA)$_3$]·0.5C$_7$H$_8$ (**4**). After washing with *n*-pentane 62.7 mg (0.067 mmol, 65 %) were yielded. ^{1}H NMR: (400 MHz, toluene-d$_8$, 298 K) δ[ppm]: 21.04 (br s, 2H, NCH), 9.11 (d, 2H, $^3J_{\text{H-H}}$ = 7.3 Hz, o-PhH$^{\text{NCN}}$), 7.62 (t, 2H, $^3J_{\text{H-H}}$ = 7.3 Hz, m-PhH$^{\text{NCN}}$), 7.57 (t, 1H, $^3J_{\text{H-H}}$ = 7.3 Hz, p-PhH$^{\text{NCN}}$), 0.44 (br s, 12H, Me). ^{13}C{^{1}H} NMR: (100.58 MHz, toluene-d$_8$, 298 K): 129.0 (p-Ph$^{\text{NCN}}$), 125.6 (m-Ph$^{\text{NCN}}$), 113.6 (o-Ph$^{\text{NCN}}$), 106.4 (i-Ph$^{\text{NCN}}$), 28.7 (Me), the signals of NCN and NCH are not visible. IR (ATR): ν [cm^{-1}] 707 (s), 728 (m), 736 (m), 780 (m), 917 (w), 1009 (m), 1077 (w), 1125 (m), 1137 (m), 1171 (m), 1203 (m), 1335 (m), 1376 (m), 1419 (m), 1445 (m), 1459 (w), 2960 (w). EA: (C$_{42.5}$H$_{61}$N$_6$ClU, 929.45 g/mol) Calc.: C, 54.9; H, 6.6; N, 9.0; Found: C, 54.3; H, 6.6; N, 9.0.

[NpCl(iPr$_2$BA)$_3$]·0.5C$_7$H$_8$ (**5**) A 6.0 mg (0.011 mmol, 1 eq) [NpCl$_4$(dme)$_2$] was dissolved in 1 mL thf to yield a pale orange solution. A solution of 9.4 mg (0.046 mmol, 4.2 eq) H*i*Pr$_2$BA and 8.0 mg (0.05 mmol, 4.5eq) LiHMDS in 1 mL thf was slowly added resulting in a color change to dark red. The solution was stirred for 16 h and the solvent subsequently removed by evaporation. The dark red residue was extracted into toluene and separated from insoluble substances by centrifugation. Slow evaporation yielded a dark red amorphous solid which was triturated with 1 mL *n*-pentane to yield 10.6 mg (0.011 mmol, 100 %) of [NpCl(*i*Pr$_2$BA)$_3$]·0.5C$_7$H$_8$ (**5**). Single crystals could be grown by diffusion of *n*-pentane into a saturated solution of **5** in toluene. ^{1}H NMR: (400 MHz, toluene-d$_8$, 363 K) δ[ppm]: 26.53 (br s, 2H, NCH), 11.58 (s, 2H, o-PhH$^{\text{NCN}}$), 8.92 (m, 2H, m-PhH$^{\text{NCN}}$), 8.48 (t, 1H, $^3J_{\text{H-H}}$ = 7.5 Hz, p-PhH$^{\text{NCN}}$), -0.79 (br s, 12H, Me). ^{13}C{^{1}H} NMR: (100.58 MHz, toluene-d$_8$, 363 K): 131.3 (p-Ph$^{\text{NCN}}$), 127.4 (m-Ph$^{\text{NCN}}$), 126.1 (o-Ph$^{\text{NCN}}$), 78.1 (i-Ph$^{\text{NCN}}$), 25.3 (Me), the signals of NCN and NCH are not visible. IR (ATR): ν [cm^{-1}] 706 (s), 728 (m), 737 (m), 780 (m), 1007 (m), 1076 (w), 1125 (m), 1138 (m), 1171 (m), 1204 (m), 1336 (s), 1376 (m), 1422 (s), 1445 (m), 1459 (w), 2960 (w). (C$_{42.5}$H$_{61}$N$_6$ClNp, 928.48 g/mol)

[ZrCl$_2$((S)-PEBA)$_2$] (**6**) A solution containing 99.2 mg (0.302 mmol, 3 eq.) (*S*)-HPEBA and 59.5 mg (0.355 mmol, 3.6 eq.) LiHMDS in 1 mL thf was slowly added to a solution of 28.3 mg (0.121 mmol, 1.2 eq) ZrCl$_4$ in 1 mL thf. The yellow solution was stirred for 16 h and all volatiles

were subsequently removed *in vacuo*. The residue was extracted into 2 mL of toluene, centrifuged from insoluble substances and slowly evaporated. After washing with *n*-pentane 35.5 mg (0.043 mmol, 43 %) [ZrCl$_2$((*S*)-PEBA)$_2$] (**6**) was obtained as crystalline solid. ^{1}H NMR: (400 MHz, toluene-d$_8$, 298 K) δ[ppm]: 7.26 (d, 4H, $^3J_{\text{H-H}}$ = 7.2 Hz, *o*-PhH), 7.08 (t, 4H, $^3J_{\text{H-H}}$ = 7.5 Hz, *m*-PhH), 7.02 (m, 2H, *p*-PhH), 6.96 (t, 1H, $^3J_{\text{H-H}}$ = 7.4 Hz, *p*-PhH$^{\text{NCN}}$), 6.89 (t, 2H, $^3J_{\text{H-H}}$ = 7.3 Hz, *m*-PhH$^{\text{NCN}}$), 6.63 (d, 2H, $^3J_{\text{H-H}}$ = 7.1 Hz, *o*-PhH$^{\text{NCN}}$), 4.26 (q, 2H, $^3J_{\text{H-H}}$ = 7.0 Hz, NC*H*), 1.71 (d, 6H, $^3J_{\text{H-H}}$ = 7.0 Hz, Me). ^{13}C{^{1}H} NMR: (100.58 MHz, toluene-d$_8$, 298 K): 183.4 (N*C*N), 146.3 (*i*-Ph), 131.4 (*i*-Ph$^{\text{NCN}}$), 129.3 (*p*-Ph$^{\text{NCN}}$), 128.4 (*m*-Ph), 128.2 (*m*-Ph$^{\text{NCN}}$), 127.6 (*o*-Ph), 126.8 (*p*-Ph), 126.7 (*o*-Ph$^{\text{NCN}}$), 59.2 (N*C*H), 24.7 (Me). ^{15}N{^{1}H} NMR: (40.55 MHz, toluene-d$_8$, 298 K): 205.8 (*N*C*N*). IR (ATR): ν [cm^{-1}] 698 (vs), 726 (s), 736 (s), 754 (s), 779 (m), 803 (m), 847 (m), 925 (m) 966 (m), 1012 (m), 1023 (s), 1056 (m), 1077 (m), 1086 (s), 1133 (m), 1181 (s), 1205 (s), 1323 (s), 1344 (s), 1373 (s), 1446 (s), 1465 (s), 1602 (m), 2974 (w). EA: (C$_{46}$H$_{46}$N$_4$Cl$_2$Zr, 816.99 g/mol) Calc.: C, 67.6; H, 5.6; N, 6.9; Found: C, 66.6; H, 5.7; N, 7.1.

[HfCl$_2$((S)-PEBA)$_2$] (**7**) A solution containing 98.4 mg (0.299 mmol, 2.9 eq.) (*S*)-HPEBA and 53.6 mg (0.320 mmol, 3.1 eq.) LiHMDS in 1 mL thf was slowly added to a solution of 33.1 mg (0.103 mmol, 1.0 eq) HfCl$_4$ in 1 mL thf. The yellow solution was stirred for 16 h and all volatiles were subsequently removed *in vacuo*. The residue was extracted into 1 mL of toluene, centrifuged from insoluble substances and slowly evaporated. After washing with *n*-pentane 44.3 mg (0.049 mmol, 49 %) [HfCl$_2$((*S*)-PEBA)$_2$] (**7**) were obtained as crystalline solid. ^{1}H NMR: (400 MHz, toluene-d$_8$, 298 K) δ[ppm]: 7.28 (d, 4H, $^3J_{\text{H-H}}$ = 7.52 Hz, *o*-PhH), 7.08 (t, 4H, $^3J_{\text{H-H}}$ = 7.6 Hz, *m*-PhH), 7.01 (m, 2H, *p*-PhH), 6.96 (m, 1H, *p*-PhH$^{\text{NCN}}$), 6.89 (t, 2H, $^3J_{\text{H-H}}$ = 7.5 Hz, *m*-PhH$^{\text{NCN}}$), 6.68 (d, 2H, $^3J_{\text{H-H}}$ = 6.9 Hz, *o*-PhH$^{\text{NCN}}$), 4.39 (q, 2H, $^3J_{\text{H-H}}$ = 6.9 Hz, NC*H*), 1.68 (d, 6H, $^3J_{\text{H-H}}$ = 6.9 Hz, Me). ^{13}C{^{1}H} NMR: (100.58 MHz, toluene-d$_8$, 298 K): 182.7 (N*C*N), 146.3 (*i*-Ph), 131.7 (*i*-Ph$^{\text{NCN}}$), 129.4 (*p*-Ph$^{\text{NCN}}$), 128.4 (*m*-Ph), 128.3 (*m*-Ph$^{\text{NCN}}$), 127.7 (*o*-Ph), 126.9 (*o*-Ph$^{\text{NCN}}$), 126.8 (*p*-Ph), 59.0 (N*C*H), 24.7 (Me). ^{15}N NMR: (40.55 MHz, toluene-d$_8$, 298 K): 200.2 (*N*C*N*). IR (ATR): ν [cm^{-1}] 695 (s), 738 (m), 756 (m), 770 (m), 915 (m), 925 (m) 967 (m), 1010 (m), 1022 (m), 1068 (m), 1077 (m), 1086 (m), 1134 (m), 1186 (m), 1205 (m), 1326 (m), 1350 (m), 1374 (m), 1442 (m), 1465 (m), 1602 (m), 2974 (w). EA: (C$_{46}$H$_{46}$N$_4$Cl$_2$Hf, 904.26 g/mol) Calc.: C, 61.0; H, 5.1; N, 6.2; Found: C, 60.7; H, 5.2; N, 6.7.

[UCl$_2$((S)-PEBA)$_2$] (**8**) A 38.5 mg (0.101 mmol, 1.0 eq.) UCl$_4$ was dissolved in 1 mL thf and a solution of 65.6 mg (0.199 mmol, 2.0 eq.) (*S*)-HPEBA and 36.6 mg (0.218 mmol, 2.2 eq.) LiHMDS in 1 mL thf was slowly added resulting in a color change from blueish green to yellowish green. The solution was stirred for 16 h and all volatiles were subsequently removed *in vacuo*. The residue was extracted into 1 mL of toluene, centrifuged from insoluble substances and slowly evaporated. After washing with n-pentane 80.1 mg (0.083 mmol, 82 %) [UCl$_2$((*S*)-PEBA)$_2$] (**8**) were obtained. Single crystals could be grown by slow evaporation of a saturated solution of **8** in toluene. ^{1}H NMR: (400 MHz, toluene-d$_8$, 298 K) δ[ppm]: 17.01 (s,

2H, NCH), 6.85 (t, 2H, $^3J_{\text{H-H}}$ = 7.5 Hz, m-PhH$^{\text{NCN}}$), 6.72 (t, 1H, $^3J_{\text{H-H}}$ = 7.4 Hz, p-PhH$^{\text{NCN}}$), 6.54 (d, 2H, $^3J_{\text{H-H}}$ = 7.4 Hz, o-PhH$^{\text{NCN}}$), 6.07 (t, 2H, $^3J_{\text{H-H}}$ = 7.4 Hz, p-PhH), 5.83 (t, 4H, $^3J_{\text{H-H}}$ = 7.4 Hz, m-PhH), 2.18 (br s, 4H, o-PhH), 0.63 (br s, 6H, Me). ^{13}C{^{1}H} NMR: (100.58 MHz, toluene-d$_8$, 298 K): 217.5 (NCN), 141.2 (i-Ph), 129.1 (p-Ph$^{\text{NCN}}$), 127.2 (m-Ph$^{\text{NCN}}$), 126.5 (m-Ph), 125.2 (p-Ph), 123.0 (o-Ph$^{\text{NCN}}$), 119.5 (i-Ph$^{\text{NCN}}$), 118.3 (o-Ph), 38.0 (NCH), 20.9 (Me). IR (ATR): ν [cm^{-1}] 694 (s), 739 (m), 758 (m), 777 (m), 962 (m), 1008 (m), 1020 (m), 1068 (m), 1081 (m), 1178 (m), 1209 (m), 1275 (m), 1308 (m), 1324 (m), 1347 (m), 1373 (m), 1401 (m), 1443 (m), 1465 (m), 1602 (m), 2969 (w). EA: (C$_{46}$H$_{46}$N$_4$Cl$_2$U, 963.60 g/mol) Calc.: C, 57.3; H, 4.8; N, 5.8; Found: C, 57.5; H, 4.9; N, 5.7.

[ThCl((S)-PEBA)₃]·C₇H₈ (**9**) A 110.3 mg (0.199 mmol, 1 eq.) [ThCl$_4$(dme)$_2$] was dissolved in 2 mL thf. A solution containing 196.9 mg (0.599 mmol, 3 eq.) (*S*)-HPEBA and 113.2 mg LiHMDS (0.677 mmol, 3.4 eq) in 2 mL thf was slowly added. The resulting yellow solution was stirred for 16 h and all volatiles were removed *in vacuo* yielding an off-white residue. The residue was extracted into 5 mL toluene. The supernatant was decanted after centrifugation and the solvent was evaporated *in vacuo* to yield a pale yellow powder which was washed with 5 mL pentane and subsequently dried. [ThCl((*S*)-PEBA)$_3$]·C$_7$H$_8$ (**9**) was obtained as a pale yellow microcrystalline powder (122.6 mg, 0.091 mmol, 46 %). Crystals of **9** could be grown by slow evaporation of a saturated solution of **9** in toluene. ^{1}H NMR: (400 MHz, toluene-d$_8$, 298 K) δ[ppm]: 7.35 (m, 4H, o-PhH), 7.00 (m, 4H, m-PhH), 6.94 (t, 2H, $^3J_{\text{H-H}}$ = 7.2 Hz, p-PhH), 6.81 (t, 1H, $^3J_{\text{H-H}}$ = 7.5 Hz, p-PhH$^{\text{NCN}}$), 6.71 (t, 2H, $^3J_{\text{H-H}}$ = 7.4 Hz, m-PhH$^{\text{NCN}}$), 6.45 (d, 2H, $^3J_{\text{H-H}}$ = 7.2 Hz, o-PhH$^{\text{NCN}}$), 4.58 (q, 2H, $^3J_{\text{H-H}}$ = 6.6 Hz, NCH), 2.05 (s, 6H, Me). ^{13}C{^{1}H} NMR: (100.58 MHz, toluene-d$_8$, 298 K): 180.3 (NCN), 149.1 (i-Ph), 135.7 (i-Ph$^{\text{NCN}}$), 128.1 (m-Ph), 127.6 (m-Ph$^{\text{NCN}}$), 127.5 (p-Ph$^{\text{NCN}}$), 127.5 (o-Ph), 126.3 (o-Ph$^{\text{NCN}}$), 126.2 (p-Ph), 60.4 (NCH), 26.0 (Me). IR (ATR): ν [cm^{-1}] 663 (m), 695 (vs), 731 (m), 742 (m), 759 (s), 778 (m), 785 (w), 895 (vw), 910 (w), 916 (w), 930 (w), 935 (w), 962 (w), 966 (w), 999 (w), 1010 (w), 1020 (w), 1029 (m), 1038 (vw), 1080 (m), 1090 (m), 1106 (vw), 1131 (m), 1155 (vw), 1176 (w), 1210 (m), 1276 (m), 1283 (w), 1305 (m), 1327 (m), 1344 (s), 1367 (m), 1373 (w), 1412 (s), 1419 (s), 1442 (m), 1492 (w), 1637 (vw), 2868 (vw), 2957 (vw). EA: (C$_{76}$H$_{77}$ClN$_6$Th, M = 1341.92 g/mol) Calc.: C, 68.0; H, 5.7; N, 6.3; Found: C, 68.3; H, 6.0; N, 6.3.

[UCl((S)-PEBA)₃]·C₇H₈ (**10**) A 76.3 mg (0.201 mmol, 1 eq.) UCl$_4$ was dissolved in 2 mL thf. A solution containing 198.1 mg (0.603 mmol, 3 eq.) (*S*)-HPEBA and 120.0 mg LiHMDS (0.717 mmol, 3.6 eq.) in 2 mL thf was slowly added resulting in a color change from light green to greenish brown. The solution was stirred for 16 h and all volatiles were subsequently removed *in vacuo* yielding a brownish residue. The residue was extracted into 5 mL toluene and centrifuged. The supernatant was decanted and the solvent was removed *in vacuo* to yield a brown residue which was washed with 5 mL *n*-pentane. This resulted in a green microcrystalline powder of [UCl((*S*)-PEBA)$_3$]·C$_7$H$_8$ (**10**) (144.9 mg, 0.107 mmol, 54 %). Single crystals of **10** were grown through slow diffusion of *n*-pentane into a saturated solution of **10** in toluene. ^{1}H-NMR: (400 MHz, toluene-d$_8$, 243 K) δ[ppm]: 36.51 (s, 1H, NCH), 21.08

(s, 1H, NC*H*), 13.87 (s, 1H, *o*-PhH^NCN^), 9.68 (s, 1H, *o*-PhH^NCN^), 8.53 (s, 1H, *m*-PhH^NCN^), 8.43 (s, 1H, *m*-PhH^NCN^), 8.31 (s, 1H, *p*-PhH^NCN^), 6.79 (s, 1H, *p*-PhH), 6.17 (s, 2H, *m*-PhH), 5.40 (br s, 3H, Me), 4.61 (s, 1H, *p*-PhH), 3.50 (s, 2H, *m*-PhH), 3.35 (s, 2H, *o*-PhH), 1.97 (s, 3H, Me), -5.22 (s, 2H, *o*-PhH). ^{13}C{^{1}H} NMR: (100.58 MHz, toluene-d_8, 243 K): 163.6 (*i*-Ph), 161.8 (*i*-Ph), 131.0 (*p*-Ph^NCN^), 129.2 (*m*-Ph^NCN^), 128.2 (*m*-Ph), 126.8 (*o*-Ph), 126.0 (*p*-Ph), 124.6 (*m*-Ph), 122.8 (*p*-Ph), 122.6 (*m*-Ph^NCN^), 122.5 (*o*-Ph^NCN^), 119.5 (*o*-Ph), 115.5 (*i*-Ph^NCN^), 106.6 (*o*-Ph^NCN^), 60.1 (N*C*H), 42.0 (N*C*H), 36.1 (Me), 24.8 (Me), the signal of N*C*N could not be observed. IR (ATR): ν [cm^{-1}] 663 (m), 696 (vs), 732 (m), 741 (m), 759 (s), 778 (m), 912 (w), 967 (w), 999 (w), 1010 (m), 1020 (m), 1029 (m), 1082 (m), 1090 (m), 1106 (w), 1130 (m), 1175 (m), 1209 (m), 1275 (m), 1283 (m), 1305 (m), 1327 (m), 1344 (s), 1367 (m), 1373 (m), 1418 (s), 1443 (m), 1493 (w), 2869 (w), 2958 (w). EA: ($C_{76}H_{77}ClN_6U$, M = 1347.91 g/mol) Calc.: C, 67.7; H, 5.7; N, 6.2; Found: C, 67.8; H, 5.8; N, 6.7.

*[NpCl(*S*)-PEBA)$_3$]· C$_7$H$_8$* (**11**) A 11.1 mg (0.02 mmol, 1 eq.) [NpCl$_4$(dme)$_2$] was dissolved in 1 mL thf. A solution of 19.7 mg (0.06 mmol, 3 eq.) (*S*)-LiPEBA in 1 mL of thf was slowly added resulting in a color change from salmon to dark red. The solution was stirred for 16 h and all volatiles were removed in vacuo yielding a dark red residue. The residue was extracted into 0.5 mL toluene and separated from unsolvable substances by centrifugation. The supernatant was decanted and slowly evaporated yielding single crystals of **11** (18.7 mg, 0.014 mmol, 69 %) suitable for structure determination. ^{1}H NMR: (400 MHz, toluene-d_8, 243 K) δ[ppm]: 50.47 (s, 1H, NC*H*), 24.72 (s, 1H, NC*H*), 17.98 (s, 1H, *o*-PhH^NCN^), 10.62 (s, 1H, *o*-PhH^NCN^), 10.37 (s, 1H, *m*-PhH^NCN^), 9.79 (s, 1H, *m*-PhH^NCN^), 9.37 (s, 1H, *p*-PhH^NCN^), 6.94 (s, 1H, *p*-PhH), 6.06 (s, 2H, *m*-PhH), 5.97 (s, 3H, Me), 3.45 (s, 1H, *p*-PhH), 2.68 (s, 2H, *o*-PhH), 1.77 (s, 2H, *m*-PhH), -0.47 (s, 3H, Me), -10.94 (s, 2H, *o*-PhH). ^{13}C{^{1}H} NMR: (100.58 MHz, toluene-d_8, 243 K): 163.0 (*i*-Ph), 150.3 (*i*-Ph), 133.6 (*o*-Ph^NCN^), 133.6 (*p*-Ph^NCN^), 130.4 (*o*-Ph), 129.1 (*m*-Ph), 128.6 (*m*-Ph^NCN^), 127.1 (*o*-Ph^NCN^), 125.9 (*p*-Ph), 124.1 (*m*-Ph^NCN^), 122.7 (*m*-Ph), 120.9 (*p*-Ph), 117.6 (*o*-Ph), 68.1 (N*C*H), 53.6 (N*C*H), 40.2 (Me), 25.5 (Me), the signals for the N*C*N and *i*-Ph^NCN^ carbons could not be observed. IR (ATR): ν [cm^{-1}] 662 (s), 694 (vs), 731 (s), 741 (s), 759 (s), 778 (m), 911 (m), 915 (m), 966 (m), 999 (m), 1010 (m), 1020 (m), 1028 (m), 1081 (s), 1089 (m), 1105 (m), 1129 (m), 1174 (m), 1208 (m), 1275 (m), 1283 (m), 1306 (s), 1327 (m), 1342 (s), 1367 (m), 1372 (m), 1418 (s), 1443 (s), 1491 (m), 2866 (w), 2958 (w). ($C_{76}H_{77}ClN_6Np$, 1346.94 g/mol).

[TiCl$_2$(iPr$_2$BA)$_2$] (**12**) A 23.0 mg (0.120 mmol, 1 eq) TiCl$_4$ was dissolved in 1 mL toluene. A solution of 70 mg (0.340 mmol, 2.8 eq) Li*i*Pr$_2$BA in 1 mL toluene was slowly added resulting in a color change from orange to dark red. The solution was stirred for 16 h, centrifuged and the solvent subsequently removed *in vacuo*. The dark red residue was washed with *n*-pentane and dried to yield 50.3 mg (0.096 mmol, 79 %) [TiCl$_2$(*i*Pr$_2$BA)$_2$] (**12**). Single crystals could be grown by slow evaporation of a saturated solution in toluene. ^{1}H NMR: (400 MHz, toluene-d_8, 298 K) δ[ppm]: 7.06 (m, 5H, PhH^NCN^), 3.46 (br s, 2H, NC*H*), 1.46 (br s, 12H, Me). ^{13}C{^{1}H} NMR: (100.58 MHz, toluene-d_8, 298 K): 176.7 (N*C*N), 130.5 (*i*-Ph^NCN^), 129.6

(p-Ph^{NCN}), 128.6 (m-Ph^{NCN}), 126.4 (o-Ph^{NCN}) 52.5 (NCH), 24.3 (Me). IR (ATR): ν [cm^{-1}] 702 (s), 724 (w), 738 (m), 776 (m), 936 (w), 1013 (m), 1075 (w), 1135 (m), 1171 (w), 1215 (m), 1341 (m), 1380 (m), 1442 (w), 1475 (w), 1515 (w), 1630 (w) 2961 (w). EA: (C$_{26}$H$_{38}$N$_4$Cl$_2$Ti, 525.38 g/mol) Calc.: C, 59.4; H, 7.2; N, 10.7; Found: C, 59.4; H, 7.3; N, 10.4.

[TiCl$_2$((S)-PEBA)$_2$] (**13**) A 20.3 mg (0.107 mmol, 1 eq) TiCl$_4$ was dissolved in 1 mL toluene. A solution of 74.3 mg (0.224 mmol, 2.1 eq) Li(S)-PEBA in 1 mL toluene was slowly added resulting in a color change from orange to dark red. The solution was stirred for 16 h, centrifuged and the solvent subsequently removed *in vacuo*. The dark red residue was washed with *n*-pentane and dried to yield 41.6 mg (0.054 mmol, 50 %) [TiCl$_2$((S)-PEBA)$_2$] (**13**). Single crystals could be grown by slow evaporation of a saturated solution in toluene. ^{1}H NMR: (400 MHz, toluene-d$_8$, 298 K) δ[ppm]: 7.25 (br s, 4H, o-PhH), 7.01 (m, 4H, m-PhH), 6.98 (m, 2H, p-PhH), 6.91 (t, 1H, $^3J_{H-H}$ = 7.6 Hz, p-PhH^{NCN}), 6.83 (m, 2H, m-PhH^{NCN}), 6.63 (m, 2H, o-PhH^{NCN}), 4.63 (s, 2H, NCH), 1.80 (br s, 6H, Me). ^{13}C{^{1}H} NMR: (100.58 MHz, toluene-d$_8$, 298 K): 180.3 (NCN), 145.8 (i-Ph), 131.1 (i-Ph^{NCN}), 129.3 (p-Ph^{NCN}), 128.3 (m-Ph), 128.2 (o-Ph), 128.2 (m-Ph^{NCN}), 126.9 (p-Ph), 126.9 (o-Ph^{NCN}), 61.5 (NCH), 23.3 (Me). IR (ATR): ν [cm^{-1}] 700 (vs), 723 (m), 737 (s), 754 (m), 770 (m), 779 (m), 803 (m), 966 (w), 1011 (m), 1022 (m), 1029 (m), 1086 (m), 1131 (m), 1181 (m), 1203 (m), 1325 (m), 1344 (m), 1371 (m), 1443 (m), 1450 (m), 1602 (w) 2980 (w). EA: (C$_{46}$H$_{46}$N$_4$Cl$_2$Ti, 773.66 g/mol) Calc.: C, 71.3; H, 5.9; N, 7.2; Found: C, 71.0; H, 5.9; N, 7.0.

[CeCl((S)-PEBA)$_3$]·C$_7$H$_8$ (**16**) A 12.1 mg (0.011 mmol, 1 eq.) [Ce((S)-PEBA)$_3$] (**15**) was dissolved in 0.5 mL toluene. A solution of 1.6 mg (0.006 mmol, 0.5 eq) PhICl$_2$ in 0.2 mL toluene was slowly added resulting in an immediate color change to dark blue. After stirring for 30 min all volatiles were removed *in vacuo* yielding a dark blue residue. This residue was triturated with 0.5 mL pentane to yield a dark blue powder. Slow evaporation of a solution of the powder in 0.5 mL toluene yielded 6.4 mg of dark blue crystalline material **16** (0.005 mmol, 48 %). ^{1}H NMR: (400 MHz, toluene-d$_8$, 298 K) δ[ppm]: 7.39 (m, 4H, o-PhH), 7.02 (m, 4H, m-PhH), 6.94 (m, 2H, p-PhH), 6.79 (t, 1H, $^3J_{H-H}$ = 7.4 Hz, p-PhH^{NCN}), 6.70 (t, 2H, $^3J_{H-H}$ = 7.6 Hz, m-PhH^{NCN}), 6.49 (d, 2H, $^3J_{H-H}$ = 7.6 Hz, o-PhH^{NCN}), 5.37 (m, 2H, NCH), 2.16 (s, 6H, Me). ^{13}C{^{1}H} NMR: (100.58 MHz, toluene-d$_8$, 298 K): 176.1 (NCN), 150.9 (i-Ph), 134.6 (i-Ph^{NCN}), 128.1 (m-Ph), 127.6 (o-Ph), 127.6 (m-Ph^{NCN}), 127.6 (p-Ph^{NCN}), 126.3 (o-Ph^{NCN}), 126.3 (p-Ph), 63.3 (NCH), 26.7 (Me). IR (ATR): ν [cm^{-1}] 659 (m), 695 (vs), 739 (s), 759 (s), 777 (m), 887 (w), 912 (m), 961 (m), 998 (m), 1009 (m), 1018 (m), 1029 (m), 1080 (s), 1106 (m), 1127 (m), 1156 (w), 1206 (m), 1273 (m), 1303 (s), 1311 (s), 1342 (s), 1367 (m), 1391 (s), 1406 (s), 1443 (m), 1492 (m), 1600 (w), 2958 (w). EA: (C$_{76}$H$_{77}$N$_6$ClCe, 1250.00 g/mol) Calc.: C, 73.0; H, 6.2; N, 6.7; Found: C, 72.7; H, 6.4; N, 7.2.

[ThF(S)-PEBA)$_3$]·C$_7$H$_8$ (**17**) A solution of 5.3 mg (0.021 mmol, 1.2 eq.) AgPF$_6$ in 0.5 mL was slowly added to a solution of 23.3 mg **9** (0.017 mmol, 1 eq.) in 1 mL toluene. The formation of a colorless precipitate is observed and the solution is stirred for 16 h overnight at room temperature. The suspension was centrifuged and the solution was transferred in a Schlenk tube

to remove the solvent *in vacuo* yielding a colorless oily residue which was extracted into 2 mL *n*-pentane. Evaporation of the solution yielded [ThF(*S*)-PEBA)$_3$]·C$_7$H$_8$ (**17**) as colorless block-shaped crystals (20.9 mg, 0.016 mmol, 93 %). ^{1}H NMR: (400 MHz, toluene-d$_8$, 243K) δ[ppm]: 7.47 (d, 2H, $^3J_{H-H}$ = 7.5 Hz, *o*-PhH), 7.21 (d, 2H, $^3J_{H-H}$ = 7.5 Hz, *o*-PhH), 7.02 (m, 4H, *m*-PhH), 6.95 (m, 2H, *p*-PhH), 6.84 (t, 1H, $^3J_{H-H}$ = 7.5 Hz, *p*-PhH^{NCN}), 6.78 (t, 1H, $^3J_{H-H}$ = 7.5 Hz, *m*-PhH^{NCN}), 6.70 (t, 1H, $^3J_{H-H}$ = 7.5 Hz, *m*-PhH^{NCN}), 6.50 (d, 1H, $^3J_{H-H}$ = 7.5 Hz, *o*-PhH^{NCN}), 6.35 (d, 1H, $^3J_{H-H}$ = 7.6 Hz, *o*-PhH^{NCN}), 4.59 (q, 1H, $^3J_{H-H}$ = 6.9 Hz, NC*H*), 4.40 (q, 1H, $^3J_{H-H}$ = 6.9 Hz, NC*H*), 2.11 (d, 3H, $^3J_{H-H}$ = 6.8 Hz, Me), 1.81 (d, 3H, $^3J_{H-H}$ = 6.8 Hz, Me). ^{13}C{^{1}H} NMR: (100.58 MHz, toluene-d$_8$, 243K): 178.7 (N*C*N), 149.8 (*i*-Ph), 148.9 (*i*-Ph), 135.7 (*i*-Ph^{NCN}), 128.1 (*m*-Ph), 127.7 (*m*-Ph^{NCN}), 127.5 (*p*-Ph^{NCN}), 127.3 (*o*-Ph), 127.1 (*o*-Ph), 126.9 (*o*-Ph^{NCN}), 126.3 (*p*-Ph), 125.6 (*o*-Ph^{NCN}), 59.5 (N*C*H), 59.4 (N*C*H), 25.9 (Me), 25.7 (Me). IR (ATR): ν [cm^{-1}] 663 (m), 697 (s), 740 (m), 759 (s), 777 (m), 839 (s), 998 (w), 1009 (w), 1020 (w), 1029 (m), 1082 (m), 1089 (m), 1116 (w), 1132 (m), 1154 (w), 1179 (w), 1210 (w), 1274 (m), 1304 (m), 1344 (s), 1367 (m), 1423 (s), 1445 (m), 1626 (vw), 2866 (vw), 2960 (vw). EA: (C$_{76}$H$_{77}$FN$_6$Th, M = 1325.50 g/mol) Calc.: C, 68.8; H, 5.8; N, 6.3; Found: C, 68.8; H, 6.0; N, 6.4.

*[UF(*S*)-PEBA)$_3$]·C$_7$H$_8$* (**18**) A solution of 13.3 mg (0.052 mmol, 1.0 eq.) AgPF$_6$ in 1 mL toluene was added to a solution of 67.0 mg **10** (0.05 mmol, 1 eq.) in 3 mL toluene resulting in the immediate color change to dark brown and the formation of a dark brown precipitate. The suspension was stirred for 16 h at room temperature. The pale green solution was decanted after centrifugation and the solvents were removed *in vacuo* yielding a dark green residue which was extracted into 2 mL *n*-pentane. Evaporation of the solution yielded **18** as pale green block-shaped crystals (66.2 mg, 0.05 mmol, 100 %). ^{1}H NMR: (400 MHz, toluene-d$_8$, 243 K) δ[ppm]: 26.42 (s, 2H, *o*-PhH), 20.10 (s, 2H, *o*-PhH), 12.86 (s, 2H, *m*-PhH), 10.74 (s, 1H, *p*-PhH), 10.00 (s, 2H, *m*-PhH), 8.10 (s, 1H, *p*-PhH), 3.79 (s, 2H, *m*-PhH^{NCN} + *p*-PhH^{NCN}), 3.34 (s, 3H, Me), 2.25 (s, 1H, NC*H*), 1.42 (s, 1H, *m*-PhH^{NCN}), 0.88 (s, 1H, NC*H*), 0.46 (s, 1H, *o*-PhH^{NCN}), -8.21 (s, 1H, *o*-PhH^{NCN}), -8.43 (s, 3H, Me). ^{13}C{^{1}H} NMR: (100.58 MHz, toluene-d$_8$, 243 K): 175.2 (*i*-Ph), 154.1 (*i*-Ph), 136.6 (*o*-Ph), 135.1 (*m*-Ph), 131.1 (*p*-Ph), 130.3 (*m*-Ph), 128.5 (*o*-Ph), 127.4 (*p*-Ph), 123.5 (*p*-Ph^{NCN}), 120.9 (*m*-Ph^{NCN}), 113.1 (*m*-Ph^{NCN}), 110.1 (*o*-Ph^{NCN}), 88.6 (*o*-Ph^{NCN}), 63.3 (*i*-Ph^{NCN}), 37.1 (Me), 14.5 (N*C*H), 3.1 (N*C*H), -2.8 (Me), the signal of N*C*N could not be observed. IR (ATR): ν [cm^{-1}] 665 (m), 698 (vs), 731 (m), 741 (m), 759 (s), 1009 (w), 1029 (m), 1086 (m), 1133 (w), 1207 (m), 1275 (m), 1298 (m), 1418 (w), 1448 (m), 1491 (m), 2924 (vw). EA: (C$_{76}$H$_{77}$FN$_6$U, M = 1331.47 g/mol) Calc.: C, 68.5; H, 5.8; N, 6.3; Found: C, 68.3; H, 6.0; N, 6.6.

*[NpF(*S*)-PEBA)$_3$]· C$_7$H$_8$* (**19**) A solution of 3.2 mg Ag[PF$_6$] (0.013 mmol, 1.1 eq) in 0.25 mL toluene was slowly added to a solution of 15.5 mg **11** (0.012 mmol, 1 eq) in 0.75 mL toluene. The color of the solution changed from dark red to orange. The solution was stirred for 16 h resulting in a turbid orange solution. The solvent was removed *in vacuo* after centrifugation. The dark orange residue was dissolved in 2 mL of pentane to give an orange solution, which

was allowed to slowly evaporate under inert conditions to yield **19** as orange crystalline solid (13.1 mg, 0.010 mmol, 82 %). ^{1}H NMR: (400 MHz, toluene-d$_8$, 243 K) δ[ppm]: 40.15 (s, 1H, NC*H*), 22.85 (s, 1H, NC*H*), 12.57 (s, 1H, *o*-PhH^{NCN}), 9.49 (s, 1H, *o*-PhH^{NCN}), 8.89 (s, 1H, *m*-PhH^{NCN}), 8.73 (s, 1H, *m*-PhH^{NCN}), 8.45 (s, 1H, *p*-PhH^{NCN}), 6.38 (s, 1H, *p*-PhH), 5.43 (s, 2H, *m*-PhH), 4.57 (s, 1H, *p*-PhH), 3.47 (s, 2H, *m*-PhH), 1.48 (s, 3H, Me), 0.86 (s, 3H, Me), -0.12 (s, 2H, *o*-PhH), -4.76 (s, 2H, *o*-PhH). ^{13}C{^{1}H} NMR: (100.58 MHz, toluene-d$_8$, 243 K): 157.0 (*i*-Ph), 151.5 (*i*-Ph), 131.7 (*p*-Ph^{NCN}), 130.1 (*o*-Ph^{NCN}), 128.6 (*o*-Ph), 127.6 (*m*-Ph) 127.2 (*m*-Ph^{NCN}), 125.3 (*p*-Ph), 124.3 (*m*-Ph), 122.3 (*p*-Ph), 122.2 (*m*-Ph^{NCN}), 121.7 (*o*-Ph^{NCN}), 119.5 (*o*-Ph), 63.7 (NC H), 54.6 (NC H), 27.67 (Me), 14.45 (Me), the signals for the NC N and *i*-Ph^{NCN} carbons could not be observed. IR (ATR): ν [cm^{-1}] 698 (vs), 741 (m), 760 (s), 919 (w), 1010 (w), 1029 (m), 1085 (m), 1112 (m), 1149 (m), 1184 (w), 1208 (m), 1254 (m), 1306 (w), 1345 (w), 1375 (w), 1418 (m), 1449 (m), 1494 (w), 2927 (vw). (C$_{76}$H$_{77}$FN$_6$Np, 1330.51 g/mol).

*[ThBr(*S*)-PEBA)$_3$]·C$_7$H$_8$* (**20**) A solution of 15.5 mg (0.101 mmol, 6 eq) trimethylsilylbromide (TMSBr) in 0.5 mL thf was slowly added to a solution of 22.2 mg (0.017 mmol, 1 eq) [ThCl((*S*)-PEBA)$_3$] (**9**). The resulting colorless solution was stirred for 16 h at room temperature. The solvents were subsequently removed *in vacuo* to yield a pale yellow residue which was washed with 2 mL of *n*-pentane to yield **20** in good yield (17.6 mg, 0.012 mmol, 70 %). Single crystals were grown by slow evaporation of a concentrated solution of **18** in toluene. ^{1}H NMR: (400 MHz, toluene-d$_8$, 243K) δ[ppm]: 7.61 (br s, 2H, *o*-PhH), 7.21 (m, 2H, *o*-PhH), 7.00 (m, 6H, *m*-PhH + p-PhH), 6.77 (t, 1H, $^3J_{H-H}$ = 7.4 Hz, *p*-PhH^{NCN}), 6.69 (br s, 1H, *m*-PhH^{NCN}), 6.64 (br s, 1H, *m*-PhH^{NCN}), 6.44 (br s, 2H, *o*-PhH^{NCN}), 4.56 (m, 2H, NC*H*), 2.34 (s, 3H, Me), 1.80 (s, 3H, Me). ^{13}C{^{1}H} NMR: (100.58 MHz, toluene-d$_8$, 243K): 180.3 (NC N), 148.8 (*i*-Ph), 135.2 (*i*-Ph^{NCN}), 128.1 (*m*-Ph), 127.6 (*o*-Ph), 127.4 (*m*-Ph), 127.4 (*m*-Ph^{NCN}), 127.4 (*p*-Ph^{NCN}), 126.5 (*o*-Ph^{NCN}), 126.3 (*p*-Ph) 125.0 (*o*-Ph^{NCN}), 60.2 (NC H), 26.1 (Me). IR (ATR): ν [cm^{-1}] 662 (m), 696 (s), 739 (m), 759 (s), 777 (m), 844 (vw), 910 (w), 967 (w), 999 (w), 1010 (m), 1020 (m), 1028 (m), 1081 (m), 1090 (m), 1107 (vw), 1131 (m), 1175 (w), 1209 (m), 1275 (m), 1283 (w), 1304 (m), 1344 (s), 1367 (m), 1373 (w), 1420 (s), 1443 (m), 2869 (vw), 2956 (vw). EA: (C$_{76}$H$_{77}$BrN$_6$Th, M = 1386.83 g/mol) Calc.: C, 65.8; H, 5.6; N, 6.1; Found: C, 65.9; H, 5.7; N, 6.1.

*[UBr(*S*)-PEBA)$_3$]·C$_7$H$_8$* (**21**) Ten drops SiMe$_3$Br were slowly added to a solution of 23.4 mg (0.017 mmol, 1 eq) [UCl((*S*)-PEBA)$_3$] (**10**) in thf. The solution was stirred for 16 h at room temperature. The solvent was subsequently removed *in vacuo* and the light green residue was washed with *n*-pentane to yield [UBr((*S*)-PEBA)$_3$] (**21**) in good yield (20.4 mg, 0.015 mmol, 88 %). Single crystals of **21** were grown by slow evaporation of a saturated toluene solution. ^{1}H-NMR: (400 MHz, toluene-d$_8$, 243 K) δ[ppm]: 40.36 (s, 1H, NC*H*), 22.78 (s, 1H, NC*H*), 16.22 (s, 1H, *o*-PhH^{NCN}), 10.36 (s, 1H, *o*-PhH^{NCN}), 9.13 (s, 1H, *m*-PhH^{NCN}), 8.94 (s, 1H, *m*-PhH^{NCN}), 8.94 (m, 1H, *p*-PhH^{NCN}), 7.65 (s, 3H, Me), 6.86 (s, 1H, *p*-PhH), 6.21 (s, 2H, *m*-PhH), 4.05 (s, 1H, *p*-PhH), 3.69 (s, 2H, *m*-PhH), 2.66 (s, 2H, *o*-PhH), 1.31 (s, 3H, Me), -8.11 (s, 2H, *o*-PhH). ^{13}C{^{1}H} NMR: (100.58 MHz, toluene-d$_8$, 243 K): 165.1 (*i*-Ph), 161.0 (*i*-Ph),

131.7 (p-Ph^{NCN}), 129.7 (m-Ph^{NCN}), 128.3 (m-Ph), 127.4 (o-Ph), 126.1 (p-Ph), 123.6 (m-Ph), 123.3 (m-Ph^{NCN}), 122.0 (o-Ph^{NCN}), 121.4 (p-Ph), 118.2 (o-Ph), 117.8 (i-Ph^{NCN}), 108.2 (o-Ph^{NCN}), 66.6 (NCH), 41.0 (NCH), 35.5 (Me), 28.2 (Me), the signal of NCN could not be observed. IR (ATR): ν [cm^{-1}] 663 (m), 696 (vs), 740 (m), 759 (s), 777 (m), 839 (m), 1010 (m), 1020 (m), 1028 (m), 1072 (m), 1090 (m), 1129 (m), 1173 (w), 1208 (m), 1275 (m), 1306 (m), 1327 (m), 1345 (m), 1416 (m), 1443 (m), 1492 (m), 2923 (w). EA: (C$_{76}$H$_{77}$BrN$_6$U, 1392.37 g/mol) Calc.: C, 65.5; H, 5.5; N, 6.0; Found: C, 65.8; H, 5.7; N, 5.9)

[NpBr(S)-PEBA)$_3$]· C$_7$H$_8$ (**22**) A 14 mg (0.011 mmol, 1 eq) [NpCl((S)-PEBA)$_3$] (**11**) was dissolved in 1 mL of thf to yield a dark red solution. Ten drops of TMSBr were slowly added resulting in a color change to salmon. The solutions were stirred for 16 h and the solvents were subsequently removed *in vacuo* to give a dark red oily residue, which was triturated with pentane to yield **22** as a pale red solid (10.6 mg, 0.0076 mmol, 76 %). Single crystals of **3** were grown by slow evaporation of a concentrated toluene solution. ^{1}H NMR: (400 MHz, toluene-d$_8$, 243 K) δ[ppm]: 51.43 (s, 1H, NC*H*), 24.28 (s, 1H, NC*H*), 18.44 (s, 1H, o-PhH^{NCN}), 10.51 (s, 2H, o-PhH^{NCN} + m-PhH^{NCN}), 9.83 (s, 1H, m-PhH^{NCN}), 9.42 (s, 1H, p-PhH^{NCN}), 6.68 (s, 3H, m-PhH + p-PhH), 6.44 (s, 3H, Me), 4.28 (s, 2H, o-PhH), 3.59 (s, 1H, p-PhH), 2.05 (s, 2H, m-PhH), -1.40 (s, 3H, Me), -10.41 (s, 2H, o-PhH). ^{13}C{^{1}H} NMR: (100.58 MHz, toluene-d$_8$, 243 K): 163.6 (i-Ph), 152.3 (i-Ph), 133.7 (o-Ph^{NCN}), 133.7 (p-Ph^{NCN}), 131.3 (o-Ph), 129.0 (m-Ph), 128.5 (m-Ph^{NCN}), 127.1 (o-Ph^{NCN}), 126.0 (p-Ph), 124.1 (m-Ph^{NCN}), 122.9 (m-Ph), 121.1 (p-Ph), 117.9 (o-Ph), 55.2 (NCH), 53.3 (NCH), 39.7 (Me), 28.0 (Me), the signals for the NCN and i-Ph^{NCN} carbons could not be observed. IR (ATR): ν [cm^{-1}] 662 (w), 698 (vs), 722 (m), 741 (m), 759 (s), 1029 (w), 1082 (m), 1246 (w), 1306 (w), 1344 (w), 1383 (w), 1418 (m), 1445 (m), 1493 (w), 2924 (w), 2954 (w). (C$_{76}$H$_{77}$BrN$_6$Np, 1391.4 g/mol)

[ThN$_3$((S)-PEBA)$_3$]·C$_7$H$_8$ (**23**) A solution of 20.0 mg (0.015 mmol, 1 eq.) [ThCl((*S*)-PEBA)$_3$] (**9**) dissolved in 1 mL thf was added to 3.6 mg NaN$_3$ (0.055 mmol, 3.7 eq.). The suspension was stirred for 16 h. All volatiles were removed *in vacuo* and the complex was extracted into 1.5 mL toluene. Slow evaporation of the solution afforded [ThN$_3$((*S*)-PEBA)$_3$]·C$_7$H$_8$ (**23**) as crystalline solid (18.6 mg, 0.014 mmol, 93 %). ^{1}H NMR: (400 MHz, toluene-d$_8$, 243K) δ[ppm]: 7.34 (m, 2H, o-PhH), 7.21 (m, 2H, o-PhH), 7.06 (m, 6H, m-PhH + p-PhH), 6.82 (m, 1H, p-PhH^{NCN}), 6.76 (m, 1H, m-PhH^{NCN}), 6.67 (m, 1H, m-PhH^{NCN}), 6.45 (br s, 2H, o-PhH^{NCN}), 4.60 (m, 1H, NC*H*), 4.46 (m, 1H, NC*H*), 2.11 (m, 3H, Me), 1.81 (s, 3H, Me). ^{13}C{^{1}H} NMR: (100.58 MHz, toluene-d$_8$, 243K): 179.5 (NCN), 149.1 (i-Ph), 148.5 (i-Ph), 135.1 (i-Ph^{NCN}), 128.4 (m-Ph), 127.5 (m-Ph^{NCN}), 127.5 (p-Ph^{NCN}), 126.8 (o-Ph^{NCN}), 126.5 (o-Ph), 126.4 (p-Ph), 126.3 (o-Ph), 125.3 (o-Ph^{NCN}), 59.7 (NCH), 26.1 (Me), 25.9 (Me). IR (ATR): ν [cm^{-1}] 663 (m), 696 (vs), 731 (s), 741 (s), 760 (s), 778 (m), 910 (w), 962 (w), 999 (m), 1009 (m), 1019 (m), 1028 (m), 1077 (m), 1089 (m), 1131 (m), 1178 (m), 1210 (m), 1275 (m), 1283 (m), 1302 (s), 1309 (s), 1323 (m), 1343 (s), 1369 (m), 1423 (s), 1443 (s), 1492 (m), 2099 (s, ν$_{as}$(N$_3$$^-$)), 2922 (w). EA: (C$_{76}H_{77}N_9$Th, 1348.52 g/mol) Calc.: C, 67.6; H, 5.7; N, 9.3; Found: C, 67.9; H, 6.0; N, 8.7.

[UN₃((S)-PEBA)₃]· C₇H₈ (**24**) A solution of 20.0 mg (0.015 mmol, 1 eq.) [UCl((*S*)-PEBA)₃] (**10**) dissolved in 1 mL thf was added to 3.5 mg NaN₃ (0.055 mmol, 3.5 eq.). The suspension was stirred for 16 h. All volatiles were subsequently removed *in vacuo* and the complex was extracted into 1.5 mL toluene. Slow evaporation of the solution afforded **24** as crystalline solid (22.3 mg, 0.015 mmol, 100 %). ^{1}H-NMR: (400 MHz, toluene-d_8, 243 K) δ[ppm]: 30.42 (s, 1H, NC*H*), 17.87 (s, 1H, NC*H*), 9.51 (s, 1H, *o*-PhH^{NCN}), 8.16 (s, 1H, *o*-PhH^{NCN}), 7.68 (s, 1H, *m*-PhH^{NCN}), 7.44 (s, 1H, *m*-PhH^{NCN}), 6.95 (m, 1H, *p*-PhH^{NCN}), 6.68 (s, 1H, *p*-PhH), 6.34 (s, 2H, *m*-PhH), 5.72 (s, 1H, *p*-PhH), 5.22 (s, 2H, *m*-PhH), 4.53 (s, 2H, *o*-PhH), 2.53 (s, 3H, Me), 2.07 (s, 3H, Me), 0.63 (s, 2H, *o*-PhH). ^{13}C-NMR: (100.58 MHz, toluene-d_8, 243 K): 163.1 (*i*-Ph), 160.4 (*i*-Ph), 129.5 (*m*-Ph^{NCN}), 128.4 (*m*-Ph), 127.6 (*m*-Ph^{NCN}), 126.4 (*m*-Ph), 125.7 (*p*-Ph), 124.3 (*p*-Ph), 124.0 (*o*-Ph), 122.3 (*o*-Ph), 120.6 (*p*-Ph^{NCN}), 120.0 (*o*-Ph^{NCN}), 102.6 (*o*-Ph^{NCN}), 48.8 (N*C*H), 41.1 (N*C*H), 36.4 (Me), 13.7 (Me), the signals of N*C*N and *i*-Ph^{NCN} could not be observed. IR (ATR): ν [cm^{-1}] 663 (s), 695 (vs), 731 (s), 740 (s), 759 (s), 777 (m), 910 (m), 964 (m), 999 (m), 1009 (m), 1019 (m), 1028 (m), 1076 (s), 1089 (m), 1105 (m), 1129 (m), 1156 (m), 1176 (m), 1209 (m), 1275 (m), 1283 (m), 1303 (s), 1308 (s), 1325 (m), 1342 (s), 1369 (s), 1419 (s), 1443 (s), 1492 (m), 2093 (s, $ν_{as}$(N₃$^-$)), 2923 (w). EA: (C₇₆H₇₇N₉U, 1354.51 g/mol) Calc.: C, 67.3; H, 5.7; N, 6.9; Found: C, 67.7; H, 5.8; N, 6.6)

[NpN₃((S)-PEBA)₃]· C₇H₈ (**25**) A solution of 22.2 mg (0.016 mmol, 1 eq.) [NpCl((*S*)-PEBA)₃] (**11**) dissolved in 1 mL of thf was added to 2.4 mg NaN₃ (0.037 mmol, 2.3 eq.). The suspension was stirred for 16 h. All volatiles were removed *in vacuo* and the complex was extracted into 0.5 mL toluene. Vapor diffusion with pentane afforded **25** as crystalline solid (10.1 mg, 0.007 mmol, 47 %). ^{1}H NMR: (400 MHz, toluene-d_8, 243 K) δ[ppm]: 48.10 (s, 1H, NC*H*), 24.31 (s, 1H, NC*H*), 16.46 (s, 1H, *o*-PhH^{NCN}), 10.41 (s, 1H, *o*-PhH^{NCN}), 9.92 (s, 1H, *m*-PhH^{NCN}), 9.59 (s, 1H, *m*-PhH^{NCN}), 9.15 (s, 1H, *p*-PhH^{NCN}), 6.54 (s, 1H, *p*-PhH), 5.67 (s, 2H, *m*-PhH), 4.24 (s, 3H, Me), 3.67 (s, 1H, *p*-PhH), 2.13 (s, 2H, *m*-PhH), 1.72 (s, 2H, *o*-PhH), 0.26 (s, 3H, Me), -9.56 (s, 2H, *o*-PhH). ^{13}C{^{1}H} NMR: (100.58 MHz, toluene-d_8, 243 K): 158.6 (*i*-Ph), 147.7 (*i*-Ph), 132.9 (*p*-Ph^{NCN}), 132.2 (*o*-Ph^{NCN}), 131.0 (*o*-Ph), 128.6 (*m*-Ph), 128.0 (*m*-Ph^{NCN}), 125.1 (*p*-Ph), 123.4 (*m*-Ph^{NCN}), 123.2 (*o*-Ph^{NCN}), 122.6 (*m*-Ph), 121.0 (*p*-Ph), 117.3 (*o*-Ph), the signals for the N*C*N, *i*-Ph^{NCN}, N*C*H and Me carbons could not be observed. IR (ATR): ν [cm^{-1}] 663 (s), 698 (vs), 731 (s), 741 (s), 759 (s), 777 (m), 999 (m), 1009 (m), 1019 (m), 1028 (m), 1072 (s), 1089 (m), 1128 (m), 1142 (m), 1176 (m), 1210 (m), 1274 (m), 1283 (m), 1300 (s), 1309 (s), 1325 (m), 1343 (s), 1371 (s), 1420 (s), 1443 (s), 1492 (m), de, 2920 (w). (C₇₆H₇₇N₉Np, 1353.53 g/mol)

5.3.2 Synthesis of trivalent metal amidinates

[NEt₄][CeCl₂((S)-PEBA)₂] (**14**) A 62.4 mg (0.102 mmol, 1 eq.) [NEt$_4$][CeCl$_6$] was suspended in 1 mL thf. A solution containing 66.5 mg (0.202 mmol, 2 eq.) (*S*)-HPEBA and 47.5 mg (0.284 mmol, 2.8 eq.) LiHMDS in 1 mL thf was slowly added and the suspension was stirred for 16 h. The supernatant was slowly evaporated after centrifugation yielding [NEt$_4$][CeCl$_2$((*S*)-PEBA)$_2$] (**14**) as pale yellow crystals (42.0 mg, 0.042 mmol, 42 %). ^{1}H NMR: (400 MHz, Toluene-d$_8$, 298 K) δ[ppm]: 11.47 (s, 2H, NC*H*), 10.95 (s, 2H, *o*-PhH^{NCN}), 8.73 (s, 2H, *m*-PhH^{NCN}), 8.42 (s, 1H, *p*-PhH^{NCN}), 6.06 (s, 2H, *p*-PhH), 5.58 (s, 4H, *m*-PhH), 2.92 (s, 4H, *o*-PhH), -0.69 (s, 6H, Me). ^{13}C{^{1}H} NMR: (100.58 MHz, Toluene-d$_8$, 298 K): 151.5 (*i*-Ph), 148.7 (*i*-Ph^{NCN}), 132.2 (*o*-Ph^{NCN}), 130.5 (*m*-Ph^{NCN}), 129.8 (*p*-Ph^{NCN}), 128.9 (*m*-Ph), 125.3 (*o*-Ph), 124.5 (*p*-Ph), 68.1 (NC*H*), 26.9 (Me), the signal of NCN could not be observed. IR (ATR): ν [cm^{-1}] 701 (vs), 740 (s), 771 (s), 786 (m), 796 (s), 796 (s), 1004 (s), 1022 (m), 1027 (m), 1066 (m), 1080 (m), 1090 (w), 1174 (m), 1184 (m), 1201 (w), 1301 (w), 1321 (m), 1331 (m), 1351 (m), 1393 (s), 1457 (vs), 1487 (m), 2964 (w). (C$_{54}$H$_{66}$N$_5$Cl$_2$Ce, 996.14 g/mol)

[Ce((S)-PEBA)₃] (**15**) A solution containing 98.4 mg (0.300 mmol, 3 eq.) (*S*)-HPEBA and 59.0 mg (0.353 mmol, 3.5 eq.) LiHMDS in 1 mL thf was slowly added to a solution of 38.9 mg (0.100 mmol, 1 eq.) CeCl$_3$·2 thf in 1 mL thf causing a color change to yellow. The solution was stirred for 16 h and the solvent subsequently removed *in vacuo* yielding a pale yellow residue which was extracted into 2 mL toluene. The resulting suspension was centrifuged and the supernatant decanted. The solvents were removed *in vacuo* and the resulting yellow residue was triturated with 5 mL pentane yielding [Ce((*S*)-PEBA)$_3$] (**15**) as a pale yellow powder (63.1 mg, 0.056 mmol, 56 %). Single crystals were obtained by slow diffusion of pentane into a saturated solution of **15** in toluene. ^{1}H NMR: (400 MHz, toluene-d$_8$, 243 K) δ[ppm]: 13.65 (s, 2H, *o*-PhH^{NCN}), 11.33 (s, 4H, *o*-PhH), 11.02 (s, 2H, NC*H*), 9.38 (s, 2H, *m*-PhH^{NCN}), 8.87 (s, 4H, *m*-PhH), 8.66 (s, 1H, *p*-PhH^{NCN}), 8.19 (s, 2H, *p*-PhH), -13.08 (s, 6H, Me). ^{13}C{^{1}H} NMR: (100.58 MHz, toluene-d$_8$, 243 K): 152.3 (*i*-Ph), 146.9 (*i*-Ph^{NCN}), 132.3 (*o*-Ph^{NCN}), 131.4 (*m*-Ph^{NCN}), 130.7 (*p*-Ph^{NCN}), 130.2 (*m*-Ph), 128.6 (*o*-Ph), 127.4 (*p*-Ph), 62.1 (NC*H*), 12.5 (Me), the signal of NCN could not be observed. IR (ATR): ν [cm^{-1}] 657 (m), 695 (vs), 732 (s), 758 (s), 772 (m), 791 (m), 914 (m), 955 (m), 999 (m), 1012 (m), 1020 (s), 1029 (m), 1039 (m), 1075 (s), 1081 (s), 1111 (w), 1129 (m), 1156 (w), 1207 (m), 1273 (m), 1298 (s), 1326 (s), 1346 (s), 1367 (s), 1412 (vs), 1432 (vs), 1492 (w), 2966 (m). EA: (C$_{69}$H$_{69}$N$_6$Ce, M = 1122.42 g/mol) Calc.: C, 73.8; H, 6.1; N, 7.5; Found: C, 74.0; H, 6.2; N, 7.2.

[U((S)-PEBA)₃] (**26**) A 62.2 mg (0.101 mmol, 1 eq.) UI$_3$, 21.6 mg (0.538 mmol, 5.4 eq) KH and 98.7 mg (0.301 mmol, 3eq.) (*S*)-HPEBA were suspended in 2 mL thf and stirred for 16 h to yield a dark violet suspension. The volatiles were subsequently removed *in vacuo* and the dark red residue was extracted into 2 mL toluene. After centrifugation, the solvent was evaporated *in vacuo* and the residue was washed with 2 mL cold *n*-pentane to yield **26** as dark violet solid (73.9 mg, 0.061 mmol, 60 %). Single crystals could be grown by cooling a saturated

solution of **26** in *n*-pentane to 253 K. ^{1}H-NMR: (400 MHz, toluene-d$_8$, 298 K) δ[ppm]: 25.36 (s, 2H, NC*H*), 12.18 (s, 2H, *o*-PhH^{NCN}), 10.01 (s, 4H, *o*-PhH), 8.97 (s, 2H, *m*-PhH^{NCN}), 8.61 (s, 1H, p-PhH^{NCN}), 8.26 (s, 4H, *m*-PhH), 7.56 (s, 2H, *p*-PhH), -10.43 (s, 6H, Me). ^{13}C{^{1}H} NMR: (100.58 MHz, toluene-d$_8$, 243 K): 129.5 (*p*-Ph^{NCN}), 127.9 (*m*-Ph), 125.1 (*m*-Ph^{NCN}), 124.7 (*o*-Ph^{NCN}), 124.2 (*p*-Ph), 96.3 (*o*-Ph), 34.2 (*i*-Ph^{NCN}), 15.6 (NC*H*), the signals of NC*N*, *i*-Ph and Me could not be observed. IR (ATR): ν [cm^{-1}] 664 (w), 698 (vs), 738 (m), 759 (m), 772 (m), 1018 (m), 1028 (m), 1071 (m), 1276 (m), 1300 (m), 1346 (m), 1369 (m), 1438 (s), 1486 (m), 2956 (w). EA: (C$_{69}$H$_{69}$N$_6$U, M = 1220.35 g/mol) Calc.: C, 67.8; H, 5.7; N, 6.9; Found: C, 67.7; H, 5.8; N, 6.6.

[Np((S)-PEBA)$_3$] (**27**) A 23.1 mg (0.017 mmol, 1 eq) [NpCl((*S*)-PEBA)$_3$] (**11**) was dissolved in 2 mL thf and added to 8 mg KC$_8$ (0.059 mmol, 3.5 eq.) resulting in a color change from red to dark brown. The suspension was stirred for 16 h at ambient temperature. The solvent was removed *in vacuo* after decantation and the dark violet residue was extracted into 1 mL toluene. Evaporation of the toluene solution yielded a dark violet residue which was extracted into 2 mL *n*-pentane. After evaporation of the solvent a dark violet oily residue was obtained (16.5 mg, 0.014 mmol, 79 %). ^{1}H NMR: (400 MHz, toluene-d$_8$, 243 K) δ[ppm]: 22.15 (s, 2H, NC*H*), 13.66 (s, 2H, *o*-PhH^{NCN}), 13.53 (s, 4H, *o*-PhH), 9.21 (m, 6H, *m*-Ph + *m*-PhH^{NCN}), 8.72 (s, 1H, *p*-PhH^{NCN}), 8.15 (s, 2H, *p*-PhH), -14.57 (s, 6H, Me). ^{13}C{^{1}H} NMR: (100.58 MHz, toluene-d$_8$, 243 K): 145.9 (*i*-Ph), 130.7 (*p*-Ph^{NCN}), 129.6 (*m*-Ph), 126.5 (*m*-Ph^{NCN}), 126.3 (*p*-Ph), 120.9 (*o*-Ph^{NCN}), 113.2 (*o*-Ph), 73.7 (*i*-Ph^{NCN}), 41.3 (NC*H*), -3.2 (Me), the signal of NC*N* could not be observed. IR (ATR): ν [cm^{-1}] 698 (vs), 758 (m), 912 (w), 1020 (m), 1027 (m), 1071 (m), 1266 (w), 1302 (m), 1345 (m), 1364 (m), 1447 (s), 1485 (m), 2958 (w). (C$_{69}$H$_{69}$N$_6$Np, M = 1219.37 g/mol)

[La((S)-PEBA)$_3$] (**28**) A 64.0 mg (0.103 mmol, 1 eq.) La(N(SiMe$_3$)$_2$)$_3$ was dissolved in 2 mL thf. A solution of 105.4 mg (0.321 mmol, 3.11 eq.) (*S*)-HPEBA in 1 mL thf was added and the combined solutions were stirred for 16 h at room temperature. The pale yellow suspension was transferred in a Schlenk-tube and the volatiles were removed *in vacuo* to yield a pale yellow residue. The residue was dissolved in 1 mL toluene and insoluble substances were separated by centrifugation. The supernatant was evaporated *in vacuo* and washed with *n*-pentane to yield 88.8 mg (0.079 mmol, 77 %) of an off-white powder. Single crystals could be grown by slow evaporation of a solution of **28** in toluene:*n*-pentane 1:2 (v/v). ^{1}H NMR: (400 MHz, toluene-d$_8$, 298 K) δ[ppm]: 7.33 (m, 4H, *o*-PhH), 7.11 (m, 11H, *m*-PhH + *p*-PhH + PhH^{NCN}), 4.30 (m, 2H, NC*H*), 1.50 (s, 6H, Me). ^{13}C{^{1}H}-NMR: (100.58 MHz, toluene-d$_8$, 298 K): 179.6 (NC*N*), 149.5 (*i*-Ph), 136.4 (*i*-Ph^{NCN}), 128.4 (*m*-Ph), 128.4 (*p*-Ph), 128.3 (*m*-Ph^{NCN}), 128.3 (*p*-Ph^{NCN}), 127.1 (*o*-Ph), 126.1 (*o*-Ph^{NCN}), 58.6 (NC*H*), 27.6 (Me). IR (ATR): ν [cm^{-1}] 657 (m), 696 (vs), 732 (m), 759 (s), 772 (m), 915 (m), 957 (m), 1012 (m), 1020 (m), 1029 (m), 1074 (m), 1129 (m), 1176 (w), 1208 (m), 1275 (m), 1345 (s), 1368 (m), 1414 (s), 1434 (vs), 2965 (w). EA: (C$_{69}$H$_{69}$N$_6$La, 1121.21 g/mol) Calc.: C, 73.8; H, 6.1; N, 7.5; Found: C, 73.9; H, 6.5; N, 7.1.

5.3.3 Synthesis of hexavalent amidinate and diimine complexes

[UO$_2$((S)-PEBA)$_2$(thf)] (**29**) A solution containing 71.6 mg (S)-HPEBA (0.218 mmol, 2.1 eq.) and 44.0 mg (0.263 mmol, 2.6 eq.) LiHMDS in 1 mL thf has been slowly added to a solution of 34.7 mg UO$_2$Cl$_2$ (0.102 mmol, 1 eq.) in 1 mL thf resulting in an immediate color change from yellow to dark red. The solution was stirred for 16 h and the volatiles were subsequently removed *in vacuo*. The dark residue has been extracted in toluene and separated from insoluble substances by centrifugation. The toluene has been removed *in vacuo* yielding **29** as dark red residue (90.5 mg, 0.091 mmol, 89 %). Single crystals could be grown by diffusion of *n*-pentane into a saturated solution of **29** in thf. ^{1}H NMR: (400 MHz, toluene-d$_8$, 298 K) δ[ppm]: 7.59 (d, 4H, $^3J_{H-H}$ = 7.6 Hz, *o*-PhH), 7.19 (m, 2H, *m*-PhH^{NCN}), 7.06 (t, 4H, $^3J_{H-H}$ = 7.6 Hz, *m*-PhH), 6.95 (t, 2H, $^3J_{H-H}$ = 7.3 Hz, *p*-PhH), 6.88 (m, 3H, *o*-PhH^{NCN} + *p*-PhH^{NCN}), 5.91 (q, 2H, $^3J_{H-H}$ = 6.9 Hz, NC*H*), 1.81 (d, 6H, $^3J_{H-H}$ = 6.9 Hz, Me). ^{13}C{^{1}H} NMR: (100.58 MHz, toluene-d$_8$, 298 K): 173.8 (N*C*N), 149.9 (*i*-Ph), 138.8 (*i*-Ph^{NCN}), 128.5 (*m*-Ph), 128.4 (*o*-Ph^{NCN}), 128.2 (*m*-Ph^{NCN}), 127.7 (*o*-Ph), 126.2 (*p*-Ph), 57.8 (N*C*H), 24.7 (Me), the signal for *p*-Ph^{NCN} carbon could not be observed. IR (ATR): ν [cm^{-1}] 696 (vs), 726 (m), 737 (s), 751 (m), 772 (m), 873 (m), 901 (vs, ν$_{as}$(O=U=O)), 1020 (m), 1029 (m), 1061 (m), 1121 (m), 1181 (w), 1210 (m), 1298 (m), 1310 (s), 1341 (m), 1442 (s), 1458 (s), 2975 (w). EA: (C$_{50}$H$_{54}$N$_4$O$_3$U, M = 997.00 g/mol) Calc.: C, 60.2; H, 5.4; N, 5.6; Found: C, 59.4; H, 5.4; N, 5.7.

[UO$_2$Cl$_2$(phen)$_2$] (**30**). A solution of 36 mg 1,10-phenanthroline (0.2 mmol, 2 eq.) in 1.0 ml acetone was slowly added to a solution of 37.1 mg UO$_2$Cl$_2$·1.7 H$_2$O (0.1 mmol, 1 eq.) in 1.0 ml acetone resulted in immediate formation of **30** as yellow precipitate (53.3 mg, 0.076 mmol, 76 %). Single crystals of **30** could be grown by recrystallization from hot acetone. IR (ATR): ν [cm^{-1}] 720 (vs), 725 (vs), 776 (w), 803 (vw), 822 (m), 843 (vs), 864 (w), 890 (s, ν$_{as}$(O=U=O)), 898 (m, ν$_{as}$(O=U=O)), 930 (vw), 1093 (vw), 1107 (w), 1142 (vw), 1154 (vw), 1209 (vw), 1222 (vw), 1345 (w), 1424 (m), 1498 (w), 1515 (w), 1571 (vw), 1592 (w), 1628 (vw), 3050 (vw), 3080 (vw). EA: (C$_{24}$H$_{16}$Cl$_2$N$_4$O$_2$U, M = 701.34 g/mol) Calc.: C, 41.1; H, 2.3; N, 8.0; Found: C, 39.9; H, 2.3; N, 7.7.

[UO$_2$(bipy)Cl$_2$(H$_2$O)] (**31**). Two mL of an acetone solution containing 77 mg 2,2′-bipyridine (0.493 mmol, 1 eq) were slowly added to a solution of 186 mg of UO$_2$Cl$_2$·1.7 H$_2$O (0.501 mmol, 1 eq) dissolved in 2 mL of degassed water. The resulting yellow solution was slowly evaporated at elevated temperatures (30°C) yielding a crystalline precipitate which was washed with tetrahydrofuran (THF) and dried at room temperature (252 mg, 0.489 mmol, 98 %). This crystalline precipitate consists of a pure phase of **31** as evidenced by powder XRD (see Figure 114 in Appendix). IR (ATR): ν [cm^{-1}] 734 (w), 746 (w), 771 (s), 892 (w), 904 (s), 928 (vs, ν$_{as}$(O=U=O)), 1006 (m), 1017 (m), 1316 (m), 1436 (m), 1475 (m), 1598 (m),

3327 (m). EA: ($C_{10}H_{10}Cl_2N_2O_3U$, M = 515.13 g/mol) Calc.: C, 23.3; H, 2.0; N, 5.4; Found: C, 23.6; H, 1.9; N, 5.4.

[UO2(phen)Cl2(act)] (32). A 1 mL of 0.1 M 1,10-phenanthroline (0.1 mmol, 1 eq.) in acetone was added to a 1 mL of 0.1 M $UO_2Cl_2 \cdot 1.7\,H_2O$ (0.1 mmol, 1 eq.) in acetone resulting in the precipitation of a pale yellow solid. The supernatant was decanted after centrifugation and slowly evaporated at ambient conditions yielding **32** as crystalline solid in low yield (9.1 mg, 0.017 mmol, 17 %) which prevented further characterization. ($C_{15}H_{14}Cl_2N_2O_3U$, M = 579.21 g/mol)

[(UO2(bipy)Cl)2(μ2-OH)2] (33). A solution of 37 mg $UO_2Cl_2 \cdot 1.7\,H_2O$ (0.100 mmol, 1 eq.) in 1 mL degassed water was slowly added to 46.8 mg 2,2′ -bipyridine (0.300 mmol, 3 eq.) in 3 mL acetone resulting in a color change from colorless to yellow. The solution was slowly evaporated at elevated temperatures (60°C), yielding a crystalline yellow precipitate. The powder X-ray diffraction pattern on the product revealed that the precipitate consists of a mixture of monomeric (**31**) and dimeric (**33**) uranyl bipyridine complexes (see Figure 116 in Appendix). Similar results are obtained when two equivalents of bipy were mixed with the UO_2Cl_2 solution. Other attempts to obtain a pure phase of **33** were not successful. Thus, no additional characterization (i.e. elemental analysis and IR measurements) was performed on this compound. ($C_{20}H_{18}Cl_2N_4O_6U_2$, M = 957.34 g/mol)

[(UO2(phen)Cl)2(μ2-OH)2]·2H2O (34). By adding a solution of 37 mg $UO_2Cl_2 \cdot 1.7\,H_2O$ (0.100 mmol, 1 eq.) in 1 mL degassed water to a solution of 36 mg 1,10-phenanthroline (0.200 mmol, 2 eq.) in 2 mL acetone a yellow precipitate is formed immediately. The supernatant was decanted after the sedimentation of the precipitate and slowly evaporated at 60°C. This resulted in a crystalline yellow precipitate in a very low yield that prevented further characterization with additional methods. Single-crystal XRD revealed the formation of **34**. ($C_{24}H_{22}Cl_2N_4O_8U_2$, M = 1041.42 g/mol)

5.3.4 Synthesis of mixed-valent polynuclear neptunium complexes

The synthesis of $NpCl_4$ has been established by reduction of a hexavalent neptunyl(VI) nitrate source with hexachloropropene.[294] Detailed investigations of this reaction revealed, that some impurities of Np^V remain in the "$NpCl_4$" product.[262] Depending on the ratio of Np^{IV}:Np^V different mixed-valent polynuclear neptunium(IV/V) complexes have been obtained. For more details see: Schöne et al. *Dalton Trans*. **2019**, *48*, 6700.[262]

[(Np^{IV}Cl$_4$)(Np^{V}O$_2$(thf)$_3$)$_2$(μ_2-Cl)$_2$] (35).
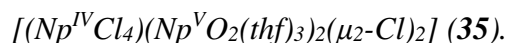
A 9 mg of $NpCl_4$ (Batch 1) was suspended in 0.5 mL thf and stirred for 3 days. The supernatant was separated from the solid residue by centrifugation and slowly evaporated, yielding compound **35** as a crystalline solid (1.6 mg). The obtained crystalline material was used for single-crystal X-ray diffraction, whilst the solid residue from the original sample mixture (7.4 mg) was characterized by PXRD (see Figure 118 in Appendix) indicating the presence of **35**. The small scales did not permit any further characterization technique.

[(Np^{IV}Cl$_3$)(Np^{V}O$_2$(thf)$_2$)$_3$(μ_2-Cl)$_2$(μ_3-Cl)] (36).
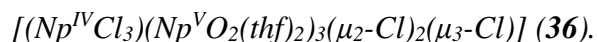
A 18 mg of $NpCl_4$ (Batch 2) was suspended in 1 mL thf and stirred for 5 days. The supernatant was separated from the solid residue by centrifugation and decanted. Slow evaporation of the decanted solution yielded a crystalline material (10.5 mg) that was found to contain compound **36** as a major phase with a minor presence of **35** and additional unidentified phases (see Figure 120 in Appendix). The small scales did not permit any further characterization techniques.

6 LITERATURE

[1]   Hahn, O.; Strassmann, F. *Naturwissenschaften* **1939**, *27*, 11-15.

[2]   Meitner, L.; Frisch, O. R. *Nature* **1939**, *143*, 239-240.

[3]   Dreizehntes Gesetz zur Änderung des Atomgesetzes (13. AtGÄndG), *Federal Republic of Germany,* **2011**.

[4]   *The Chemistry of Actinide and Transactinide Elements*. 4th ed.; Morss, L. R.; Edelstein, N. M.; Fuger, J., Eds. Springer Netherlands: Dordrecht, **2011**, Vol. 6.

[5]   Gorden, A. E. V.; DeVore, M. A.; Maynard, B. A. *Inorg. Chem.* **2013**, *52*, 3445-3458.

[6]   Adam, C.; Kaden, P.; Beele, B. B.; Müllich, U.; Trumm, S.; Geist, A.; Panak, P. J.; Denecke, M. A. *Dalton Trans.* **2013**, *42*, 14068-14074.

[7]   Maher, K.; Bargar, J. R.; Brown, G. E. *Inorg. Chem.* **2013**, *52*, 3510-3532.

[8]   Minasian, S. G.; Boland, K. S.; Feller, R. K.; Gaunt, A. J.; Kozimor, S. A.; May, I.; Reilly, S. D.; Scott, B. L.; Shuh, D. K. *Inorg. Chem.* **2012**, *51*, 5728-5736.

[9]   Minasian, S. G.; Keith, J. M.; Batista, E. R.; Boland, K. S.; Clark, D. L.; Conradson, S. D.; Kozimor, S. A.; Martin, R. L.; Schwarz, D. E.; Shuh, D. K.; Wagner, G. L.; Wilkerson, M. P.; Wolfsberg, L. E.; Yang, P. *J. Am. Chem. Soc.* **2012**, *134*, 5586-5597.

[10]   Gogolev, A. V.; Grigoriev, M. S.; Budantseva, N. A.; Fedosseev, A. M. *Russ. J. Coord. Chem.* **2013**, *39*, 271-277.

[11]   Jones, M. B.; Gaunt, A. J.; Gordon, J. C.; Kaltsoyannis, N.; Neu, M. P.; Scott, B. L. *Chem. Sci.* **2013**, *4*, 1189-1203.

[12]   Behrle, A. C.; Levin, J. R.; Kim, J. E.; Drewett, J. M.; Barnes, C. L.; Schelter, E. J.; Walensky, J. R. *Dalton Trans.* **2015**, *44*, 2693-2702.

[13]   Jewula, P.; Berthet, J. C.; Chambron, J. C.; Rousselin, Y.; Thuéry, P.; Meyer, M. *Eur. J. Inorg. Chem.* **2015**, *2015*, 1529-1541.

[14]   Gregson, M.; Lu, E.; Tuna, F.; McInnes, E. J. L.; Hennig, C.; Scheinost, A. C.; McMaster, J.; Lewis, W.; Blake, A. J.; Kerridge, A.; Liddle, S. T. *Chem. Sci.* **2016**, *7*, 3286-3297.

[15]   Behrle, A. C.; Myers, A. J.; Kerridge, A.; Walensky, J. R. *Inorg. Chem.* **2018**, *57*, 10518-10524.

[16]   Cary, S. K.; Livshits, M.; Cross, J. N.; Ferrier, M. G.; Mocko, V.; Stein, B. W.; Kozimor, S. A.; Scott, B. L.; Rack, J. J. *Inorg. Chem.* **2018**, *57*, 3782-3797.

[17]   Klamm, B. E.; Windorff, C. J.; Celis-Barros, C.; Marsh, M. L.; Meeker, D. S.; Albrecht-Schmitt, T. E. *Inorg. Chem.* **2018**, *57*, 15389-15398.

[18]   Berryman, V. E. J.; Whalley, Z. J.; Shephard, J. J.; Ochiai, T.; Price, A. N.; Arnold, P. L.; Parsons, S.; Kaltsoyannis, N. *Dalton Trans.* **2019**, *48*, 2939-2947.

[19]   Edelmann, F. T. *Chem. Soc. Rev.* **2012**, *41*, 7657-7672.

[20]   Edelmann, F. T., Advances in the Coordination Chemistry of Amidinate and Guanidinate Ligands. In *Advances in Organometallic Chemistry*, Anthony, F. H.; Mark, J. F., Eds. Academic Press: Cambridge, **2008**, Vol. 57, pp 183-352.

[21]   Liu, W.-M.; Overhand, M.; Ubbink, M. *Coord. Chem. Rev.* **2014**, *273-274*, 2-12.

[22]   *Nomenclature of Inorganic Chemistry*. Connely, N. G.; Damhus, T.; Hartshorn, R. M.; Hutton, A. T., Eds. The Royal Society of Chemistry: Cambridge, **2005**.

[23]   Hoffman, D. C.; Lawrence, F. O.; Mewherter, J. L.; Rourke, F. M. *Nature* **1971**, *234*, 132-134.

[24] Lachner, J.; Dillmann, I.; Faestermann, T.; Korschinek, G.; Poutivtsev, M.; Rugel, G.; Lierse von Gostomski, C.; Türler, A.; Gerstmann, U. *Phys. Rev. C* **2012**, *85*, 015801.

[25] Peppard, D. F.; Studier, M. H.; Gergel, M. V.; Mason, G. W.; Sullivan, J. C.; Mech, J. F. *J. Am. Chem. Soc.* **1951**, *73*, 2529-2531.

[26] McMillan, E.; Abelson, P. H. *Phys. Rev.* **1940**, *57*, 1185-1186.

[27] Seaborg, G. T.; Wahl, A. C.; Kennedy, J. W. *Phys. Rev.* **1946**, *69*, 367-367.

[28] Ghiorso, A.; James, R. A.; Morgan, L. O.; Seaborg, G. T. *Phys. Rev.* **1950**, *78*, 472-472.

[29] OECD/NEA *Actinide and Fission Product Partitioning and Transmutation, Status and Assessment Report*; **1999**.

[30] Liddle, S. T. *Angew. Chem. Int. Ed.* **2015**, *54*, 8604-8641.

[31] Minasian, S. G.; Krinsky, J. L.; Arnold, J. *Chem. Eur. J.* **2011**, *17*, 12234-12245.

[32] Lukens, W. W.; Speldrich, M.; Yang, P.; Duignan, T. J.; Autschbach, J.; Kögerler, P. *Dalton Trans.* **2016**, *45*, 11508-11521.

[33] Neidig, M. L.; Clark, D. L.; Martin, R. L. *Coord. Chem. Rev.* **2013**, *257*, 394-406.

[34] Jung, J.; Atanasov, M.; Neese, F. *Inorg. Chem.* **2017**, *56*, 8802-8816.

[35] Kelley, M. P.; Su, J.; Urban, M.; Luckey, M.; Batista, E. R.; Yang, P.; Shafer, J. C. *J. Am. Chem. Soc.* **2017**, *139*, 9901-9908.

[36] Vitova, T.; Pidchenko, I.; Fellhauer, D.; Bagus, P. S.; Joly, Y.; Pruessmann, T.; Bahl, S.; Gonzalez-Robles, E.; Rothe, J.; Altmaier, M.; Denecke, M. A.; Geckeis, H. *Nature Commun.* **2017**, *8*, 16053.

[37] Sadhu, B.; Dolg, M. *Inorg. Chem.* **2019**, *58*, 9738-9748.

[38] Su, J.; Batista, E. R.; Boland, K. S.; Bone, S. E.; Bradley, J. A.; Cary, S. K.; Clark, D. L.; Conradson, S. D.; Ditter, A. S.; Kaltsoyannis, N.; Keith, J. M.; Kerridge, A.; Kozimor, S. A.; Löble, M. W.; Martin, R. L.; Minasian, S. G.; Mocko, V.; La Pierre, H. S.; Seidler, G. T.; Shuh, D. K.; Wilkerson, M. P.; Wolfsberg, L. E.; Yang, P. *J. Am. Chem. Soc.* **2018**, *140*, 17977-17984.

[39] Platts, J. A.; Baker, R. J. *Dalton Trans.* **2020**, *49*, 1077-1088.

[40] Dognon, J.-P. *Coord. Chem. Rev.* **2014**, *266-267*, 110-122.

[41] Huang, Q.-R.; Kingham, J. R.; Kaltsoyannis, N. *Dalton Trans.* **2015**, *44*, 2554-2566.

[42] Kerridge, A. *Chem. Commun.* **2017**, *53*, 6685-6695.

[43] Kerridge, A. *RSC Adv.* **2014**, *4*, 12078-12086.

[44] Kaltsoyannis, N. *Inorg. Chem.* **2013**, *52*, 3407-3413.

[45] Kaltsoyannis, N. *Chem. Eur. J.* **2018**, *24*, 2815-2825.

[46] Clark, D. L. *Los Alamos Sci.* **2000**, *28*, 364-381.

[47] Altmaier, M.; Gaona, X.; Fanghänel, T. *Chem. Rev.* **2013**, *113*, 901-943.

[48] Natrajan, L. S.; Swinburne, A. N.; Andrews, M. B.; Randall, S.; Heath, S. L. *Coord. Chem. Rev.* **2014**, *266–267*, 171-193.

[49] Schöne, S.; Radoske, T.; März, J.; Stumpf, T.; Ikeda-Ohno, A. *Inorg. Chem.* **2018**, *57*, 13318-13329.

[50] Neck, V.; Kim, J. I. *Radiochim. Acta* **2001**, *89*, 1-16.

[51] Walther, C.; Denecke, M. A. *Chem. Rev.* **2013**, *113*, 995-1015.

[52] Denning, R. G. *J. Phys. Chem. A* **2007**, *111*, 4125-4143.

[53] Sullivan, J. C.; Hindman, J. C.; Zielen, A. J. *J. Am. Chem. Soc.* **1961**, *83*, 3373-3378.

[54] Guillaume, B.; Hobart, D. E.; Bourges, J. Y. *J. Inorg. Nucl. Chem.* **1981**, *43*, 3295-3299.

[55] Krot, N. N.; Grigoriev, M. S. *Russ. Chem. Rev.* **2004**, *73*, 89-100.

[56] Sullens, T. A.; Jensen, R. A.; Shvareva, T. Y.; Albrecht-Schmitt, T. E. *J. Am. Chem. Soc.* **2004**, *126*, 2676-2677.

[57] Andrews, M. B.; Cahill, C. L. *Chem. Rev.* **2013**, *113*, 1121-1136.

[58] Wang, S.; Diwu, J.; Alekseev, E. V.; Jouffret, L. J.; Depmeier, W.; Albrecht-Schmitt, T. E. *Inorg. Chem.* **2012**, *51*, 7016-7018.

[59] Apostolidis, C.; Schimmelpfennig, B.; Magnani, N.; Lindqvist-Reis, P.; Walter, O.; Sykora, R.; Morgenstern, A.; Colineau, E.; Caciuffo, R.; Klenze, R.; Haire Richard, G.; Rebizant, J.; Bruchertseifer, F.; Fanghänel, T. *Angew. Chem. Int. Ed.* **2010**, *49*, 6343-6347.

[60] Thuéry, P.; Atoini, Y.; Harrowfield, J. *Cryst. Growth Des.* **2018**, *18*, 3167-3177.

[61] Langeslay, R. R.; Fieser, M. E.; Ziller, J. W.; Furche, F.; Evans, W. J. *Chem. Sci.* **2015**, *6*, 517-521.

[62] MacDonald, M. R.; Fieser, M. E.; Bates, J. E.; Ziller, J. W.; Furche, F.; Evans, W. J. *J. Am. Chem. Soc.* **2013**, *135*, 13310-13313.

[63] Su, J.; Windorff, C. J.; Batista, E. R.; Evans, W. J.; Gaunt, A. J.; Janicke, M. T.; Kozimor, S. A.; Scott, B. L.; Woen, D. H.; Yang, P. *J. Am. Chem. Soc.* **2018**, *140*, 7425-7428.

[64] Windorff, C. J.; Chen, G. P.; Cross, J. N.; Evans, W. J.; Furche, F.; Gaunt, A. J.; Janicke, M. T.; Kozimor, S. A.; Scott, B. L. *J. Am. Chem. Soc.* **2017**, *139*, 3970-3973.

[65] Guo, F.-S.; Tsoureas, N.; Huang, G.-Z.; Tong, M.-L.; Mansikkamäki, A.; Layfield, R. A. *Angew. Chem. Int. Ed.* **2020**, *59*, 2299-2303.

[66] La Pierre, H. S.; Meyer, K. *Prog. Inorg. Chem.* **2014**, *58*, 303-415.

[67] Karmel, I. S. R.; Batrice, R. J.; Eisen, M. S. *Inorganics* **2015**, *3*, 392-428.

[68] Eisen, M.; Liu, H.; Ghatak, T. *Chem. Commun.* **2017**, *53*, 11278-11297.

[69] Kanellakopulos, B.; Dornberger, E.; Baumgaertner, F. *Inorg. Nucl. Chem. Lett.* **1974**, *10*, 155-160.

[70] Evans, W. J.; Walensky, J. R.; Ziller, J. W. *Chem. Eur. J.* **2009**, *15*, 12204-12207.

[71] Ephritikhine, M. *Organometallics* **2013**, *32*, 2464-2488.

[72] Arnold, P. L.; Dutkiewicz, M. S.; Walter, O. *Chem. Rev.* **2017**, *117*, 11460-11475.

[73] Dutkiewicz, M. S.; Apostolidis, C.; Walter, O.; Arnold, P. L. *Chem. Sci.* **2017**, *8*, 2553-2561.

[74] Pattenaude, S. A.; Anderson, N. H.; Bart, S. C.; Gaunt, A. J.; Scott, B. L. *Chem. Commun.* **2018**, *54*, 6113-6116.

[75] Galley, S. S.; Sperling, J. M.; Windorff, C. J.; Zeller, M.; Albrecht-Schmitt, T. E.; Bart, S. C. *Organometallics* **2019**, *38*, 606-609.

[76] Cantat, T.; Scott, B. L.; Kiplinger, J. L. *Chem. Commun.* **2010**, *46*, 919-921.

[77] Patel, D.; Wooles, A. J.; Hashem, E.; Omorodion, H.; Baker, R. J.; Liddle, S. T. *New J. Chem.* **2015**, *39*, 7559-7562.

[78] Reilly, S. D.; Brown, J. L.; Scott, B. L.; Gaunt, A. J. *Dalton Trans.* **2014**, *43*, 1498-1501.

[79] Jones, M. B.; Gaunt, A. J. *Chem. Rev.* **2013**, *113*, 1137-1198.

[80] Cowie, B. E.; Purkis, J. M.; Austin, J.; Love, J. B.; Arnold, P. L. *Chem. Rev.* **2019**, *119*, 10595-10637.

[81] Fortier, S.; Hayton, T. W. *Coord. Chem. Rev.* **2010**, *254*, 197-214.

[82] Schöne, S.; Radoske, T.; März, J.; Stumpf, T.; Patzschke, M.; Ikeda-Ohno, A. *Chem. Eur. J.* **2017**, *23*, 13574-13578.

[83] Carter, K. P.; Kalaj, M.; Kerridge, A.; Ridenour, J. A.; Cahill, C. L. *Inorg. Chem.* **2018**, *57*, 2714-2723.

[84] Hayton, T. W. *Dalton Trans.* **2018**, *47*, 1003-1009.

[85] Edelmann, F. T.; Farnaby, J. H.; Jaroschik, F.; Wilson, B. *Coord. Chem. Rev.* **2019**, *398*, 113005.

[86] Hyeon, J.-Y.; Gottfriedsen, J.; Edelmann, F. T. *Coord. Chem. Rev.* **2005**, *249*, 2787-2844.

[87] Edelmann, F. T. *Coord. Chem. Rev.* **2006**, *250*, 2511-2564.

[88] Gottfriedsen, J.; Edelmann, F. T. *Coord. Chem. Rev.* **2006**, *250*, 2347-2410.

[89] Gottfriedsen, J.; Edelmann, F. T. *Coord. Chem. Rev.* **2007**, *251*, 142-202.

[90] Edelmann, F. T. *Coord. Chem. Rev.* **2009**, *253*, 2515-2587.

[91] Edelmann, F. T. *Coord. Chem. Rev.* **2009**, *253*, 343-409.

[92] Edelmann, F. T. *Coord. Chem. Rev.* **2011**, *255*, 1834-1920.

[93] Edelmann, F. T. *Coord. Chem. Rev.* **2012**, *256*, 2641-2740.

[94] Edelmann, F. T. *Coord. Chem. Rev.* **2012**, *256*, 1151-1228.

[95] Edelmann, F. T. *Coord. Chem. Rev.* **2013**, *257*, 1122-1231.

[96] Edelmann, F. T. *Coord. Chem. Rev.* **2014**, *261*, 73-155.

[97] Edelmann, F. T. *Coord. Chem. Rev.* **2015**, *284*, 124-205.

[98] Edelmann, F. T. *Coord. Chem. Rev.* **2016**, *306*, 346-419.

[99] Edelmann, F. T. *Coord. Chem. Rev.* **2016**, *318*, 29-130.

[100] Edelmann, F. T. *Coord. Chem. Rev.* **2017**, *338*, 27-140.

[101] Edelmann, F. T. *Coord. Chem. Rev.* **2018**, *370*, 129-223.

[102] Pearson, R. G. *Inorg. Chim. Acta* **1995**, *240*, 93-98.

[103] Sessler, J. L.; Melfi, P. J.; Pantos, G. D. *Coord. Chem. Rev.* **2006**, *250*, 816-843.

[104] Hayes, C. E.; Leznoff, D. B. *Coord. Chem. Rev.* **2014**, *266-267*, 155-170.

[105] Shriner, R. L.; Neumann, F. W. *Chem. Rev.* **1944**, *35*, 351-425.

[106] Sanger, A. R. *Inorg. Nucl. Chem. Lett.* **1973**, *9*, 351-354.

[107] Edelmann, F. T., Recent Progress in the Chemistry of Metal Amidinates and Guanidinates: Syntheses, Catalysis and Materials. In *Advances in Organometallic Chemistry*, Anthony, F. H.; Mark, J. F., Eds. Academic Press: Cambridge, **2013**, Vol. 61, pp 55-374.

[108] Gautier, J.-A.; Miocque, M.; Farnoux, C. C., Preparation and synthetic uses of amidines. In *Amidines and Imidates* John Wiley & Sons, Ltd.: Hoboken, **1975**, pp 283-348.

[109] Pornet, J.; Miginiac, L. *Bull. Soc. Chim. Fr.* **1974**, *5-6*, 994-998.

[110] Van der Maelen, J. F.; Brugos, J.; García-Álvarez, P.; Cabeza, J. A. *J. Mol. Struct.* **2020**, *1201*, 127217.

[111] Liebing, P.; Harmgarth, N.; Lorenz, V.; Zörner, F.; Hilfert, L.; Busse, S.; Edelmann, F. T. *Z. Anorg. Allg. Chem.* **2019**, *645*, 440-446.

[112] Schuster, J. K.; Roy, D. K.; Lenczyk, C.; Mies, J.; Braunschweig, H. *Inorg. Chem.* **2019**, *58*, 2652-2658.

[113] Srinivas, B.; Chang, C.-C.; Chen, C.-H.; Y. Chiang, M.; Chen, I. T.; Wang, Y.; Lee, G.-H. *J. Chem. Soc., Dalton Trans.* **1997**, 957-964.

[114] Mayo, D. H.; Peng, Y.; Zavalij, P.; Bowen, K. H.; Eichhorn, B. W. *Acta Crystallogr. C* **2013**, *69*, 1120-1123.

[115] Junold, K.; Burschka, C.; Bertermann, R.; Tacke, R. *Dalton Trans.* **2010**, *39*, 9401-9413.

[116] Junold, K.; Burschka, C.; Bertermann, R.; Tacke, R. *Dalton Trans.* **2011**, *40*, 9844-9857.

[117] Junold, K.; Baus, J. A.; Burschka, C.; Vent-Schmidt, T.; Riedel, S.; Tacke, R. *Inorg. Chem.* **2013**, *52*, 11593-11599.

[118] Junold, K.; Nutz, M.; Baus, J. A.; Burschka, C.; Fonseca Guerra, C.; Bickelhaupt, F. M.; Tacke, R. *Chem. Eur. J.* **2014**, *20*, 9319-9329.

[119] Yadav, S.; Swamy, V. S. V. S. N.; Gonnade, R.; Sen, S. S. *ChemistrySelect* **2016**, *1*, 1066-1071.

[120] Protchenko, A. V.; Urbano, J.; Abdalla, J. A. B.; Campos, J.; Vidovic, D.; Schwarz, A. D.; Blake, M. P.; Mountford, P.; Jones, C.; Aldridge, S. *Angew. Chem. Int. Ed.* **2017**, *56*, 15098-15102.

[121] Cabeza, J. A.; García-Álvarez, P.; Gobetto, R.; González-Álvarez, L.; Nervi, C.; Pérez-Carreño, E.; Polo, D. *Organometallics* **2016**, *35*, 1761-1770.

[122] Liguori, D.; Centore, R.; Tuzi, A.; Grisi, F.; Sessa, I.; Zambelli, A. *Macromolecules* **2003**, *36*, 5451-5458.

[123] Ren, S.; Qiu, Z.; Xie, Z. *Organometallics* **2013**, *32*, 4292-4300.

[124] Keane, A. J.; Yonke, B. L.; Hirotsu, M.; Zavalij, P. Y.; Sita, L. R. *J. Am. Chem. Soc.* **2014**, *136*, 9906-9909.

[125] Yamaguchi, Y.; Ozaki, S.; Hinago, H.; Kobayashi, K.; Ito, T. *Inorg. Chim. Acta* **2005**, *358*, 2363-2370.

[126] Farrell, W. S.; Zavalij, P. Y.; Sita, L. R. *Organometallics* **2016**, *35*, 2361-2366.

[127] Wang, S.; Harmgarth, N.; Liebing, P.; Edelmann, F. T. *Acta Crystallogr. E* **2016**, *72*, 1786-1790.

[128] Peng, T.; Yang, Y.; Liu, Y.; Ma, D.; Hou, Z.; Wang, Y. *Chem. Commun.* **2011**, *47*, 3150-3152.

[129] Li, G.; Li, P.; Zhuang, X.; Ye, K.; Liu, Y.; Wang, Y. *ACS Appl. Mater. Interfaces* **2017**, *9*, 11749-11758.

[130] Lai, P.-N.; Brysacz, C. H.; Alam, M. K.; Ayoub, N. A.; Gray, T. G.; Bao, J.; Teets, T. S. *J. Am. Chem. Soc.* **2018**, *140*, 10198-10207.

[131] Yu, Z.-T.; Yuan, Y.-J.; Cai, J.-G.; Zou, Z.-G. *Chem. Eur. J.* **2013**, *19*, 1303-1310.

[132] Drose, P.; Hrib, C. G.; Blaurock, S.; Edelmann, F. T. *Acta Crystallogr. E* **2010**, *66*, m1474.

[133] Brunner, H.; Lukassek, J.; Agrifoglio, G. *J. Organomet. Chem.* **1980**, *195*, 63-76.

[134] Brunner, H.; Agrifoglio, G. *Monatsh. Chem.* **1980**, *111*, 275-287.

[135] Korp, J. D.; Bernal, I. *Chem. Scr.* **1983**, *22*, 60-63.

[136] Appel, R.; Kleinstück, R.; Ziehn, K.-d. *Chem. Ber.* **1971**, *104*, 1335-1336.

[137] Hiatt, R. R.; Shaio, M.-J.; Georges, F. *J. Org. Chem.* **1979**, *44*, 3265-3266.

[138] Drabowicz, J.; Pacholczyk, M. *Phosphorus Sulfur* **1987**, *29*, 257-263.

[139] Schlama, T.; Gouverneur, V.; Mioskowski, C. *Tetrahedron Lett.* **1996**, *37*, 7047-7048.

[140] Hasegawa, T.; Morino, K.; Tanaka, Y.; Katagiri, H.; Furusho, Y.; Yashima, E. *Macromolecules* **2006**, *39*, 482-488.

[141] Benndorf, P.; Preuß, C.; Roesky, P. W. *J. Organomet. Chem.* **2011**, *696*, 1150-1155.

[142] He, M.; Gamer, M. T.; Roesky, P. W. *Organometallics* **2016**, *35*, 2638-2644.

[143] Brunner, T. S.; Hartenstein, L.; Roesky, P. W. *J. Organomet. Chem.* **2013**, *730*, 32-36.

[144] Benndorf, P.; Jenter, J.; Zielke, L.; Roesky, P. W. *Chem. Commun.* **2011**, *47*, 2574-2576.

[145] Benndorf, P.; Kratsch, J.; Hartenstein, L.; Preuss, C. M.; Roesky, P. W. *Chem. Eur. J.* **2012**, *18*, 14454-14463.

[146] Kratsch, J.; Kuzdrowska, M.; Schmid, M.; Kazeminejad, N.; Kaub, C.; Oña-Burgos, P.; Guillaume, S. M.; Roesky, P. W. *Organometallics* **2013**, *32*, 1230-1238.

[147] Brunner, T. S.; Benndorf, P.; Gamer, M. T.; Knöfel, N.; Gugau, K.; Roesky, P. W. *Organometallics* **2016**, *35*, 3474-3487.

[148] Brunner, T.; Roesky, P. W. *J. Organomet. Chem.* **2017**, *849-850*, 150-156.

[149] He, M.; Chen, Z.; Moreno Pineda, E.; Liu, X.; Bouwman, E.; Ruben, M.; Roesky, P. W. *Eur. J. Inorg. Chem.* **2016**, *2016*, 5506-5506.

[150] Wedler, M.; Roesky, H. W.; Edelmann, F. *J. Organomet. Chem.* **1988**, *345*, C1-C3.

[151] Wedler, M.; Knösel, F.; Noltemeyer, M.; Edelmann, F. T.; Behrens, U. *J. Organomet. Chem.* **1990**, *388*, 21-45.

[152] Wedler, M.; Knösel, F.; Edelmann, F. T.; Behrens, U. *Chem. Ber.* **1992**, *125*, 1313-1318.

[153] Villiers, C.; Thuéry, P.; Ephritikhine, M. *Eur. J. Inorg. Chem.* **2004**, *2004*, 4624-4632.

[154] Villiers, C.; Thuery, P.; Ephritikhine, M. *Chem. Commun.* **2007**, 2832-2834.

[155] Sarsfield, M. J.; Helliwell, M.; Raftery, J. *Inorg. Chem.* **2004**, *43*, 3170-3179.

[156] Evans, W. J.; Walensky, J. R.; Ziller, J. W. *Inorg. Chem.* **2010**, *49*, 1743-1749.

[157] Karmel, I. S. R.; Elkin, T.; Fridman, N.; Eisen, M. S. *Dalton Trans.* **2014**, *43*, 11376-11387.

[158] Karmel, I. S. R.; Fridman, N.; Eisen, M. S. *Organometallics* **2015**, *34*, 636-643.

[159] Sarsfield, M. J.; Helliwell, M. *J. Am. Chem. Soc.* **2004**, *126*, 1036-1037.

[160] Kaes, C.; Katz, A.; Hosseini, M. W. *Chem. Rev.* **2000**, *100*, 3553-3590.

[161] Blau, F. *Monatsh. Chem.* **1889**, *10*, 375-388.

[162] Roy, B. C.; Chakrabarti, K.; Shee, S.; Paul, S.; Kundu, S. *Chem. Eur. J.* **2016**, *22*, 18147-18155.

[163] Malkov, A. V.; Kocovsky, P. *Curr. Org. Chem.* **2003**, *7*, 1737-1757.

[164] Le Bozec, H.; Guerchais, V. *C. R. Chim.* **2013**, *16*, 1172-1182.

[165] Happ, B.; Winter, A.; Hager, M. D.; Schubert, U. S. *Chem. Soc. Rev.* **2012**, *41*, 2222-2255.

[166] Adelaide, M.; James, O. O. *Elixir Appl. Chem.* **2014**, *67*, 21413-21420.

[167] Barton, J. K. *Science* **1986**, *233*, 727-734.

[168] Newkome, G. R.; Patri, A. K.; Holder, E.; Schubert, U. S. *Eur. J. Org. Chem.* **2004**, *2004*, 235-254.

[169] Bencini, A.; Lippolis, V. *Coord. Chem. Rev.* **2010**, *254*, 2096-2180.

[170] Constable, E. C., Homoleptic Complexes of 2,2'-Bipyridine. In *Advances in Inorganic Chemistry*, Sykes, A. G., Ed. Academic Press: Cambridge, **1989**, Vol. 34, pp 1-63.

[171] Sammes, P. G.; Yahioglu, G. *Chem. Soc. Rev.* **1994**, *23*, 327-334.

[172] Constable, E. C.; Housecroft, C. E. *Coord. Chem. Rev.* **2017**, *350*, 84-104.

[173] Carter, K. P.; Kalaj, M.; Cahill, C. L. *Eur. J. Inorg. Chem.* **2016**, *2016*, 126-137.

[174] Thuéry, P. *Eur. J. Inorg. Chem.* **2013**, *2013*, 4563-4573.

[175] Berthet, J.-C.; Nierlich, M.; Ephritikhine, M. *Chem. Commun.* **2003**, 1660-1661.

[176] Charushnikova, I. A.; Krot, N. N.; Starikova, Z. A. *Radiochim. Acta* **2007**, *95*, 495-499.

[177] Adelani, P. O.; Burns, P. C. *Inorg. Chem.* **2012**, *51*, 11177-11183.

[178] Thuéry, P.; Harrowfield, J. *CrystEngComm* **2016**, *18*, 3905-3918.

[179] Bragg, W. L.; Bragg, W. H. *Proc. Roy. Soc. A - Math. Phys.* **1913**, *89*, 248-277.

[180] Patterson, A. L. *Phys. Review* **1934**, *46*, 372-376.

[181] Hauptman, H. *Science* **1986**, *233*, 178-183.

[182] Oszlanyi, G.; Suto, A. *Acta Crystallogr. A* **2004**, *60*, 134-141.

[183] Sheldrick, G. M. *Acta Crystallogr. A* **2015**, *71*, 3-8.

[184] Sheldrick, G. M. *Acta Crystallogr. A* **2008**, *64*, 112-122.

[185] Václav, P.; Michal, D.; Lukáš, P. *Z. Krist. - Cryst. Mater.* **2014**, *229*, 345-352.

[186] Bijvoet, J. M.; Peerdeman, A. F.; van Bommel, A. J. *Nature* **1951**, *168*, 271-272.

[187] Friedel, G. *Compt. rend.* **1913**, *156*, 1676-1679.

[188] Flack, H. D.; Bernardinelli, G. *Chirality* **2007**, *20*, 681-690.

[189] Flack, H. D. *Acta Crystallogr. A* **1983**, *39*, 876-881.

[190] Massa, W., *Kristallstrukturbestimmung*. 5th ed.; Vieweg+Teubner: Wiesbaden, **2007**.

[191] Luger, P., *Modern X-Ray Analysis on Single Crystals*. 2nd ed.; De Gruyter: Berlin, Boston, **2014**.

[192] Günther, H., *NMR Spektroskopie*. 3rd ed.; Georg Thieme Verlag Stuttgart, **1992**.

[193] Parigi, G. *Prog. Nucl. Magn. Reson. Spectrosc.* **2019**, *114-115*, 211-236.

[194] Piguet, C.; Geraldes, C. F. G. C., Paramagnetic NMR lanthanide induced shifts for extracting solution structures. In *Handbook on the Physics and Chemistry of Rare Earths*, Elsevier: Amsterdam, **2003**, Vol. 33, pp 353-463.

[195] Funk, A. M.; Finney, K.-L. N. A.; Harvey, P.; Kenwright, A. M.; Neil, E. R.; Rogers, N. J.; Kanthi Senanayake, P.; Parker, D. *Chem. Sci.* **2015**, *6*, 1655-1662.

[196] Bertini, I.; Luchinat, C.; Parigi, G. *Prog. Nucl. Magn. Reson. Spectrosc.* **2002**, *40*, 249-273.

[197] Kurland, R. J.; McGarvey, B. R. *J. Magn. Reson.* **1970**, *2*, 286-301.

[198] Bleaney, B. *J. Magn. Reson.* **1972**, *8*, 91-100.

[199] Suturina, E. A.; Mason, K.; Geraldes, C. F. G. C.; Kuprov, I.; Parker, D. *Angew. Chem. Int. Ed.* **2017**, *56*, 12215-12218.

[200] Martin, B.; Autschbach, J. *J. Chem. Phys.* **2015**, *142*, 054108.

[201] Kreidt, E.; Bischof, C.; Platas-Iglesias, C.; Seitz, M. *Inorg. Chem.* **2016**, *55*, 5549-5557.

[202] Harnden, A. C.; Suturina, E. A.; Batsanov, A. S.; Senanayake, P. K.; Fox, M. A.; Mason, K.; Vonci, M.; McInnes, E. J. L.; Chilton, N. F.; Parker, D. *Angew. Chem. Int. Ed.* **2019**, *58*, 10290-10294.

[203] Ravera, E.; Parigi, G.; Luchinat, C. *J. Magn. Reson.* **2019**, *306*, 173-179.

[204] Pintacuda, G.; John, M.; Su, X.-C.; Otting, G. *Acc. Chem. Res.* **2007**, *40*, 206-212.

[205] Grey, C. P.; Dupré, N. *Chem. Rev.* **2004**, *104*, 4493-4512.

[206] Seymour, I. D.; Middlemiss, D. S.; Halat, D. M.; Trease, N. M.; Pell, A. J.; Grey, C. P. *J. Am. Chem. Soc.* **2016**, *138*, 9405-9408.

[207] Wall, T. F.; Jan, S.; Autillo, M.; Nash, K. L.; Guerin, L.; Naour, C. L.; Moisy, P.; Berthon, C. *Inorg. Chem.* **2014**, *53*, 2450-2459.

[208] Autillo, M.; Guerin, L.; Guillaumont, D.; Moisy, P.; Bolvin, H.; Berthon, C. *Inorg. Chem.* **2016**, *55*, 12149-12157.

[209] Evans, D. F. *J. Chem. Soc.* **1959**, 2003-2005.

[210] Autillo, M.; Guerin, L.; Dumas, T.; Grigoriev, M. S.; Fedoseev, A. M.; Cammelli, S.; Solari, P. L.; Guillaumont, D.; Guilbaud, P.; Moisy, P.; Bolvin, H.; Berthon, C. *Chem. Eur. J.* **2019**, *25*, 4435-4451.

[211] Bader, R. F. W., *Atoms in Molecules: A Quantum Theory*. 1st ed.; Oxford University Press: Oxford, **1990**.

[212] Weinhold, F. *J. Comput. Chem.* **2012**, *33*, 2363-2379.

[213] Reed, A. E.; Weinstock, R. B.; Weinhold, F. *J. Chem. Phys.* **1985**, *83*, 735-746.

[214] Fichter, S.; Kaufmann, S.; Kaden, P.; Brunner, T. S.; Stumpf, T.; Roesky, P. W.; März, J. *Chem. Eur. J.* **2020**, 10.1002/chem.202001865.

[215] Schöne, S. Vierwertige Actinidkomplexe chiraler Benzamidinate - Synthese und Charakterisierung. Master Thesis, Dresden University of Technology, **2016**.

[216] Schöne, S.; März, J.; Kaden, P.; Patzschke, M.; Ikeda-Ohno, A. *Synthesis and characterization of chiral thorium(IV) and uranium(IV) benzamidinate complexes*; Annual Report; Institute for Resource Ecology: **2017**, p 18.

[217] Dröse, P.; Crozier, A. R.; Lashkari, S.; Gottfriedsen, J.; Blaurock, S.; Hrib, C. G.; Maichle-Mössmer, C.; Schädle, C.; Anwander, R.; Edelmann, F. T. *J. Am. Chem. Soc.* **2010**, *132*, 14046-14047.

[218] Jordan, R. F.; Dasher, W. E.; Echols, S. F. *J. Am. Chem. Soc.* **1986**, *108*, 1718-1719.

[219] Uhrhammer, R.; Su, Y.-X.; Swenson, D. C.; Jordan, R. F. *Inorg. Chem.* **1994**, *33*, 4398-4402.

[220] Wang, M.; Weyhermüller, T.; England, J.; Wieghardt, K. *Inorg. Chem.* **2013**, *52*, 12763-12776.

[221] Il'in, E. G.; Shcherbakova, M. N.; Buslaev, Y. A. *Koord. Khim.* **1975**, *1*, 1179-1189.

[222] Roussel, P.; Alcock, N. W.; Boaretto, R.; Kingsley, A. J.; Munslow, I. J.; Sanders, C. J.; Scott, P. *Inorg. Chem.* **1999**, *38*, 3651-3656.

[223] King, D. M.; Tuna, F.; McInnes, E. J. L.; McMaster, J.; Lewis, W.; Blake, A. J.; Liddle, S. T. *Nature Chem.* **2013**, *5*, 482-488.

[224] Fortier, S.; Wu, G.; Hayton, T. W. *Dalton Trans.* **2010**, *39*, 352-354.

[225] Wildman, E. P.; Ostrowski, J. P. A.; King, D. M.; Lewis, W.; Liddle, S. T. *Polyhedron* **2017**, *125*, 2-8.

[226] Settineri, N. S.; Shiau, A. A.; Arnold, J. *Chem. Commun.* **2018**, *54*, 10913-10916.

[227] Stobbe, B. C.; Powell, D. R.; Thomson, R. K. *Dalton Trans.* **2017**, *46*, 4888-4892.

[228] Shannon, R. *Acta Crystallogr. A* **1976**, *32*, 751-767.

[229] Jones, C.; Junk, P. C.; Leary, S. G.; Smithies, N. A. *Inorg. Chem. Commun.* **2003**, *6*, 1126-1128.

[230] Kempe, R.; Arndt, P. *Inorg. Chem.* **1996**, *35*, 2644-2649.

[231] Ong, T.-G.; Yap, G. P. A.; Richeson, D. S. *Chem. Commun.* **2003**, 2612-2613.

[232] Ong, T.-G.; Yap, G. P. A.; Richeson, D. S. *J. Am. Chem. Soc.* **2003**, *125*, 8100-8101.

[233] Cook, T. M.; Steren, C. A.; Xue, Z.-L. *Dalton Trans.* **2018**, *47*, 11030-11040.

[234] Zhang, Y.; Xie, J.-R.; Guo, J.-P.; Wei, X.-H.; Huang, S.-P.; Liu, D.-S. *Inorg. Chim. Acta* **2009**, *362*, 583-586.

[235] Zhou, M.; Tong, H.; Wei, X.; Liu, D. *J. Organomet. Chem.* **2007**, *692*, 5195-5202.

[236] Raymond, K. N.; Eigenbrot, C. W. *Acc. Chem. Res.* **1980**, *13*, 276-283.

[237] Bursten, B. E.; Palmer, E. J.; Sonnenberg, J. L., On the role of f-orbitals in the bonding in f-element complexes: the "feudal" model as applied to organoactinide and actinide aquo complexes. In *Recent Advances in Actinide Science, Special Publications* May, I.; Bryan, N. D.; Alvares, R., Eds. The Royal Society of Chemistry: London, **2006**, pp 157-162.

[238] Beekmeyer, R.; Kerridge, A. *Inorganics* **2015**, *3*, 482-499.

[239] Cheisson, T.; Kersey, K. D.; Mahieu, N.; McSkimming, A.; Gau, M. R.; Carroll, P. J.; Schelter, E. J. *J. Am. Chem. Soc.* **2019**, *141*, 9185-9190.

[240] Cary, S. K.; Vasiliu, M.; Baumbach, R. E.; Stritzinger, J. T.; Green, T. D.; Diefenbach, K.; Cross, J. N.; Knappenberger, K. L.; Liu, G.; Silver, M. A.; DePrince, A. E.; Polinski, M. J.; Van Cleve, S. M.; House, J. H.; Kikugawa, N.; Gallagher, A.; Arico, A. A.; Dixon, D. A.; Albrecht-Schmitt, T. E. *Nature Commun.* **2015**, *6*, 6827.

[241] Cross, J. N.; Su, J.; Batista, E. R.; Cary, S. K.; Evans, W. J.; Kozimor, S. A.; Mocko, V.; Scott, B. L.; Stein, B. W.; Windorff, C. J.; Yang, P. *J. Am. Chem. Soc.* **2017**, *139*, 8667-8677.

[242] Cary, S. K.; Su, J.; Galley, S. S.; Albrecht-Schmitt, T. E.; Batista, E. R.; Ferrier, M. G.; Kozimor, S. A.; Mocko, V.; Scott, B. L.; Van Alstine, C. E.; White, F. D.; Yang, P. *Dalton Trans.* **2018**, *47*, 14452-14461.

[243] Yang, P.; Zhou, E.; Fang, B.; Hou, G.; Zi, G.; Walter, M. D. *Organometallics* **2016**, *35*, 2129-2139.

[244] Dame, A. N.; Bharara, M. S.; Barnes, C. L.; Walensky, J. R. *Eur. J. Inorg. Chem.* **2015**, *2015*, 2996-3005.

[245] Thomson, R. K.; Cantat, T.; Scott, B. L.; Morris, D. E.; Batista, E. R.; Kiplinger, J. L. *Nature Chem.* **2010**, *2*, 723-729.

[246] Diana, E.; Gatterer, K.; Kettle, S. F. A. *Phys. Chem. Chem. Phys.* **2016**, *18*, 414-425.

[247] Pyykkö, P. *Phys. Scripta* **1979**, *20*, 647-651.

[248] Blackburn, O. A.; Chilton, N. F.; Keller, K.; Tait, C. E.; Myers, W. K.; McInnes, E. J. L.; Kenwright, A. M.; Beer, P. D.; Timmel, C. R.; Faulkner, S. *Angew. Chem. Int. Ed.* **2015**, *54*, 10783-10786.

[249] Blackburn, O. A.; Kenwright, A. M.; Beer, P. D.; Faulkner, S. *Dalton Trans.* **2015**, *44*, 19509-19517.

[250] Blackburn, O. A.; Routledge, J. D.; Jennings, L. B.; Rees, N. H.; Kenwright, A. M.; Beer, P. D.; Faulkner, S. *Dalton Trans.* **2016**, *45*, 3070-3077.

[251] Brown, J. L.; Gaunt, A. J.; King, D. M.; Liddle, S. T.; Reilly, S. D.; Scott, B. L.; Wooles, A. J. *Chem. Commun.* **2016**, *52*, 5428-5431.

[252] Roger, M.; Barros, N.; Arliguie, T.; Thuéry, P.; Maron, L.; Ephritikhine, M. *J. Am. Chem. Soc.* **2006**, *128*, 8790-8802.

[253] Mazzanti, M.; Wietzke, R.; Pécaut, J.; Latour, J.-M.; Maldivi, P.; Remy, M. *Inorg. Chem.* **2002**, *41*, 2389-2399.

[254] Berthet, J.-C.; Rivière, C.; Miquel, Y.; Nierlich, M.; Madic, C.; Ephritikhine, M. *Eur. J. Inorg. Chem.* **2002**, *2002*, 1439-1446.

[255] Berthet, J.-C.; Onno, J.-M.; Gupta, F.; Rivière, C.; Thuéry, P.; Nierlich, M.; Madic, C.; Ephritikhine, M. *Polyhedron* **2012**, *45*, 107-125.

[256] Meinrath, G. *J. Radioanal. Nucl. Chem.* **1997**, *224*, 119-126.

[257] Müller, K.; Foerstendorf, H.; Steudtner, R.; Tsushima, S.; Kumke, M. U.; Lefèvre, G.; Rothe, J.; Mason, H.; Szabó, Z.; Yang, P.; Adam, C. K. R.; André, R.; Brennenstuhl, K.; Chiorescu, I.; Cho, H. M.; Creff, G.; Coppin, F.; Dardenne, K.; Den Auwer, C.; Drobot, B.; Eidner, S.; Hess, N. J.; Kaden, P.; Kremleva, A.; Kretzschmar, J.; Krüger, S.; Platts, J. A.; Panak, P. J.; Polly, R.; Powell, B. A.; Rabung, T.; Redon, R.; Reiller, P. E.; Rösch, N.; Rossberg, A.; Scheinost, A. C.; Schimmelpfennig, B.; Schreckenbach, G.; Skerencak-Frech, A.; Sladkov, V.; Solari, P. L.; Wang, Z.; Washton, N. M.; Zhang, X. *ACS Omega* **2019**, *4*, 8167-8177.

[258] Burns, P. C.; Ewing, R. C.; Hawthorne, F. C. *Can. Mineral.* **1997**, *35*, 1551-1570.

[259] Baker, R. J. *Chem. Eur. J.* **2012**, *18*, 16258-16271.

[260] Pedrick, E. A.; Schultz, J. W.; Wu, G.; Mirica, L. M.; Hayton, T. W. *Inorg. Chem.* **2016**, *55*, 5693-5701.

[261] Copping, R.; Jeon, B.; Pemmaraju, C. D.; Wang, S.; Teat, S. J.; Janousch, M.; Tyliszczak, T.; Canning, A.; Grønbech-Jensen, N.; Prendergast, D.; Shuh, D. K. *Inorg. Chem.* **2014**, *53*, 2506-2515.

[262] Schöne, S.; März, J.; Stumpf, T.; Ikeda-Ohno, A. *Dalton Trans.* **2019**, *48*, 6700-6703.

[263] Cornet, S. M.; Haller, L. J. L.; Sarsfield, M. J.; Collison, D.; Helliwell, M.; May, I.; Kaltsoyannis, N. *Chem. Commun.* **2009**, 917-919.

[264] Brown, J. L.; Batista, E. R.; Boncella, J. M.; Gaunt, A. J.; Reilly, S. D.; Scott, B. L.; Tomson, N. C. *J. Am. Chem. Soc.* **2015**, *137*, 9583-9586.

[265] Bruker *APEX3* Bruker AXS Inc.: Madison, Wisconsin, USA, **2016**.

[266] Sheldrick, G. M. *SADABS*, University of Göttingen: Göttingen, **1996**.

[267] Huebschle, C. B.; Sheldrick, G. M.; Dittrich, B. *J. Appl. Crystallogr.* **2011**, *44*, 1281-1284.

[268] Spek, A. *Acta Crystallogr. C* **2015**, *71*, 9-18.

[269] Sheldrick, G. M. *TWINABS 2012/1*, Bruker: Madison, Wisconsin, USA, **2012**.

[270] *TURBOMOLE V7.1 2016 , a development of University of Karlsruhe and Forschungszentrum Karlsruhe GmbH , 1989-2007, TURBOMOLE GmbH , since 2007; available from http://www.turbomole.com* . **2016**.

[271] Neese, F. *Comput. Mol. Sci.* **2012**, *2*, 73-78.

[272] *AIMAll (Version 17.11.14), Todd A. Keith, TK Gristmill Software, Overland Park KS, USA, 2017; available from http://aim.tkgristmill.com*, **2017**.

[273] Perdew, J. P.; Burke, K.; Ernzerhof, M. *Phys. Rev. Lett.* **1996**, *77*, 3865-3868.

[274] Weigend, F.; Häser, M.; Patzelt, H.; Ahlrichs, R. *Chem. Phys. Lett.* **1998**, *294*, 143-152.

[275] Schäfer, A.; Huber, C.; Ahlrichs, R. *J. Chem. Phys.* **1994**, *100*, 5829-5835.

[276] Dolg, M.; Stoll, H.; Preuss, H. *J. Chem. Phys.* **1989**, *90*, 1730-1734.

[277] Küchle, W.; Dolg, M.; Stoll, H.; Preuss, H. *J. Chem. Phys.* **1994**, *100*, 7535-7542.

[278] Cao, X.; Dolg, M.; Stoll, H. *J. Chem. Phys.* **2003**, *118*, 487-496.

[279] Weigend, F. *Phys. Chem. Chem. Phys.* **2002**, *4*, 4285-4291.

[280] Klamt, A.; Schüürmann, G. *J. Chem. Soc.* **1993**, *2*, 799-805.

[281] Grimme, S.; Antony, J.; Ehrlich, S.; Krieg, H. *J. Chem. Phys.* **2010**, *132*, 154104.

[282] Perdew, J. P.; Ernzerhof, M.; Burke, K. *J. Chem. Phys.* **1996**, *105*, 9982-9985.

[283] Weigend, F.; Ahlrichs, R. *Phys. Chem. Chem. Phys.* **2005**, *7*, 3297-3305.

[284] Pantazis, D.; Neese, F. *J. Chem. Theory Comput.* **2009**, *5*, 2229-2238.

[285] Pantazis, D.; Neese, F. *J. Chem. Theory Comput.* **2011**, *7*, 677-684.

[286] Wolf, A.; Reiher, M.; Hess, B. *J. Chem. Phys.* **2002**, *117*, 9215-9226.

[287] Neese, F.; Wennmohs, F.; Hansen, A.; Becker, U. *Chem. Phys.* **2009**, *356*, 98-109.

[288] Stoychev, G.; Auer, A.; Neese, F. *J. Chem. Theory Comput.* **2017**, *13*, 554-562.

[289] Schäfer, A.; Horn, H.; Ahlrichs, R. *J. Chem. Phys.* **1992**, *97*, 2571-2577.

[290] Kuprov, I. *Spinach Libary*, v 1.4.5157; Southampton.

[291] Barry, J.; Du Preez, J. G. H.; Els, E.; Rohwer, H. E.; Wright, P. J. *Inorg. Chim. Acta* **1981**, *53*, L17-L18.

[292] Wilkerson, M. P.; Burns, C. J.; Paine, R. T.; Blosch, L. L.; Andersen, R. A. *Inorg. Synth.* **2004**, *34*, 93-95.

[293] Carmichael, C. D.; Jones, N. A.; Arnold, P. L. *Inorg. Chem.* **2008**, *47*, 8577-8579.

[294] Martin, N. P.; Volkringer, C.; Roussel, P.; März, J.; Hennig, C.; Loiseau, T.; Ikeda-Ohno, A. *Chem. Commun.* **2018**, *54*, 10060-10063.

[295] Zhao, X.-F.; Zhang, C. *Synthesis* **2007**, *2007*, 551-557.

[296] Weitz, I. S.; Rabinovitz, M. *J. Chem. Soc., Dalton Trans.* **1993**, 117-120.

[297] Aharonovich, S.; Botoshansky, M.; Balazs, Y. S.; Eisen, M. S. *Organometallics* **2012**, *31*, 3435-3438.

[298] Wang, M.; Yao, Y.-M.; Zhang, Y.; Zhang, Z.-Q.; Shi, L.-Y. *Acta Crystallogr. E* **2011**, *67*, m125.

[299] Roesky, H. W.; Meller, B.; Noltemeyer, M.; Schmidt, H.-G.; Scholz, U.; Sheldrick, G. M. *Chem. Ber.* **1988**, *121*, 1403-1406.

[300] Bailey, P. J.; Grant, K. J.; Mitchell, L. A.; Pace, S.; Parkin, A.; Parsons, S. *J. Chem. Soc., Dalton Trans.* **2000**, 1887-1891.

[301] Mullins, S. M.; Duncan, A. P.; Bergman, R. G.; Arnold, J. *Inorg. Chem.* **2001**, *40*, 6952-6963.

[302] R. Hagadorn, J.; Arnold, J. *J. Chem. Soc., Dalton Trans.* **1997**, 3087-3096.

[303] Wood; Yap, G. P. A.; Richeson, D. S. *Inorg. Chem.* **1999**, *38*, 5788-5794.

[304] Aharonovich, S.; Kulkarni, N. V.; Zhang, J.-S.; Botoshansky, M.; Kapon, M.; Eisen, M. S. *Dalton Trans.* **2013**, *42*, 16762-16772.

[305] Duncan, A. P.; Mullins, S. M.; Arnold, J.; Bergman, R. G. *Organometallics* **2001**, *20*, 1808-1819.

[306] Xu, K.; Milanov, A. P.; Winter, M.; Barreca, D.; Gasparotto, A.; Becker, H.-W.; Devi, A. *Eur. J. Inorg. Chem.* **2010**, *2010*, 1679-1688.

[307] Walther, D.; Fischer, R.; Görls, H.; Koch, J.; Schweder, B. *J. Organomet. Chem.* **1996**, *508*, 13-22.

[308] Settineri, N. S.; Garner, M. E.; Arnold, J. *J. Am. Chem. Soc.* **2017**, *139*, 6261-6269.

[309] Rabinovich, E.; Aharonovich, S.; Botoshansky, M.; Eisen, M. S. *Dalton Trans.* **2010**, *39*, 6667-6676.

[310] Ren, W.; Zi, G.; Walter, M. D. *Organometallics* **2012**, *31*, 672-679.

[311] Erickson, K. A.; Lichtscheidl, A. G.; Monreal, M. J.; Nelson, A. T.; Scott, B. L.; Morris, D. E.; Kiplinger, J. L. *J. Organomet. Chem.* **2018**, *857*, 180-186.

[312] Mikhailov, Y. N.; Lobanova, G. M.; Kanishcheva, A. S.; Sergeev, A. V.; Bolotova, G. T.; Shchelokov, R. N. *Koord. Khim.* **1985**, *11*, 545-553.

[313] Voliotis, S. *Acta Crystallogr. B* **1979**, *35*, 2899-2904.

[314] Ren, W.; Song, H.; Zi, G.; Walter, M. D. *Dalton Trans.* **2012**, *41*, 5965-5973.

[315] Gotthelf, G.; Stuber, M. A.; Kornienko, A. Y.; Emge, T. J.; Brennan, J. G. *Chem. Commun.* **2018**, *54*, 12018-12020.

[316] Wedal, J. C.; Bekoe, S.; Ziller, J. W.; Furche, F.; Evans, W. J. *Dalton Trans.* **2019**, *48*, 16633-16640.

[317] Siladke, N. A.; Webster, C. L.; Walensky, J. R.; Takase, M. K.; Ziller, J. W.; Grant, D. J.; Gagliardi, L.; Evans, W. J. *Organometallics* **2013**, *32*, 6522-6531.

[318] Rabinovich, D.; Schimek, G. L.; Pennington, W. T.; Nielsen, J. B.; Abney, K. D. *Acta Crystallogr. C* **1997**, *53*, 1794-1797.

[319] Rabinovich, D.; Scott, B. L.; Nielsen, J. B.; Abney, K. D. *J. Chem. Crystallogr.* **1999**, *29*, 243-246.

[320] Al-Daher, A. G. M.; Bagnall, K. W.; Benetollo, F.; Polo, A.; Bombieri, G. *J. Less Common Met.* **1986**, *122*, 167-173.

[321] Clark, D. L.; Frankcom, T. M.; Miller, M. M.; Watkin, J. G. *Inorg. Chem.* **1992**, *31*, 1628-1633.

[322] Zhang, C.; Hou, G.; Zi, G.; Ding, W.; Walter, M. D. *J. Am. Chem. Soc.* **2018**, *140*, 14511-14525.

[323] Ryan, R. R.; Penneman, R. A.; Kanellakopulos, B. *J. Am. Chem. Soc.* **1975**, *97*, 4258-4260.

[324] Lukens, W. W.; Beshouri, S. M.; Blosch, L. L.; Stuart, A. L.; Andersen, R. A. *Organometallics* **1999**, *18*, 1235-1246.

[325] Zi, G.; Jia, L.; Werkema, E. L.; Walter, M. D.; Gottfriedsen, J. P.; Andersen, R. A. *Organometallics* **2005**, *24*, 4251-4264.

[326] Thomson, R. K.; Graves, C. R.; Scott, B. L.; Kiplinger, J. L. *Dalton Trans.* **2010**, *39*, 6826-6831.

[327] Spirlet, M. R.; Rebizant, J.; Apostolidis, C.; Andreetti, G. D.; Kanellakopulos, B. *Acta Crystallogr. C* **1989**, *45*, 739-741.

[328] Lichtscheidl, A. G.; Pagano, J. K.; Scott, B. L.; Nelson, A. T.; Kiplinger, J. L. *Inorganics* **2016**, *4*, 1.

[329] Schnaars, D. D.; Wu, G.; Hayton, T. W. *Dalton Trans.* **2008**, 6121-6126.

[330] Du Preez, J. G. H.; Zeelie, B.; Casellato, U.; Graziani, R. *Inorg. Chim. Acta* **1986**, *122*, 119-126.

[331] Budantseva, N. A.; Andreev, G. B.; Fedoseev, A. M.; Antipin, M. Y. *Radiochem.* **2003**, *45*, 335-338.

[332] Zhang, Z.; Parker, B. F.; Lohrey, T. D.; Teat, S. J.; Arnold, J.; Rao, L. *Dalton Trans.* **2018**, *47*, 8134-8141.

[333] Brewster, J. T.; Mangel, D. N.; Gaunt, A. J.; Saunders, D. P.; Zafar, H.; Lynch, V. M.; Boreen, M. A.; Garner, M. E.; Goodwin, C. A. P.; Settineri, N. S.; Arnold, J.; Sessler, J. L. *J. Am. Chem. Soc.* **2019**, *141*, 17867-17874.

[334] Zachariasen, W. *Acta Crystallogr.* **1949**, *2*, 388-390.

[335] Bagnall, K. W.; Payne, G. F.; Alcock, N. W.; Flanders, D. J.; Brown, D. *J. Chem. Soc., Dalton Trans.* **1986**, 783-787.

[336] Magette, M.; Fuger, J. *Inorg. Nucl. Chem. Lett.* **1977**, *13*, 529-536.

[337]   Thuéry, P.; Harrowfield, J. *Eur. J. Inorg. Chem.* **2017**, *2017*, 979-987.

[338]   Carter, K. P.; Kalaj, M.; Surbella, R. G.; Ducati, L. C.; Autschbach, J.; Cahill, C. L. *Chem. Eur. J.* **2017**, *23*, 15355-15369.

[339]   Thuéry, P. *Eur. J. Inorg. Chem.* **2014**, *2014*, 58-68.

[340]   Carter, K. P.; Kalaj, M.; Cahill, C. L. *Inorg. Chem. Front.* **2017**, *4*, 65-78.

[341]   Wu, S.; Mei, L.; Li, F.; An, S.; Hu, K.; Nie, C.; Chai, Z.; Shi, W. *Inorg. Chem.* **2018**, *57*, 14772-14785.

7 SYMBOLS AND ABBREVIATIONS

Chemical abbreviations

^{1}H	hydrogen isotope without neutrons, I = ½
12C4	12-crown-4
^{13}C	carbon isotope with 7 neutrons, I = ½
^{19}F	fluorine isotope with 10 neutrons, I = ½
Ac^{III}	trivalent actinium
act	acetone
An	actinide element
An^{IV}	tetravalent actinide element
bipy	2,2′-bipyridine
chdc	cyclohexyldicarboxylic acid
Ce^{III}	trivalent cerium
CN	coordination number
Cp	cyclopentadienyl
Cp*	pentamethylcyclopentadienyl
Cp**	tetramethylcyclopentadienyl
Cp′	(trimethylsilyl)cyclopentadienyl
Cp″	1,3-bis(trimethylsilyl)cyclopentadienyl
Cp^R	penta(*iso*propyl)cyclopentadienyl
Cp^t	1,3-bis(*tert*butyl)cyclopentadienyl
Cp^{tt}	1,2,4-tris(*tert*butyl)cyclopentadienyl
COT	cyclooctatetraenyl
Dipp	1,5-di*iso*propylphenyl
dme	1,2-dimethoxyethane
d_n	degree of deuteration in solvent molecules
edta	ethylenediaminetetraacetate
eq.	equivalents
Et	ethyl group
HMDS	hexamethyldisilazide
i-	*ipso*-position
*i*Pr	*iso*propyl group
*i*Pr$_2$BA	*N,N*′-bis(isopropyl)-benzamidinate
L^N	ligand
Ln	lanthanide element

m-	*meta*-position
M	metal
Me	methyl group
Mes*	2,4,6-tris(*tert*butyl)-phenyl
Np^{IV}	tetravalent neptunium
Np^{V}	pentavalent neptunium
Np^{VII}	heptavalent neptunium
o-	*ortho*-position
p-	*para*-position
Pa^{IV}	tetravalent protactinium
Pa^{V}	pentavalent protactinium
PEBA	*N,N′*-bis-(1-phenylethyl)-benzamidinate
Ph	phenyl group
Ph^{NCN}	phenyl group attached at central carbon atom of amidinate moiety
phen	1,10-phenanthroline
py	pyridine
PyN	2-aminopyridine
rac	racemic
^{t}Bu	*tert*-butyl group
thf	tetrahydrofuran
Th^{IV}	tetravalent thorium
TMS	trimethylsilyl
TREN	triamidoamine
U^{IV}	tetravalent uranium
U^{VI}	hexavalent uranium
X	hetero atom
Zr^{IV}	tetravalent zirconium

Methodological terms

ATR	attenuated total reflection
BCP	bond critical point
CAS	complete active space
CCI	cation-cation interaction
COSMO	conductor-like screening model
COSY	correlated spectroscopy
DFT	density functional theory
DI	delocalization index

EA	elemental analysis
EPR	electron paramagnetic resonance
FCS	FERMI contact shift
HMBC	heteronuclear multiple bond correlation
HSAB	hard and soft acids and bases
HSQC	heteronuclear single quantum coherence
IR	infrared spectroscopy
NBO	natural bond orbital
NMR	nuclear magnetic resonance
NPA	natural population analysis
PCS	pseudocontact shift
PT2	second order perturbation theory
P-XRD	powder X-ray diffraction
QTAIM	quantum theory of atoms in molecules
r.t.	room temperature
SCF	self-consistent field
SC-XRD	single crystal X-ray diffraction
SG	space-group type
SO	spin-orbit coupling
VT	variable temperature

Symbols and units

$\otimes$	tensorial product
$\propto$	proportional to
(*R*)	orientation of stereo center (clockwise)
(*S*)	orientation of stereo center (counter clockwise)
a	year
a.u.	arbitrary unit
ax	axial
A	electron-nucleus hyperfine coupling constant
br s	broad singlet (NMR signal)
d	distance, doublet (NMR signal)
D	density matrix
eq	equatorial
F	structure factor
g	tensor of gyromagnetic factors (g-values)
h	hour *or* PLANCK constant: $6.626 \cdot 10^{-34}$ J·s

h	reciprocal lattice vector
Hz	hertz, 1/s
I	intensity of diffracted beam
J	joule
$^{n}J_{X-Y}$	coupling constant between X and Y nuclei in n bond distance
k_b	BOLTZMANN constant: $1.381 \cdot 10^{-23}$ J·K^{-1}
k_c	rate constant of isomerization
m	meter *or* medium (IR signal)
MHz	megahertz
n	integer value (0, 1, 2,…)
q	electronic charge *or* quartet (NMR signal)
pm	picometer
ppm	parts per million
r	distance metal-nucleus
r	vector between metal and nucleus
R	universal gas constant: 8.314 J·K^{-1}·mol^{-1}
r_{ion}	ionic radius
s	singlet (NMR signal)
t	triplet (NMR signal)
$t_{1/2}$	half-life
T	temperature or tesla
T_c	coalescence temperature
Tr	trace of matrix
vw	very weak (IR signal)
w	weak (IR signal)
α	angle of plane normal of N–C–N plane towards M–X axis
β	An–N–N attachment angle in An^{IV} azide complexes
δ	chemical shift
δ_{dia}	diamagnetic shift
δ_{HF}	hyperfine shift
δ_{tot}	observed chemical shift
Δ	right-handed helicity
$\Delta\delta_{1H}$	difference of ^1H chemical shift
$\Delta G_c^{\ddagger}$	GIBBS free enthalpy of transition state
$\Delta\chi_{ax}$	axial anisotropy of magnetic susceptibility tensor
$\Delta\chi_{rh}$	rhombic anisotropy of magnetic susceptibility tensor
ε	dielectricity constant

η^n	hapticity of ligand, coordination via n contiguous atoms
θ	glancing angle *or* polar angle of spherical coordinate system
κ	denticity of ligand
λ	wavelength *or* mixing parameter
Λ	left-handed helicity
μ_B	BOHR magneton: 9.274 J·T^{-1}
ν_{as}	asymmetric stretching vibration
ρ	electron density
σ	standard deviation
φ	phase of wave function *or* azimuthal angle of spherical coordinate system
χ	magnetic susceptibility tensor
χ_M	molar magnetic susceptibility
$\tilde{\chi}_{xx}$	principal component of magnetic susceptibility tensor in x direction
$\tilde{\chi}_{yy}$	principal component of magnetic susceptibility tensor in y direction
$\tilde{\chi}_{zz}$	principal component of magnetic susceptibility tensor in z direction
Ψ	wave function

Miscellaneous

calc.	calculated
e.g.	Latin: *exempli gratia*; for example
Eq.	Equation
exp.	experimental
i.e.	Latin: *id est*; that is
et al.	Latin: *et alii*; and others
resp.	respective
vs.	versus

8 APPENDIX

8.1 Tetravalent metal complexes with *i*Pr₂BA

8.1.1 Bis(amidinate) complexes

8.1.1.1 Comparison

Table 11. Crystallographic data for bis(amidinate) complexes [MCl₂(*i*Pr₂BA)₂] **12** (M = Ti) and **1** (M = Hf).

	12	**1**
Empirical formula	[$C_{26}H_{38}Cl_2N_4Ti$]	[$C_{26}H_{38}Cl_2N_4Hf$]
M (g/mol)	525.40	655.99
Crystal system	Orthorhombic	Orthorhombic
Space group	*Pbcn*	*Pbca*
a (Å)	19.8057(15)	20.1067(10)
b (Å)	8.2525(6)	8.4192(4)
c (Å)	16.9052(13)	16.8212(8)
V (Å³)	2763.1(4)	2847.5(2)
T (K)	100	100
Z	4	4
ρ_{calcd} (Mg/m³)	1.263	1.530
abs coeff (mm⁻¹)	0.524	3.871
Θ_{max} (°)	28.30	30.030
R [$I > 2\sigma(I)$]	0.031	0.016
wR2(int)	0.080	0.035
w scheme d, e	0.0371, 1.6085	0.0112, 2.3751
Data/Param	3438/154	4155/154
res. Dens (eÅ⁻³)	0.393, -0.371	0.428, -0.676
R_{int}	0.037	0.032
GooF	1.070	1.055

Table 12. Comparison of intramolecular distances of bis(amidinate) $[MCl_2(L^N)_2]$ compounds **1**, **6**, **7**, **8**, **12**, **13** with literature data. Bond lengths M–Cl1, M–Cl2 are averaged to M–Cl; distances M–N1, M–N3 to M–N_{long} and distances M–N2, M–N4 to M–N_{short}.

d(M–X) [Å]	M–Cl	M–N_{long}	M–N_{short}
$[TiCl_2(iPr_2BA)_2]$ (**12**)	2.293	2.104	2.038
$[TiCl_2((S)\text{-}PEBA)_2]$ (**13**)	2.296	2.116	2.040
$[TiCl_2(L^1)_2]^{[297]}$	2.277	2.100	2.066
$[TiCl_2(L^2)_2]^{[298]}$	2.328	2.108	2.040
$[TiCl_2(L^3)_2]^{[299]}$	2.257	2.107	2.067
$[TiCl_2(L^4)_2]^{[300]}$	2.296	2.078	2.056
$[TiCl_2(L^5)_2]^{[301]}$	2.328	2.077	2.054
$[TiCl_2(L^6)_2]^{[123]}$	2.286	2.100	2.049
$[ZrCl_2(iPr_2BA)_2]^{[123]}$	2.416	2.207	2.197
$[ZrCl_2((S)\text{-}PEBA)_2]$ (**6**)	2.421	2.238	2.177
$[ZrCl_2(L^3)_2]^{[302]}$	2.403	2.252	2.208
$[ZrCl_2(L^6)_2]^{[123]}$	2.430	2.233	2.195
$[ZrCl_2(L^7)_2]^{[303]}$	2.425	2.222	2.208
$[ZrCl_2(L^8)_2]^{[303]}$	2.420	2.264	2.219
$[ZrCl_2(L^9)_2]^{[304]}$	2.427	2.238	2.204
$[ZrCl_2(L^{10})_2]^{[305]}$	2.443	2.208	2.203
$[ZrCl_2(L^{11})_2]^{[123]}$	2.430	2.202	2.197
$[HfCl_2(iPr_2BA)_2]$ (**1**)	2.398	2.201	2.178
$[HfCl_2((S)\text{-}PEBA)_2]$ (**7**)	2.408	2.216	2.187
$[HfCl_2(L^7)_2]^{[303]}$	2.413	2.209	2.196
$[HfCl_2(L^{10})_2]^{[306]}$	2.434	2.192	2.178
$[HfCl_2(L^{11})_2]^{[306]}$	2.418	2.200	2.180
$[UCl_2((S)\text{-}PEBA)_2]$ (**8**)	2.603	2.370	2.361
$[UCl_2(L^{12})_2]^{[151]}$	2.543	2.470	2.409

L^1 = N,N'-bis(trimethylsilyl)-4-trifluormethyl-benzamidinate; L^2 = N,N'-bis(iso-propyl)-piperidinoguanidinate;

L^3 = N,N'-bis(trimethylsilyl)-benzamidinate; L^4 = N,N'-bis(phenyl)-di(ethyl)guanidinate;

L^5 = N,N'-bis(isopropyl)-di(ethyl)guanidinate; L^6 = N,N'-bis(cyclohexyl)-benzamidinate;

L^7 = N,N'-bis(cyclohexyl)-bis(trimethylsilyl)guanidinate; L^8 = N,N'-bis(isopropyl)-bis(trimethylsilyl)guanidinate;

L^9 = N,N'-bis(trimethylsilyl)-4-methoxy-benzamidinate; L^{10} = N,N'-bis(isopropyl)-di(methyl)guanidinate;

L^{11} = N,N'-bis(isopropyl)-methylamidinate;

L^{12} = N,N'-bis(trimethylsilyl)-2,4,6-tris(trifluoromethyl)benzamidinate
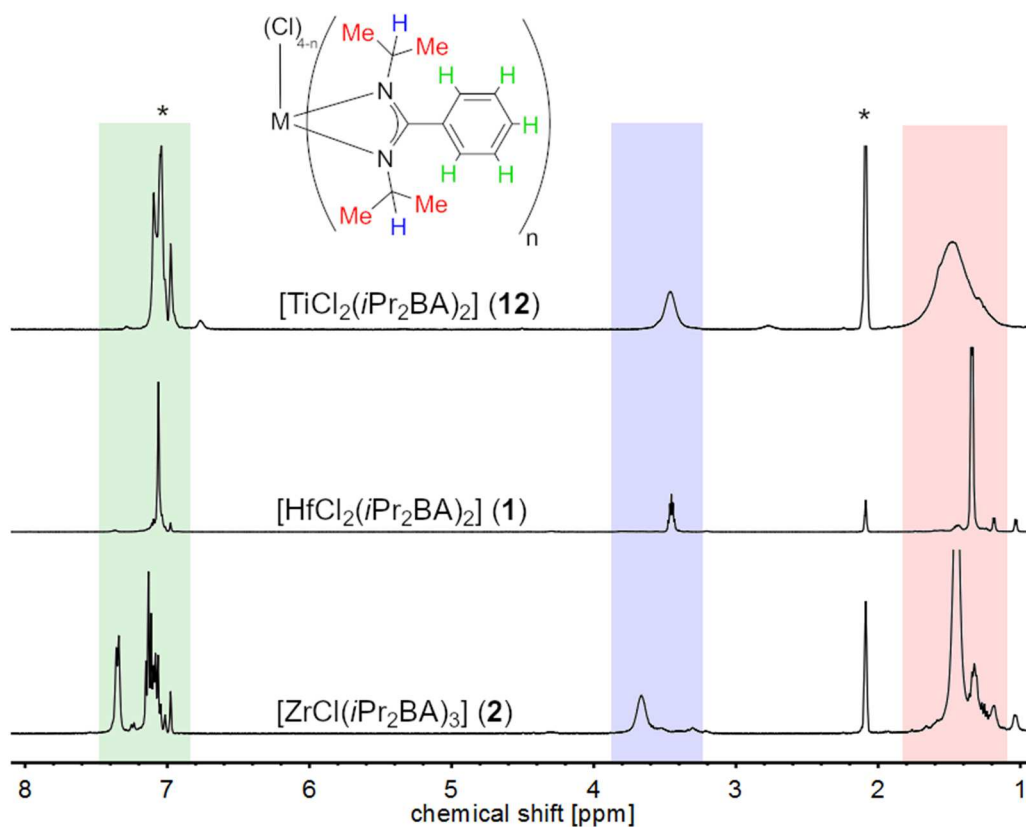
Figure 36. ^{1}H NMR spectra of [TiCl$_2$(iPr$_2$BA)$_2$] (**12**, top), [HfCl$_2$(iPr$_2$BA)$_2$] (**1**, middle) and [ZrCl(iPr$_2$BA)$_3$] (**2**, bottom) in toluene-d$_8$ at 298 K. Signals are marked with colors: blue (NCH), red (Me) and green (Ph). Asterisks indicate solvent signals (i.e. toluene).

Table 13. ^{13}C chemical shifts of isostructural bis(amidinate) complexes [MCl$_2$(iPr$_2$BA)$_2$] (M = Ti (**12**), Zr,[123] Hf (**1**)) at 298 K in toluene-d$_8$ (for **1**, **12**) or benzol-d$_6$ ([ZrCl$_2$(iPr$_2$BA)$_2$]).

δ [ppm]	[TiCl$_2$(iPr$_2$BA)$_2$] (**12**)	[ZrCl$_2$(iPr$_2$BA)$_2$][123]	[HfCl$_2$(iPr$_2$BA)$_2$] (**1**)
NCN	176.7	178.3	179.2
i-Ph	130.5	131.1	131.7
o-Ph	128.6	129.0	129.0
m-Ph	126.4	126.1	126.2
p-Ph	129.6	129.4	129.4
NCH	52.5	49.9	49.7
Me	24.3	24.8	24.9

8.1.1.2 [TiCl₂(iPr₂BA)₂] (12)
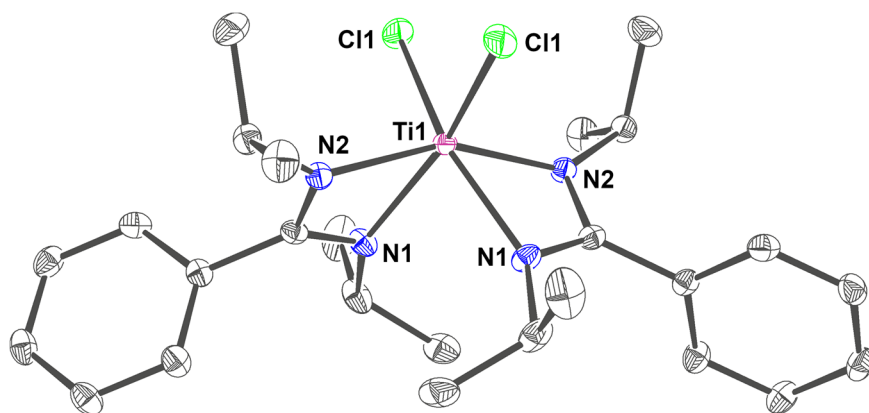
Figure 37. Molecular structure of [TiCl$_2$(iPr$_2$BA)$_2$] (**12**). Ellipsoids are drawn at 50 % probability level. Hydrogen atoms are omitted for clarity. Color code: carbon (C, dark gray), chlorine (Cl, green), nitrogen (N, blue), and titanium (Ti, violet red).
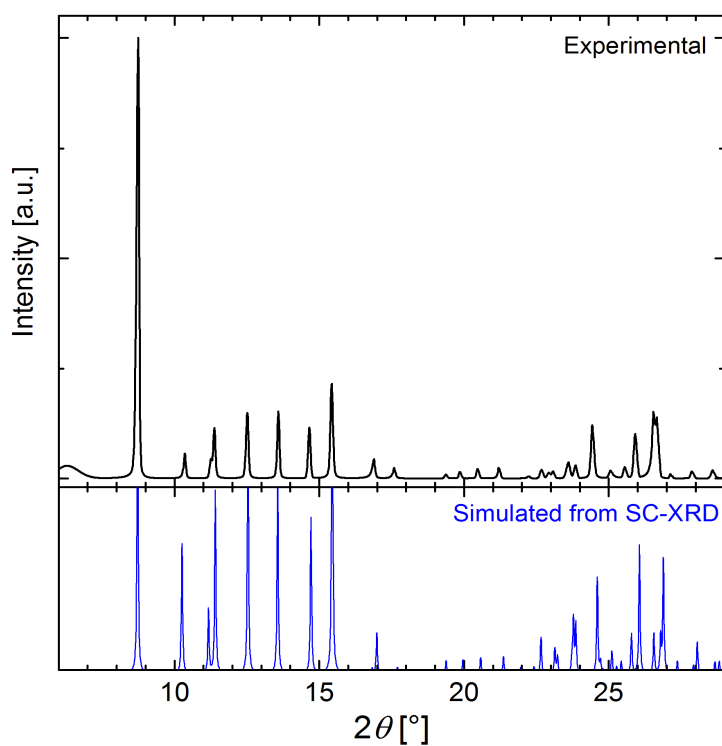
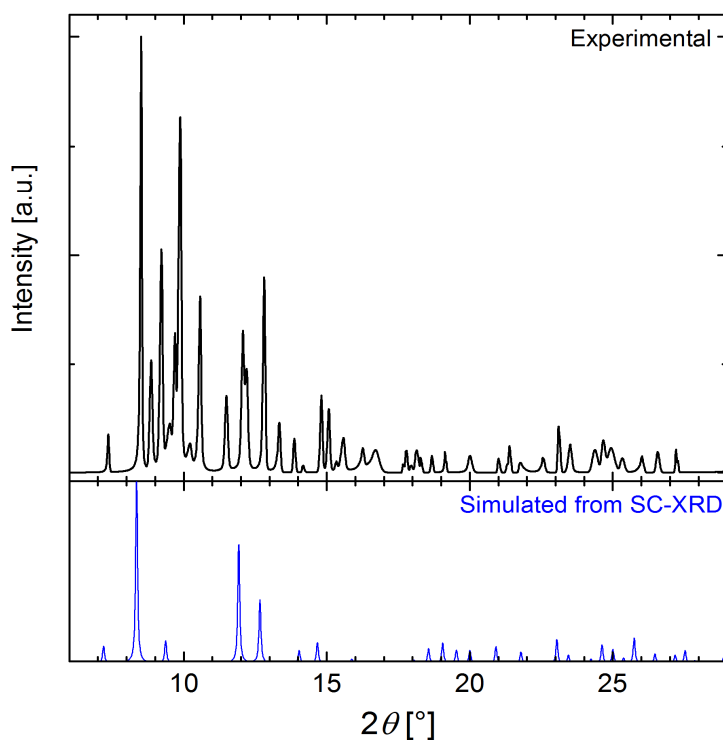**Figure 38.** Powder X-ray diffraction pattern of [TiCl$_2$(iPr$_2$BA)$_2$] (**12**, top) with simulated diffraction pattern based on single-crystal XRD data (bottom).

8.1.1.3 [HfCl$_2$(iPr$_2$BA)$_2$] (1)
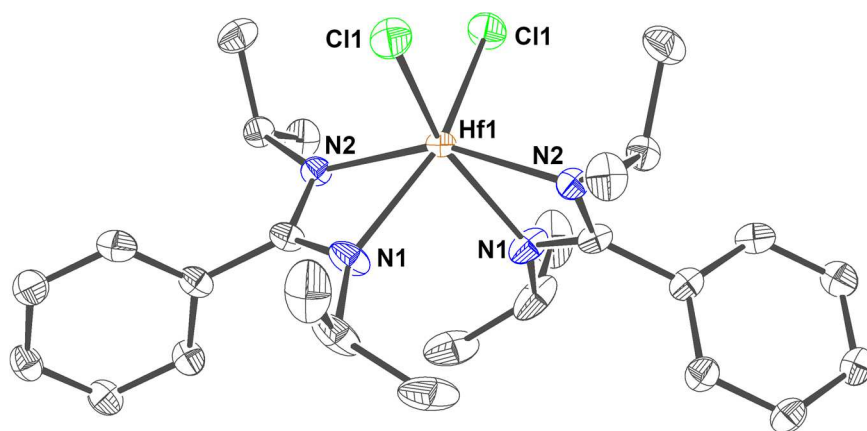
Figure 39. Molecular structure of [HfCl$_2$(*i*Pr$_2$BA)$_2$] (**1**). Ellipsoids are drawn at 50 % probability level. Hydrogen atoms are omitted for clarity. Color code: carbon (C, dark gray), chlorine (Cl, green), nitrogen (N, blue), and hafnium (Hf, pale brown).
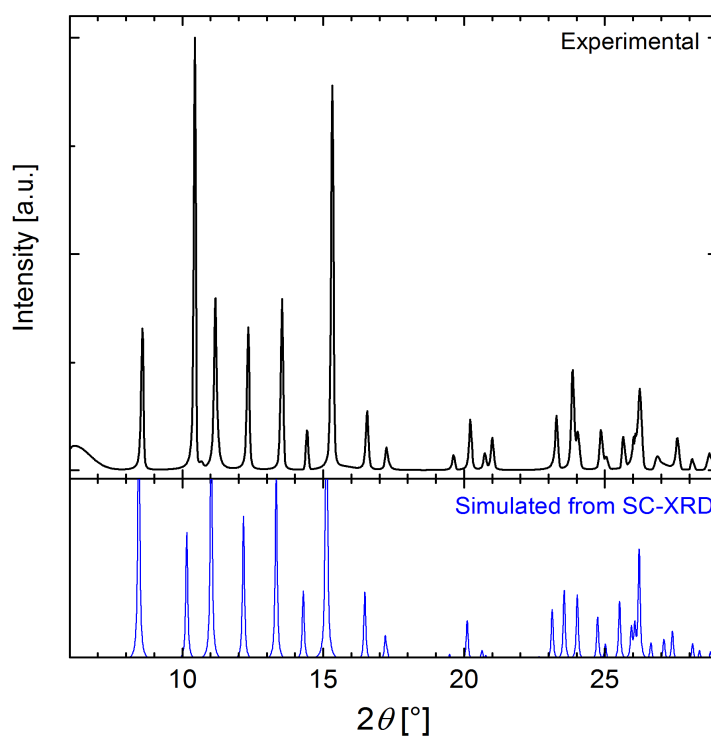
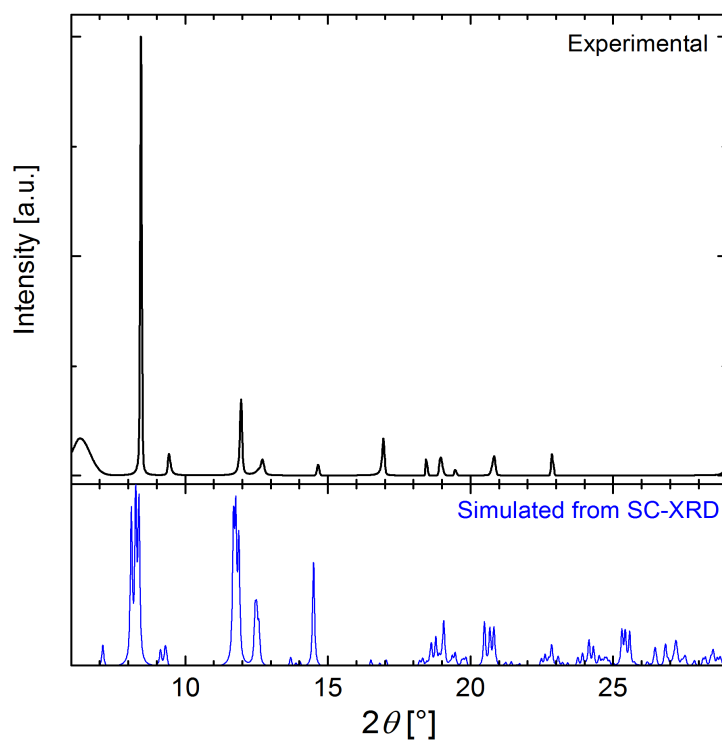**Figure 40.** Powder X-ray diffraction pattern of [HfCl$_2$(*i*Pr$_2$BA)$_2$] (**1**, top) with simulated diffraction pattern based on single-crystal XRD data (bottom).

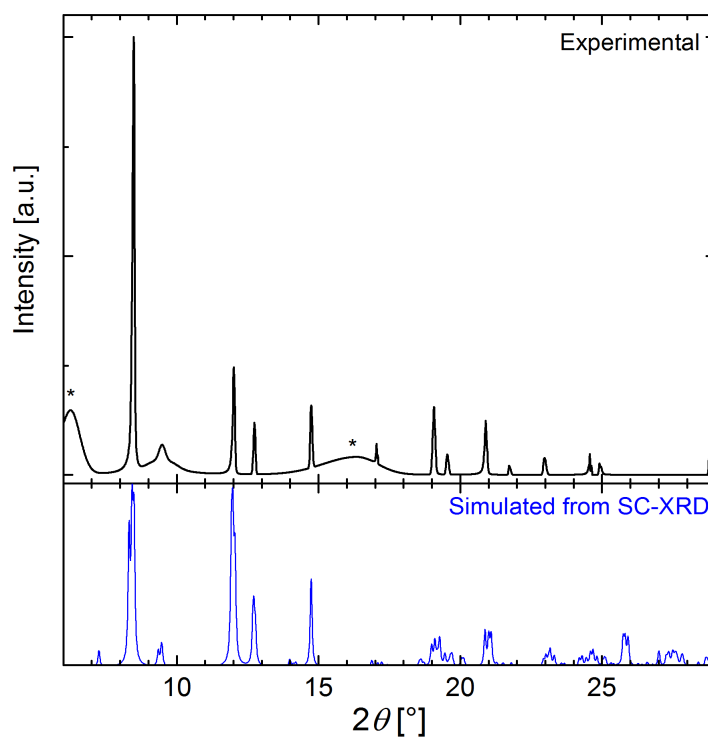## 8.1.2 Tris(amidinate) complexes

8.1.2.1 Comparison

Table 14. Crystallographic data for tris(amidinate) complexes [MCl(iPr$_2$BA)$_3$] **2** (M = Zr), **3** (M = Th), **4** (M = U), **5** (M = Np).

	2	**3**	**4**	**5**
Empirical formula	[C$_{39}$H$_{57}$ClN$_6$Zr] ·0.5C$_7$H$_8$	[C$_{39}$H$_{57}$ClN$_6$Th] ·0.5C$_7$H$_8$	[C$_{39}$H$_{57}$ClN$_6$U] ·0.5C$_7$H$_8$	[C$_{39}$H$_{57}$ClN$_6$Np] ·0.5C$_7$H$_8$
M (g/mol)	782.65	923.46	929.45	928.42
Crystal system	Cubic	Orthorhombic	Orthorhombic	Orthorhombic
Space group	*Pa*-3	*Pbca*	*Pbca*	*Pbca*
a (Å)	20.344(1)	20.555(4)	20.498(1)	20.558(2)
b (Å)	20.344(1)	20.287(4)	20.336(1)	20.358(2)
c (Å)	20.344(1)	20.933(4)	20.750(1)	20.806(2)
V (Å^3)	8420(1)	8729(3)	8650(1)	8708(2)
T (K)	100	100	100	100
Z	8	8	8	8
ρ_{calcd} (Mg/m^3)	1.235	1.405	1.428	1.416
abs coeff (mm^{-1})	0.360	3.512	3.850	2.483
Θ_{max} (°)	26.36	25.040	27.880	28.370
R [$I > 2\sigma(I)$]	0.029	0.018	0.044	0.041
wR2(int)	0.078	0.037	0.115	0.085
w scheme d, e	0.0343, 7.8910	0.0117, 8.8966	0.0340, 86.7049	0, 51.7978
Data/Param	2880/157	7725/488	10316/488	10892/488
res. Dens (eÅ^{-3})	0.420, -0.489	0.487, -0.359	3.889, -1.769	2.298, -1.907
R_{int}	0.026	0.042	0.054	0.047
GooF	1.091	1.037	1.064	1.192

Table 15. Intramolecular distances between metal center M and coordinating atoms in isostructural tris(amidinate) [MCl(iPr$_2$BA)$_3$] complexes **2**-**5**.

d(M–X) [Å]	**2** (M = Zr)	**3** (M = Th)	**4** (M = U)	**5** (M = Np)
Cl1	2.501(1)	2.725(2)	2.678(2)	2.663(2)
N1	2.331(2)	2.521(2)	2.470(4)	2.455(3)
N2	2.214(2)	2.435(2)	2.386(5)	2.365(3)
N3		2.509(2)	2.453(4)	2.437(3)
N4		2.445(2)	2.399(5)	2.378(3)
N5		2.511(2)	2.455(4)	2.442(3)
N6		2.453(2)	2.395(4)	2.372(3)

Table 16. Comparison of intramolecular distances of tris(amidinate) [MCl(L$_N$)$_3$] compounds **2**, **3**, **4**, **9**, **10**, and **16** with literature data. Bond lengths M–N1, M–N3, M–N5 are averaged to M–N$_{long}$ and distances M–N2, M–N4, M–N6 to M–N$_{short}$.

d(M–X) [Å]	M–Cl	M–N$_{long}$	M–N$_{short}$
[ZrCl(iPr$_2$BA)$_3$] (**2**)	2.501	2.331	2.214
[ZrCl(L^3)$_3$][307]	2.464	2.324	2.247
[ZrCl(L^{11})$_3$][233]	2.513	2.305	2.211
[HfCl(L^{11})$_3$][233]	2.501	2.286	2.195
[HfCl(L^{13})$_3$][234]	2.457	2.272	2.208
[HfCl(L^{14})$_3$][235]	2.497	2.268	2.193
[HfCl(L^{15})$_3$][235]	2.475	2.244	2.222
[ThCl(iPr$_2$BA)$_3$] (**3**)	2.725	2.514	2.444
[ThCl((S)-PEBA))$_3$] (**9**)	2.701	2.560	2.439
[ThCl(L^{11})$_3$][308]	2.736	2.519	2.439
[ThCl(L^{16})$_3$][309]	2.718	2.548	2.454
[UCl(iPr$_2$BA)$_3$] (**4**)	2.678	2.459	2.387
[UCl((S)-PEBA)$_3$] (**10**)	2.641	2.499	2.379
[UCl(L^1)$_3$][151]	2.634	2.485	2.408
[UCl(L^3)$_3$][151]	2.659	2.448	2.414
[UCl(L^{17})$_3$][153]	2.678	2.457	2.395
[UCl(L^{18})$_3$][226]	2.662	2.473	2.413
[CeCl((S)-PEBA)$_3$] (**16**)	2.644	2.512	2.365)
[CeCl(L^9)$_3$][217]	2.655	2.470	2.393

L^1 = *N,N′*-bis(trimethylsilyl)-4-trifluormethyl-benzamidinate;   L^3 = *N,N′*-bis(trimethylsilyl)-benzamidinate;

L^9 = *N,N′*-bis(trimethylsilyl)-4-methoxy-benzamidinate;   L^{11} = *N,N′*-bis(isopropyl)-methylamidinate;

L^{13} = *N*-benzyl-*N′*-(trimethylsilyl)benzamidinate;   L^{14} = *N*-phenyl-*N′*-(trimethylsilyl)-dimethylguanidinate;

L^{15} = *N*-phenyl-*N′*-(trimethylsilyl)piperidinoguanidinate;   L^{16} = *N,N′*-bis(trimethylsilyl)-2-pyridylamidinate;

L^{17} = *N,N′*-bis(cyclohexyl)-methylamidinate;   L^{18} = *N,N′*-bis(isopropyl)-di(isopropyl)guanidinate
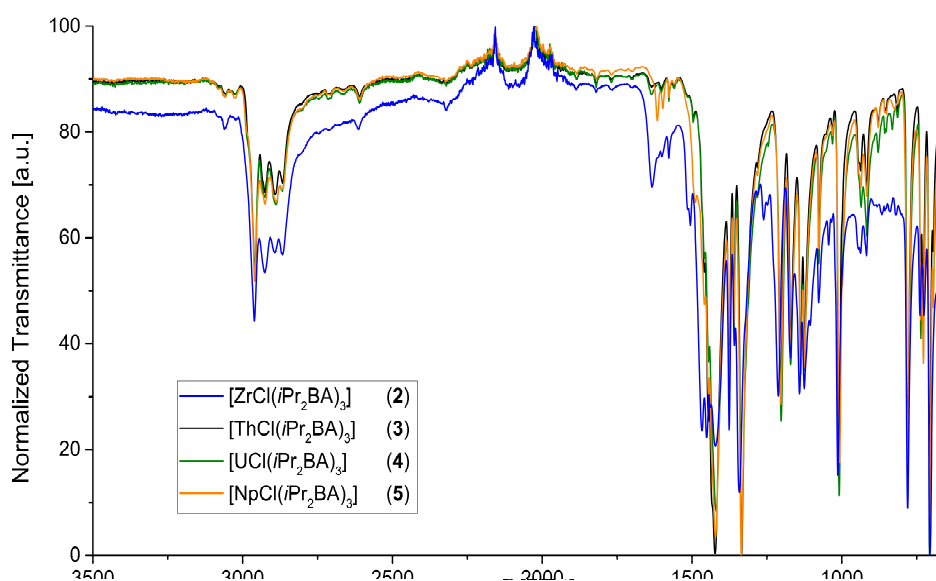
Figure 41. Normalized ATR-IR spectra of [MCl(iPr$_2$BA)$_3$] (M = Zr (**2**), Th (**3**), U (**4**), Np (**5**)).
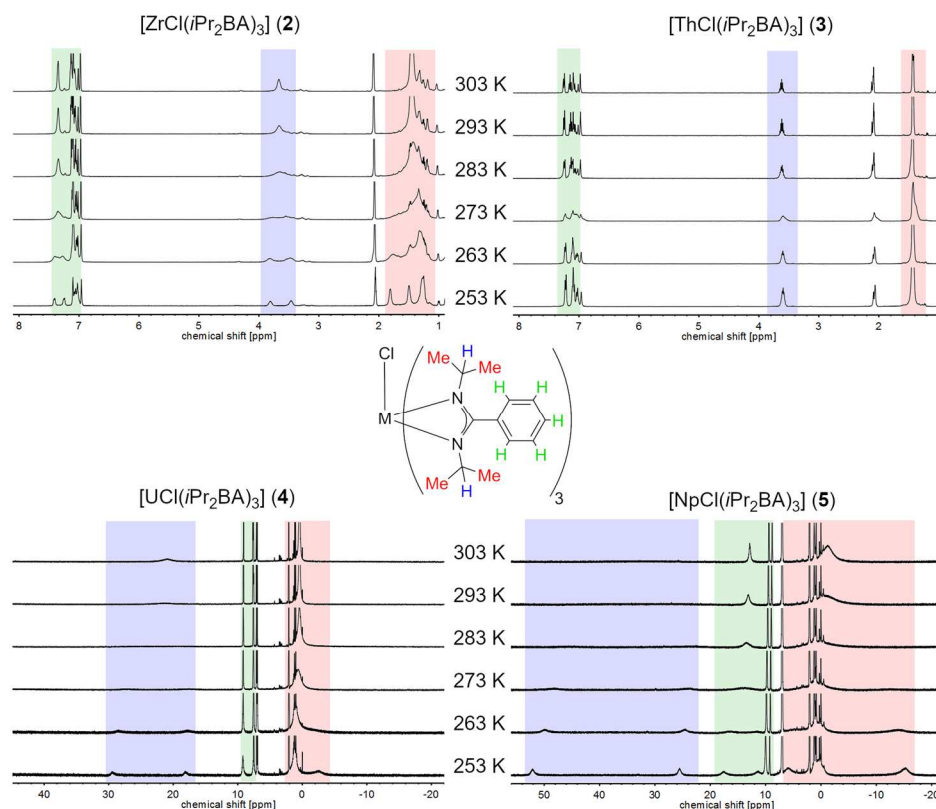
Figure 42. ^{1}H NMR spectra of [MCl(*i*Pr₂BA)₃] (M = Zr (**2**, top left), Th (**3**, top right), U (**4**, bottom left), Np (**5**, bottom right)) in toluene-d₈ recorded in a temperature range from 253 K to 303 K. Signals are marked with colors: blue (NC*H*), red (Me) and green (Ph).

Table 17. Determined coalescence temperatures for different ^{1}H in [MCl(*i*Pr₂BA)₃] (M = Zr (**2**), Th (**3**), U (**4**), Np (**5**)) complexes together with the ionic radii for CN = 7.

	Zr (**2**)	Np (**5**)	U (**4**)	Th (**3**)
NC*H*	283 K	> 303 K	293 K	< 253 K
Me	283 K	293 K	263 K	< 253 K
o-Ph	273 K	273 K	< 253 K	< 253 K
r$_{ion}$ (CN = 7)	0.78 Å	0.93 Å	0.95 Å	1.00 Å

Table 18. Derived FERMI contact and pseudocontact contributions of paramagnetic shifts for [AnCl(*i*Pr₂BA)₃] (An = U (**4**), Np (**5**)) based on BLEANEY method at 298 K. Brackets indicate error of last digits by linear regression analysis. Values in grey belong to linear regression models with R² < 0.98.

	[UCl(*i*Pr₂BA)₃] (**4**)		[NpCl(*i*Pr₂BA)₃] (**5**)	
	FCS [ppm]	PCS [ppm]	FCS [ppm]	PCS [ppm]
Me	-1.62(02)	0.63(02)	-2.04(09)	-0.82(10)
NC*H*	18.74(24)	-1.13(27)	21.86(19)	7.22(23)
o-Ph	2.75(01)	-0.88(01)	2.88(03)	2.86(03)
m-Ph	1.27(02)	-0.78(02)	1.38(03)	0.92(04)
p-Ph	1.16(02)	-0.64(02)	1.41(04)	0.38(05)

8.1.2.2 [ZrCl(iPr₂BA)₃] (2)
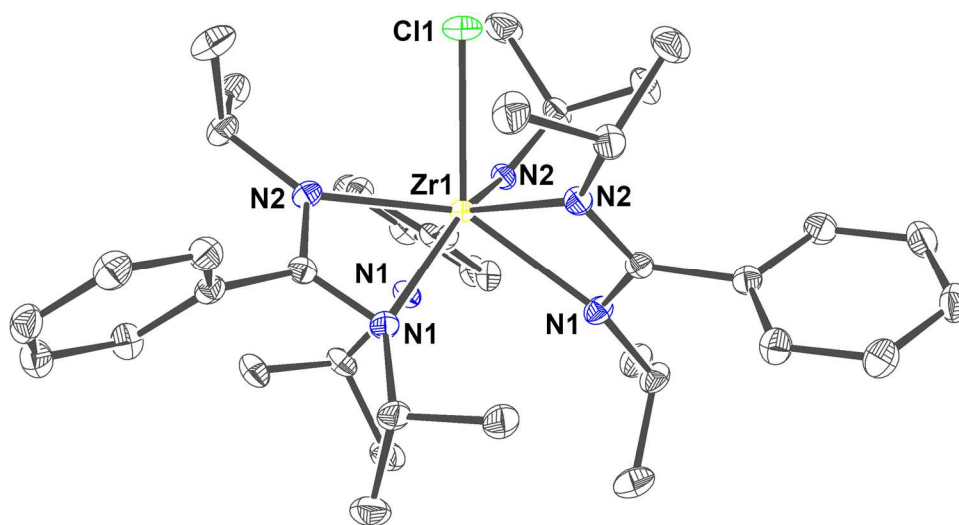
Figure 43. Molecular structure of [ZrCl(*i*Pr₂BA)₃] (**2**). Ellipsoids are drawn at 50 % probability level. Hydrogen atoms and solvent molecules are omitted for clarity. Color code: carbon (C, dark gray), chlorine (Cl, green), nitrogen (N, blue), and zirconium (Zr, yellow).

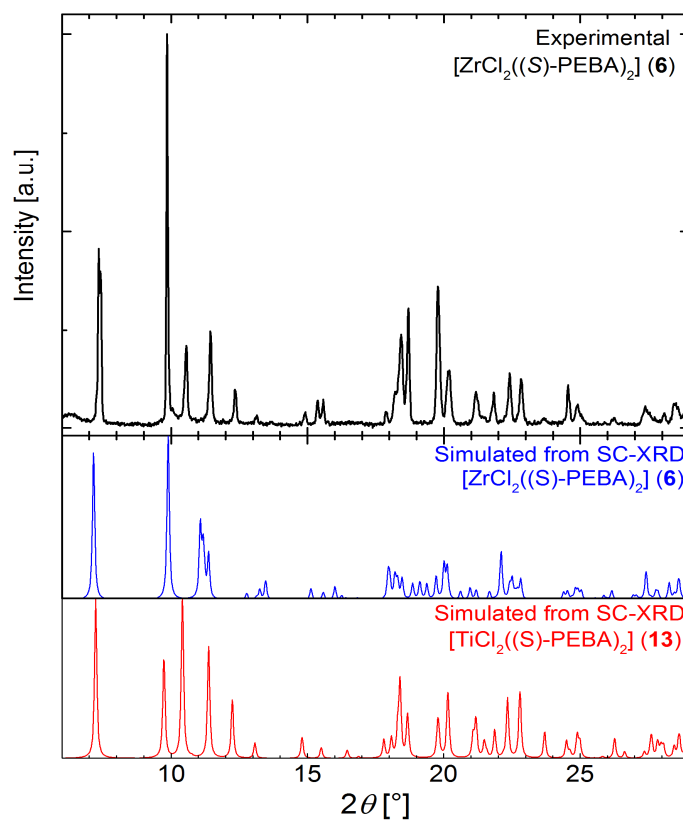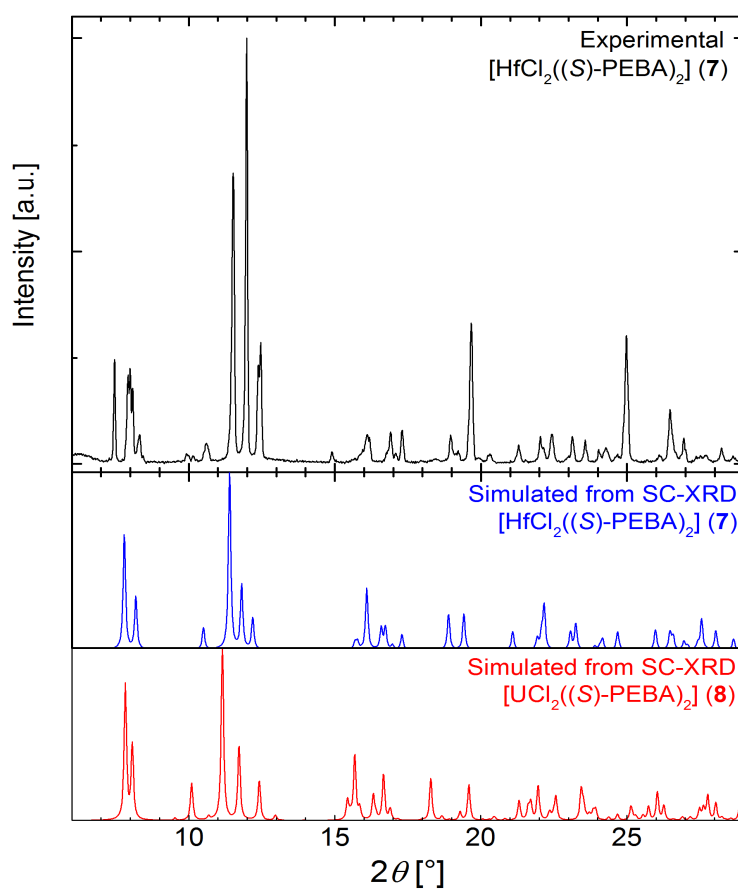**Figure 44.** Powder X-ray diffraction pattern of [ZrCl(*i*Pr₂BA)₃] (**2**, top) with simulated diffraction pattern based on single-crystal XRD data (bottom). Additional reflections refer to unidentified side products.

8.1.2.3 *[ThCl(iPr₂BA)₃] (3)*
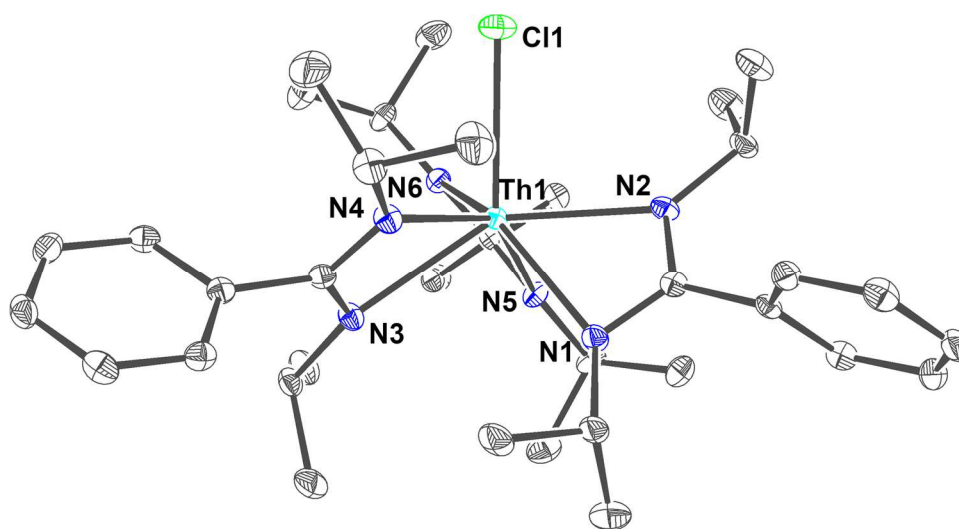
Figure 45. Molecular structure of [ThCl(*i*Pr$_2$BA)$_3$] (**3**). Ellipsoids are drawn at 50 % probability level. Hydrogen atoms and solvent molecules are omitted for clarity. Color code: carbon (C, dark gray), chlorine (Cl, green), nitrogen (N, blue), and thorium (Th, pale blue).
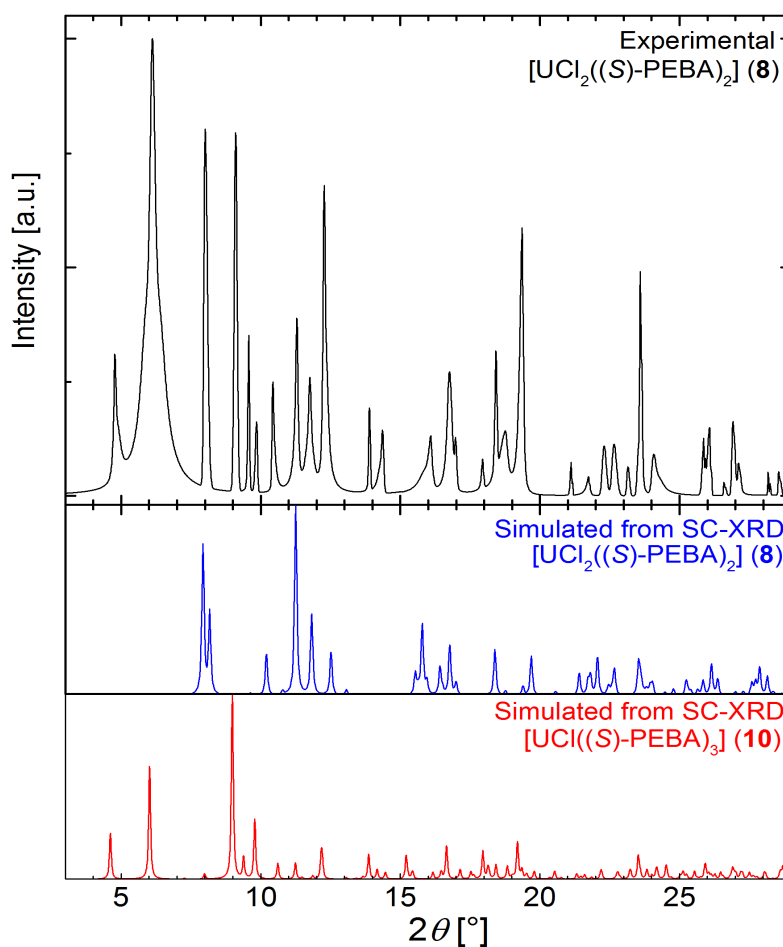

Figure 46. Powder X-ray diffraction pattern of [ThCl(*i*Pr$_2$BA)$_3$] (**3**, top) with simulated diffraction pattern based on single-crystal XRD data (bottom).

8.1.2.4 [UCl(iPr₂BA)₃] (4) & [NpCl(iPr₂BA)₃] (5)
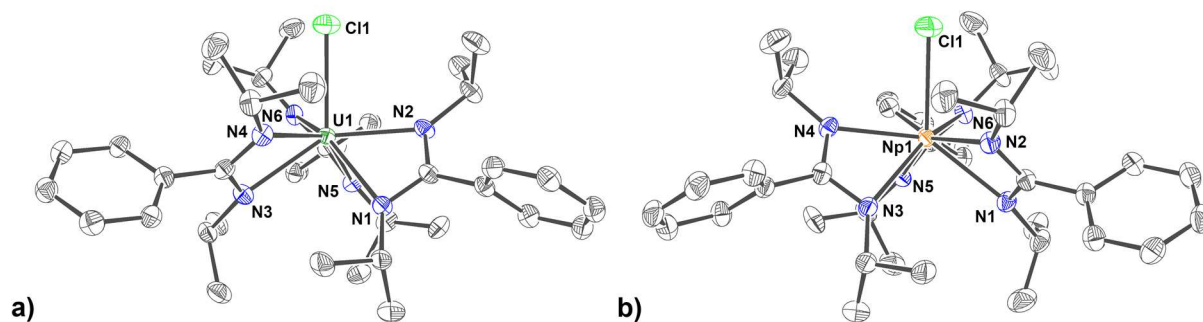
Figure 47. Molecular structure of a) [UCl(*i*Pr₂BA)₃] (**4**) and b) [NpCl(*i*Pr₂BA)₃] (**5**). Ellipsoids are drawn at 50 % probability level. Hydrogen atoms and solvent molecules are omitted for clarity. Color code: carbon (C, dark gray), chlorine (Cl, green), nitrogen (N, blue), uranium (U^IV, dark green), and neptunium (Np^IV, orange red).

Figure 48. Powder X-ray diffraction pattern of [UCl(*i*Pr₂BA)₃] (**4**, top) with simulated diffraction pattern based on single-crystal XRD data (bottom). Asterisks indicate residual reflection of sample holder.

8.2 Tetravalent chloro amidinate complexes with (*S*)-PEBA

8.2.1 Bis(amidinate) complexes

8.2.1.1 Comparison

Table 19. Crystallographic data for bis(amidinate) complexes [MCl$_2$((*S*)-PEBA)$_2$] **13** (M = Ti), **6** (M = Zr), **7** (M = Hf), **8** (M = U).

	13	**6**	**7**	**8**
Empirical formula	[C$_{46}$H$_{46}$Cl$_2$N$_4$Ti]	[C$_{46}$H$_{46}$Cl$_2$N$_4$Zr]	[C$_{46}$H$_{46}$Cl$_2$N$_4$Hf]	[C$_{46}$H$_{46}$Cl$_2$N$_4$U]
M (g/mol)	773.64	816.99	904.26	963.80
Crystal system	Monoclinic	Monoclinic	Monoclinic	Monoclinic
Space group	*P*2$_1$	*C*2	*C*2	*C*2
a (Å)	9.5215(5)	16.0518(6)	21.2086(8)	22.3712(18)
b (Å)	23.3649(12)	10.5222(4)	8.5445(3)	8.6896(7)
c (Å)	9.5358(5)	24.7251(12)	14.2099(6)	21.7234(17)
β (°)	113.144(1)	107.282(1)	129.209(1)	101.553(2)
V (Å^3)	1950.7(2)	3987.5(3)	1995.3(2)	4137.4(6)
T (K)	100	100	100	100
Z	2	4	2	4
ρ_{calcd} (Mg/m^3)	1.317	1.361	1.505	1.547
abs coeff (mm^{-1})	0.0395	0.448	2.786	4.089
Θ_{max} (°)	27.87	28.32	30.59	30.030
R [*I* > 2σ(*I*)]	0.025	0.025	0.009	0.015
wR2(int)	0.066	0.061	0.023	0.035
w scheme *d*, *e*	0.0356, 0.6622	0.0289, 2.9940	0.0034, 0	0.0109, 1.8595
Data/Param	9320/483	9938/483	6132/242	12103/483
res. Dens (eÅ^{-3})	0.17, -0.33	0.77, -0.59	0.46, -0.52	0.495, -1.407
R$_{int}$	0.042	0.038	0.0253	0.039
GooF	1.066	1.062	1.070	1.097
Flack x	0.005(5)	0.016(8)	0.013(2)	0.059(3)

Table 20. Intramolecular distances between metal center M and coordinating atoms in isostructural bis(amidinate) [MCl$_2$((*S*)-PEBA)$_2$] complexes **2**-**5**.

d(M–X) [Å]	**13** (M = Ti)	**6** (M = Zr)	**7** (M = Hf)	**8** (M = U)
Cl1	2.297(1)	2.421(1)	2.408(1)	2.605(7)
Cl2	2.295(1)			2.600(7)
N1	2.116(2)	2.238(2)	2.216(2)	2.376(2)
N2	2.041(2)	2.177(2)	2.187(2)	2.360(2)
N3	2.116(2)			2.363(2)
N4	2.039(2)			2.362(2)

For comparison with literature date of isostructural bis(amidinate) complexes see Table 12.

Table 21. ^{13}C chemical shifts of [MCl$_2$((S)-PEBA)$_2$] (M = Ti (**13**), Zr (**6**), Hf (**7**)) in toluene-d$_8$ at 298 K.

	[TiCl$_2$((S)-PEBA)$_2$] (**13**)	[ZrCl$_2$((S)-PEBA)$_2$] (**6**)	[HfCl$_2$((S)-PEBA)$_2$] (**7**)
NCN	180.3	183.4	182.7
i-Ph^{NCN}	131.1	131.4	131.7
o-Ph^{NCN}	126.9	126.7	126.9
m-Ph^{NCN}	128.2	128.3	128.3
p-Ph^{NCN}	129.3	129.3	129.4
i-Ph	145.8	146.3	146.3
NCH	61.5	59.2	59.0
Me	23.3	24.7	24.7
o-Ph	128.2	127.6	127.7
m-Ph	128.3	128.4	128.4
p-Ph	126.9	126.8	126.8

8.2.1.2 [TiCl₂((S)-PEBA)₂] (13)
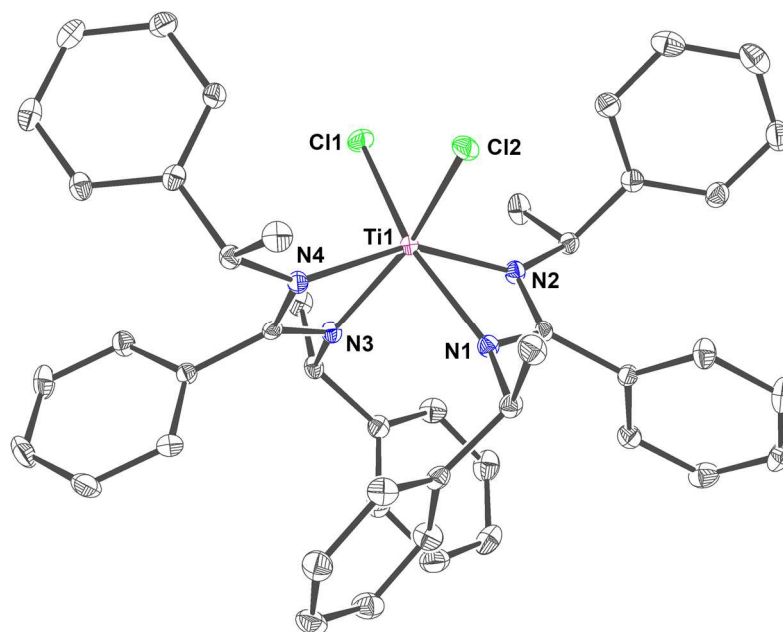
Figure 49. Molecular structure of Δ-[TiCl₂((*S*)-PEBA)₂] (**13**). Ellipsoids are drawn at 50 % probability level. Hydrogen atoms are omitted for clarity. Color code: carbon (C, dark gray), chlorine (Cl, green), nitrogen (N, blue), and titanium (Ti, violet red).
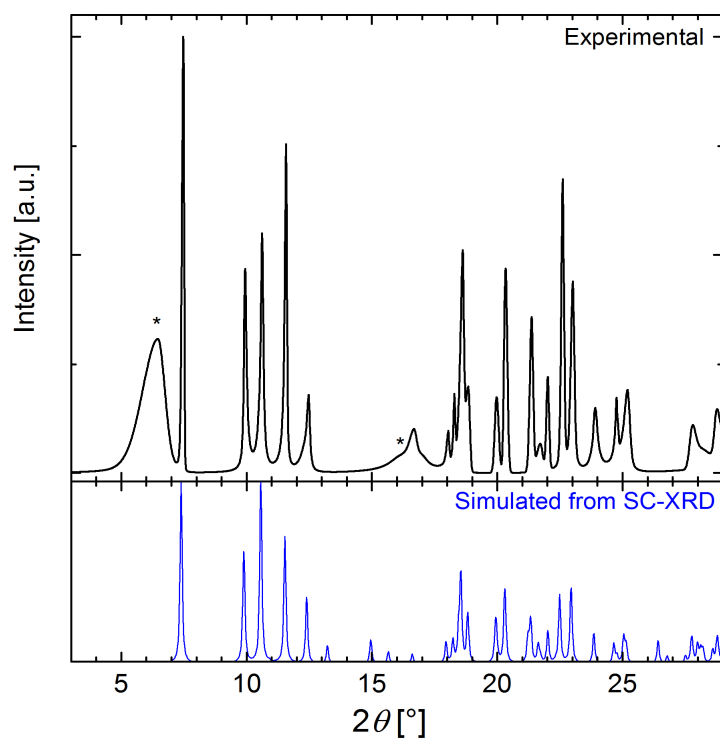
Figure 50. Powder X-ray diffraction pattern of [TiCl₂((*S*)-PEBA)₂] (**13**, top) with simulated diffraction pattern based on single-crystal XRD data (bottom). Asterisks indicate residual reflections from sample holder.

8.2.1.3   [ZrCl$_2$((S)-PEBA)$_2$] (6)
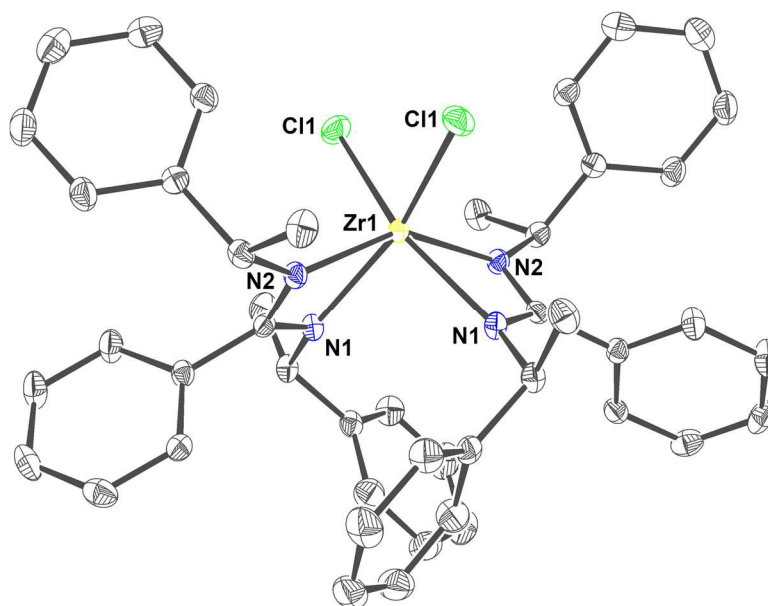
Figure 51. Molecular structure of Δ-[ZrCl$_2$((*S*)-PEBA)$_2$] (**6**). Ellipsoids are drawn at 50 % probability level. Hydrogen atoms are omitted for clarity. Color code: carbon (C, dark gray), chlorine (Cl, green), nitrogen (N, blue), and zirconium (Zr, yellow).

Figure 52. Powder X-ray diffraction pattern of [ZrCl$_2$((*S*)-PEBA)$_2$] (**6**, top), with simulated diffraction patterns for [ZrCl$_2$((*S*)-PEBA)$_2$] (**6**, middle) and [TiCl$_2$((*S*)-PEBA)$_2$] (**13**, bottom).

8.2.1.4 [HfCl₂((S)-PEBA)₂] (7)
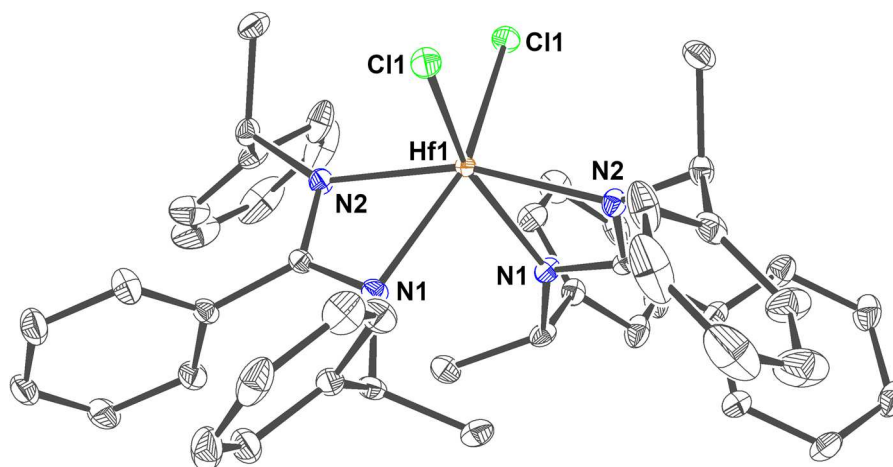
Figure 53. Molecular structure of Λ-[HfCl$_2$((*S*)-PEBA)$_2$] (**7**). Ellipsoids are drawn at 50 % probability level. Hydrogen atoms are omitted for clarity. Color code: carbon (C, dark gray), chlorine (Cl, green), nitrogen (N, blue), and hafnium (Hf, pale brown).

Figure 54. Powder X-ray diffraction pattern of [HfCl$_2$((*S*)-PEBA)$_2$] (**7**, top), with simulated diffraction patterns for [HfCl$_2$((*S*)-PEBA)$_2$] (**7**, middle) and [UCl$_2$((*S*)-PEBA)$_2$] (**8**, bottom).

8.2.1.5 [UCl₂((S)-PEBA)₂] (8)
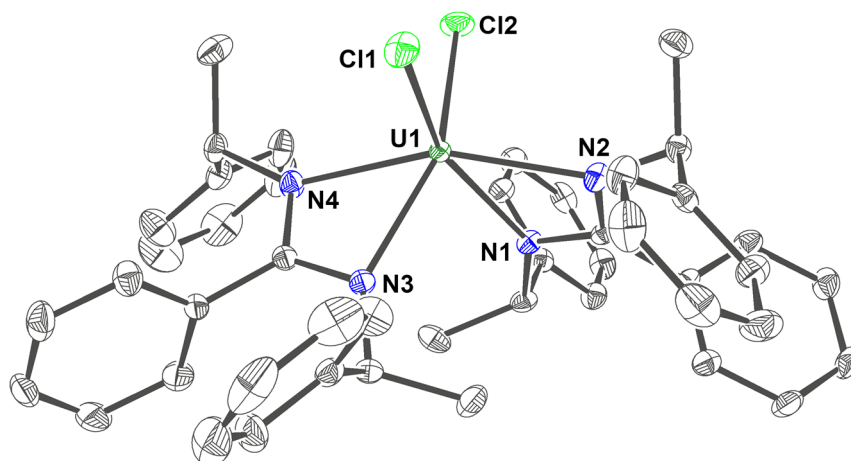
Figure 55. Molecular structure of Λ-[UCl$_2$((*S*)-PEBA)$_2$] (**8**). Ellipsoids are drawn at 50 % probability level. Hydrogen atoms are omitted for clarity. Color code: carbon (C, dark gray), chlorine (Cl, green), nitrogen (N, blue), and uranium (U^{IV}, dark green).


Figure 56. Powder X-ray diffraction pattern of residue after synthesis of [UCl$_2$((*S*)-PEBA)$_2$] (**8**, top) with simulated diffraction patterns based on single-crystal XRD data of [UCl$_2$((*S*)-PEBA)$_2$] (**8**, middle) and [UCl((*S*)-PEBA)$_3$] (**10**, bottom).
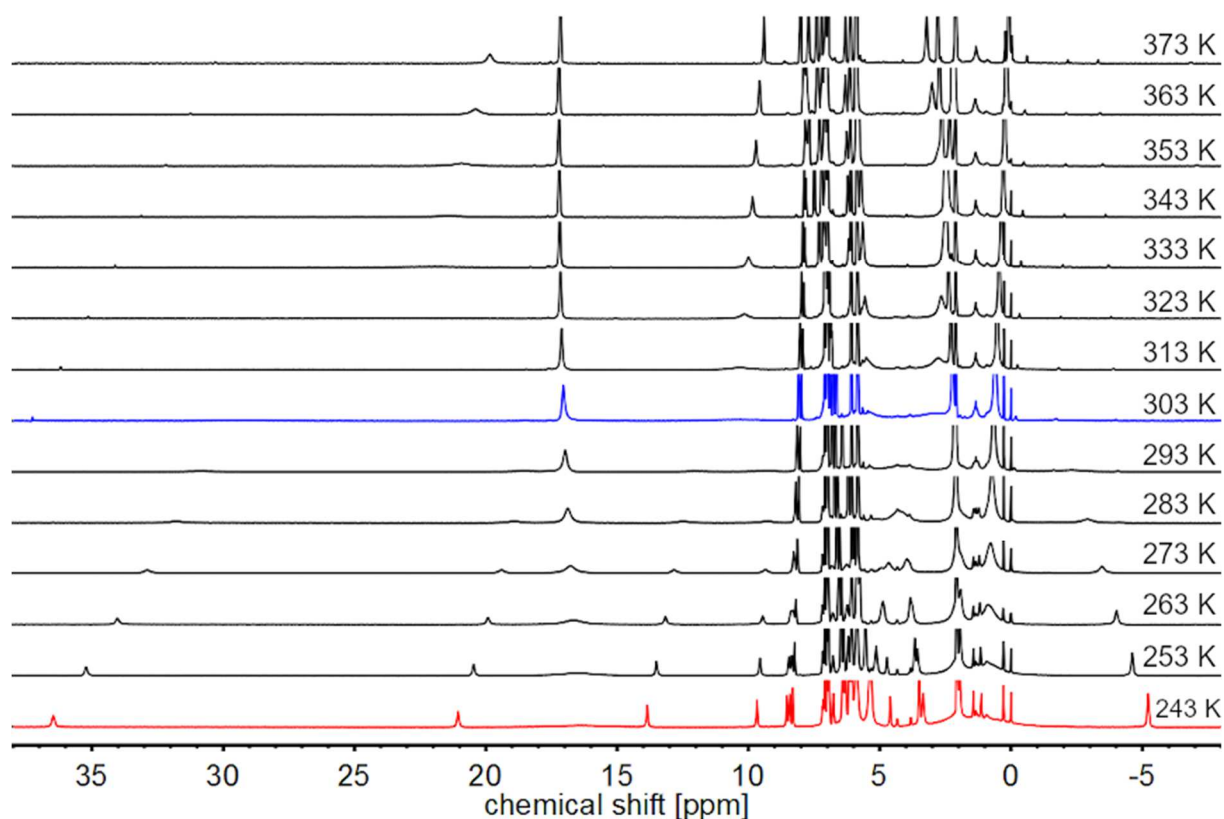
Figure 57. VT ^{1}H NMR spectra of [UCl$_2$((*S*)-PEBA)$_2$] (**8**) with impurities of [UCl((*S*)-PEBA)$_3$] (**10**).

[UCl$_2$((*S*)-PEBA)$_2$] ^{1}H NMR: (400 MHz, toluene-d$_8$, 303 K) δ[ppm]: 17.05 (s, 2H, NC*H*), 6.90 (t, 2H, $^3J_{\text{H-H}}$ = 7.5 Hz, *m*-PhH$^{\text{NCN}}$), 6.76 (t, 1H, $^3J_{\text{H-H}}$ = 7.4 Hz, *p*-PhH$^{\text{NCN}}$), 6.66 (d, 2H, $^3J_{\text{H-H}}$ = 7.4 Hz, *m*-PhH$^{\text{NCN}}$), 6.08 (t, 2H, $^3J_{\text{H-H}}$ = 7.4 Hz, *p*-PhH), 5.84 (t, 4H, $^3J_{\text{H-H}}$ = 7.4 Hz, *m*-PhH), 2.22 (br s, 4H, *o*-PhH), 0.60 (br s, 6H, Me).

[UCl((*S*)-PEBA)$_3$] ^{1}H NMR: (400 MHz, toluene-d$_8$, 243 K) δ[ppm]: 37.10 (s, 1H, NC*H*), 21.37 (s, 1H, NC*H*), 14.03 (s, 1H, *o*-PhH$^{\text{NCN}}$), 9.72 (s, 1H, *o*-PhH$^{\text{NCN}}$), 8.58 (s, 1H, *m*-PhH$^{\text{NCN}}$), 8.47 (s, 1H, *m*-PhH$^{\text{NCN}}$), 8.34 (s, 1H, *p*-PhH$^{\text{NCN}}$), 6.78 (s, 1H, *p*-PhH), 6.16 (s, 2H, *m* PhH), 5.54 (br s, 3H, Me), 4.56 (s, 1H, *p*-PhH), 3.43 (s, 2H, *m*-PhH), 3.25 (s, 2H, *o*-PhH), 1.98 (s, 3H, Me), -5.50 (s, 2H, *o*-PhH).

8.2.2 Tris(amidinate) complexes

8.2.2.1 General comparison

Table 22. Crystallographic data for tris(amidinate) complexes [MCl((*S*)-PEBA)$_3$] **16** (M = Ce), **9** (M = Th), **10** (M = U), **11** (M = Np).

	16	**9**	**10**	**11**
Empirical formula	[C$_{69}$H$_{69}$ClN$_6$Ce]· C$_7$H$_8$	[C$_{69}$H$_{69}$ClN$_6$Th]· C$_7$H$_8$	[C$_{69}$H$_{69}$ClN$_6$U]· C$_7$H$_8$	[C$_{69}$H$_{69}$ClN$_6$Np]· C$_7$H$_8$
M (g/mol)	1250.01	1341.93	1347.92	1346.94
Crystal system	Orthorhombic	Orthorhombic	Orthorhombic	Orthorhombic
Space group	*P*2$_1$2$_1$2$_1$	*P*2$_1$2$_1$2$_1$	*P*2$_1$2$_1$2$_1$	*P*2$_1$2$_1$2$_1$
a (Å)	11.271(1)	11.352(2)	11.239(1)	11.274(2)
b (Å)	15.390(2)	15.435(2)	15.366(2)	15.356(2)
c (Å)	36.744(3)	36.744(6)	36.704(3)	36.654(5)
V (Å^3)	6374(1)	6438(2)	6339(1)	6346(2)
T (K)	100	100	100	100
Z	4	4	4	4
ρ_{calcd} (Mg/m^3)	1.303	1.385	1.413	1.410
abs coeff (mm^{-1})	0.804	2.405	2.652	1.728
Θ_{max} (°)	25.03	25.05	26.02	25.04
R [*I* > 2σ(*I*)]	0.048	0.036	0.029	0.031
wR2(int)	0.081	0.068	0.052	0.101
w scheme *d*, *e*	0.0142, 13.9475	0.0207, 0	0.0150, 6.0873	0.0343, 8.9548
Data/Param	11238/746	11382/717	12459/759	11206/752
res. Dens (eÅ^{-3})	0.77, -0.61	1.12, -1.75	0.72, -0.92	1.39, -2.01
R$_{int}$	0.1211	0.069	0.083	0.043
GooF	1.037	1.029	1.022	1.137
Flack x	0.022(6)	0.032(4)	0.016(2)	0.014(4)

Table 23. Intramolecular distances between metal center M and coordinating atoms in isostructural tris(amidinate) [MCl((*S*)-PEBA)$_3$] complexes **16**, **9-11**.

d(M–X) [Å]	**16**	**9**	**10**	**11**
Cl1	2.644(2)	2.701(2)	2.641(1)	2.630(1)
N1	2.507(5)	2.548(5)	2.495(4)	2.494(5)
N2	2.362(5)	2.439(5)	2.372(4)	2.362(5)
N3	2.508(6)	2.555(5)	2.497(4)	2.494(6)
N4	2.392(5)	2.456(5)	2.406(4)	2.389(5)
N5	2.521(6)	2.577(6)	2.505(4)	2.503(6)
N6	2.341(5)	2.423(6)	2.360(4)	2.353(5)

Table 24. Tilting angles α of different amidinate moieties in tris(amidinate) complexes [MCl((*S*)-PEBA)$_3$] (M = Ce (**16**), Th (**9**), U (**10**), Np (**11**)). The definition of the angle α between plane normal and An–Cl bond is depicted in inset right.

α [°]	**16** (M = Ce)	**9** (M = Th)	**10** (M = U)	**11** (M = Np)	
A	53.4	53.0°	53.3°	53.3°	
B	46.6	47.9°	46.5°	46.5°	
C	40.9	40.1°	40.7°	40.8°	
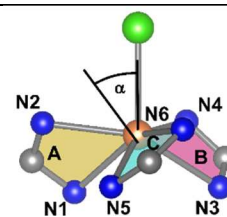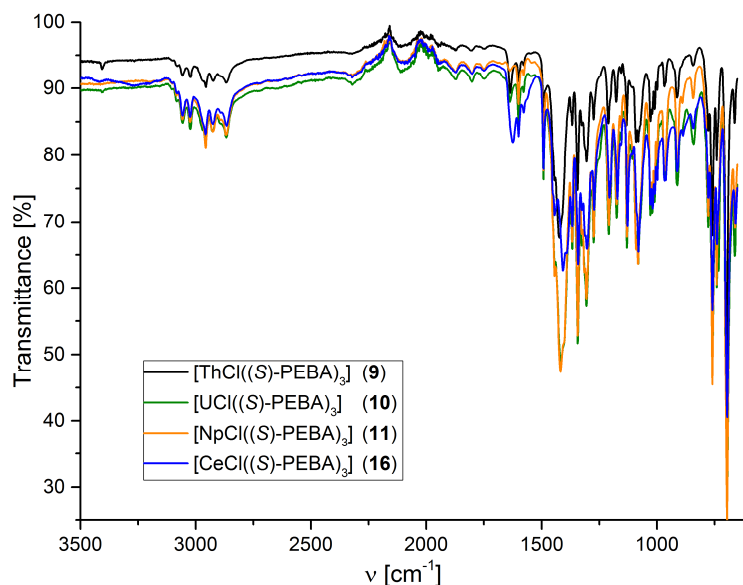
Figure 58. ATR-IR spectra of isostructural [MCl((*S*)-PEBA)₃] (**16**, **9-11**) compounds.

Table 25. ^{13}C chemical shifts of diamagnetic [MCl((*S*)-PEBA)₃] (M = Ce (**16**), Th (**9**)) in toluene-d₈ at 298 K.

	[CeCl((*S*)-PEBA)₃] (**16**)	[ThCl((*S*)-PEBA)₂] (**9**)
N*C*N	176.1	180.3
i-Ph^{NCN}	134.6	135.7
o-Ph^{NCN}	126.3	126.3
m-Ph^{NCN}	127.6	127.6
p-Ph^{NCN}	127.6	127.5
i-Ph	150.9	149.1
N*C*H	63.3	60.4
Me	26.7	26.0
o-Ph	127.6	127.5
m-Ph	128.1	128.1
p-Ph	126.3	126.2

Table 26. Derived FERMI contact and pseudocontact contributions of paramagnetic shifts for [AnCl((*S*)-PEBA)₃] (An = U (**10**), Np (**11**)) based on BLEANEY method at 298 K. Brackets indicate error of last digits by linear regression analysis. Values in grey belong to linear regression models with R^2 < 0.95.

	[UCl((*S*)-PEBA)₃] (**10**)		[NpCl((*S*)-PEBA)₃] (**11**)	
	FCS [ppm]	PCS [ppm]	FCS [ppm]	PCS [ppm]
Me	-3.24(16)	4.22(19)	-6.05(34)	6.13(39)
N*C*H	12.97(26)	7.42(31)	-	-
o-Ph^{NCN}	1.62(30)	2.56(34)	1.99(11)	3.81(13)
m-Ph^{NCN}	0.66(04)	0.74(04)	0.77(04)	1.73(04)
p-Ph^{NCN}	0.61(04)	0.59(05)	0.72(05)	1.18(05)
o-Ph	1.34(29)	-7.99(35)	-	-
m-Ph	0.10(04)	-1.78(05)	0.94(10)	-3.09(11)
p-Ph	0.07(03)	-1.03(03)	0.60(06)	-1.83(07)

8.2.2.2 [CeCl((S)-PEBA)₃] (16)
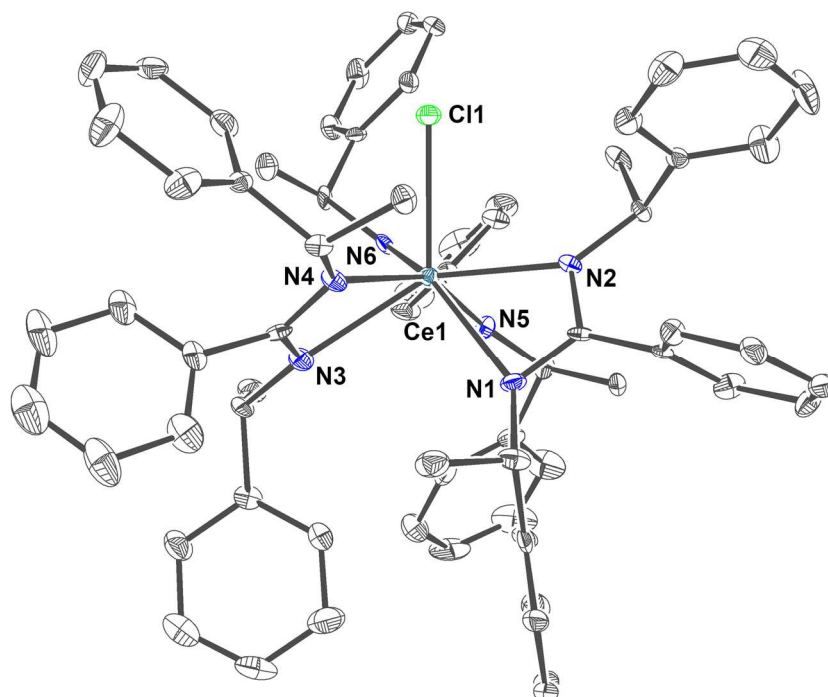
Figure 59. Molecular structure of Δ-[CeCl((*S*)-PEBA)₃] (**16**). Ellipsoids are drawn at 50 % probability level. Hydrogen atoms and solvent molecules are omitted for clarity. Color code: carbon (C, dark gray), chlorine (Cl, green), nitrogen (N, blue), and cerium (Ce, dark blue).
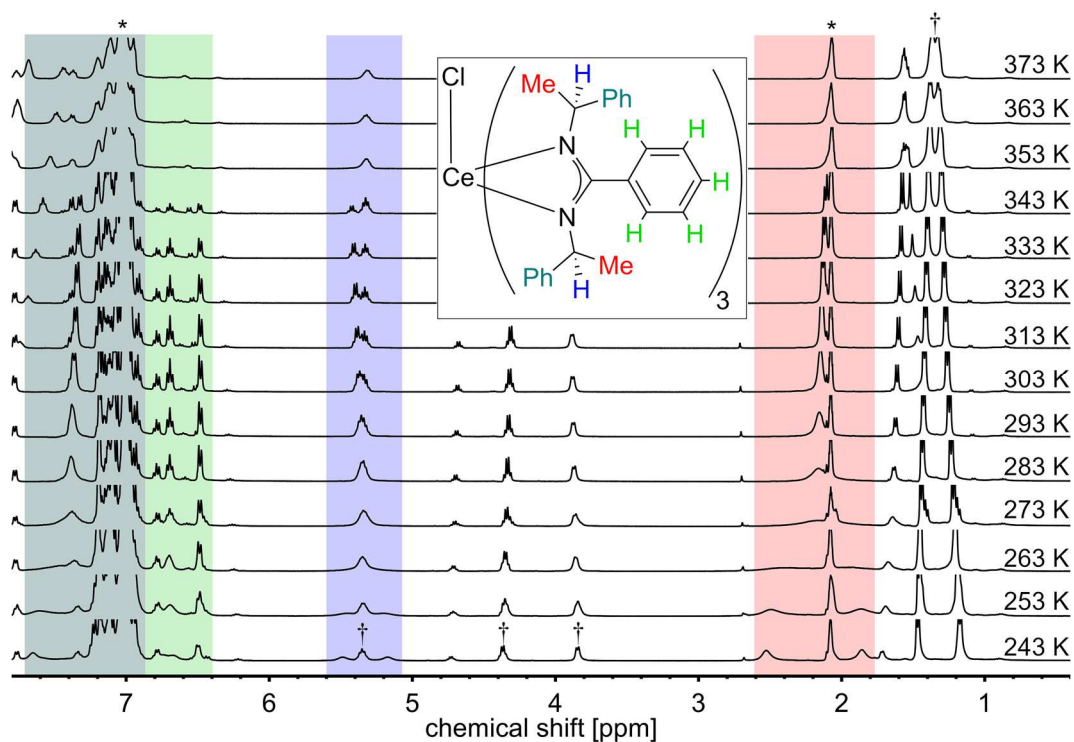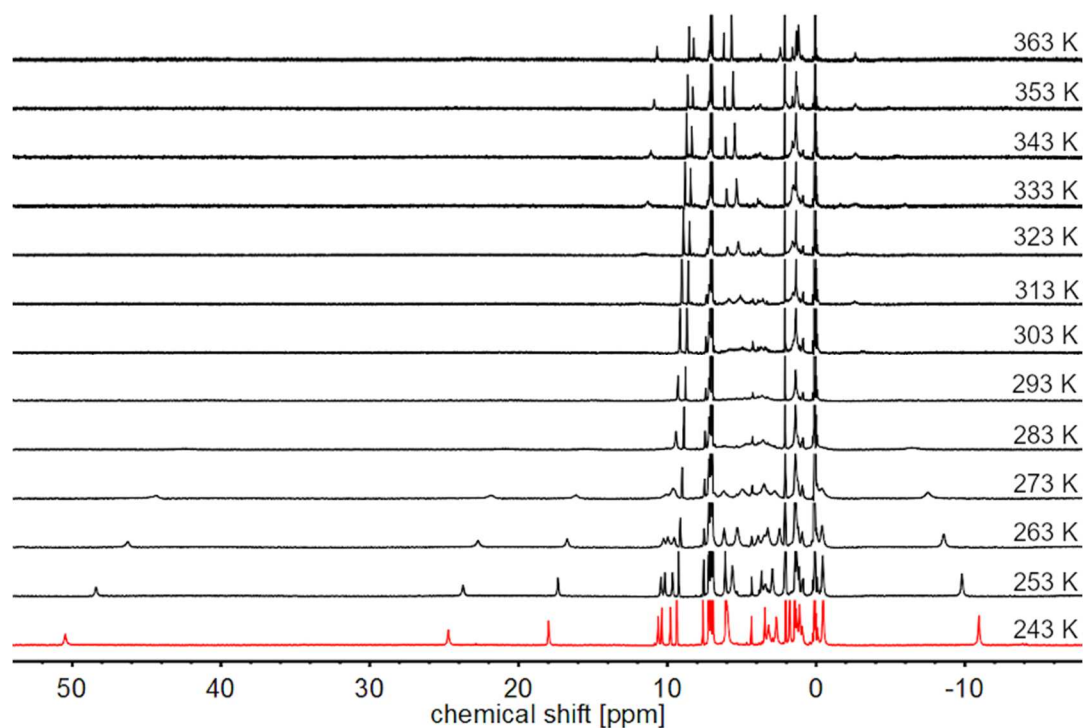

Figure 60. VT-¹H NMR spectra of [CeCl((*S*)-PEBA)₃] (**16**) in toluene-d₈. Signals are marked with colors: blue (NC*H*), red (Me), green (Ph^NCN) and petrol green (Ph). Asterisks indicate solvent signals (i.e. toluene) and dagger impurity of (*S*)-HPEBA.

8.2.2.3 [ThCl((S)-PEBA)₃] (9)
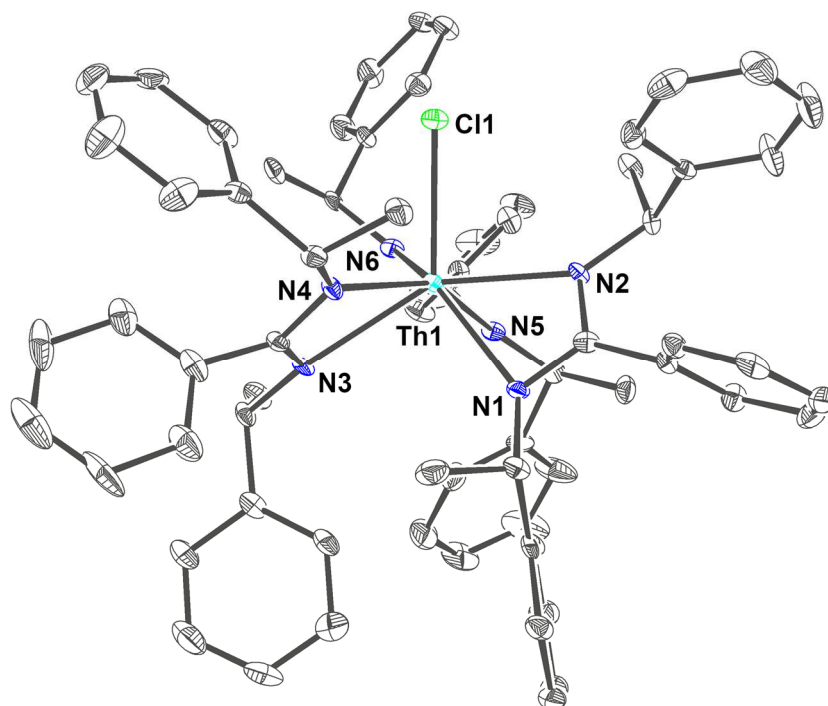
Figure 61. Molecular structure of Δ-[ThCl((S)-PEBA)₃] (**9**). Ellipsoids are drawn at 50 % probability level. Hydrogen atoms and solvent molecules are omitted for clarity. Color code: carbon (C, dark gray), chlorine (Cl, green), nitrogen (N, blue), and thorium (Th, pale blue).
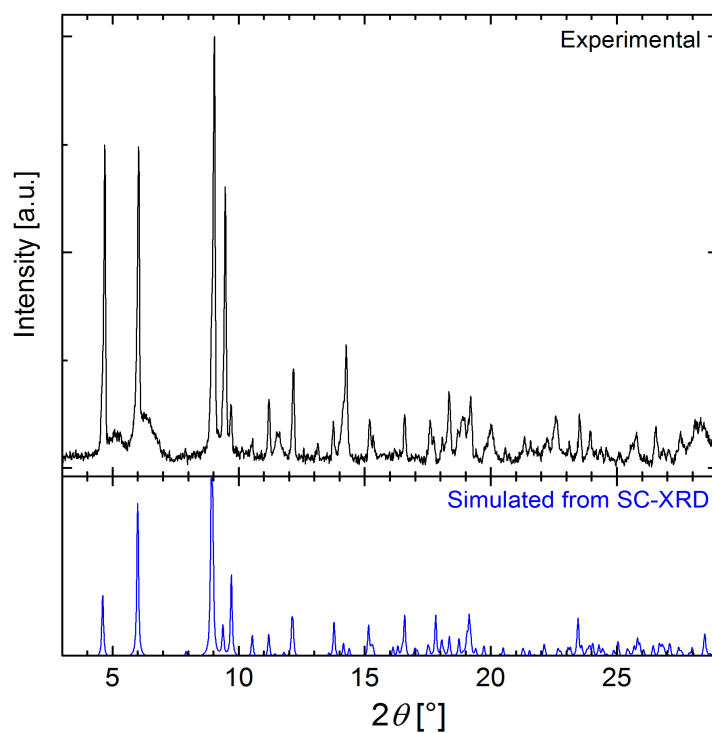
Figure 62. Powder X-ray diffraction pattern of [ThCl((S)-PEBA)₃] (**9**, top) with simulated diffraction pattern based on single-crystal XRD data (bottom).
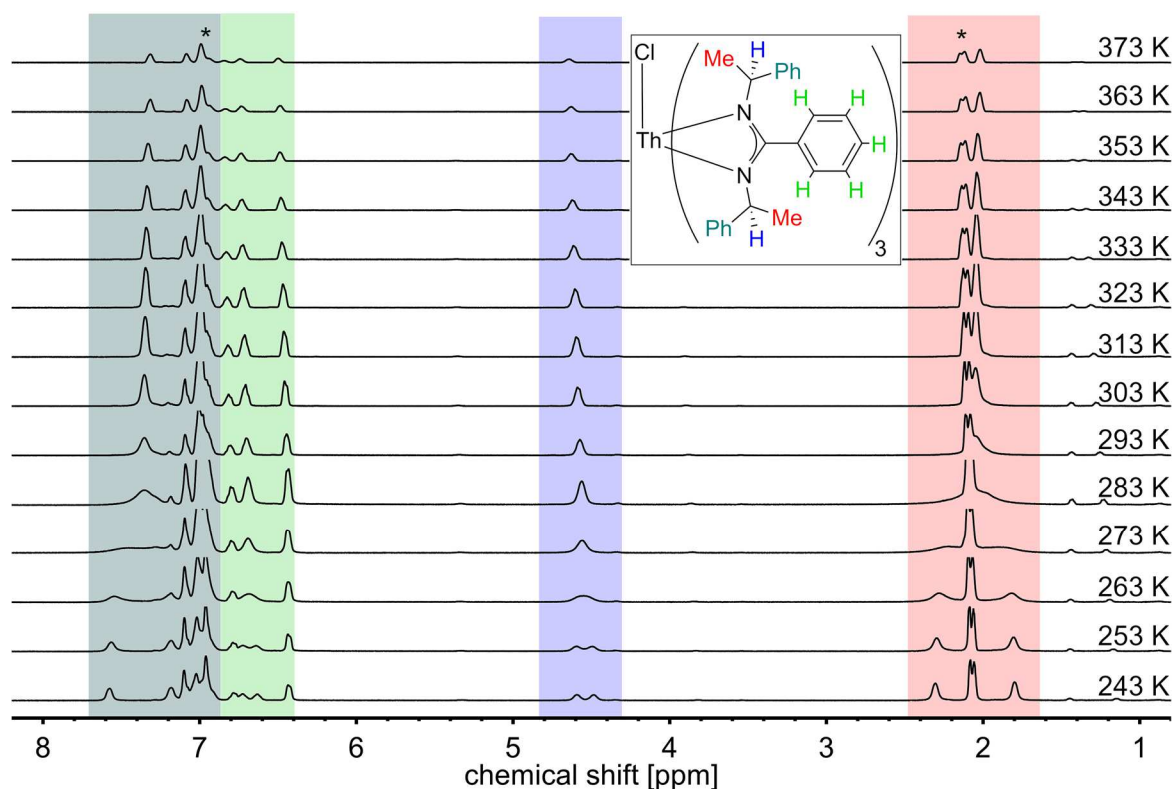
Figure 63. VT-^{1}H NMR spectra of [ThCl((*S*)-PEBA)₃] (**9**) in toluene-d₈. Signals are marked with colors: blue (NC*H*), red (Me), green (Ph^NCN) and petrol green (Ph). Asterisks indicate solvent signals (i.e. toluene).
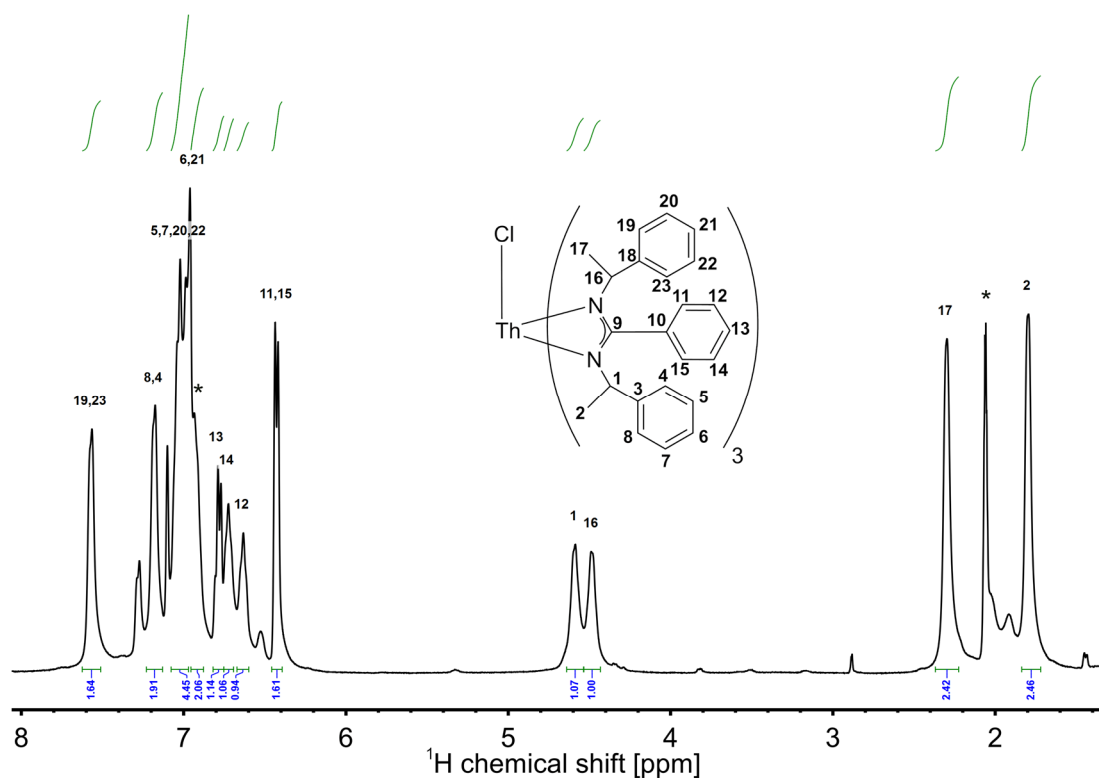
Figure 64. ^{1}H NMR spectrum of [ThCl((*S*)-PEBA)₃] (**9**) in toluene-d₈ at 243 K with signal assignments. Asterisks indicate solvent signals (i.e. toluene).
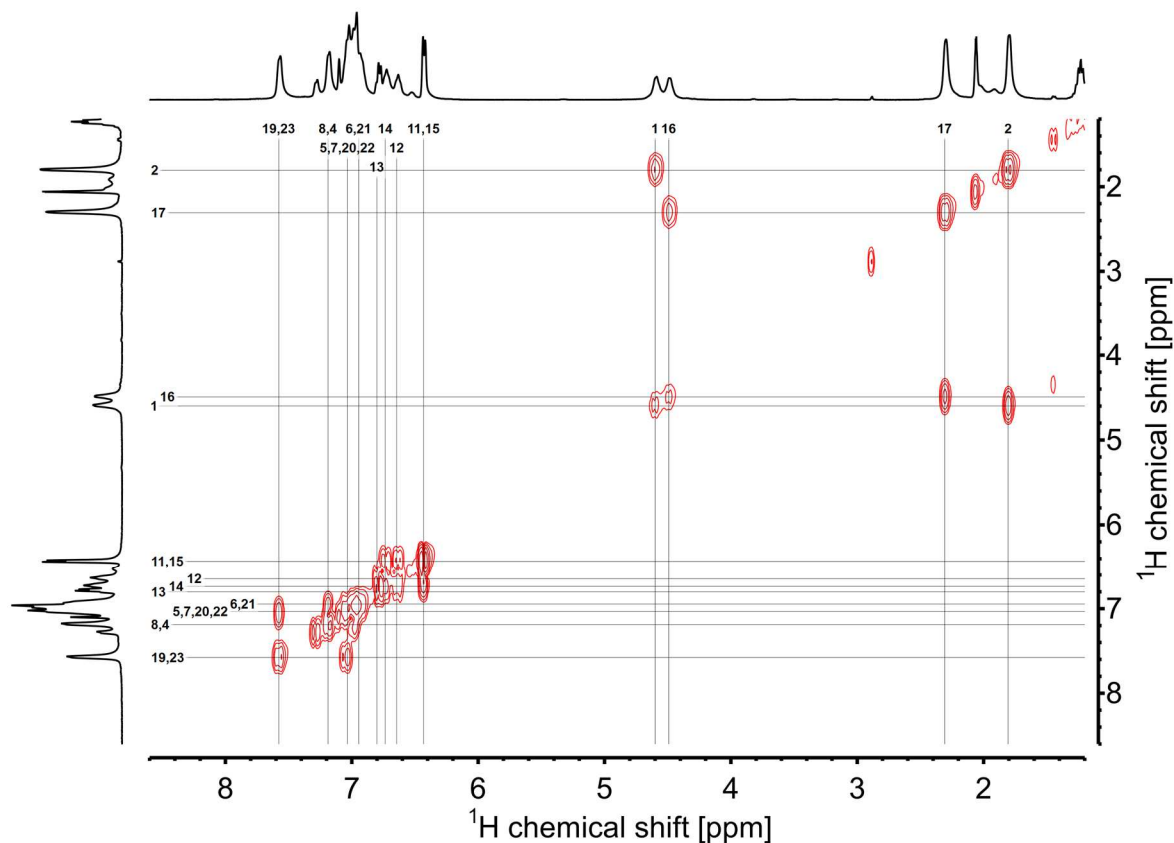
Figure 65. ^{1}H-^{1}H-COSY spectrum of [ThCl((*S*)-PEBA)$_3$] (**9**) in toluene-d$_8$ at 243 K with signal assignments.
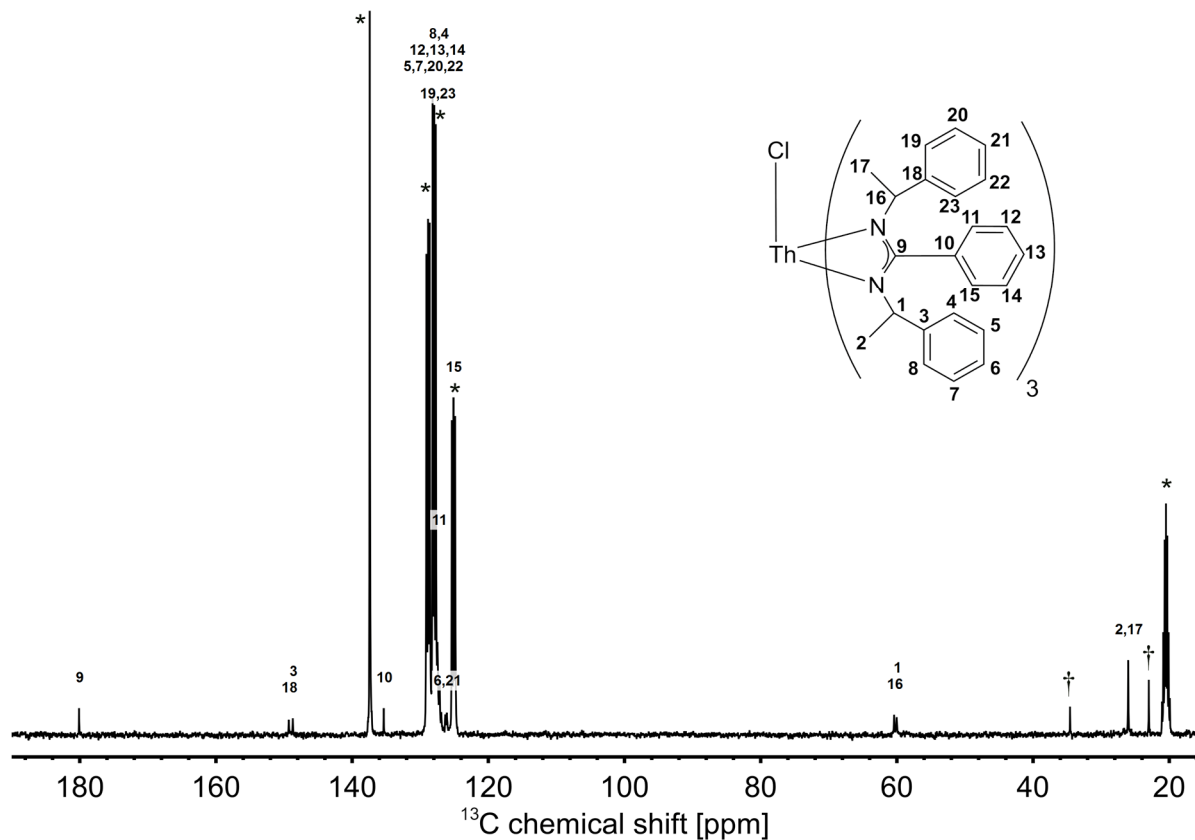
Figure 66. ^{13}C NMR spectrum of [ThCl((*S*)-PEBA)$_3$] (**9**) in toluene-d$_8$ at 243 K with signal assignments based on HSQC and HMBC. Asterisks indicate solvent signals (i.e. toluene) and dagger impurity of *n*-pentane.

Figure 67. Part of ^{1}H-^{13}C-HSQC spectrum of [ThCl((*S*)-PEBA)$_3$] at 253 K (a, left) and at 298 K (b, right).

Figure 68. Parts of ^{1}H-^{13}C-HSQC spectrum of [ThCl((*S*)-PEBA)$_3$] (**9**) in toluene-d$_8$ at 243 K with signal assignments. Aliphatic region is depicted in a) and aromatic region in b).

Figure 69. ^{1}H-^{13}C-HMBC spectrum of [ThCl((*S*)-PEBA)$_3$] (**9**) in toluene-d$_8$ at 243 K with signal assignments.
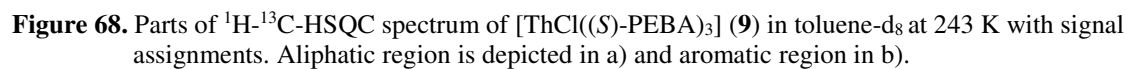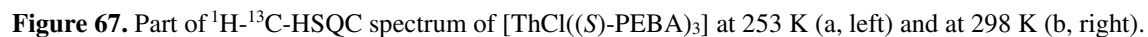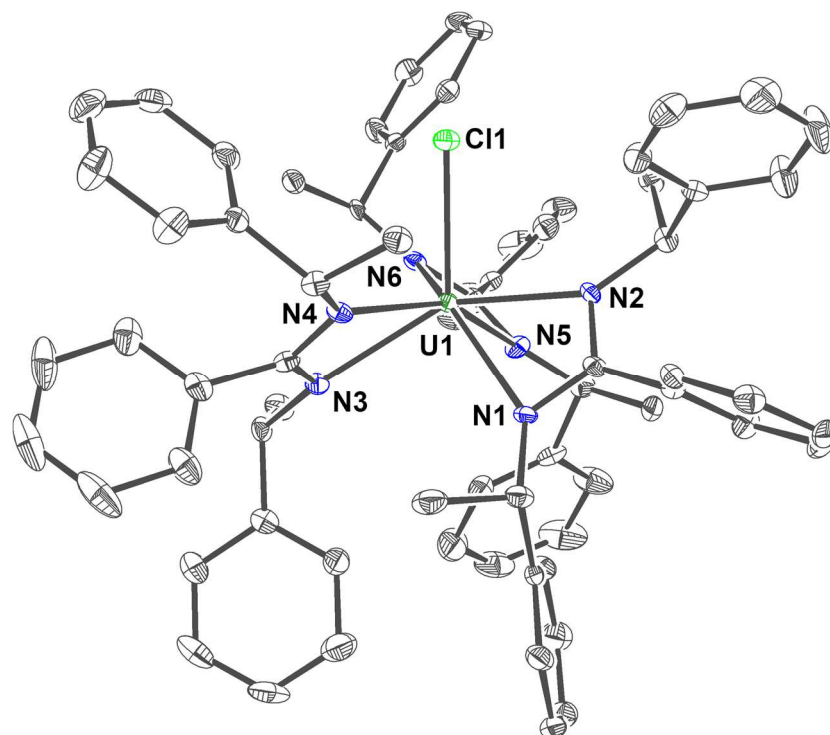
8.2.2.4   [UCl((S)-PEBA)₃] (10)

Figure 70. Molecular structure of Δ-[UCl((S)-PEBA)₃] (**10**). Ellipsoids are drawn at 50 % probability level. Hydrogen atoms and solvent molecules are omitted for clarity. Color code: carbon (C, dark gray), chlorine (Cl, green), nitrogen (N, blue), and uranium (U^{IV}, dark green).
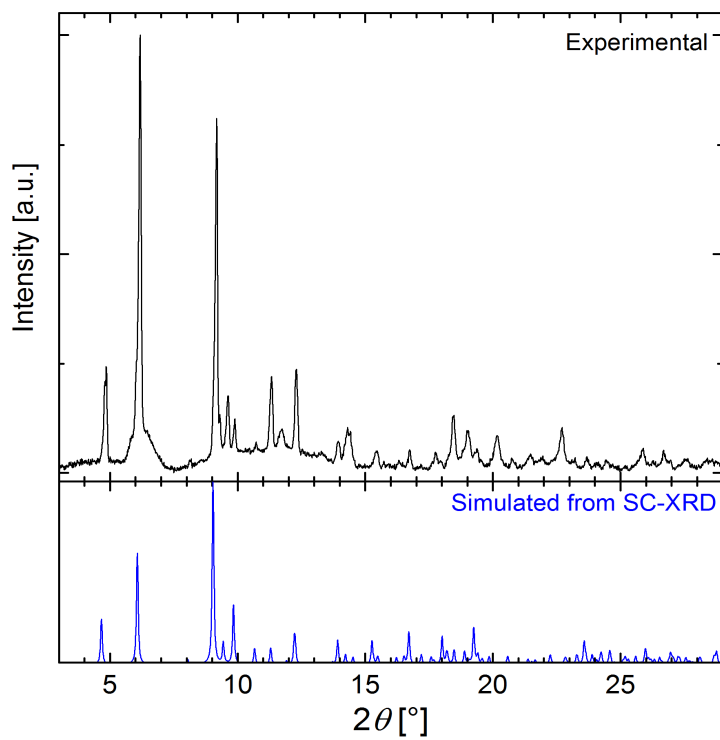
Figure 71. Powder X-ray diffraction pattern of [UCl((S)-PEBA)₃] (**10**, top) with simulated diffraction pattern based on single-crystal XRD data (bottom).
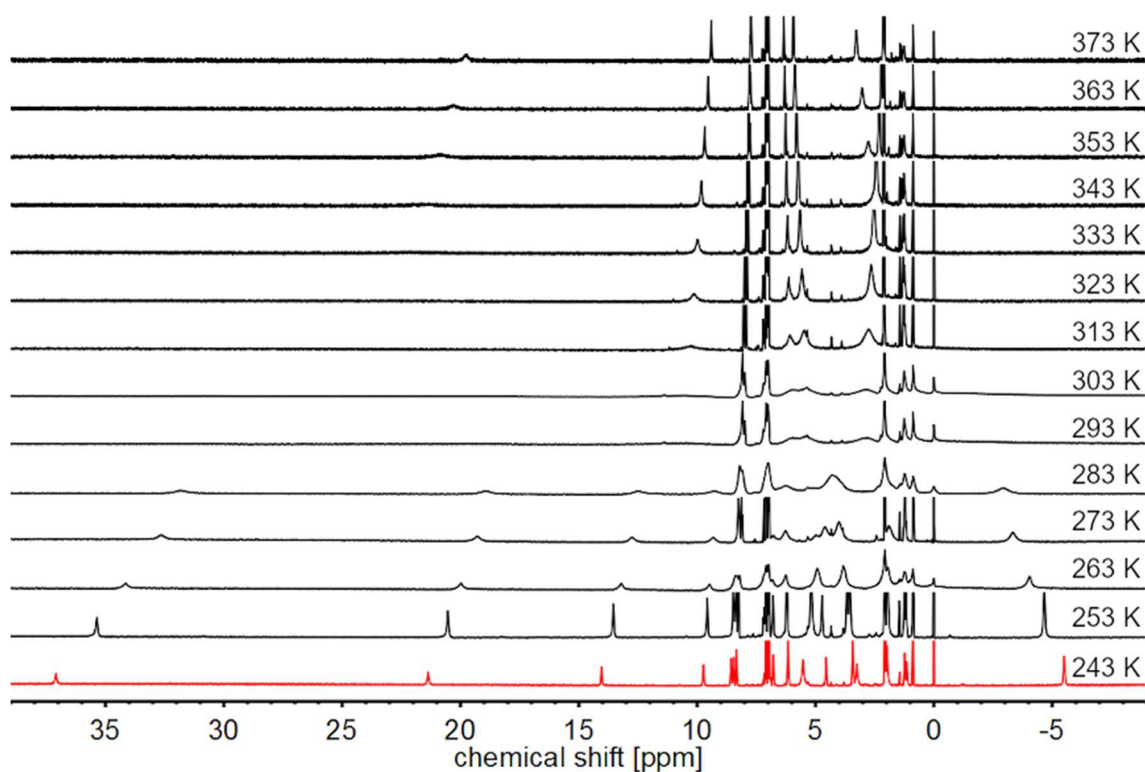
Figure 72. VT-¹H NMR spectra of [UCl((*S*)-PEBA)₃] (**10**) in toluene-d₈.

¹H NMR: (400 MHz, toluene-d₈, 243 K) δ[ppm]: 37.10 (s, 1H, NC*H*), 21.37 (s, 1H, NC*H*), 14.03 (s, 1H, *o*-PhH^NCN), 9.72 (s, 1H, *o*-PhH^NCN), 8.58 (s, 1H, *m*-PhH^NCN), 8.47 (s, 1H, *m*-PhH^NCN), 8.34 (s, 1H, *p*-PhH^NCN), 6.78 (s, 1H, *p*-PhH), 6.16 (s, 2H, *m* PhH), 5.54 (br s, 3H, Me), 4.56 (s, 1H, *p*-PhH), 3.43 (s, 2H, *m*-PhH), 3.25 (s, 2H, *o*-PhH), 1.98 (s, 3H, Me), -5.50 (s, 2H, *o*-PhH).
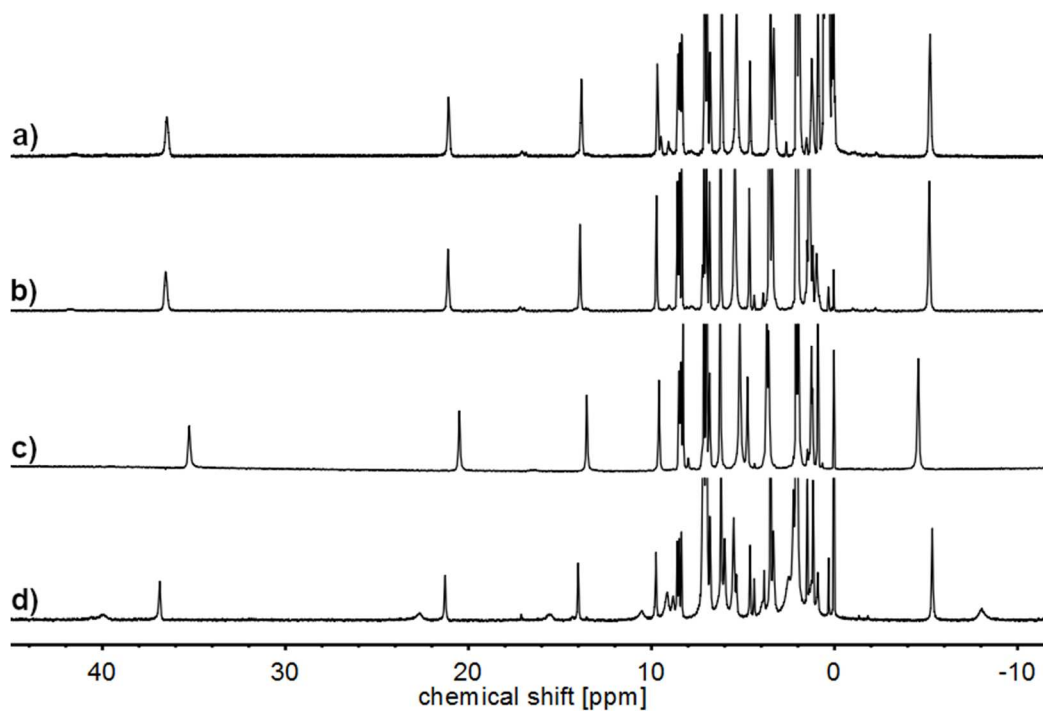
Figure 73. ¹H-NMR spectra of dissolved residues after reaction of [UCl((*S*)-PEBA)₃] (**10**) with TMSI (a), KI (b), NaBPh₄ (c) and KCN (d) in toluene-d₈ at 243 K.

8.2.2.5   *[NpCl((S)-PEBA)₃] (11)*
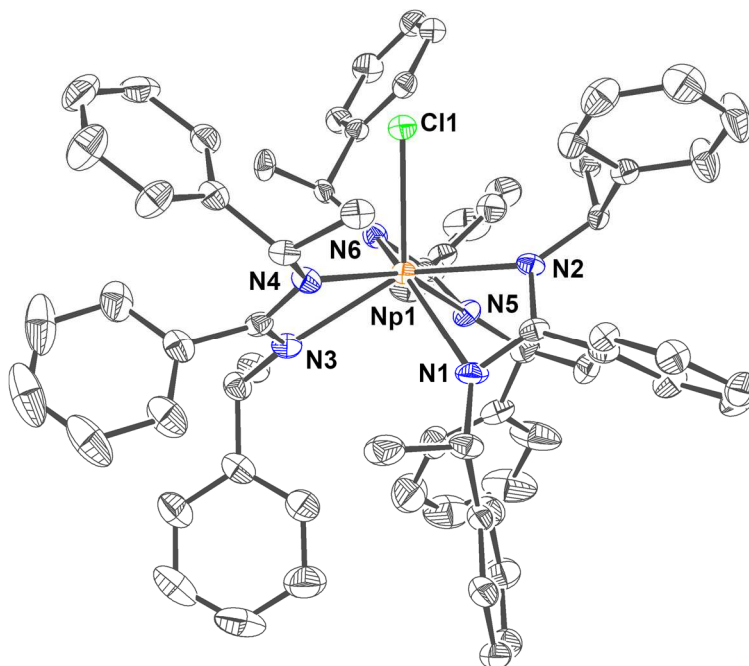
Figure 74. Molecular structure of Δ-[NpCl((S)-PEBA)₃] (**11**). Ellipsoids are drawn at 50 % probability level. Hydrogen atoms and solvent molecules are omitted for clarity. Color code: carbon (C, dark gray), chlorine (Cl, green), nitrogen (N, blue), and neptunium (Np^{IV}, orange red).

Figure 75. VT-^{1}H NMR spectra of [NpCl((S)-PEBA)₃] (**11**) in toluene-d₈.

^{1}H NMR: (400 MHz, toluene-d₈, 243 K) δ[ppm]: 50.47 (s, 1H, NC*H*), 24.72 (s, 1H, NC*H*), 17.98 (s, 1H, *o*-PhH^{NCN}), 10.62 (s, 1H, *o*-PhH^{NCN}), 10.37 (s, 1H, *m*-PhH^{NCN}), 9.79 (s, 1H, *m*-PhH^{NCN}), 9.37 (s, 1H, *p*-PhH^{NCN}), 6.94 (s, 1H, *p*-PhH), 6.06 (s, 2H, *m*-PhH), 5.97 (s, 3H, Me), 3.45 (s, 1H, *p*-PhH), 2.68 (s, 2H, *o*-PhH), 1.77 (s, 2H, *m*-PhH), -0.47 (s, 3H, Me), -10.94 (s, 2H, *o*-PhH).

8.2.3 Tetravalent pseudo(halide) amidinate complexes with (*S*)-PEBA

8.2.3.1 General comparison

Table 27. Intramolecular distances between actinide An and coordinating atoms X in isostructural [AnX((*S*)-PEBA)₃] complexes (An = Th, U, Np) **9-11**, **17-25**.

d(Th–X) [Å]	**9** (X = Cl)	**17** (X = F)	**20** (X = Br)	**23** (X = N₃)
X	2.701(2)	2.151(4)	2.865(1)	2.342(16)
N1	2.548(5)	2.597(5)	2.550(3)	2.556(15)
N2	2.439(5)	2.439(7)	2.441(3)	2.427(15)
N3	2.555(5)	2.566(6)	2.554(3)	2.566(17)
N4	2.456(5)	2.488(6)	2.459(3)	2.456(16)
N5	2.577(6)	2.577(7)	2.560(3)	2.559(17)
N6	2.423(6)	2.449(6)	2.422(3)	2.407(16)
d(U–X) [Å]	**10** (X = Cl)	**18** (X = F)	**21** (X = Br)	**24** (X = N₃)
X	2.641(1)	2.113(3)	2.808(1)	2.293(6)
N1	2.495(4)	2.542(4)	2.503(4)	2.483(6)
N2	2.372(4)	2.393(4)	2.387(4)	2.375(6)
N3	2.497(4)	2.515(4)	2.495(5)	2.488(6)
N4	2.406(4)	2.415(4)	2.411(4)	2.394(5)
N5	2.505(4)	2.534(5)	2.500(6)	2.511(7)
N6	2.360(4)	2.373(4)	2.375(4)	2.397(6)
d(Np–X) [Å]	**11** (X = Cl)	**19** (X = F)	**22** (X = Br)	**25** (X = N₃)
X	2.630(1)	2.126(14)	2.792(1)	2.230(30)
N1	2.494(5)	2.551(18)	2.488(3)	2.460(30)
N2	2.362(5)	2.420(20)	2.359(3)	2.370(40)
N3	2.494(6)	2.490(20)	2.486(4)	2.470(30)
N4	2.389(5)	2.479(17)	2.382(3)	2.420(30)
N5	2.503(6)	2.530(20)	2.493(4)	2.540(30)
N6	2.353(5)	2.330(20)	2.351(3)	2.360(30)

Table 28. Angles α of plane normal of N1–An–N2 (A), N3–An–N4 (B) and N5–An–N6 (C) against An–X bond in isostructural [AnX((*S*)-PEBA)₃]. The definition of the angle α between plane normal C (N5–M1–N6) and An–Cl bond is depicted in inset right.

Th	**9** (X = Cl)	**17** (X = F)	**20** (X = Br)	**23** (X = N₃)
A	53.0	53.9	53.3	52.7
B	47.9	47.9	48.3	47.5
C	40.1	36.4	39.9	40.2
U	**10** (X = Cl)	**18** (X = F)	**21** (X = Br)	**24** (X = N₃)
A	53.3	52.4	53.0	56.9
B	46.5	47.8	47.3	47.7
C	40.7	40.5	40.0	35.9
Np	**11** (X = Cl)	**19** (X = F)	**22** (X = Br)	**25** (X = N₃)
A	53.3°	55.2°	53.8°	57°
B	46.5°	45.5°	47.1°	43°
C	40.8°	36.7°	40.4°	38°
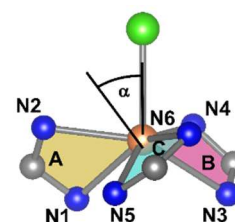
Table 29. Coalescence temperatures (T_C) of ^{1}H NMR signals of [AnX((S)-PEBA)$_3$] compounds **9-11** and **17-25**.

Th	F (**17**)	Cl (**9**)	Br (**20**)	N$_3$ (**23**)
NC*H*	293 K	263 K	253 K	263 K
Me	293 K	283 K	273 K	273 K
o-Ph^{NCN}	293 K	-	-	-
m-Ph^{NCN}	293 K	263 K	253 K	263 K
o-Ph	293 K	283 K	273 K	263 K
m-Ph	-	-	-	-
p-Ph	-	-	-	-
U	**F (18)**	**Cl (10)**	**Br (21)**	**N$_3$ (24)**
NC*H*	>373 K	323 K	323 K	333 K
Me	>373 K	303 K	303 K	293 K
o-Ph^{NCN}	>373 K	293 K	293 K	293 K
m-Ph^{NCN}	333 K	273 K	263 K	-
o-Ph	343 K	353 K	333 K	323 K
m-Ph	333 K	303 K	303 K	293 K
p-Ph	333 K	303 K	303 K	293 K
Np	**F (19)**	**Cl (11)**	**Br (22)**	**N$_3$ (25)**
NC*H*	>373 K	373 K	313 K	353 K
Me	-	343 K	333 K	343 K
o-Ph^{NCN}	343 K	313 K	303 K	323 K
m-Ph^{NCN}	313 K	273 K	263 K	273 K
o-Ph	353 K	363 K	333 K	353 K
m-Ph	343 K	313 K	293 K	313 K
p-Ph	343 K	313 K	293 K	313 K

Table 30. Calculated rate constants k_c for dynamic processes in diamagnetic tris(amidinate) compounds [ThX((S)-PEBA)$_3$] (X = F (**17**), Cl (**9**), Br (**20**), N$_3$ (**23**)). Error in brackets corresponds to $\Delta\Delta\delta_{1H}$ = 0.01 ppm.

k_c [Hz]	F (**17**)	Cl (**9**)	Br (**20**)	N$_3$ (**23**)
Me	267(9)	444(9)	480(9)	258(9)
NC*H*	169(9)	98(9)	27(9)	116(9)
m-H^{NCN}	71(9)	80(9)	44(9)	80(9)
o-H	231(9)	347(9)	355(9)	116(9)
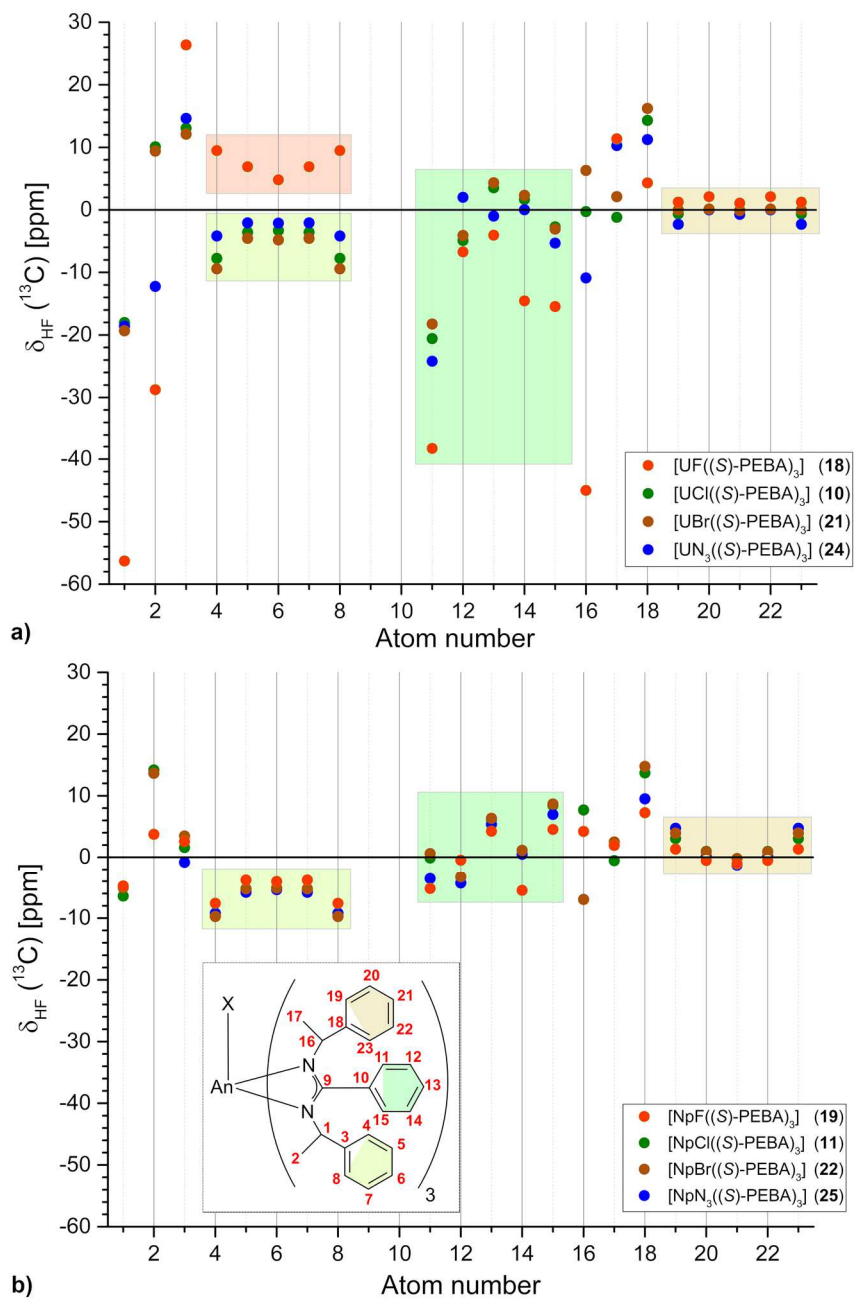
Figure 76. Plot of the ^{13}C hyperfine shift in toluene-d$_8$ at 243 K for a) [UX((*S*)-PEBA)$_3$] (X = F (**18**), Cl (**10**), Br (**21**), N$_3$ (**24**)) and b) [NpX((*S*)-PEBA)$_3$] (X = F (**19**), Cl (**11**), Br (**22**), N$_3$ (**25**)). Signals for C1, C2, C16, C17 of **25** have not been visible in the NMR spectra.

8.2.3.2 Comparison thorium complexes

Table 31. Crystallographic data for thorium tris(amidinate) complexes [ThX((S)-PEBA)₃] **17** (X = F), **9** (X = Cl), **20** (X = Br), **23** (X = N₃).

	17	9	20	23
Empirical formula	[C$_{69}$H$_{69}$FN$_6$Th] ·C$_7$H$_8$	[C$_{69}$H$_{69}$ClN$_6$Th] ·C$_7$H$_8$	[C$_{69}$H$_{69}$BrN$_6$Th] ·C$_7$H$_8$	[C$_{69}$H$_{69}$N$_9$Th] ·C$_7$H$_8$
M (g/mol)	1325.50	1341.93	1386.38	1302.43
Crystal system	Orthorhombic	Orthorhombic	Orthorhombic	Orthorhombic
Space group	$P2_12_12_1$	$P2_12_12_1$	$P2_12_12_1$	$P2_12_12_1$
a (Å)	11.405(1)	11.352(2)	11.414(1)	11.443(3)
b (Å)	15.688(2)	15.435(2)	15.443(1)	15.396(3)
c (Å)	36.237(3)	36.744(6)	36.595(2)	37.274(8)
V (Å^3)	6484(1)	6438(2)	6451(1)	6567(3)
T (K)	100	100	100	100
Z	4	4	4	4
ρ_{calcd} (Mg/m^3)	1.263	1.385	1.428	1.317
abs coeff (mm^{-1})	2.345	2.405	2.979	2.318
Θ_{max} (°)	28.280	25.05	28.270	25.03
R [$I > 2\sigma(I)$]	0.034	0.036	0.022	0.073
wR2(int)	0.079	0.068	0.046	0.205
w scheme d, e	0.0091, 16.8035	0.0207, 0	0.0169, 1.9037	0, 181.0673
Data/Param	16082/701	11382/717	15989/764	11565/692
res. Dens (eÅ^{-3})	4.119, -1.941	1.12, -1.75	0.829, -0.910	4.267/-7.528
R_{int}	0.026	0.069	0.039	0.0451
GooF	1.200	1.029	1.040	1.372
Flack x	0.042(2)	0.032(4)	0.009(2)	0.11(2)

Table 32. Comparison of intramolecular Th–F distance of Th fluoro complex **17** with literature data of structurally characterized Th–F compounds heaving terminal fluoro ligands.

	d(Th–F) [Å]
[ThF((S)-PEBA)₃] (**17**)	2.154
[ThF$_2$(^{tt}Cp)$_2$][310]	2.134, 2.117
[ThF$_2$(py)(Cp*)$_2$][311]	2.157, 2.176
[C(NH$_2$)$_3$]$_3$[ThF$_3$(edta)][312]	2.267, 2.288, 2.296
[C(NH$_2$)$_3$]$_5$[ThF$_3$(CO$_3$)$_3$][313]	2.273, 2.287, 2.299
[ThF(^{t}Cp)(μ_3-F)ThF(^{t}Cp)(bipy)][314]	2.188, 2.138
[ThF(py)$_4$(SC$_6$F$_5$)(μ_3-F)ThF(py)$_3$(SC$_6$F$_5$)$_2$][315]	2.165, 2.155

^{tt}Cp = η^5-(1,2,4-(Me$_3$C)$_3$C$_5$H$_2$);   Cp* = η^5-C$_5$Me$_5$;   edta = ethylenediaminetetraacetate;

^{t}Cp = η^5-(1,3-(Me$_3$C)$_2$C$_5$H$_3$); py = pyridine; bipy = 2,2′-bipyridine

Table 33. Comparison of intramolecular Th–Br distance of Th bromo compound **20** with literature data of structurally characterized Th–Br compounds heaving a terminal bromo ligand.

	d(Th–Br) [Å]
[ThBr((S)-PEBA)₃] (**20**)	2.865
[ThBr(Cp′)₃][316]	2.852
[ThBr(Cp**)₃][317]	2.837
[ThBr₂(ᵗCp)₂][314]	2.779, 2.810
[ThBr₂(Cp*)₂][318]	2.800
[ThBr₄(dme)₂][319]	2.852, 2.871, 2.863, 2.863
[ThBr₄(OC(NEt₂)₂)₂][320]	2.834
[ThBr₄(thf)₄][321]	2.854, 2.833, 2.873, 2.876

Cp′ = η^5-((SiMe₃)C₅H₄);   Cp** = η^5-(1,2,3,4-Me₄C₅H);
ᵗCp = η^5-(1,3-(Me₃C)₂C₅H₃);   Cp* = η^5-C₅Me₅;
dme = dimethoxyethane;   thf = tetrahydrofuran

Table 34. Comparison of intramolecular Th^{IV}–N distances and Th–N–N angles of Th azide **23** with literature data of structurally characterized Th^{IV} compounds heaving terminal azido ligands.

	d(Th–N) [Å]	α(Th–N–N) [°]
[ThN₃((S)-PEBA)₃] (**23**)	2.342	160.1
[ThN₃(Cp*)₂(N(SiMe₃)₂)][243]	2.301	166.1
[ThN₃(ᵗᵗCp)₂(NPMes*)][322]	2.306	172.9
[Th(N₃)₂(L²¹)₂][244]	2.439	145.7

Cp* = η^5-C₅Me₅; ᵗᵗCp = η^5-(1,2,4-(Me₃C)₃C₅H₂); Mes* = 2,4,6-(Me₃C)₃C₆H₂;
L²¹ = ((NC₉H₆)N=C(H)C₆H₂ᵗBu₂O-κ^3(O,N,N′))

Table 35. ^{13}C chemical shifts of diamagnetic [ThX((S)-PEBA)₃] (X = F (**17**), Cl (**9**), Br (**20**), N₃ (**23**)) in toluene-d₈ at 243 K.

|	[ThF((S)-PEBA)₂] (**17**)	[ThCl((S)-PEBA)₂] (**9**)	[ThBr((S)-PEBA)₂] (**20**)	[ThN₃((S)-PEBA)₂] (**23**)
NCN	178.7	180.1	180.3	179.5
NCH (1)	59.5	60.4	60.2	59.7
NCH (16)	59.4	60.1	60.2	59.7
Me (2)	25.9	26.0	26.1	26.1
Me (17)	25.7	26.0	26.1	25.9
i-Ph^NCN (10)	135.7	135.4	135.2	135.1
o-Ph^NCN (11)	126.9	127.1	126.5	126.8
o-Ph^NCN (15)	125.6	125.0	125.0	125.3
m-Ph^NCN (12)	127.7	127.5	127.4	127.5
m-Ph^NCN (14)	127.7	127.5	127.4	127.5
p-Ph^NCN (13)	127.5	127.5	127.4	127.5
i-Ph^NCN (3)	149.8	149.3	148.8	149.1
o-Ph (4,8)	127.3	127.4	127.6	126.5
m-Ph (5,7)	128.1	128.1	128.1	128.4
p-Ph (6)	126.3	126.0	126.3	126.4
i-Ph^NCN (18)	148.8	148.7	148.8	148.5
o-Ph (19,23)	127.1	127.2	127.6	126.3
m-Ph (20,22)	128.1	128.1	127.4	128.4
p-Ph (21)	126.3	126.0	126.3	126.4

8.2.3.3 [ThF((S)-PEBA)₃] (17)
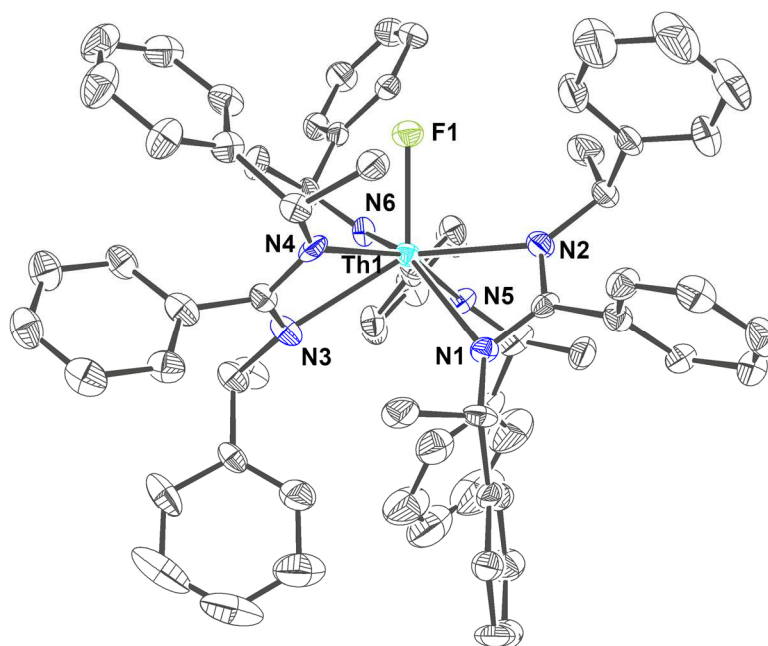
Figure 77. Molecular structure of Δ-[ThF((S)-PEBA)₃] (**17**). Ellipsoids are drawn at 50 % probability level. Hydrogen atoms and solvent molecules are omitted for clarity. Color code: carbon (C, dark gray), fluorine (F, pale green), nitrogen (N, blue), and thorium (Th, pale blue).
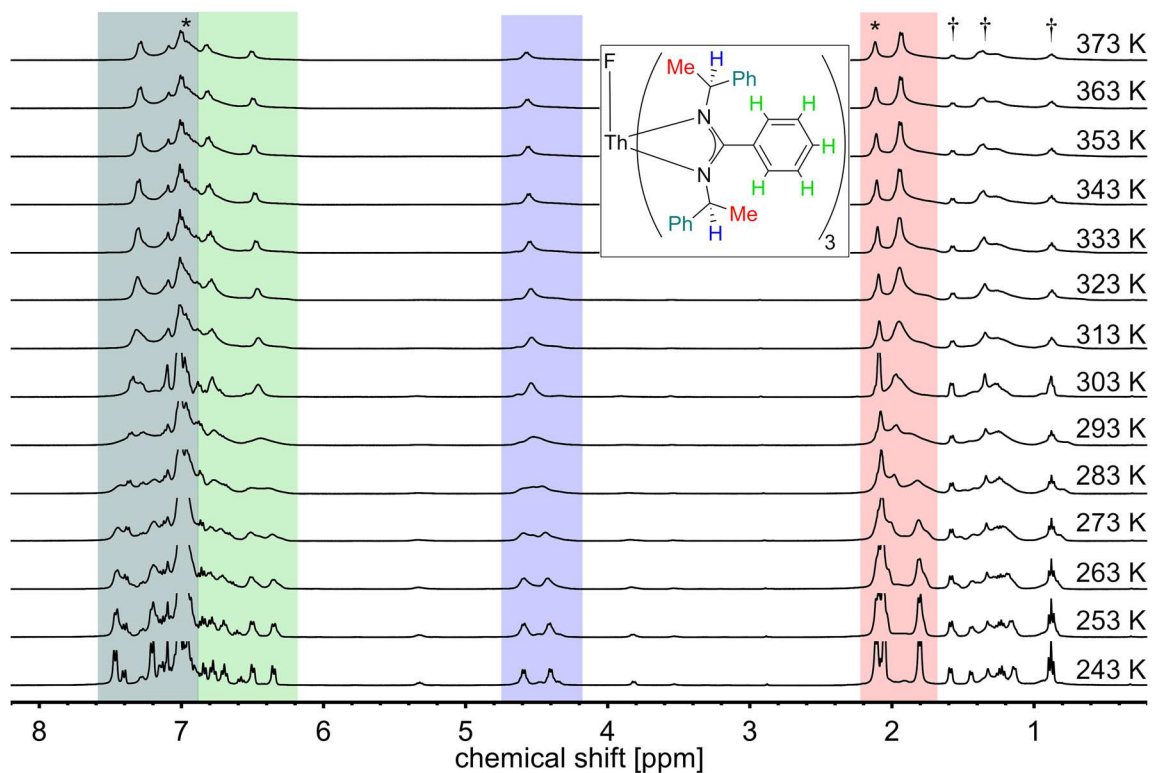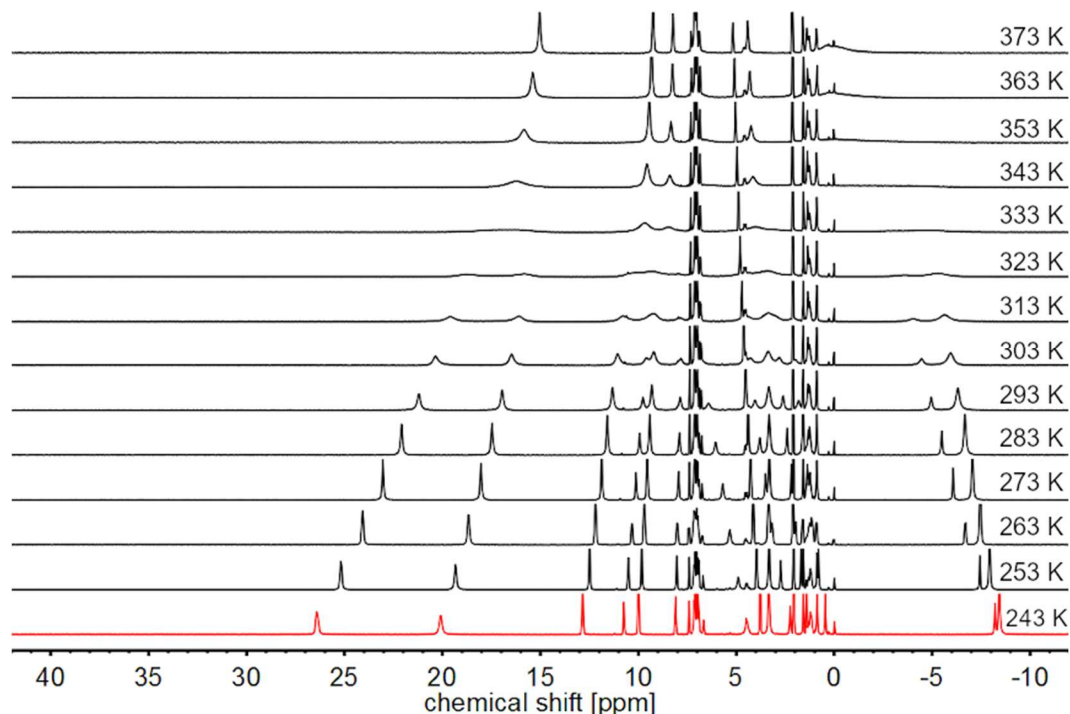

Figure 78. VT-^{1}H NMR spectra of [ThF((S)-PEBA)₃] (**17**) in toluene-d₈. Signals are marked with colors: blue (NC*H*), red (Me), green (Ph^{NCN}) and petrol green (Ph). Asterisks indicate solvent signals (i.e. toluene) and dagger impurities of *n*-pentane and (S)-HPEBA.

8.2.3.4 [ThBr((S)-PEBA)₃] (20)
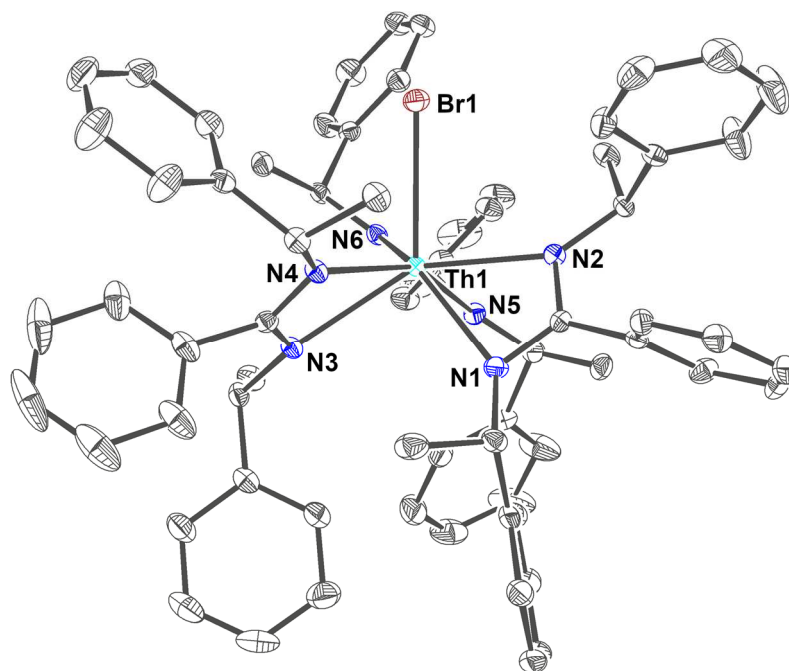
Figure 79. Molecular structure of Δ-[ThBr((S)-PEBA)₃] (**20**). Ellipsoids are drawn at 50 % probability level. Hydrogen atoms and solvent molecules are omitted for clarity. Color code: carbon (C, dark gray), bromine (Br, brown), nitrogen (N, blue), and thorium (Th, pale blue).
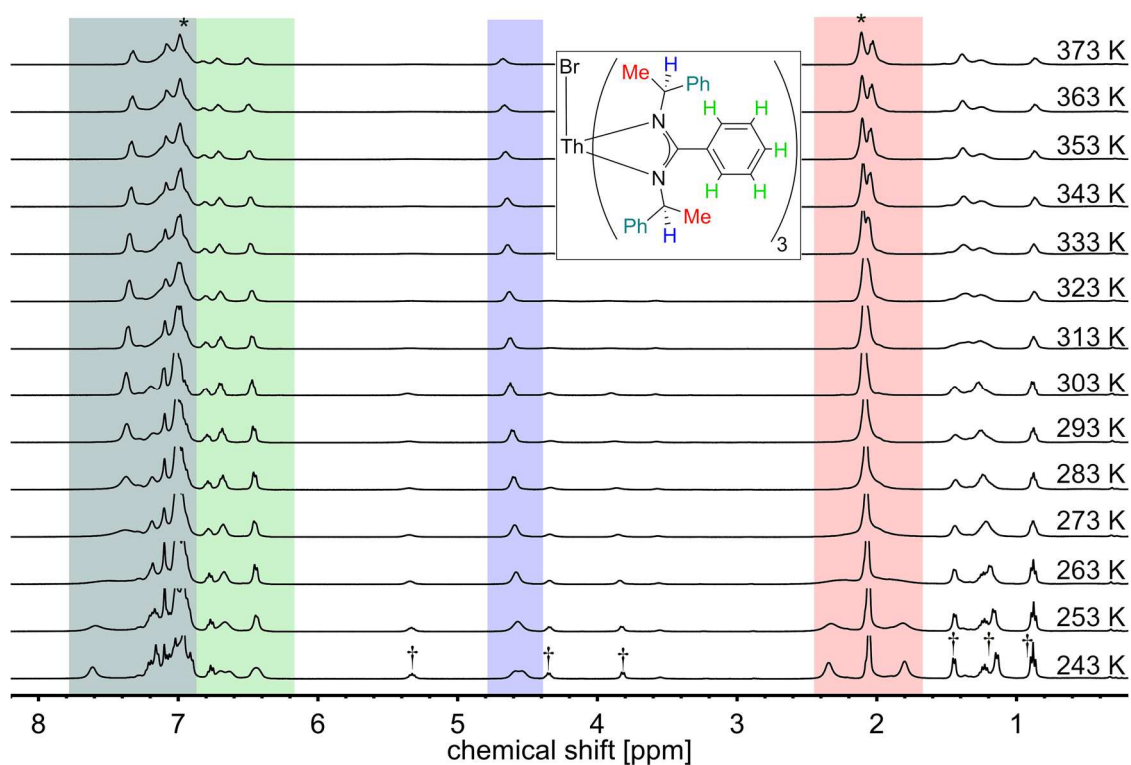
Figure 80. VT-¹H NMR spectra of [ThBr((S)-PEBA)₃] (**20**) in toluene-d₈. Signals are marked with colors: blue (NCH), red (Me), green (PhNCN) and petrol green (Ph). Asterisks indicate solvent signals (i.e. toluene) and dagger impurities of *n*-pentane and (S)-HPEBA.

8.2.3.5 [ThN₃((S)-PEBA)₃] (23)
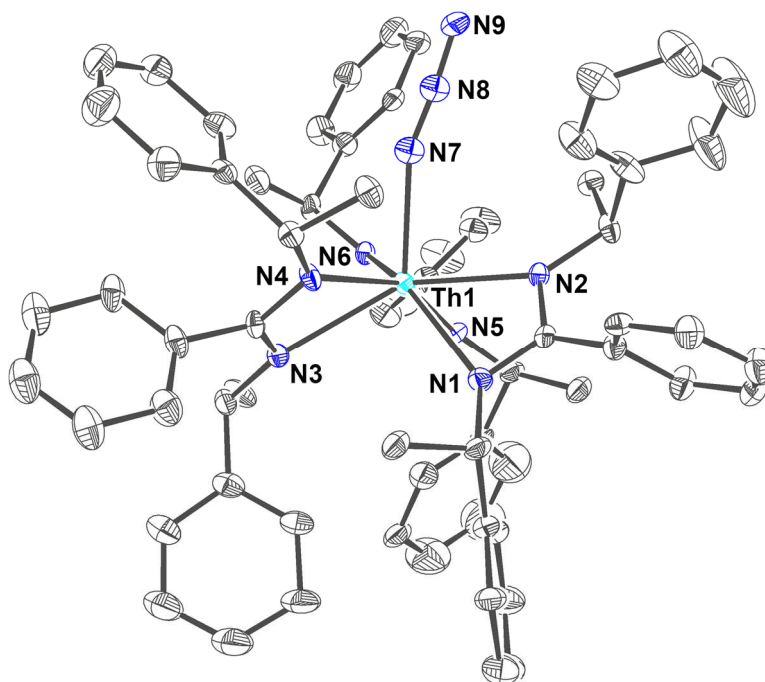
Figure 81. Molecular structure of Δ-[ThN₃((*S*)-PEBA)₃] (**23**). Ellipsoids are drawn at 50 % probability level. Hydrogen atoms and solvent molecules are omitted for clarity. Color code: carbon (C, dark gray), nitrogen (N, blue), and thorium (Th, pale blue).
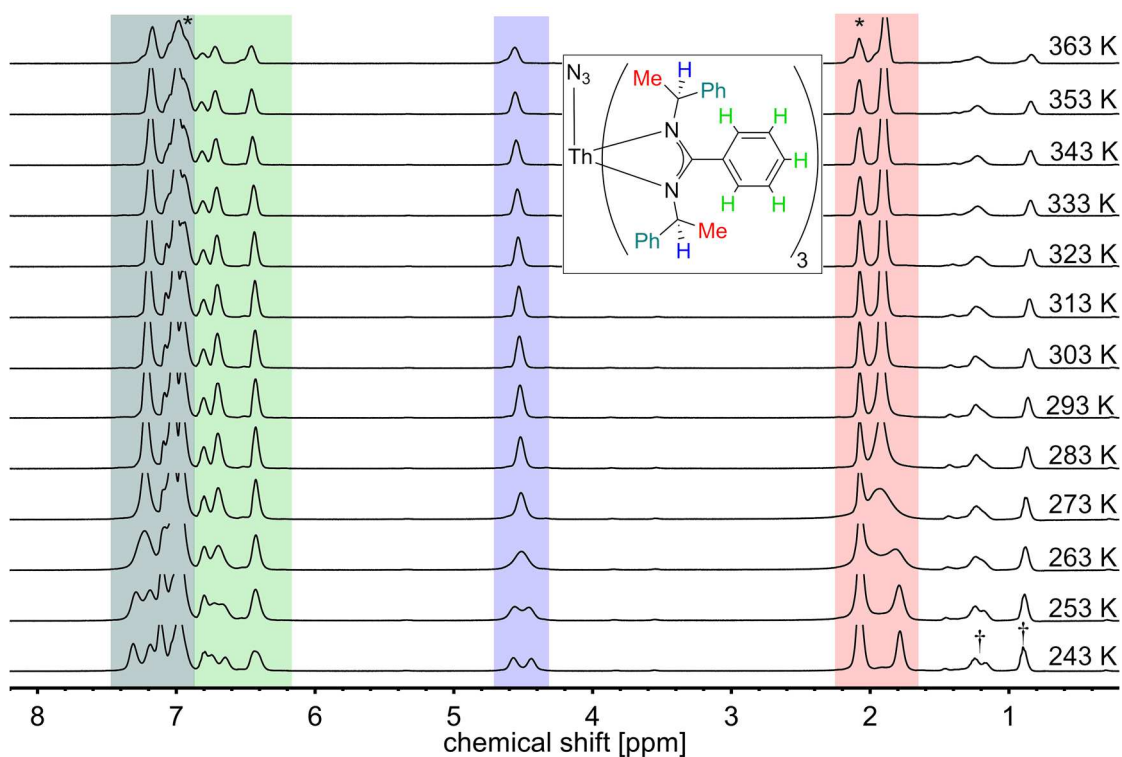
Figure 82. VT-¹H NMR spectra of [ThN₃((*S*)-PEBA)₃] (**23**) in toluene-d₈. Signals are marked with colors: blue (NC*H*), red (Me), green (Ph^NCN) and petrol green (Ph). Asterisks indicate solvent signals (i.e. toluene) and dagger impurities of *n*-pentane and (*S*)-HPEBA.

8.2.3.6 Comparison uranium complexes

Table 36. Crystallographic data for uranium tris(amidinate) complexes [UX((S)-PEBA)$_3$] **18** (X = F), **10** (X = Cl), **21** (X = Br), **24** (X = N$_3$).

	18	10	21	24
Empirical formula	[C$_{69}$H$_{69}$FN$_6$U] ·C$_7$H$_8$	[C$_{69}$H$_{69}$ClN$_6$U] ·C$_7$H$_8$	[C$_{69}$H$_{69}$BrN$_6$U] ·C$_7$H$_8$	[C$_{69}$H$_{69}$N$_9$U] ·C$_7$H$_8$
M (g/mol)	1331.47	1347.92	1392.37	1354.50
Crystal system	Orthorhombic	Orthorhombic	Orthorhombic	Orthorhombic
Space group	$P2_12_12_1$	$P2_12_12_1$	$P2_12_12_1$	$P2_12_12_1$
a (Å)	11.349(5)	11.239(1)	11.356(3)	11.406(2)
b (Å)	15.192(6)	15.366(2)	15.415(4)	15.961(3)
c (Å)	37.503(15)	36.704(3)	36.650(9)	36.196(6)
V (Å^3)	6466(5)	6339(1)	6416(3)	6590(2)
T (K)	100	100	100	100
Z	4	4	4	4
ρ_{calcd} (Mg/m^3)	1.368	1.413	1.441	1.365
abs coeff (mm^{-1})	2.560	2.652	3.201	2.513
Θ_{max} (°)	26.41	26.02	26.40	26.02
R [$I > 2\sigma(I)$]	0.029	0.029	0.029	0.036
wR2(int)	0.066	0.052	0.065	0.086
w scheme d, e	0.0212, 7.9138	0.0150, 6.0873	0.0270, 5.3942	0.0068/21.0648
Data/Param	13141/716	12459/759	1312/764	12879/782
res. Dens (eÅ^{-3})	1.00, -1.64	0.72, -0.92	0.722, -1.545	1.68/-2.80
R_{int}	0.049	0.083	0.060	0.047
GooF	1.125	1.022	1.055	1.248
Flack x	0.047(2)	0.016(2)	0.023(3)	0.072(2)

Table 37. Comparison of intramolecular U^{IV}–F distances of U fluoro compound **18** with literature data of structurally characterized U^{IV}–F compounds heaving terminal fluoro ligands.

	d(U–F) [Å]
[UF((S)-PEBA)$_3$] (**18**)	2.113
[UFCp$_3$][323]	2.106
[UFL^{19}][223]	2.124
[UF$_2$(^{t}Cp)$_2$][324]	2.086
[UF$_2$(^{tt}Cp)$_2$][325]	2.072, 2.090
[UF$_2$(py)(Cp*)$_2$][326]	2.146
[C(NH$_2$)$_3$]$_3$[UF$_3$(edta)][312]	2.216, 2.224, 2.241

Cp = cyclopentadienyl (η^5-C$_5$H$_5$);
L^{19} = N(CH$_2$CH$_2$NSi(iPr)$_3$)$_3$ (TREN);
^{t}Cp = η^5-(1,3-(Me$_3$C)$_2$C$_5$H$_3$);
^{tt}Cp = η^5-(1,2,4-(Me$_3$C)$_3$C$_5$H$_2$);
py = pyridine;
Cp* = η^5-C$_5$Me$_5$;
edta = ethylenediaminetetraacetate

Table 38. Comparison of intramolecular U^{IV}–Br distances of U bromo compound **21** with literature data of structurally characterized U^{IV}–Br compounds heaving terminal bromo ligands.

	d(U–Br) [Å]
[UBr((S)-PEBA)₃] (**21**)	2.808
[UBrL²⁰][222]	2.823, 2.835
[UBrCp₃][327]	2.820
[UBr₂(Cp*)₂][328]	2.758
[UBr₄(dme)₂][329]	2.783, 2.802, 2.799, 2.805
[UBr₄(OC(NMe₂)₂)₂][330]	2.780, 2.786

L²⁰ = N(CH₂CH₂NSiMe₂ᵗBu)₃; Cp = cyclopentadienyl (η⁵-C₅H₅);
Cp* = η⁵-C₅Me₅; dme = dimethoxyethane

Table 39. Comparison of intramolecular U^{IV}–N distances and U–N–N angles of U azide **24** with literature data of structurally characterized U^{IV} compounds heaving terminal azido ligands.

	d(U–N) [Å]	α(U–N–N) [°]
[UN₃((S)-PEBA)₃] (**24**)	2.293	155.7
[UN₃(L¹⁸)][226]	2.326	167.8
[UN₃(L¹⁹)][223]	2.305	176.0
[UN₃(Cp*)₂(N(SiMe₃)₂)][245]	2.26, 2.30	163.5; 164.0
[U(N₃)₂(L²¹)₂][244]	2.358	143.0

L¹⁸ = N,N′-bis(isopropyl)-di(isopropyl)guanidinate;
L¹⁹ = N(CH₂CH₂NSi(iPr)₃)₃ (TREN);
Cp* = η⁵-C₅Me₅;
L²¹ = ((NC₉H₆)N=C(H)C₆H₂ᵗBu₂O-κ³(O,N,N'))

8.2.3.7 [UF((S)-PEBA)₃] (18)
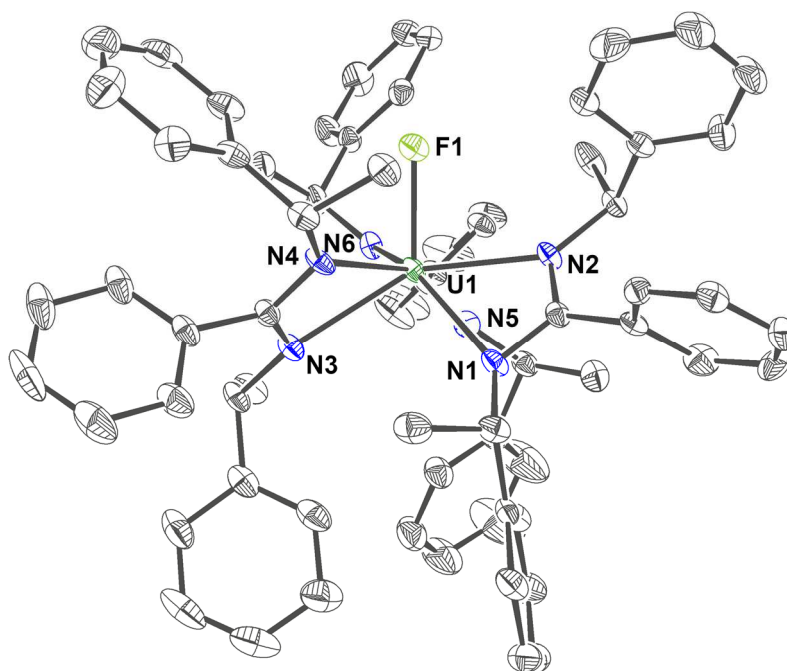
Figure 83. Molecular structure of Δ-[UF((*S*)-PEBA)₃] (**18**). Ellipsoids are drawn at 50 % probability level. Hydrogen atoms and solvent molecules are omitted for clarity. Color code: carbon (C, dark gray), fluorine (F, pale green), nitrogen (N, blue), and uranium (U^{IV}, dark green).

Figure 84. VT-¹H NMR spectra of [UF((*S*)-PEBA)₃] (**18**) in toluene-d₈.

¹H NMR: (400 MHz, toluene-d₈, 243 K) δ[ppm]: 26.42 (s, 2H, *o*-PhH), 20.10 (s, 2H, *o*-PhH), 12.86 (s, 2H, *m*-PhH), 10.74 (s, 1H, *p*-PhH), 10.00 (s, 2H, *m*-PhH), 8.10 (s, 1H, *p*-PhH), 3.79 (s, 2H, *m,p*-PhH^{NCN}), 3.34 (s, 3H, Me), 2.25 (s, 1H, NC*H*), 1.42 (s, 1H, *m*-PhH^{NCN}), 0.88 (s, 1H, NC*H*), 0.46 (s, 1H, *o*-PhH^{NCN}), -8.21 (s, 1H, *o*-PhH^{NCN}), -8.43 (s, 3H, Me).

8.2.3.8 [UBr((S)-PEBA)₃] (21)
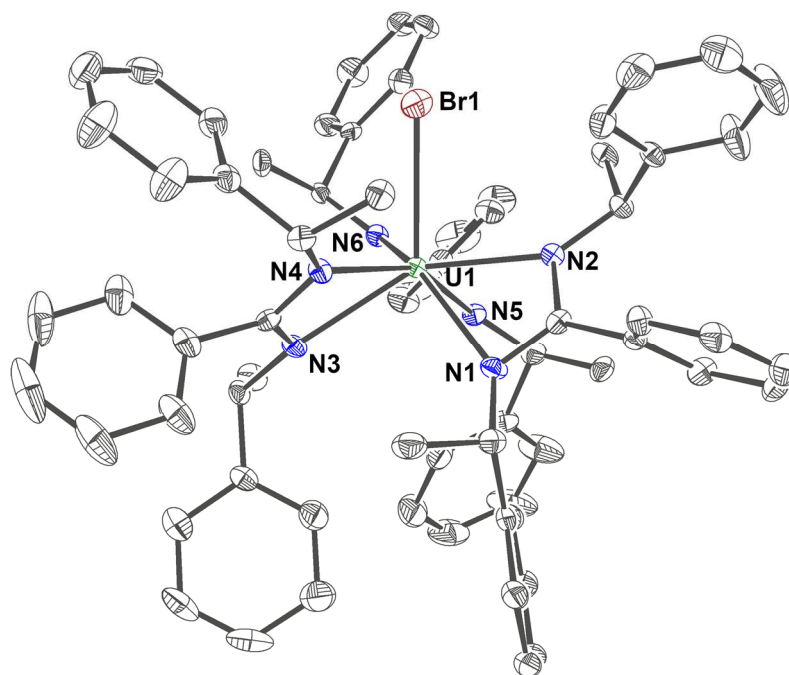
Figure 85. Molecular structure of Δ-[UBr((S)-PEBA)₃] (**21**). Ellipsoids are drawn at 50 % probability level. Hydrogen atoms and solvent molecules are omitted for clarity. Color code: carbon (C, dark gray), bromine (Br, brown), nitrogen (N, blue), and uranium (U^{IV}, dark green).
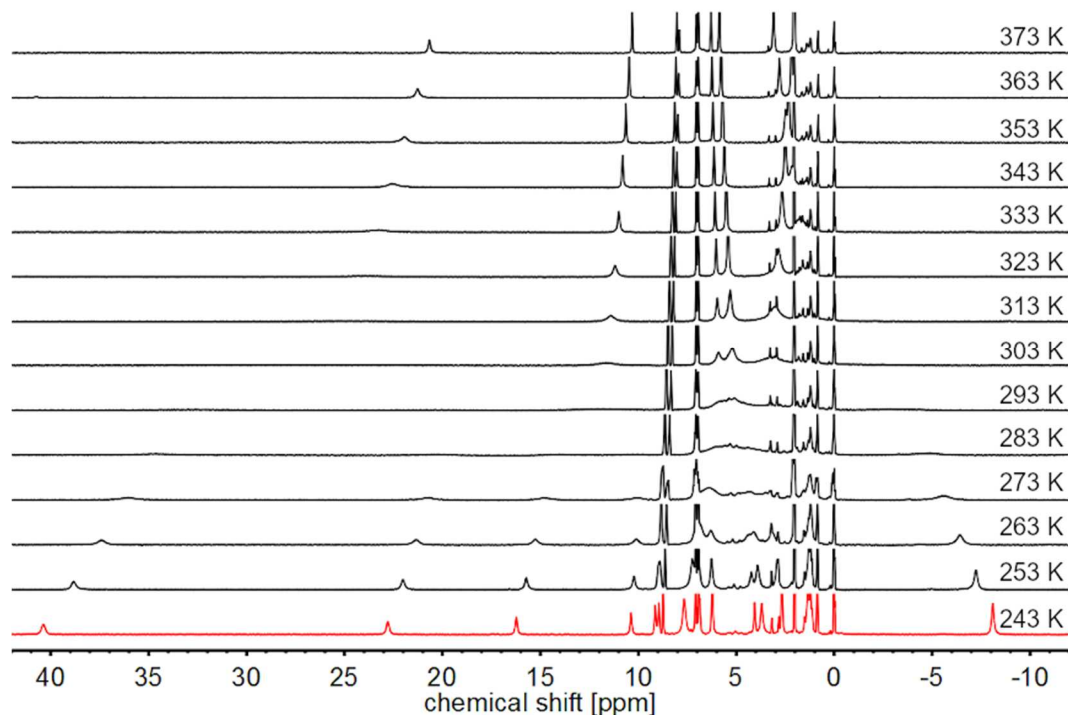
Figure 86. VT-^{1}H NMR spectra of [UBr((S)-PEBA)₃] (**21**) in toluene-d₈.

^{1}H-NMR: (400 MHz, toluene-d₈, 243 K) δ[ppm]: 40.36 (s, 1H, NC*H*), 22.78 (s, 1H, NC*H*), 16.22 (s, 1H, o-PhH^{NCN}), 10.36 (s, 1H, o-PhH^{NCN}), 9.13 (s, 1H, m-PhH^{NCN}), 8.94 (s, 1H, m-PhH^{NCN}), 8.94 (m, 1H, p-PhH^{NCN}), 7.65 (s, 3H, Me), 6.86 (s, 1H, p-PhH), 6.21 (s, 2H, m-PhH), 4.05 (s, 1H, p-PhH), 3.69 (s, 2H, m-PhH), 2.66 (s, 2H, o-PhH), 1.31 (s, 3H, Me), -8.11 (s, 2H, o-PhH).

8.2.3.9 *[UN₃((S)-PEBA)₃] (24)*
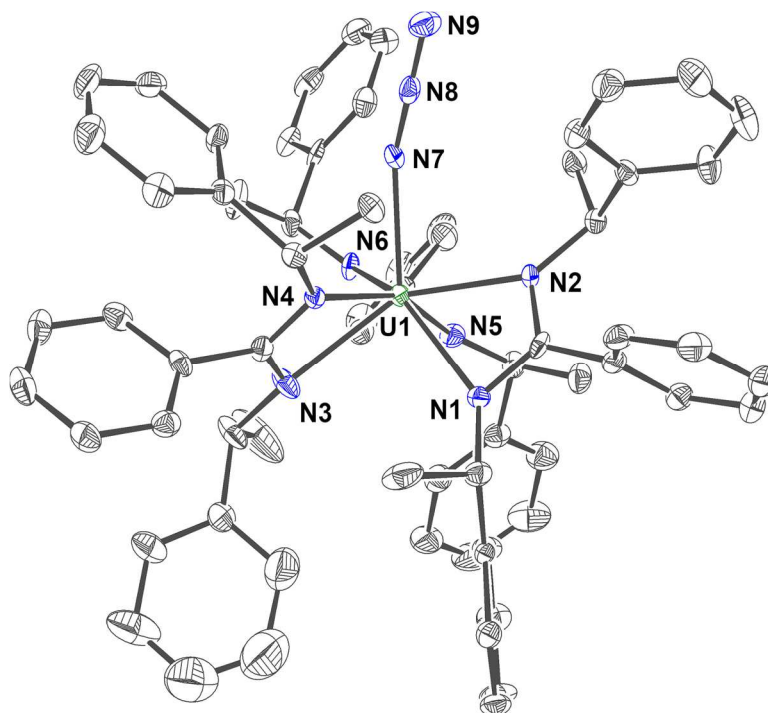
Figure 87. Molecular structure of Δ-[UN₃((S)-PEBA)₃] (**24**). Ellipsoids are drawn at 50 % probability level. Hydrogen atoms and solvent molecules are omitted for clarity. Color code: carbon (C, dark gray), nitrogen (N, blue), and uranium (U^IV, dark green).
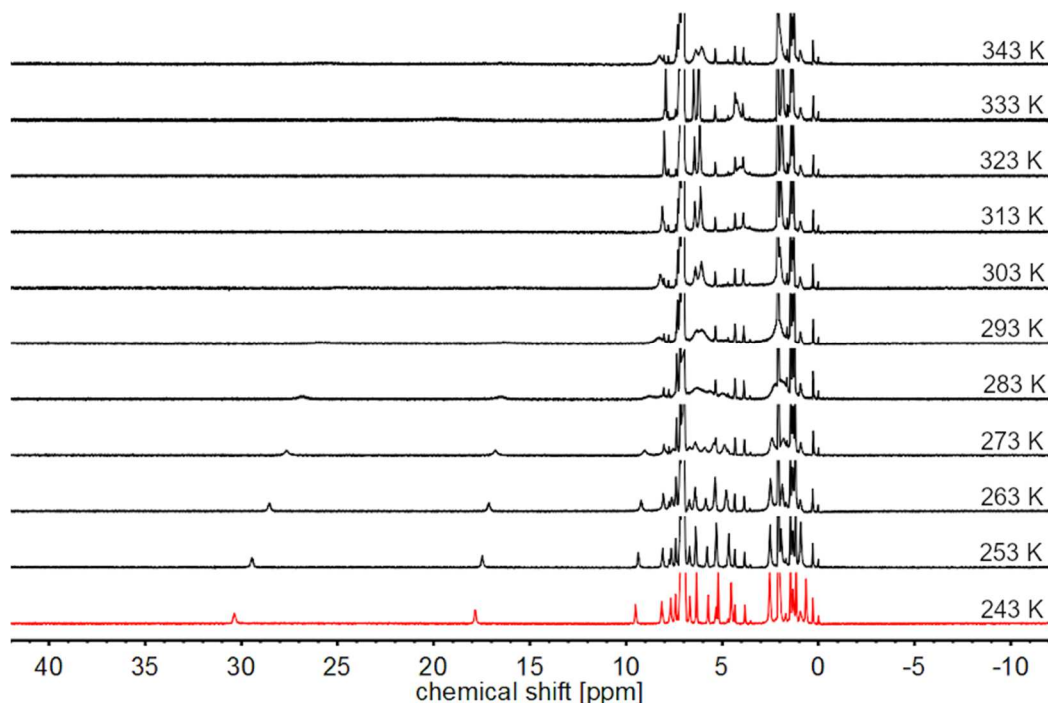
Figure 88. VT-^{1}H NMR spectra of [UN₃((S)-PEBA)₃] (**24**) in toluene-d₈.

^{1}H-NMR: (400 MHz, toluene-d₈, 243 K) δ[ppm]: 30.42 (s, 1H,NC*H*), 17.87 (s, 1H, NC*H*), 9.51 (s, 1H, o-PhH^{NCN}), 8.16 (s, 1H, o-PhH^{NCN}), 7.68 (s, 1H, m-PhH^{NCN}), 7.44 (s, 1H, m-PhH^{NCN}), 6.95 (m, 1H, p-PhH^{NCN}), 6.68 (s, 1H, p-PhH), 6.34 (s, 2H, m-PhH), 5.72 (s, 1H, p-PhH), 5.22 (s, 2H, m-PhH), 4.53 (s, 2H, o-PhH), 2.53 (s, 3H, Me), 2.07 (s, 3H, Me), 0.63 (s, 2H, o-PhH).

8.2.3.10 Comparison neptunium complexes

Table 40. Crystallographic data for neptunium tris(amidinate) complexes $[NpX((S)\text{-PEBA})_3]$ **19** (X = F), **11** (X = Cl), **22** (X = Br), **25** (X = N_3).

	19	**11**	**22**	**25**
Empirical formula	$[C_{69}H_{69}F_{0.88}Cl_{0.12}N_6Np]$ ·C_7H_8	$[C_{69}H_{69}ClN_6Np]$ ·C_7H_8	$[C_{69}H_{69}BrN_6Np]$ ·C_7H_8	$[C_{69}H_{69}N_9Np]$· C_7H_8
M (g/mol)	1332.53	1346.94	1391.39	1353.46
Crystal system	Orthorhombic	Orthorhombic	Orthorhombic	Orthorhombic
Space group	$P2_12_12_1$	$P2_12_12_1$	$P2_12_12_1$	$P2_12_12_1$
a (Å)	11.307(3)	11.274(2)	11.316(1)	11.454(3)
b (Å)	15.798(4)	15.356(2)	15.414(1)	15.975(4)
c (Å)	36.118(8)	36.654(5)	36.535(2)	36.264(9)
V (Å^3)	6452(3)	6346(2)	6372(1)	6636(3)
T (K)	100	100	100	100
Z	4	4	4	4
ρ_{calcd} (Mg/m^3)	1.371	1.410	1.450	1.355
abs coeff (mm^{-1})	1.661	1.728	2.306	1.615
Θ_{max} (°)	25.05	25.04	26.420	19.780
R [$I > 2\sigma(I)$]	0.1385	0.031	0.025	0.090
wR2(int)	0.3182	0.101	0.051	0.2448
w scheme d, e	0.0001, 588.0975	0.0343, 8.9548	0.0208, 3.6223	0, 365.3019
Data/Param	11412/679	11206/752	13096/764	5548/631
res. Dens (eÅ^{-3})	2.267, -6.742	1.39, -2.01	1.080, -0.868	3.145/-1.684
R_{int}	0.085	0.043	0.049	0.0914
GooF	1.149	1.137	1.047	1.147
Flack x	0.38(9)	0.014(4)	0.006(4)	0.033(17)

Table 41. Comparison of intramolecular Np^{IV}–N distances of Np compounds **5**, **11**, **19**, **22**, and **25** with literature data of structurally characterized compounds containing Np^{IV}-N bonds (CCDC, May 2020). Bond lengths Np–N1, Np–N3, Np–N5 are averaged to Np–N_{long} and distances Np–N2, Np–N4, Np–N6 to Np–N_{short} and represent other Np–N distances in cited complexes.

d(Np–X) [Å]	N_{long}	N_{short}	N_o
$[NpCl(iPr_2BA)_3]$ (**5**)	2.445	2.372	
$[NpCl((S)\text{-PEBA})_3]$ (**11**)	2.497	2.368	
$[NpF((S)\text{-PEBA})_3]$ (**19**)	2.520	2.411	
$[NpBr((S)\text{-PEBA})_3]$ (**22**)	2.489	2.364	
$[NpN_3((S)\text{-PEBA})_3]$ (**25**)	2.49	2.38	2.23 (azide)
$[NMe_4][Np(NCS)_8]$[331]	2.40		
$[Np(H_2L^{22})_3][ClO_4]$[332]	2.497	2.479	
$[NpCl_2(H_2L^{22})_2]$[332]	2.454		
$[NpCl(L^{19})]$[251]	2.605 (amine)	2.223 (amide)	
$[Np(OSiMe_3)_2(L^{23})]$[333]	2.635 (pyridine)	2.697 (pyrrol)	2.677 (pyrrolidene)

L^{19} = $N(CH_2CH_2NSi(iPr)_3)_3$ (TREN); L^{22} = glutaroimide-dioxime; L^{23} = dipyriamethyrin

Table 42. Comparison of intramolecular Np^{IV}–X distances of Np compounds **5**, **11**, **19**, and **25** with literature data of structurally characterized Np^{IV}–X compounds (X = F, Cl, Br).

d(Np–X) [Å]	F	Cl	Br
[NpF((*S*)-PEBA)₃] (**19**)	2.126		
NpF₄[334]	2.130- 2.331		
[NpCl(*i*Pr₂BA)₃] (**5**)		2.663	
[NpCl((*S*)-PEBA)₃] (**11**)		2.630	
[NpCl₄(dme)₂][78]		2.608	
[NpCl₄(thf)₃][74]		2.586	
[PPh₄][NpCl₆][8]		2.610	
[NpCl₃Cp(Ph₂MePO)₂][335]		2.641	
[NpBr((*S*)-PEBA)₃] (**22**)			2.792
Cs₂NpBr₆[336]			2.771
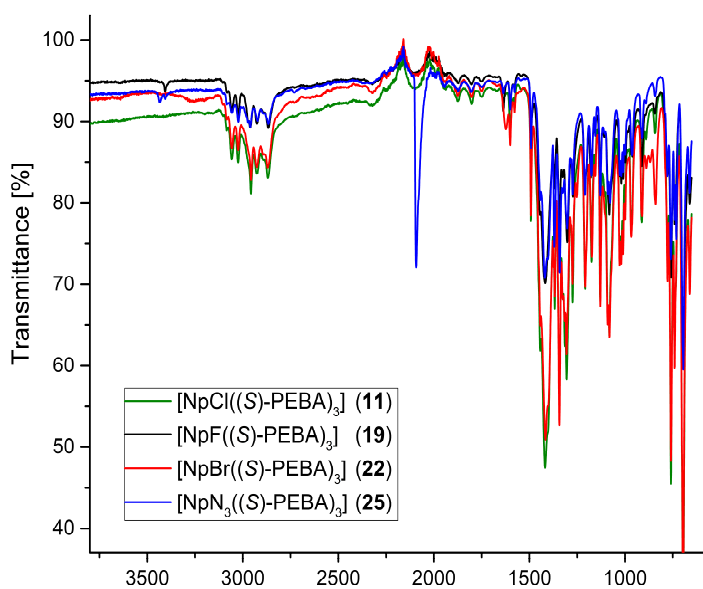
Figure 89. ATR-IR spectra of chiral tris(amidinate) [NpX((*S*)-PEBA)₃] (X = Cl (**11**), F (**19**), Br (**22**), N₃ (**25**)) complexes.
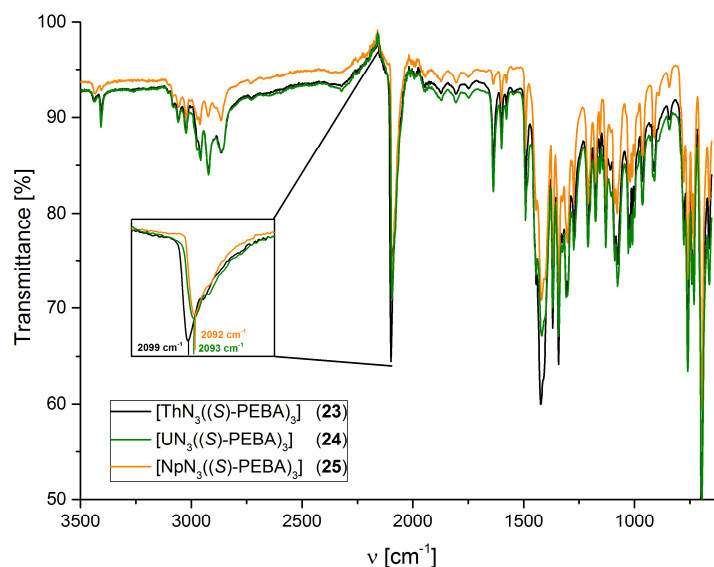
Figure 90. ATR-IR spectra of isostructural [AnN₃((*S*)-PEBA)₃] (**23-25**) compounds.

8.2.3.11 [NpF((S)-PEBA)₃] (19)
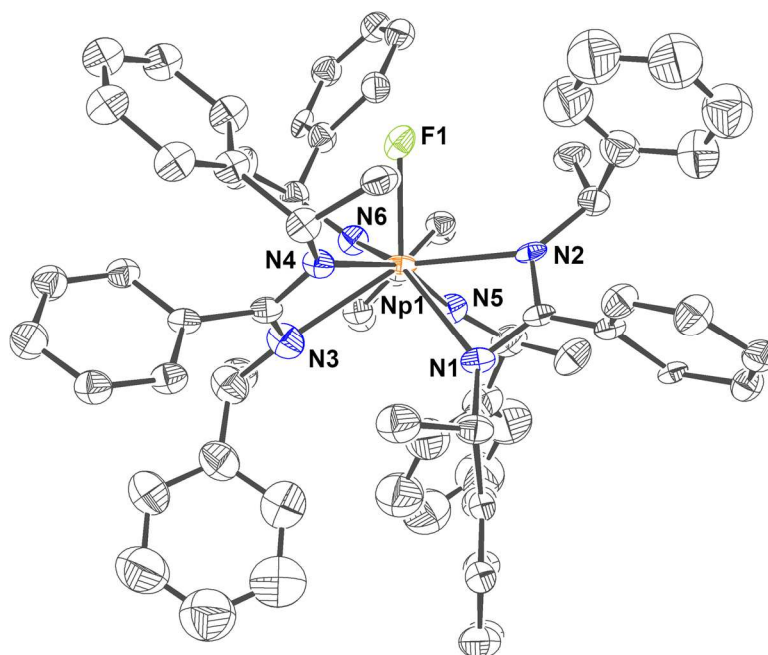
Figure 91. Molecular structure of Δ-[NpF((*S*)-PEBA)₃] (**19**). Ellipsoids are drawn at 50 % probability level. Partial chloride occupancy is omitted for clarity. Hydrogen atoms and solvent molecules are omitted for clarity. Color code: carbon (C, dark gray), fluorine (F, pale green), nitrogen (N, blue), and neptunium (Np^{IV}, orange red).
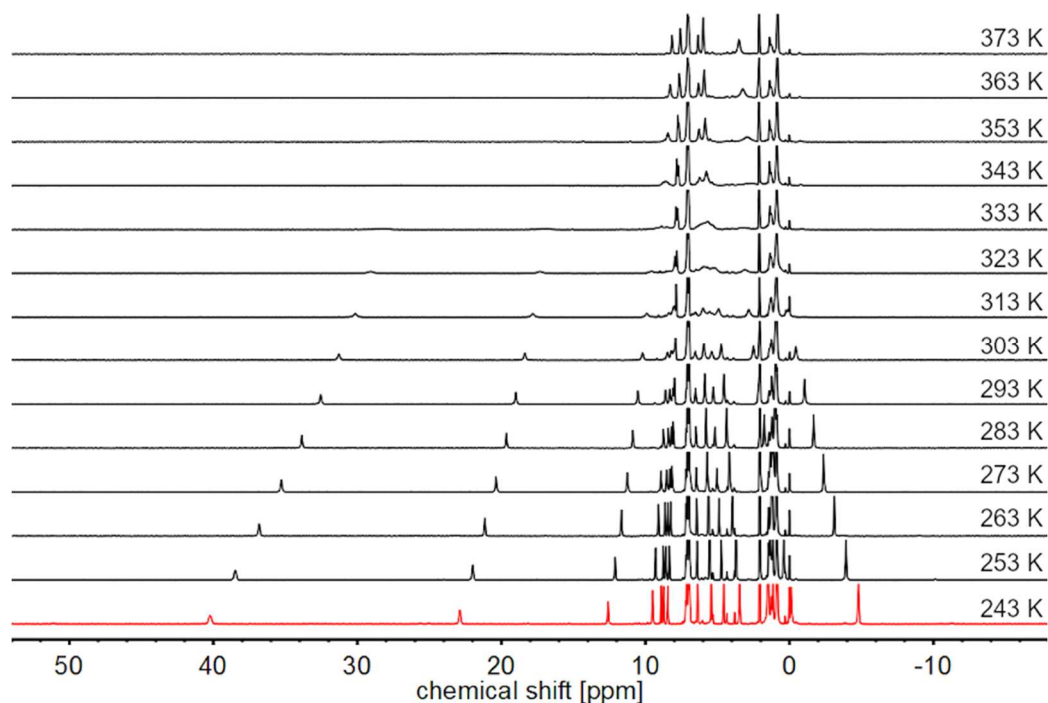
Figure 92. VT-¹H NMR spectra of [NpF((*S*)-PEBA)₃] (**19**) in toluene-d₈.

¹H NMR: (400 MHz, toluene-d₈, 243 K) δ[ppm]: 40.15 (s, 1H, NC*H*), 22.85 (s, 1H, NC*H*), 12.57 (s, 1H, *o*-PhH^{NCN}), 9.49 (s, 1H, *o*-PhH^{NCN}), 8.89 (s, 1H, *m*-PhH^{NCN}), 8.73 (s, 1H, *m*-PhH^{NCN}), 8.45 (s, 1H, *p*-PhH^{NCN}), 6.38 (s, 1H, *p*-PhH), 5.43 (s, 2H, *m*-PhH), 4.57 (s, 1H, *p*-PhH), 3.47 (s, 2H, *m*-PhH), 1.48 (s, 3H, Me), 0.86 (s, 3H, Me), -0.12 (s, 2H, *o*-PhH), -4.76 (s, 2H, *o*-PhH).
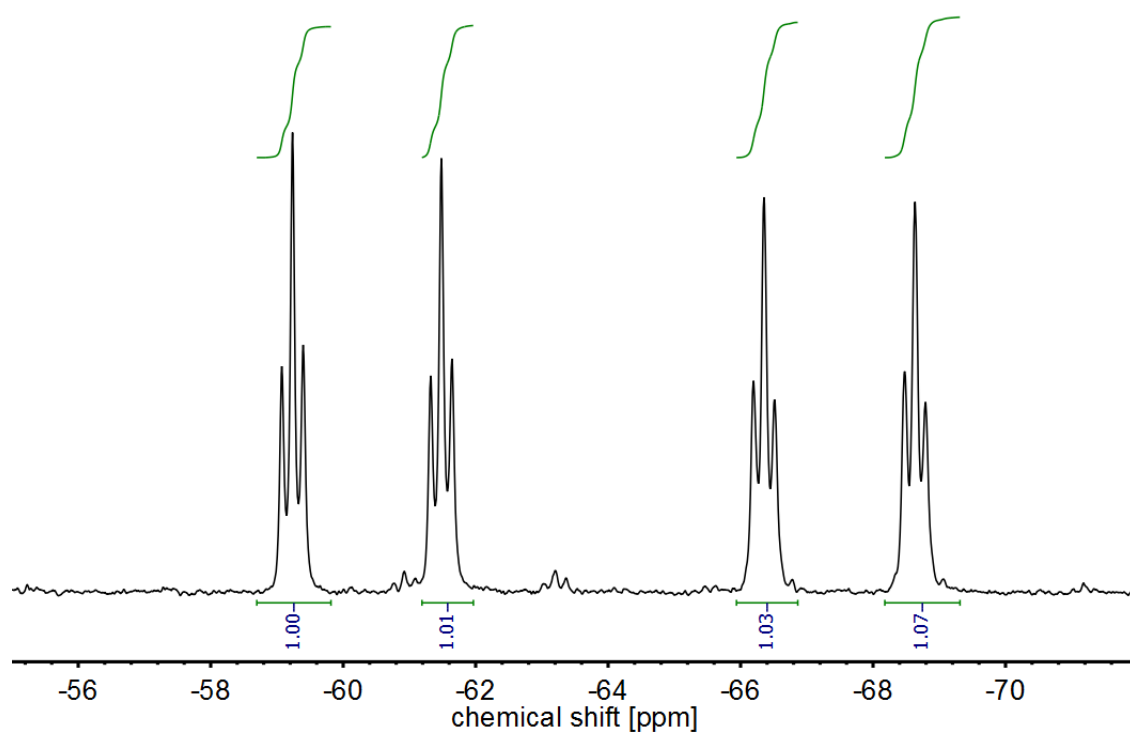
Figure 93. Part of ^{19}F NMR spectra of the reaction mixture of [NpF((S)-PEBA)$_3$] (**19**) in toluene-d$_8$ at 243 K. The coupling pattern is in accordance with the formation of a *cis*-[PF$_4$Cl$_2$]$^-$ anion (-60.36 ppm (dt, ^{1}J$_{F-P}$ = 845.2 Hz, ^{2}J$_{F-F}$ = 60.9 Hz, 2F, F$_{eq}$); -67.49 ppm (dt, ^{1}J$_{F-P}$ = 857.1 Hz, ^{2}J$_{F-F}$ = 60.5 Hz, 2F, F$_{ax}$).[221]
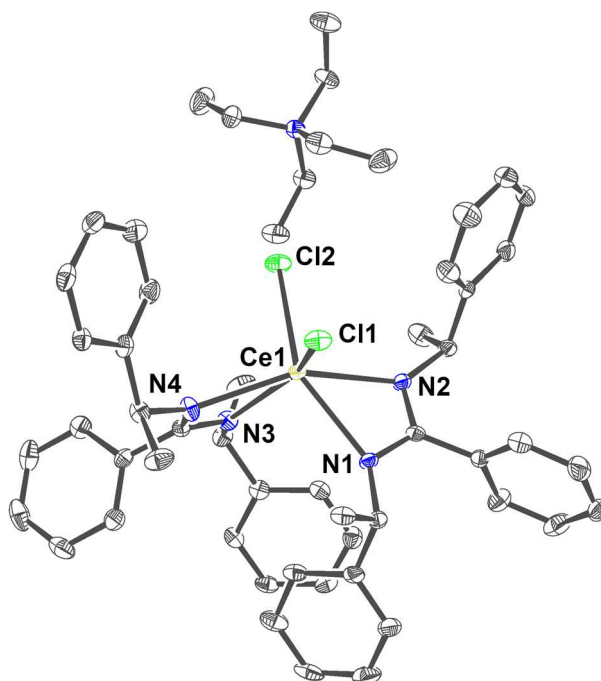
8.2.3.12 [NpBr((S)-PEBA)₃] (22)
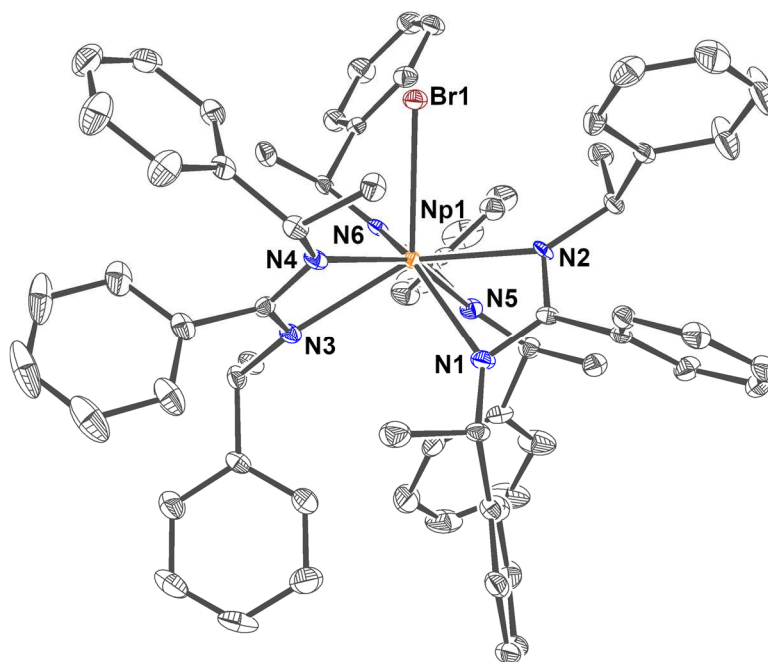
Figure 94. Molecular structure of Δ-[NpBr((*S*)-PEBA)₃] (**22**). Ellipsoids are drawn at 50 % probability level. Hydrogen atoms and solvent molecules are omitted for clarity. Color code: carbon (C, dark gray), bromine (Br, brown), nitrogen (N, blue), and neptunium (Np^{IV}, orange red).
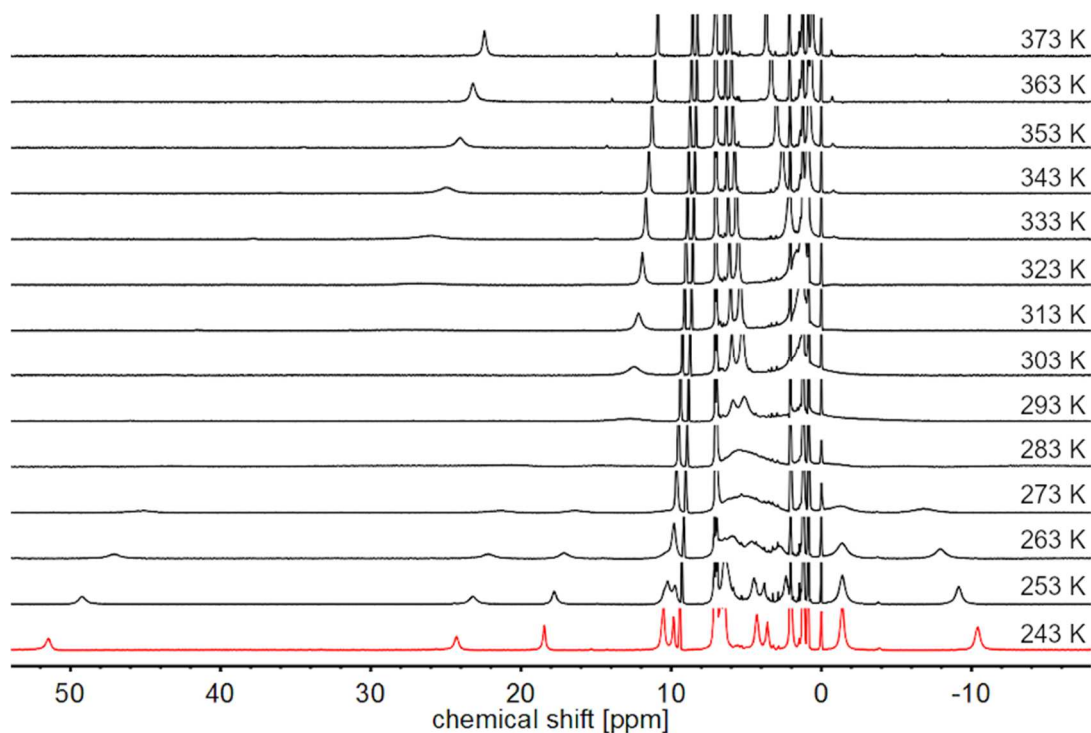
Figure 95. VT-^{1}H NMR spectra of [NpBr((*S*)-PEBA)₃] (**22**) in toluene-d₈.

^{1}H NMR: (400 MHz, toluene-d₈, 243 K) δ[ppm]: 51.43 (s, 1H, NC*H*), 24.28 (s, 1H, NC*H*), 18.44 (s, 1H, *o*-PhH^{NCN}), 10.51 (s, 2H, *o*-PhH^{NCN}, *m*-PhH^{NCN}), 9.83 (s, 1H, *m*-PhH^{NCN}), 9.42 (s, 1H, *p*-PhH^{NCN}), 6.68 (s, 3H, *m*-PhH, *p*-PhH), 6.44 (s, 3H, Me), 4.28 (s, 2H, *o*-PhH), 3.59 (s, 1H, *p*-PhH), 2.05 (s, 2H, *m*-PhH), -1.40 (s, 3H, Me), -10.41 (s, 2H, *o*-PhH).

8.2.3.13 [NpN₃((S)-PEBA)₃] (25)
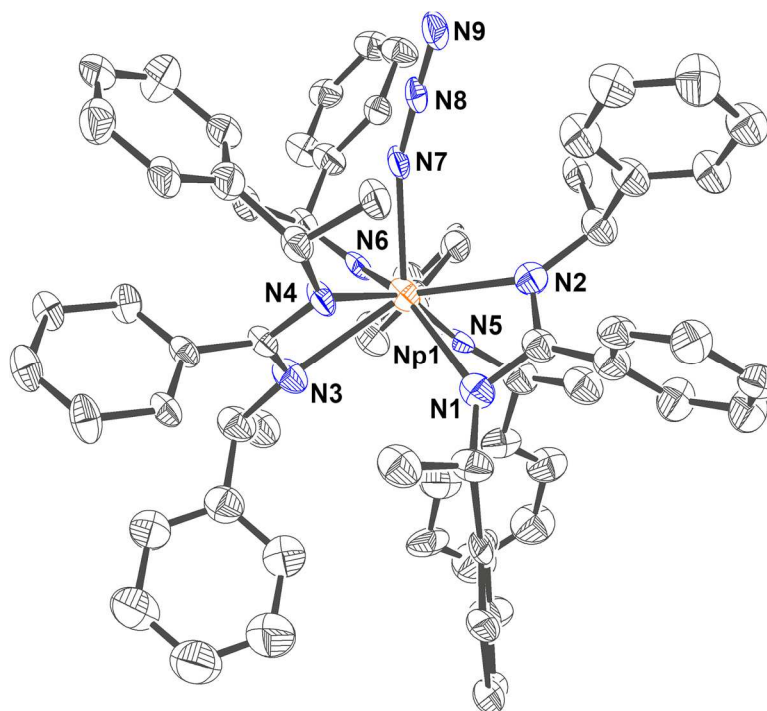
Figure 96. Molecular structure of Δ-[NpN₃((*S*)-PEBA)₃] (**25**). Ellipsoids are drawn at 50 % probability level. Hydrogen atoms and solvent molecules are omitted for clarity. Color code: carbon (C, dark gray), nitrogen (N, blue), and neptunium (Np^{IV}, orange red).
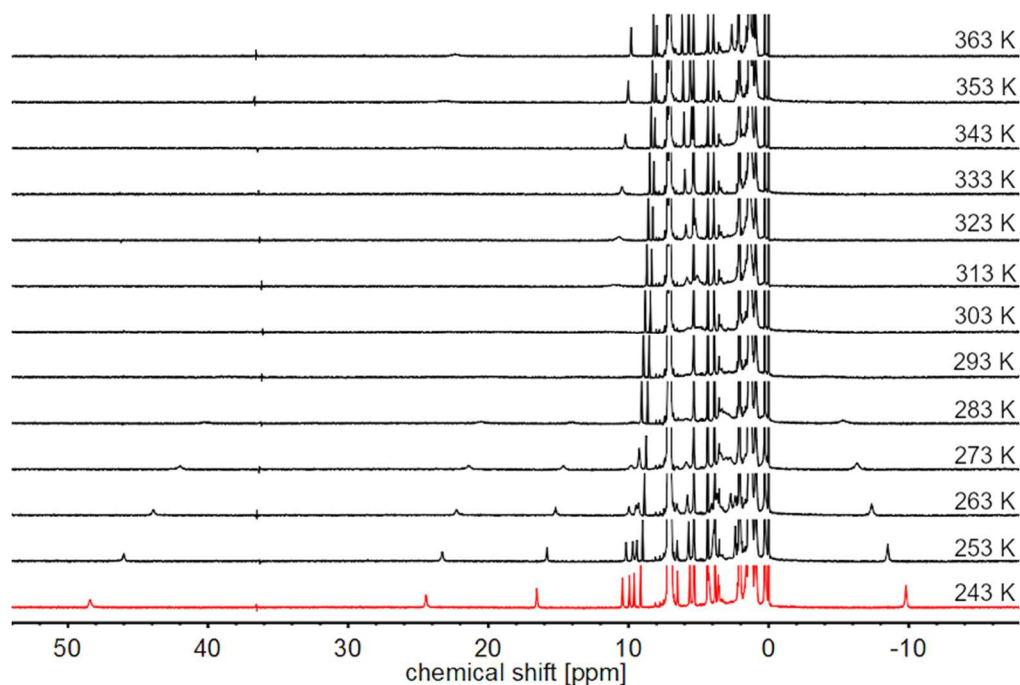
Figure 97. VT-^{1}H NMR spectra of [NpN₃((*S*)-PEBA)₃] (**25**) in toluene-d₈.

^{1}H NMR: (400 MHz, toluene-d₈, 243 K) δ[ppm]: 48.10 (s, 1H, NC*H*), 24.31 (s, 1H, NC*H*), 16.46 (s, 1H, *o*-PhH^{NCN}), 10.41 (s, 1H, *o*-PhH^{NCN}), 9.92 (s, 1H, *m*-PhH^{NCN}), 9.59 (s, 1H, *m*-PhH^{NCN}), 9.15 (s, 1H, *p*-PhH^{NCN}), 6.54 (s, 1H, *p*-PhH), 5.67 (s, 2H, *m*-PhH), 4.24 (s, 3H, Me), 3.67 (s, 1H, *p*-PhH), 2.13 (s, 2H, *m*-PhH), 1.72 (s, 2H, *o*-PhH), 0.26 (s, 3H, Me), -9.56 (s, 2H, *o*-PhH).

8.3 Trivalent amidinate complexes with (*S*)-PEBA

8.3.1 Bis(amidinate) complexes

Table 43. Crystallographic data for cerium bis(amidinate) complex [NEt$_4$][CeCl$_2$((*S*)-PEBA)$_2$] (**14**).

	14
Empirical formula	[C$_8$H$_{20}$N][C$_{46}$H$_{46}$Cl$_2$N$_4$Ce]
M (g/mol)	996.14
Crystal system	Orthorhombic
Space group	*P*2$_1$2$_1$2$_1$
a (Å)	12.514(1)
b (Å)	17.275(1)
c (Å)	23.085(2)
V (Å^3)	4991(1)
T (K)	100
Z	4
ρ_{calcd} (Mg/m^3)	1.326
abs coeff (mm^{-1})	1.059
Θ_{max} (°)	26.02
R [*I* > 2σ(*I*)]	0.032
wR2(int)	0.062
w scheme *d*, *e*	0.025, 0
Data/Param	9819/567
res. Dens (eÅ^{-3})	0.60, -1.01
R$_{int}$	0.064
GooF	1.045
Flack x	0.009(6)

Figure 98. Molecular structure of [NEt$_4$][Δ-CeCl$_2$((*S*)-PEBA)$_2$] (**14**). Ellipsoids are drawn at 50 % probability level. Hydrogen atoms are omitted for clarity. Color code: carbon (C, dark gray), chlorine (Cl, light green), nitrogen (N, blue), and cerium (Ce^{III}, yellow green).
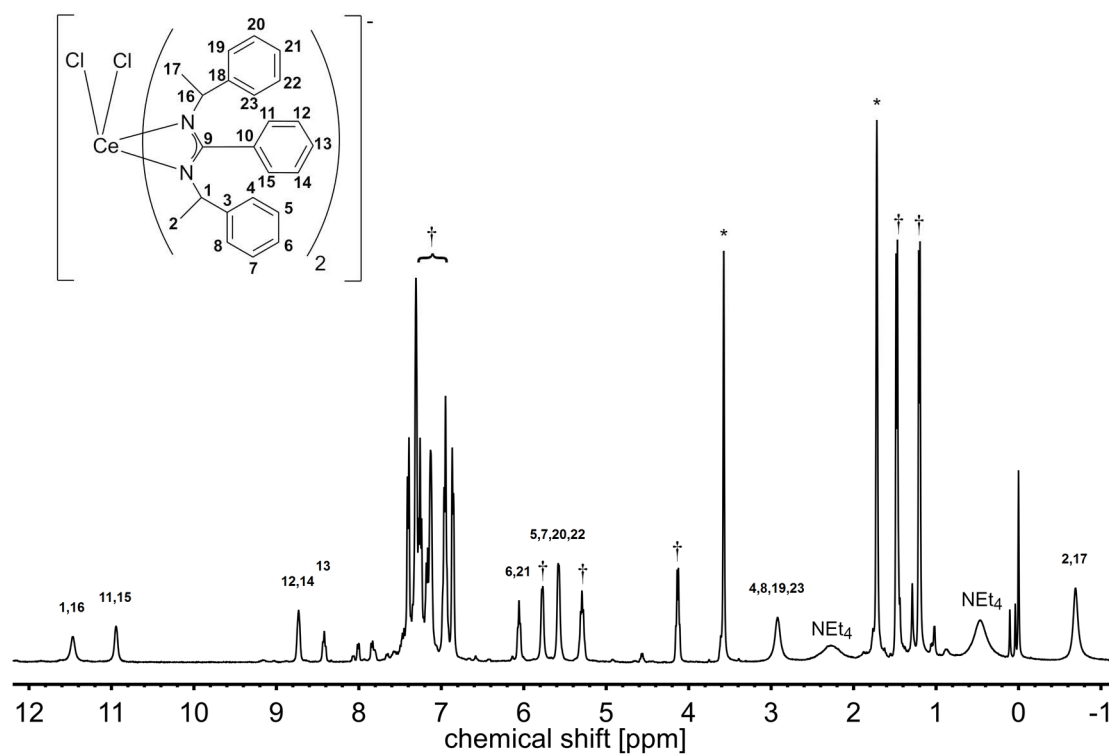
Figure 99. ^{1}H NMR spectrum of [NEt$_4$][CeCl$_2$((S)-PEBA)$_3$] (**14**) in thf-d$_8$. Asterisk indicate solvent signals and dagger impurity of (S)-HPEBA.

8.3.2 Tris(amidinate) complexes

8.3.2.1 Comparison

Table 44. Crystallographic data for trivalent tris(amidinate) complexes [M((S)-PEBA)$_3$] **28** (M = La), **15** (M = Ce), **26** (M = U).

	28	**15**	**26**
Empirical formula	[C$_{69}$H$_{69}$N$_6$La]	[C$_{69}$H$_{69}$N$_6$Ce]	[C$_{69}$H$_{69}$N$_6$U]
M (g/mol)	1121.21	1122.42	1220.33
Crystal system	Cubic	Cubic	Cubic
Space group	$P2_13$	$P2_13$	$P2_13$
a (Å)	18.5735(5)	18.5568(5)	18.5584(15)
V (Å^3)	6407.4(5)	6390.1(5)	6391.8(15)
T (K)	100	100	100
Z	4	4	4
ρ_{calcd} (Mg/m^3)	1.162	1.167	1.268
abs coeff (mm^{-1})	0.709	0.755	2.582
Θ_{max} (°)	25.03	28.28	22.81
R [$I > 2\sigma(I)$]	0.082	0.038	0.063
wR2(int)	0.2479	0.110	0.1822
w scheme d, e	0.1393, 10.0799	0.0754, 2.0138	0.1044, 14.0454
Data/Param	3798/189	5291/231	2906/189
res. Dens (eÅ^{-3})	0.901, -0.901	1.54, -0.47	0.888, -0.936
R$_{int}$	0.0357	0.029	0.058
GooF	1.069	1.099	1.106
Flack x	0.024(9)	0.000(5)	0.046(8)
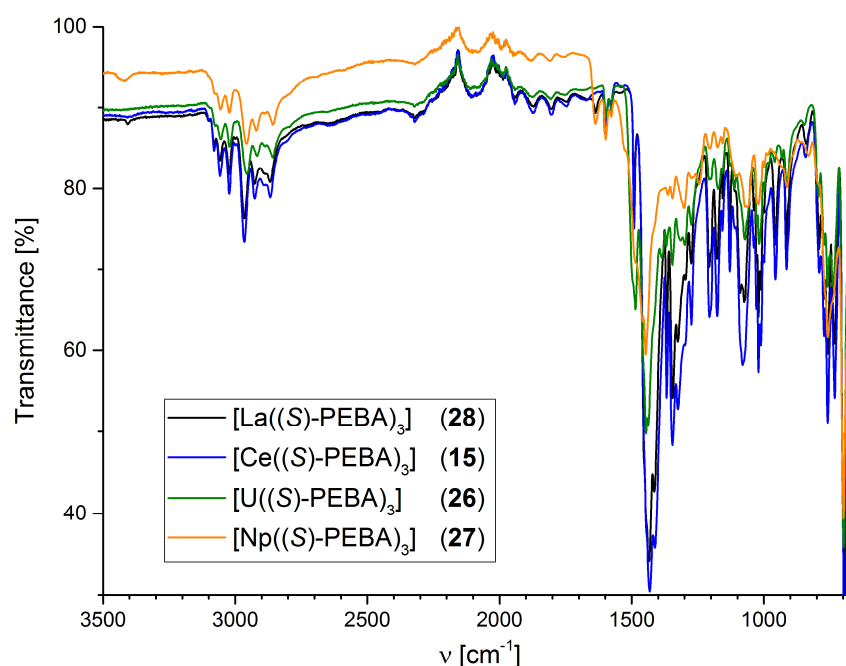
Figure 100. ATR-IR spectra of trivalent tris(amidinate) complexes [M((S)-PEBA)$_3$] (M = Ce (**15**), U (**26**), Np (**27**), La (**28**)).
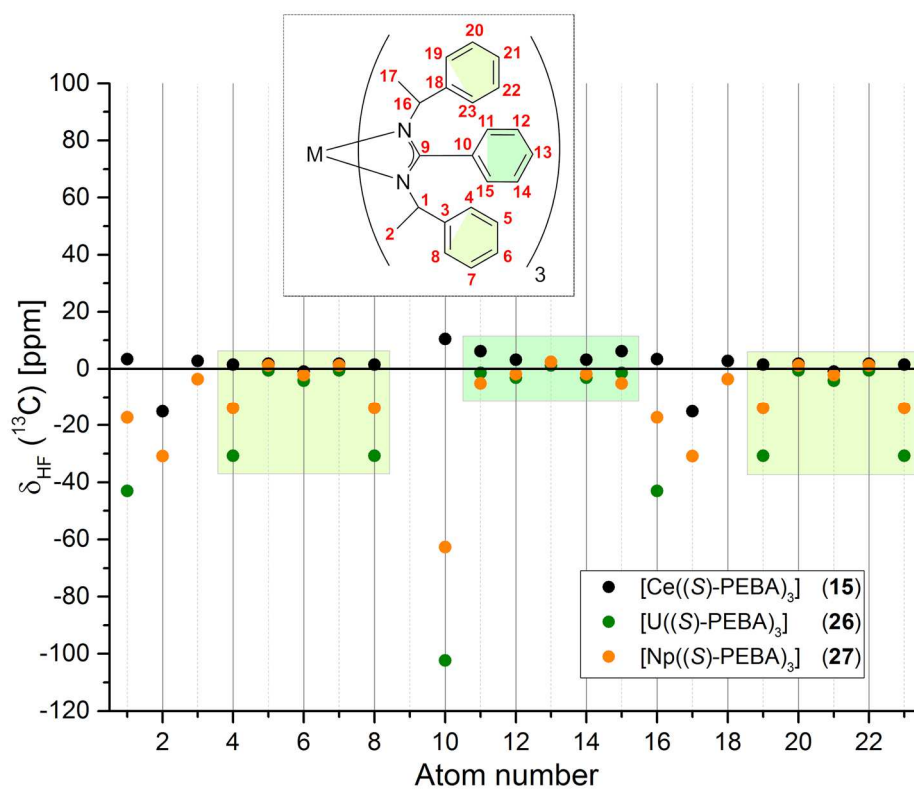
Figure 101. Plot of the ^{13}C hyperfine shift of trivalent tris(amidinates) [M((*S*)-PEBA)$_3$] (M = Ce (**15**), U (**26**) and Np (**27**)) in toluene-d$_8$ at 243 K.

8.3.2.2 [La((S)-PEBA)₃] (28)
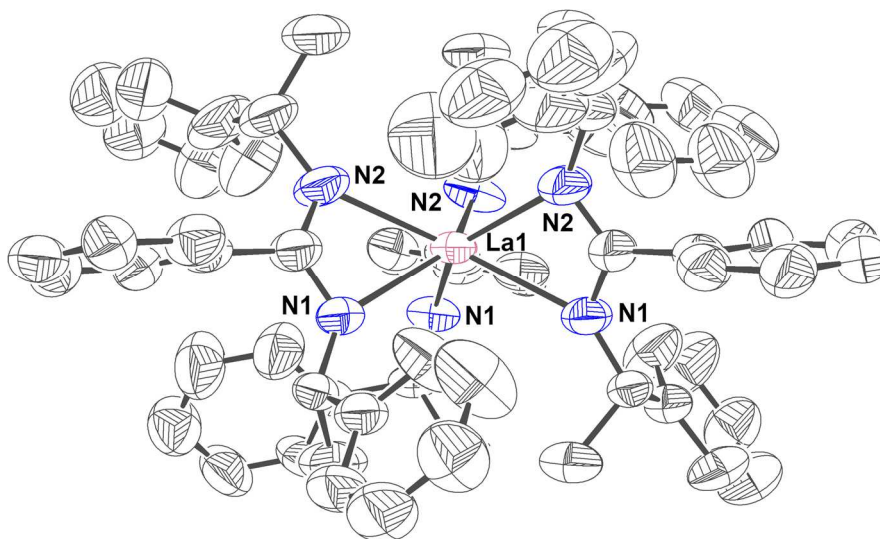
Figure 102. Molecular structure of Λ-[La((S)-PEBA)₃] (**28**). Ellipsoids are drawn at 30 % probability level. Hydrogen atoms are omitted for clarity. Color code: carbon (C, dark gray), nitrogen (N, blue), and lanthanum (La, rose).
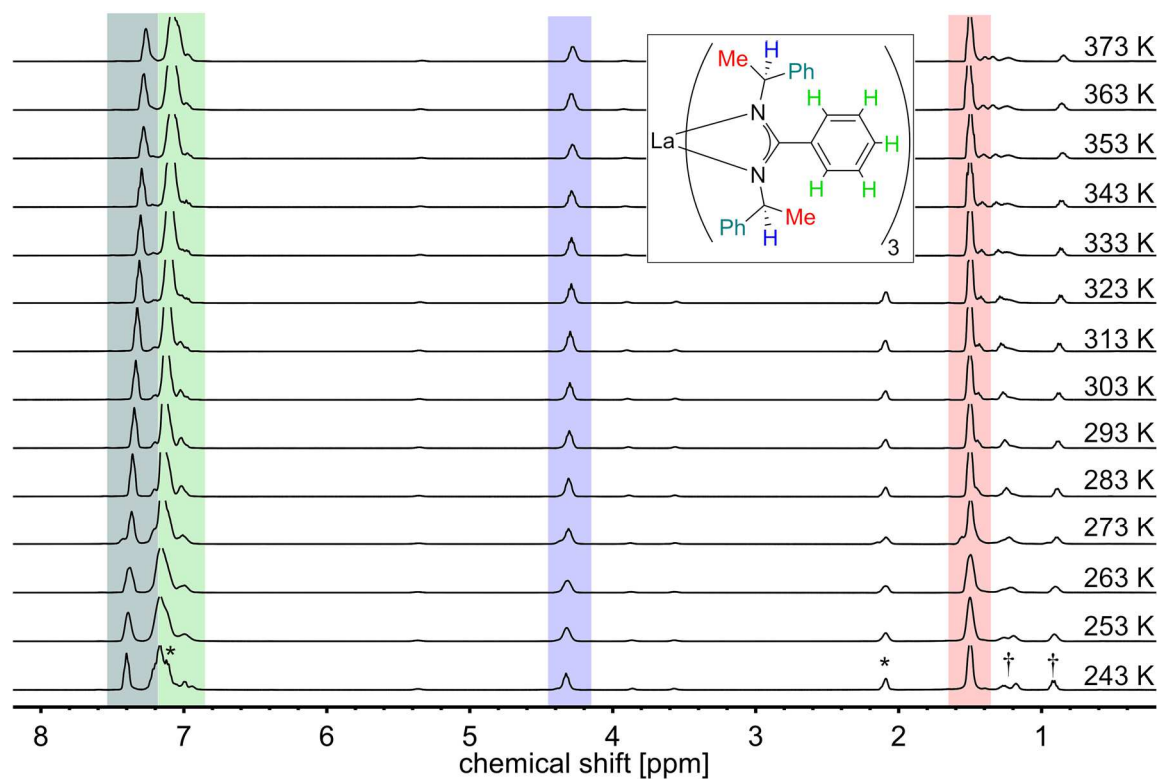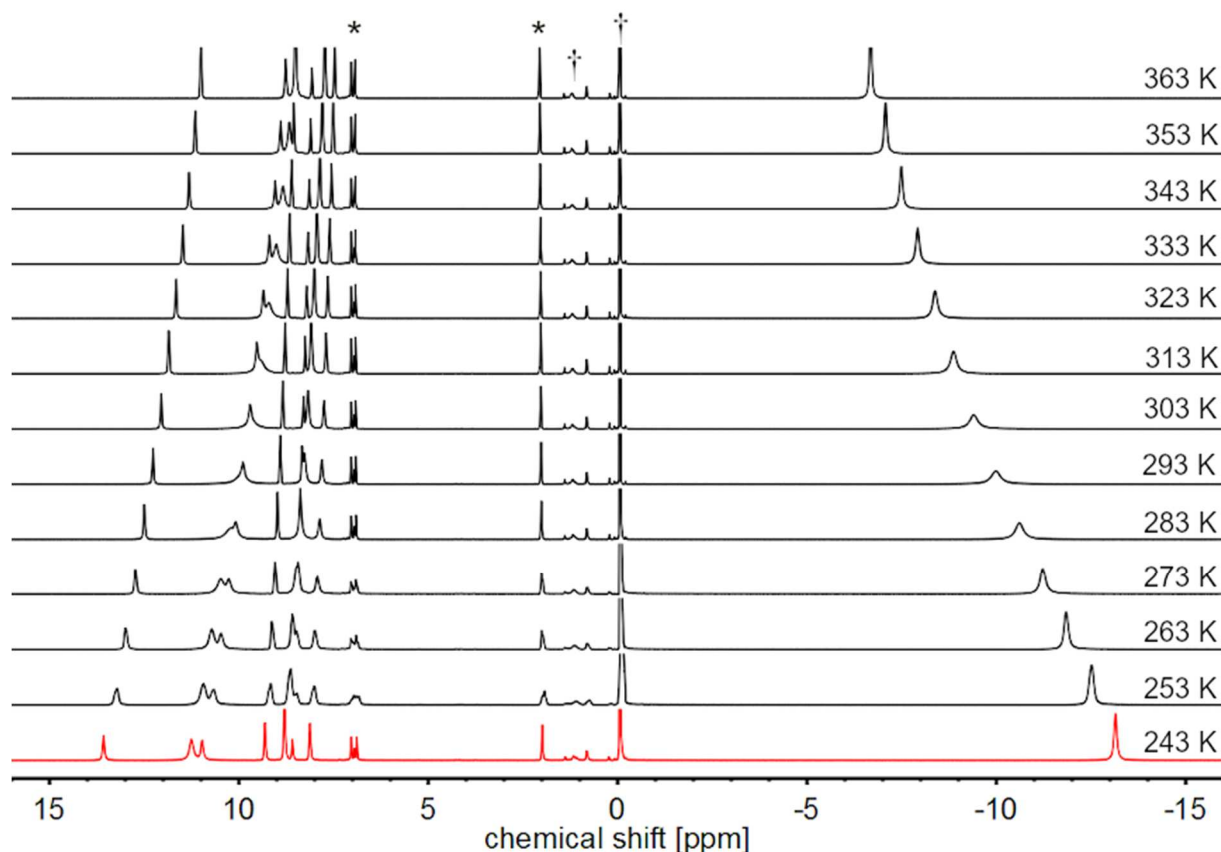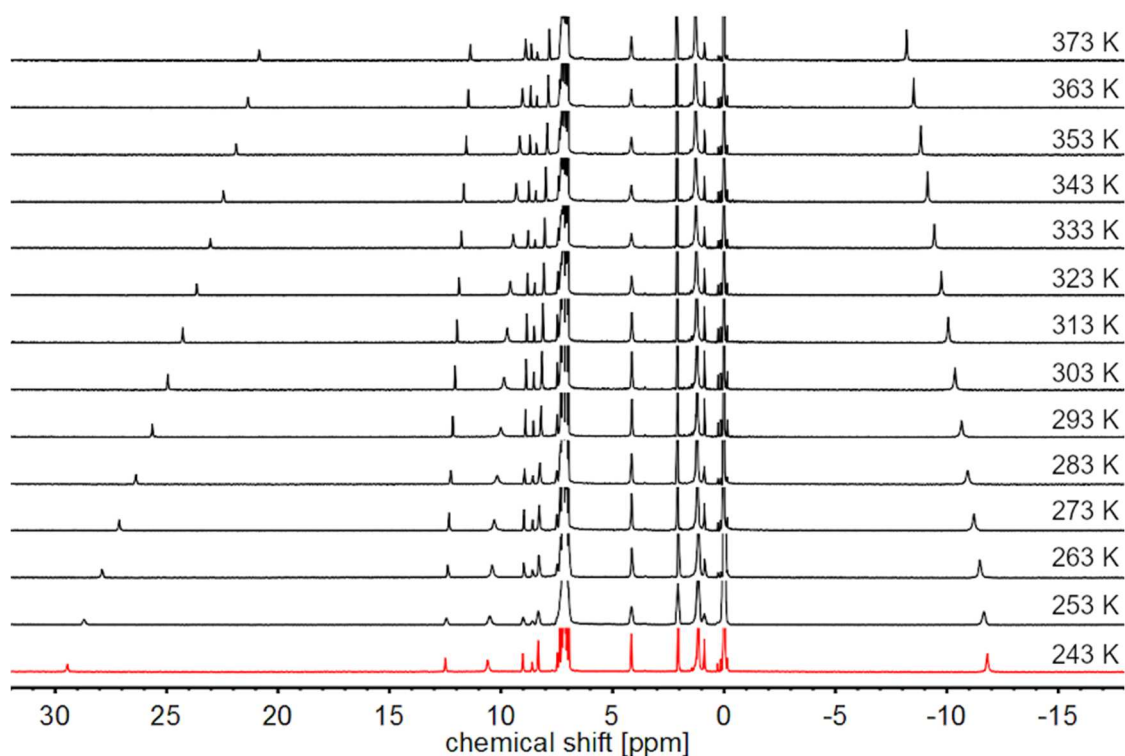

Figure 103. VT-¹H NMR spectra of [La((S)-PEBA)₃] (**28**) in toluene-d₈. Signals are marked with colors: blue (NC*H*), red (Me), green (Ph^NCN) and petrol green (Ph). Asterisks indicate solvent signals (i.e. toluene) and dagger impurities of *n*-pentane and (S)-HPEBA.

8.3.2.3 [Ce((S)-PEBA)₃] (15)
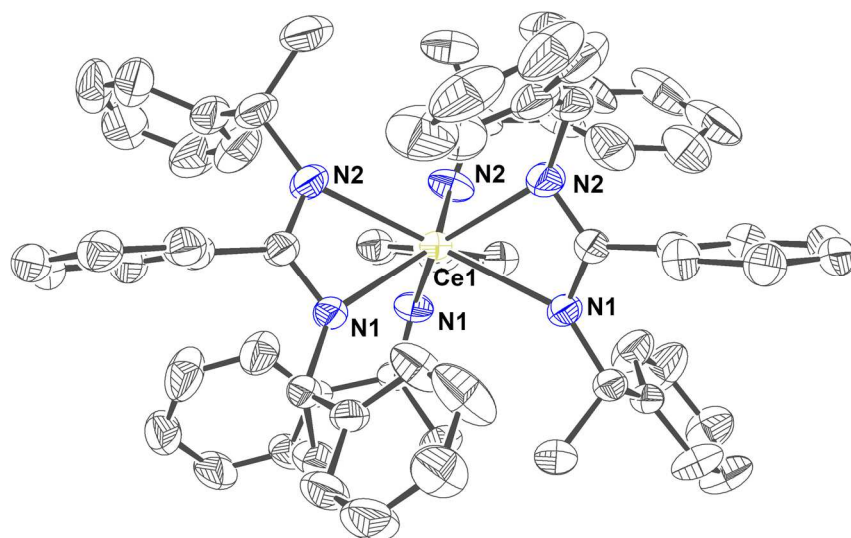
Figure 104. Molecular structure of Λ-[Ce((S)-PEBA)₃] (**15**). Ellipsoids are drawn at 50 % probability level. Hydrogen atoms are omitted for clarity. Color code: carbon (C, dark gray), nitrogen (N, blue), and cerium (Ce, yellow green).

Figure 105. VT-¹H NMR spectra of [Ce((S)-PEBA)₃] (**15**) in toluene-d₈. Asterisks indicate solvent signals (i.e. toluene) and dagger impurities of *n*-pentane and grease.

¹H NMR: (400 MHz, toluene-d₈, 243 K) δ[ppm]: 13.65 (s, 2H, *o*-PhH^{NCN}), 11.33 (s, 4H, *o*-PhH), 11.02 (s, 2H, NC*H*), 9.38 (s, 2H, *m*-PhH^{NCN}), 8.87 (s, 4H, *m*-PhH), 8.66 (s, 1H, *p*-PhH^{NCN}), 8.19 (s, 2H, *p*-PhH), -13.08 (s, 6H, Me).

8.3.2.4 [U((S)-PEBA)₃] (26)
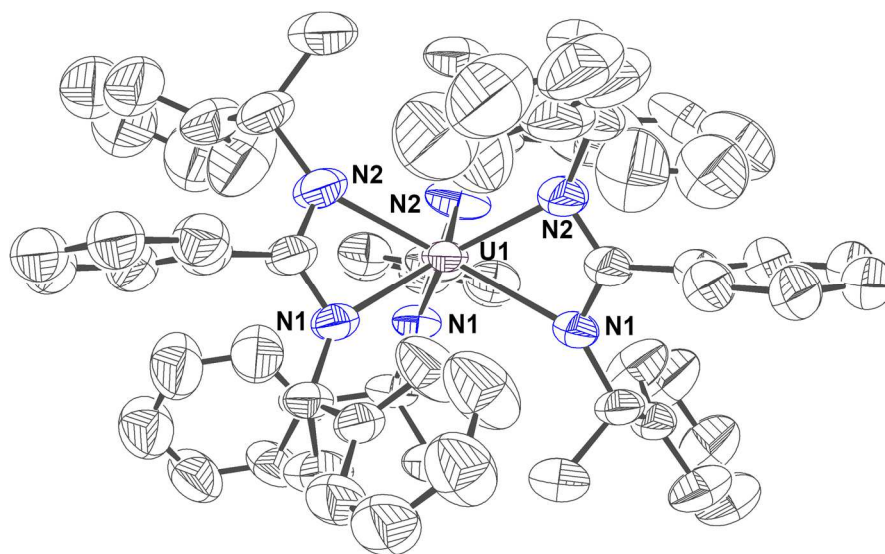
Figure 106. Molecular structure of Λ-[U((*S*)-PEBA)₃] (**26**). Ellipsoids are drawn at 30 % probability level. Hydrogen atoms are omitted for clarity. Color code: carbon (C, dark gray), nitrogen (N, blue), and uranium (U^{III}, purple).

Figure 107. VT-¹H NMR spectra of [U((*S*)-PEBA)₃] (**26**) in toluene-d₈.

¹H-NMR: (400 MHz, toluene-d₈, 243 K) δ[ppm]: 29.47 (s, 2H, NC*H*), 12.51 (s, 2H, *o*-PhH^{NCN}), 10.56 (s, 4H, *o*-PhH), 8.02 (s, 2H, *m*-PhH^{NCN}), 8.60 (s, 1H, p-PhH^{NCN}), 8.34 (s, 4H, *m*-PhH), 7.46 (s, 2H, *p*-PhH), -11.85 (s, 6H, Me).

8.3.2.5   [Np((S)-PEBA)₃] (27)
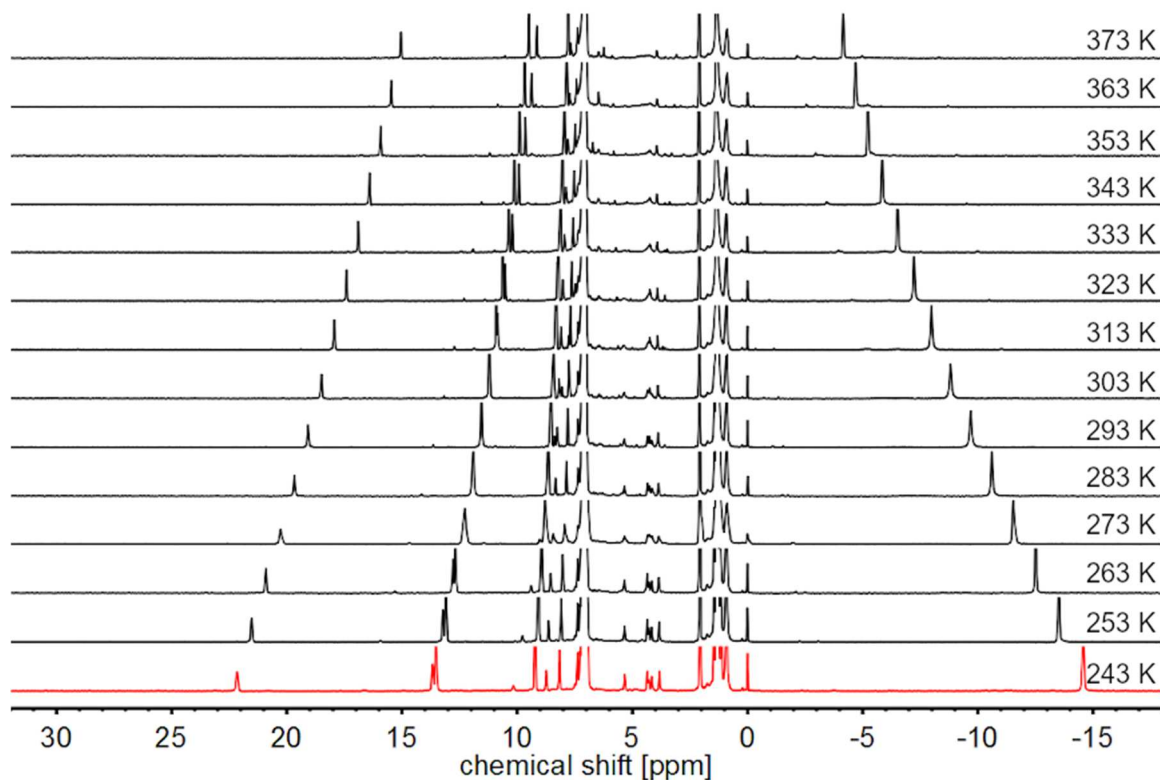
Figure 108. VT-¹H NMR spectra of [Np((*S*)-PEBA)₃] (**27**) in toluene-d₈.

¹H NMR: (400 MHz, toluene-d₈, 243 K) δ[ppm]: 22.15 (s, 2H, NC*H*), 13.66 (s, 2H, *o*-PhH^NCN), 13.53 (s, 4H, *o*-PhH), 9.21 (m, 2H, *m*-Ph, *m*-PhH^NCN), 8.72 (s, 1H, *p*-PhH^NCN), 8.15 (s, 2H, *p*-PhH), -14.57 (s, 6H, Me).

8.4 Hexavalent uranium complexes with amidinates and diimines

8.4.1 Amidinate complexes

Table 45. Crystallographic data for hexavalent uranium bis(amidinate) complex [UO$_2$((S)-PEBA)$_2$(thf)] (**29**).

	29
Empirical formula	[C$_{50}$H$_{54}$N$_4$O$_3$U]
M (g/mol)	997.00
Crystal system	Orthorhombic
Space group	$P2_12_12_1$
a (Å)	13.949(1)
b (Å)	14.204(1)
c (Å)	21.795(2)
V (Å^3)	4318.3(6)
T (K)	100
Z	4
ρ_{calcd} (Mg/m^3)	1.533
abs coeff (mm^{-1})	3.806
Θ_{max} (°)	22.71
R [$I > 2\sigma(I)$]	0.050
wR2(int)	0.075
w scheme d, e	0, 9.7009
Data/Param	5795/467
res. Dens (eÅ^{-3})	0.915, -1.128
R$_{int}$	0.126
GooF	1.060
Flack x	0.052(7)
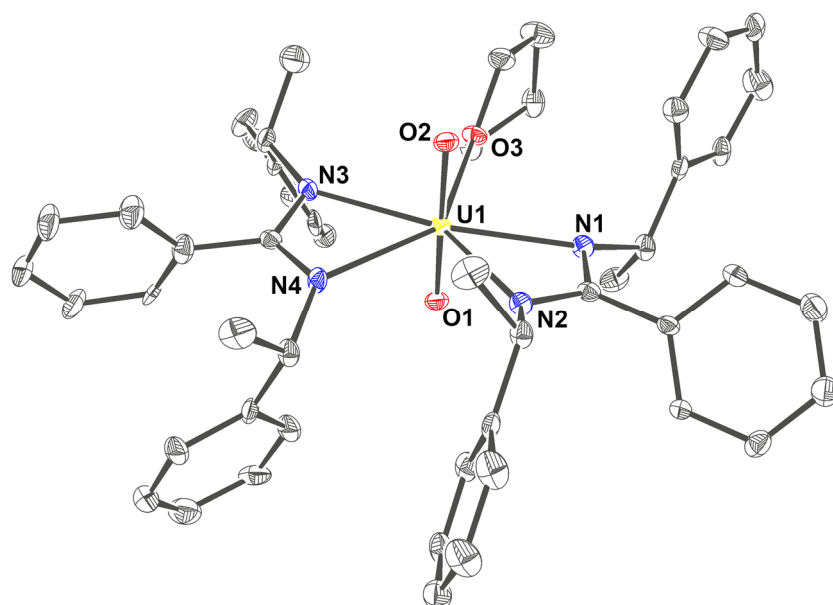
Figure 109. Molecular structure of [UO$_2$((S)-PEBA)$_2$(thf)] (**29**). Ellipsoids are drawn at 50 % probability level. Hydrogen atoms are omitted for clarity. Color code: carbon (C, dark gray), nitrogen (N, blue), oxygen (O, red), and uranium (U^{VI}, yellow).
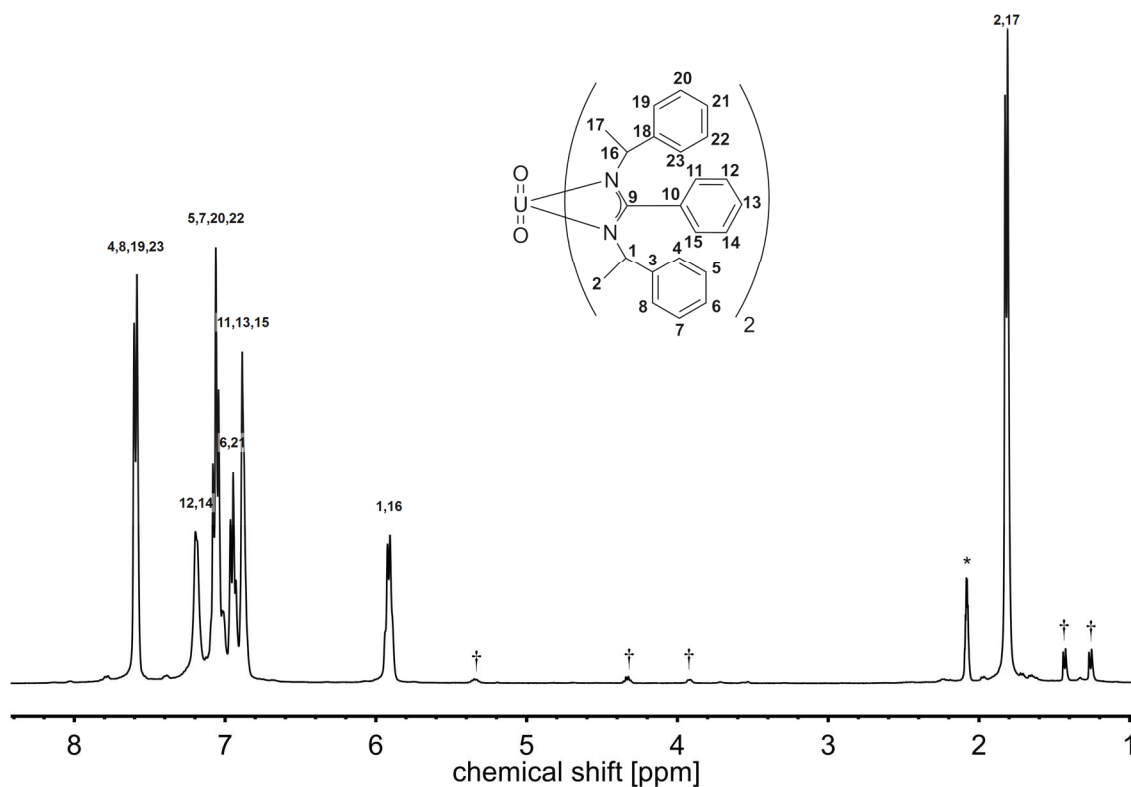
Figure 110. ¹H NMR spectrum of [UO₂((*S*)-PEBA)₂(thf)] (**29**) in toluene-d₈. Asterisk indicate solvent signal and dagger impurity of (*S*)-HPEBA. Signals of coordinated thf are not visible due to prior drying of **29**.

Table 46. Comparison of structural parameters in uranyl bis(amidinate) complexes. L³ corresponds to *N*,*N*′-bis(trimethylsilyl)-benzamidinate. The angle τ is defined by the vector between O2 and O1 and the plane normal of N1–U1–N2 (a) and N3–U1–N4 (b), respectively.

Compound	**29**	[UO₂(L³)₂(thf)][159]	[UO₂(L³)₂][155]
d(U–O1) [Å]	1.774	1.778	1.749
d(U–O2) [Å]	1.783	1.777	
∠(O1–U–O2) [°]	175.8	169.6	179.4
τ (a) [°]	8.7	23.5	4.4
τ (b) [°]	4.0	20.4	
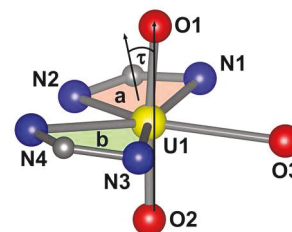
8.4.2 Diimine complexes

8.4.2.1 Comparison

Table 47. Crystallographic data for hexavalent uranium diimine complexes [UO$_2$Cl$_2$(phen)$_2$] (**30**), [UO$_2$Cl$_2$(bipy)(H$_2$O)] (**31**), [UO$_2$Cl$_2$(phen)(act)] (**32**), [(UO$_2$Cl(bipy))$_2$(μ$_2$-OH)$_2$] (**33**), and [(UO$_2$Cl(phen))$_2$(μ$_2$-OH)$_2$] (**34**).

	30	31	32	33	34
Empirical formula	[C$_{10}$H$_{10}$Cl$_2$N$_2$O$_3$U]	[C$_{24}$H$_{16}$Cl$_2$N$_4$O$_2$U]	[C$_{15}$H$_{14}$Cl$_2$N$_2$O$_3$U]	[C$_{20}$H$_{18}$Cl$_2$N$_4$O$_6$U$_2$]	[C$_{24}$H$_{18}$Cl$_2$N$_4$O$_6$U$_2$]·2H$_2$O
M (g/mol)	515.13	701.34	579.21	957.34	1041.42
Crystal system	Monoclinic	Triclinic	Monoclinic	Triclinic	Triclinic
Space group	$P2_1/n$	P-1	$P2_1/c$	P-1	P-1
a (Å)	12.134(5)	8.528(1)	8.791(1)	8.413(1)	7.164(7)
b (Å)	6.866(3)	9.411(1)	26.099(2)	8.796(1)	9.453(5)
c (Å)	15.325(6)	14.579(1)	14.712(1)	9.515(1)	11.180(8)
$α$ (°)	90	79.982(2)	90	116.188(1)	104.75(3)
$β$ (°)	96.614(8)	89.776(2)	90.449(2)	108.350(1)	108.63(4)
$γ$ (°)	90	71.925(2)	90	91.576(1)	91.45(3)
V (Å^3)	1268.4(9)	1093.8(1)	3375.2(3)	588.18(6)	689.1(9)
T (K)	100	100	100	100	100
Z	4	2	8	1	1
$ρ_{calcd}$ (Mg/m^3)	2.698	2.129	2.280	2.703	2.510
abs coeff (mm^{-1})	13.22	7.70	9.949	14.02	11.99
$Θ_{max}$ (°)	30.4	30.5	28.3	32.6	28.3
R [$I > 2σ(I)$]	0.027	0.030	0.029	0.010	0.059
wR2(int)	0.050	0.059	0.044	0.045	0.101
w scheme d, e	0.0200,1.9161	0.0173, 3.9159	0, 12.5198	0.0146,0.3331	0.0257, 8.9072
Data/Param	4191/175	6667/298	8382/419	4282/154	3091/189
res. Dens (eÅ^{-3})	0.99, -1.56	3.16/-2.80	0.077,-1.11	1.59, -0.77	1.86, -1.94
R$_{int}$	0.037	0.050	0.058	0.019	0.028
GooF	1.05	1.17	1.04	1.14	1.07

Table 48. Comparison of selected structure parameters of hydroxy-bridged dimeric uranyl bipy/phen complexes (Cambridge Structural Database, March 2020).

Chemical formula	d(U–N) [Å]	α(N1–U–N2) [°]	β(N1-C5-C9-N2) [°]
[(UO$_2$Cl(bipy))$_2$(μ_2-OH)$_2$] (**33**)	2.578, 2.636	61.94	-17.12
[(UO$_2$(1,5-nds)(bipy))$_2$(μ_2-OH)$_2$]·2 H$_2$O[337]	2.609, 2.614, 2.606, 2.633	62.07, 62.10	1.15, 2.71
[(UO$_2$(1,5-nds)(bipy))$_2$(μ_2-OH)$_2$]·bipy[337]	2.578, 2.584	62.87	7.00
[(UO$_2$Cl(phen))$_2$(μ_2-OH)$_2$]·2 H$_2$O (**34**)	2.630, 2.641	62.7	4.11
[(UO$_2$(C$_2$H$_3$O$_2$)(phen))$_2$(μ_2-OH)$_2$][338]	2.644, 2.656	62.3	0.44
[(UO$_2$(1,2-eds)(phen))$_2$(μ_2-OH)$_2$]·4 H$_2$O[339]	2.609, 2.631	63.06	3.13
[(UO$_2$(1,5-nds)(phen))$_2$(μ_2-OH)$_2$][337]	2.616, 2.586	63.20	1.54
[(UO$_2$(C$_7$H$_2$F$_3$O$_2$)(phen))$_2$(μ_2-OH)$_2$][83]	2.613, 2.621	62.83	0.37
[(UO$_2$(C$_7$H$_3$Cl$_2$O$_2$)(phen))$_2$(μ_2-OH)$_2$]·2 H$_2$O[173]	2.613, 2.604	63.05	3.25
[(UO$_2$(C$_7$H$_2$Cl$_3$O$_2$)(phen))$_2$(μ_2-OH)$_2$][83]	2.613, 2.622	62.83	0.37
[(UO$_2$(C$_7$H$_3$Br$_2$O$_2$)(phen))$_2$(μ_2-OH)$_2$][338]	2.626, 2.618	62.61	2.24
[(UO$_2$(C$_7$H$_2$Br$_3$O$_2$)(phen))$_2$(μ_2-OH)$_2$][83]	2.633, 2.642	62.66	-2.25
[(UO$_2$(C$_7$H$_3$I$_2$O$_2$)(phen))$_2$(μ_2-OH)$_2$][340]	2.625, 2.587	63.26	1.35
[(UO$_2$(C$_8$H$_6$NO$_2$)(phen))$_2$(μ_2-OH)$_2$]·2 H$_2$O[341]	2.606, 2.625	62.94	-2.5

1,2-eds: 1,2-ethanedisulfonate, 1,5-nds: 1,5-naphthalenedisulfonate

Table 49. Intramolecular distances and uranyl bending angle of hexavalent amidinate and diimine compounds **29**-**34**.

Compound	d(U–O$_{yl}$) [Å]	∠(O1–U–O2) [°]	d(U–N) [Å]
[UO$_2$Cl$_2$(phen)$_2$] (**30**)	1.775, 1.781	161.8	2.666, 2.664, 2.750, 2.764
[UO$_2$Cl$_2$(bipy)(H$_2$O)] (**31**)	1.768, 1.771	177.3	2.604, 2.613
[UO$_2$Cl$_2$(phen)(act)] (**32**)	1.769, 1.767, 1.764, 1.768	178.1, 178.4	2.578, 2.637, 2.581, 2.654
[(UO$_2$Cl(bipy))$_2$(μ_2-OH)$_2$] (**33**)	1.781, 1.782	178.7	2.578, 2.636
[(UO$_2$Cl(phen))$_2$(μ_2-OH)$_2$] (**34**)	1.775, 1.781	176.7	2.630, 2.641

Table 50. Dihedral angle of N1–U1–N2 plane against equatorial plane in uranyl diimine complexes **30**-**34** expressed as angles of the respective plane normals against each other. Positive angles correspond to clockwise rotation of plane normals, negative angles correspond to counterclockwise rotation. The equatorial plane is defined by Cl1–U1–Cl2 in **30**-**32** and by Cl1–U1–O3 in **33** and **34**.

Compound	Dihedral angle [°]
[UO$_2$Cl$_2$(phen)$_2$] (**30**)	-3.2, 89
[UO$_2$Cl$_2$(bipy)(H$_2$O)] (**31**)	34.0
[UO$_2$Cl$_2$(phen)(act)] (**32**)	22.7, -28.3
[(UO$_2$Cl(bipy))$_2$(μ_2-OH)$_2$] (**33**)	-23.4
[(UO$_2$Cl(phen))$_2$(μ_2-OH)$_2$] (**34**)	-10.8

8.4.2.2 [UO₂Cl₂(phen)₂] (30)
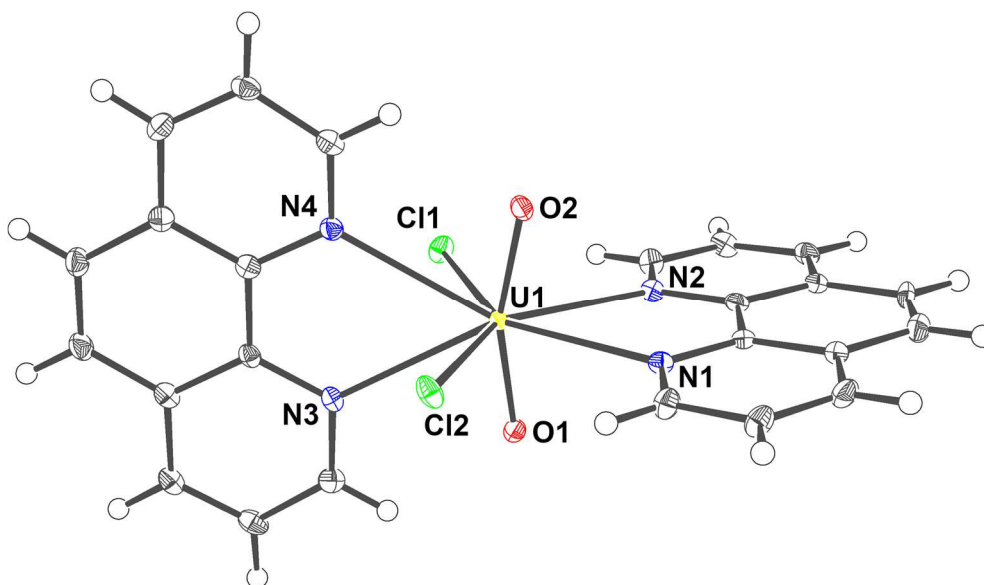
Figure 111. Molecular structure of [UO$_2$Cl$_2$(phen)$_2$] (**30**). Ellipsoids are drawn at 50 % probability level. Color code: hydrogen (H, white), carbon (C, dark gray), nitrogen (N, blue), chlorine (Cl, green), and uranium (U^{VI}, yellow).
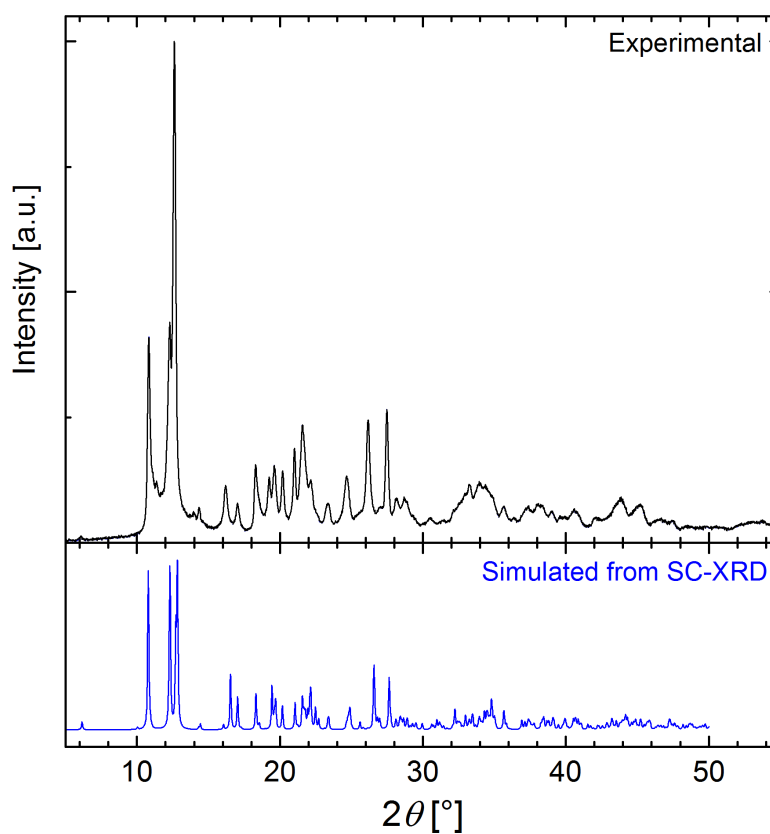

Figure 112. Powder X-ray diffraction pattern of [UO$_2$Cl$_2$(phen)$_2$] (**30**, top) with simulated diffraction pattern based on single-crystal XRD data (bottom).
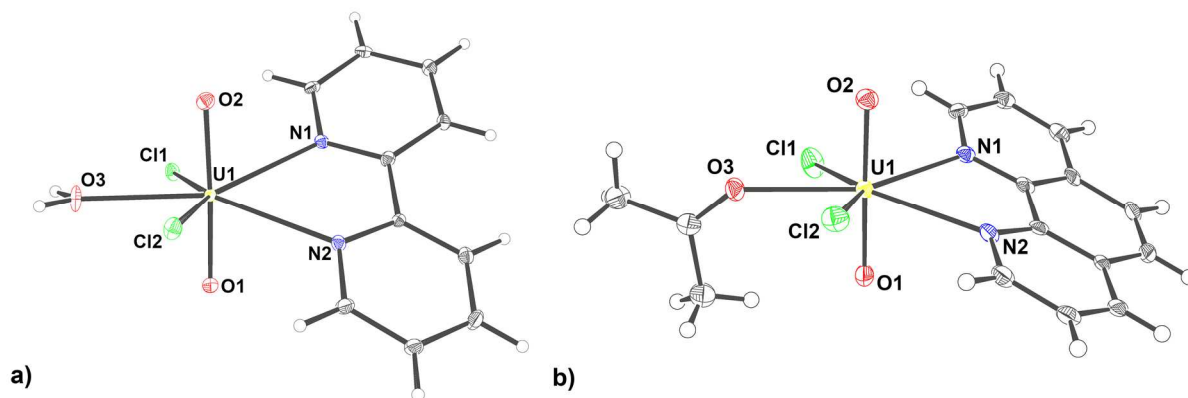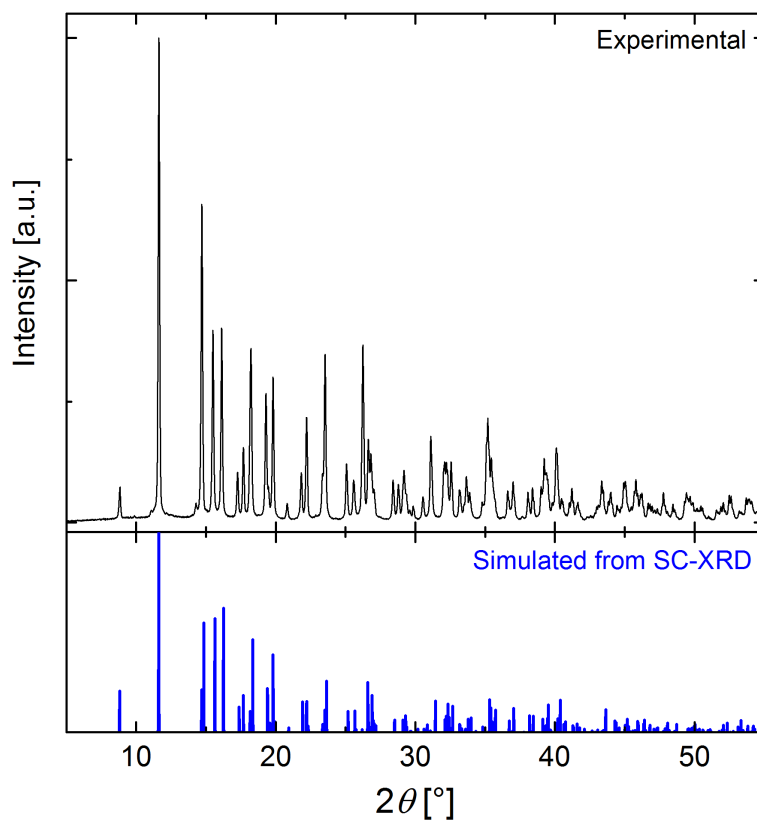
8.4.2.3 *[UO₂Cl₂(bipy)(H₂O)] (31) & [UO₂Cl₂(phen)(act)] (32)*

Figure 113. Molecular structure of a) $[UO_2Cl_2(bipy)(H_2O)]$ (**31**) and b) $[UO_2Cl_2(phen)(act)]$ (**32**). Ellipsoids are drawn at 50 % probability level. Color code: hydrogen (H, white), carbon (C, dark gray), nitrogen (N, blue), oxygen (O, red), chlorine (Cl, green), and uranium (U^{VI}, yellow).
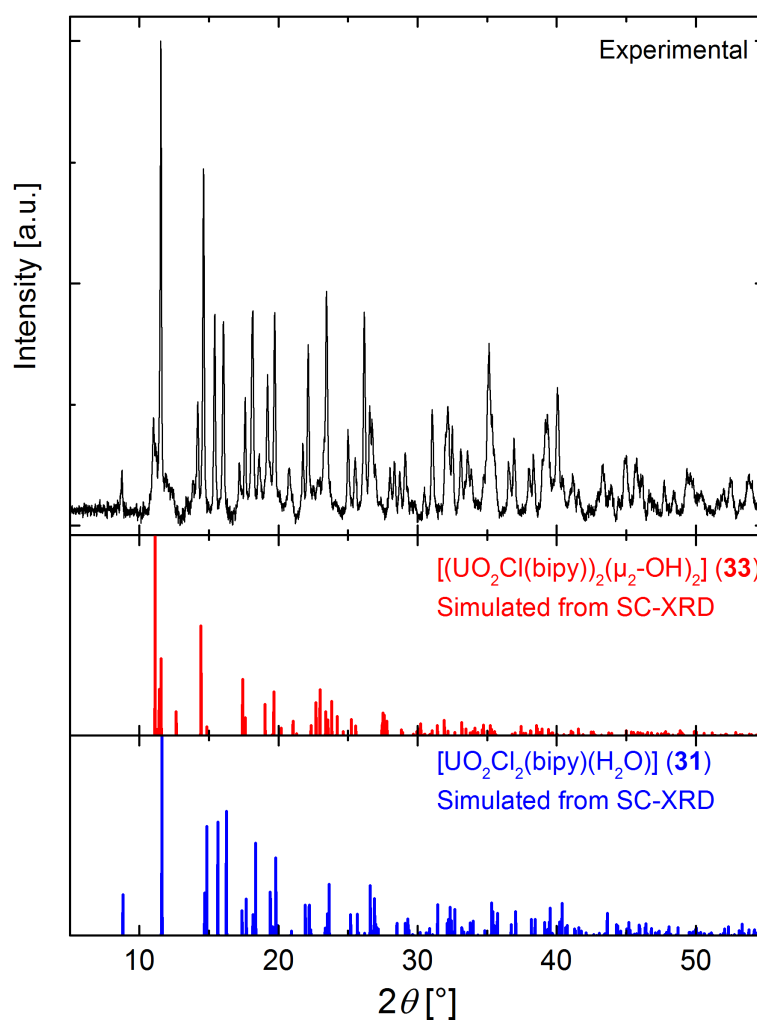

Figure 114. Powder X-ray diffraction pattern of $[UO_2Cl_2(bipy)(H_2O)]$ (**31**, top) with simulated diffraction pattern based on single-crystal XRD data (bottom).

8.4.2.4 [(UO₂Cl(bipy))₂(μ₂-OH)₂] (33) & [(UO₂Cl(phen))₂(μ₂-OH)₂] (34)
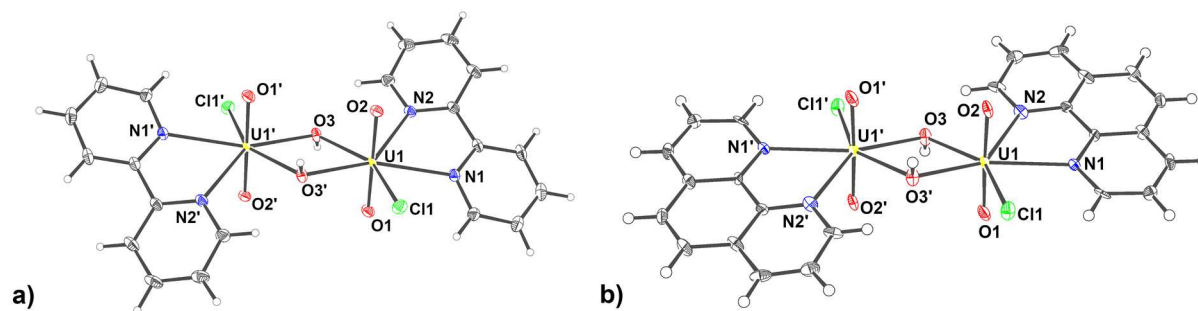
Figure 115. Molecular structure of a) $[(UO_2Cl(bipy))_2(\mu_2\text{-}OH)_2]$ **(33)** and b) $[(UO_2Cl(phen))_2(\mu_2\text{-}OH)_2]$ **(34)**. Ellipsoids are drawn at 50 % probability level. Color code: hydrogen (H, white), carbon (C, dark gray), nitrogen (N, blue), oxygen (O, red), chlorine (Cl, green), and uranium (U^{VI}, yellow).

Figure 116. Powder X-ray diffraction pattern of precipitate from synthesis with excess of bipyridine (top) indicating a mixture of hydrolyzed dimeric complex $[(UO_2Cl(bipy))_2(\mu_2\text{-}OH)_2]$ **(33,** middle) and monomeric $[UO_2Cl_2(bipy)(H_2O)]$ **(31,** bottom). Diffraction patterns of **31** and **33** are simulated based on single-crystal XRD data.

8.5 Mixed-valent polynuclear neptunium complexes

8.5.1.1 Comparison

Table 51. Crystallographic data for mixed-valent polynuclear neptunium complexes **35** and **36**.

	35	36
Empirical formula	$[C_{28}H_{56}Cl_6Np_3O_{11}]$	$[C_{24}H_{48}Cl_7Np_4O_{12}]$
M (g/mol)	1492.42	1724.77
Crystal system	monoclinic	monoclinic
Space group	$P2_1/c$	$C2/c$
a (Å)	15.345(2)	15.009(4)
b (Å)	24.156(3)	14.159(3)
c (Å)	11.5292(8)	40.069(9)
β (°)	90.060(3)	91.406(2)
V (Å^3)	4274(1)	8513(3)
T (K)	100.(2)	100.(2)
Z	4	8
ρ_{calcd} (Mg/m^3)	2.320	2.692
Abs coeff (mm^{-1})	7.664	10.173
Θ_{max} (°)	27.880	23.2596
R [$I > 2\sigma(I)$]	0.0207	0.1402
$wR2$(int)	0.0382	0.3249
w scheme d, e	0.0103, 8.3544	0.0001, 6904.4883
Data/param	10184/433	6089/418
Res. Dens (eÅ^{-3})	1.294, -1.101	6.554, -5.350
R_{int}	0.0334	0.0596
GooF	1.072	1.358

Table 52. Comparison of intramolecular distances of trinuclear mixed-valent neptunium(IV/V) complex $[(Np^{IV}Cl_4)(Np^VO_2(thf)_3)_2(\mu_2\text{-}Cl)_2]$ (**35**) with isostructural neptunium(IV/V) complex $[(Np^{VI}O_2Cl)(Np^VO_2(thf)_3)_2(\mu_2\text{-}Cl)_2]$.[263]

d [Å]	$Np^{IV}Np^V_2$ (**35**)	$Np^{VI}Np^V_2$[263]
$Np^{IV}1$–O1	2.249	2.303
$Np^{IV}1$–O3	2.270	2.316
Np^V2–O1	1.918	1.912
Np^V2–O2	1.793	1.804
Np^V3–O3	1.911	1.885
Np^V3–O4	1.794	1.752
$Np^{IV}1$–Np^V2	4.084	4.105
$Np^{IV}1$–Np^V3	4.089	4.108
Np^V2–Np^V3	4.298	4.340

8.5.1.2 $[(Np^{IV}Cl_4)(Np^VO_2(thf)_3)_2(\mu_2\text{-}Cl)_2]\cdot thf$ (35)
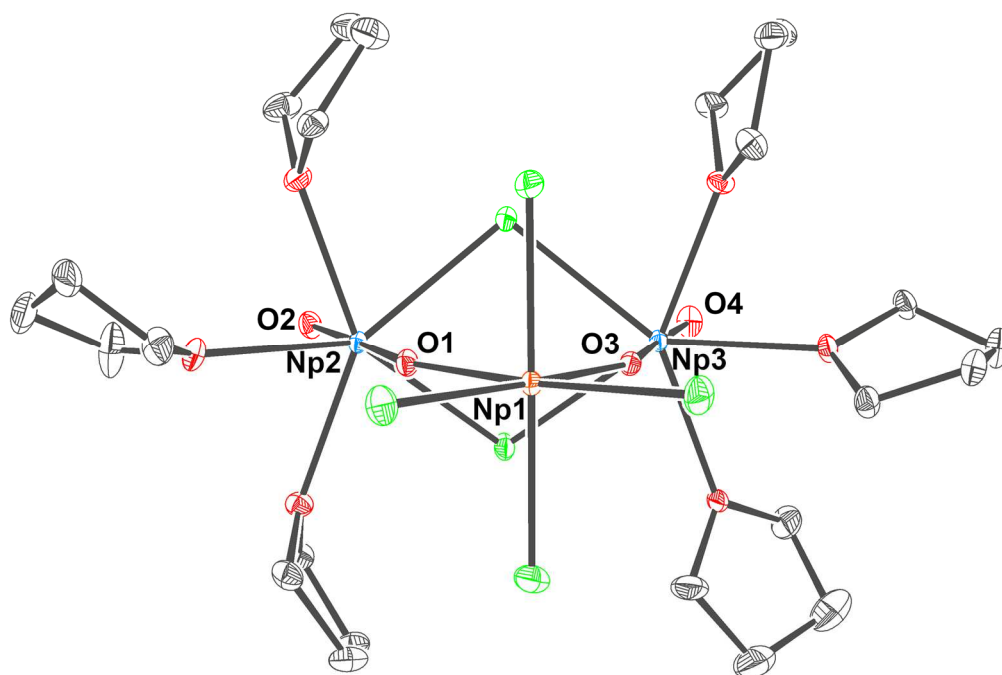
Figure 117. Molecular structure of $[(NpCl_4)(NpO_2(thf)_3)_2(\mu_2\text{-}Cl)_2]$ (**35**). Ellipsoids are drawn at 50 % probability level. Hydrogen atoms and solvent molecules are omitted for clarity. Color code: carbon (C, dark gray), oxygen (O, red), chlorine (Cl, green), and neptunium (Np^{IV}, orange red; Np^V, pale blue).
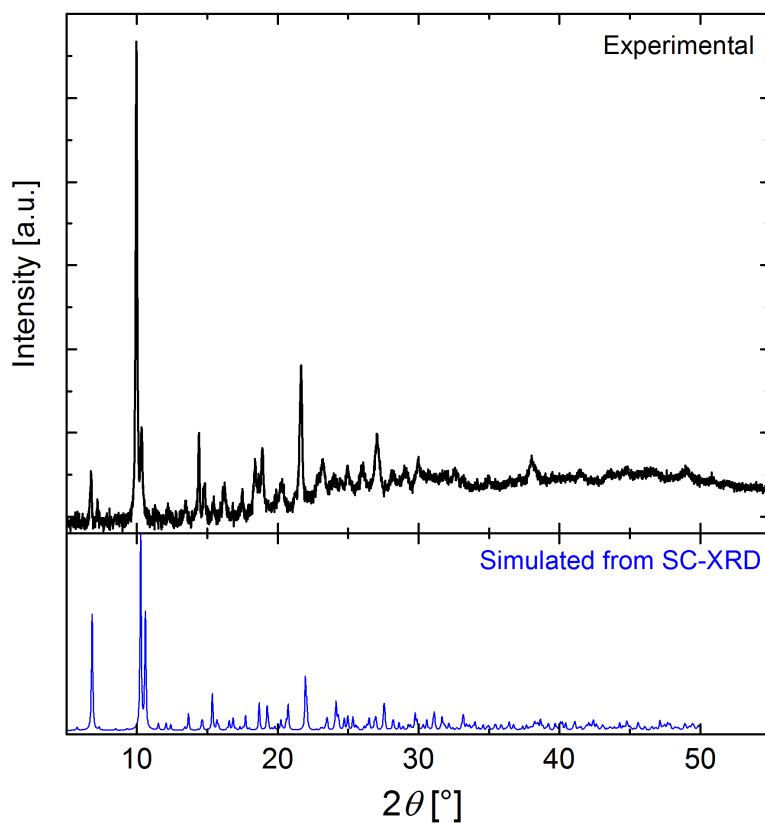

Figure 118. Powder X-ray diffraction pattern of $[(NpCl_4)(NpO_2(thf)_3)_2(\mu_2\text{-}Cl)_2]$ (**35**, top) with simulated diffraction pattern based on single-crystal XRD data (bottom).
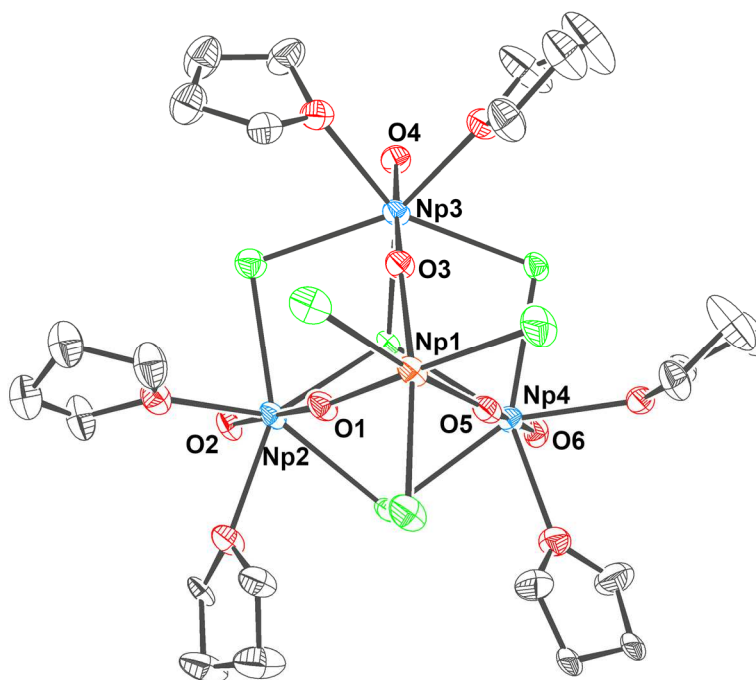
8.5.1.3 $[(Np^{IV}Cl_3)(Np^{V}O_2(thf)_2)_3(\mu_2\text{-}Cl)_3(\mu_3\text{-}Cl)]$ (36)

Figure 119. Molecular structure of $[(NpCl_3)(NpO_2(thf)_2)_3(\mu_2\text{-}Cl)_3(\mu_3\text{-}Cl)]$ (**36**). Ellipsoids are drawn at 50 % probability level. Hydrogen atoms and solvent molecules are omitted for clarity. Color code: carbon (C, dark gray), oxygen (O, red), chlorine (Cl, green), and neptunium (Np^{IV}, orange red; Np^{V}, pale blue).
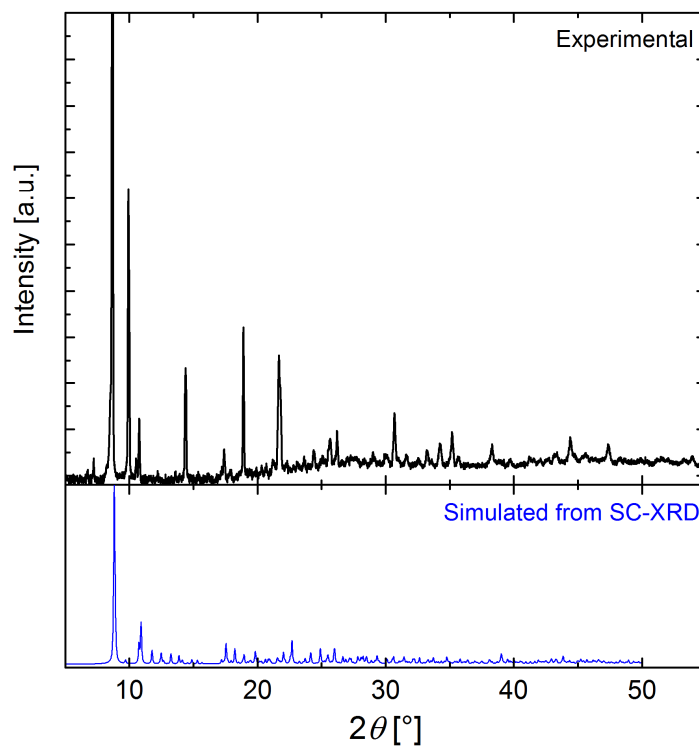

Figure 120. Powder X-ray diffraction pattern of $[(NpCl_3)(NpO_2(thf)_2)_3(\mu_2\text{-}Cl)_3(\mu_3\text{-}Cl)]$ (**36**, top) with simulated diffraction pattern based on single-crystal XRD data (bottom).

8.6 Quantum chemical calculations data

The imaginary wavenumbers produced by frequency analyses of all optimized complexes within the harmonic approximation are shown in Table 53. It is still expected that the obtained structures can be used for further analysis since the wavenumbers are small and by visual inspection the modes can be assigned to bending motions of the phenyl rings of the ligands. Consequently, the arrangement of the ligands around the metal centers as well as the metal-ligand bond-lengths are reasonable. Nevertheless, the calculated IR spectra are not compared with the experimentally obtained ones, since the introduced error cannot be neglected.

Table 53. Imaginary wavenumbers by frequency analysis of optimized complexes.

complex		Imaginary wavenumbers [cm^{-1}]
[CeCl((*S*)-PEBA)$_3$]	(**16**)	0.00
[ThCl((*S*)-PEBA)$_3$]	(**9**)	5.13
[PaCl((*S*)-PEBA)$_3$]		0.00
[UCl((*S*)-PEBA)$_3$]	(**10**)	20.11
[NpCl((*S*)-PEBA)$_3$]	(**11**)	17.44
[PuCl((*S*)-PEBA)$_3$]		0.00
[UF((*S*)-PEBA)$_3$]	(**18**)	0.00
[NpF((*S*)-PEBA)$_3$]	(**19**)	0.00
[Ce((*S*)-PEBA)$_3$]	(**15**)	0.00
[U((*S*)-PEBA)$_3$]	(**26**)	0.00
[Np((*S*)-PEBA)$_3$]	(**27**)	0.00
[Sm((*S*)-PEBA)$_3$]		0.00

The comparison of the experimental determined (SC-XRD) and the geometry optimized structure is shown in Figure 121 for the [NpCl((*S*)-PEBA)$_3$] (**11**) complex. The differences between both structures are minor, only visible by a different rotation of some phenyl rings. Both structures are only possessing a C_1 symmetry.
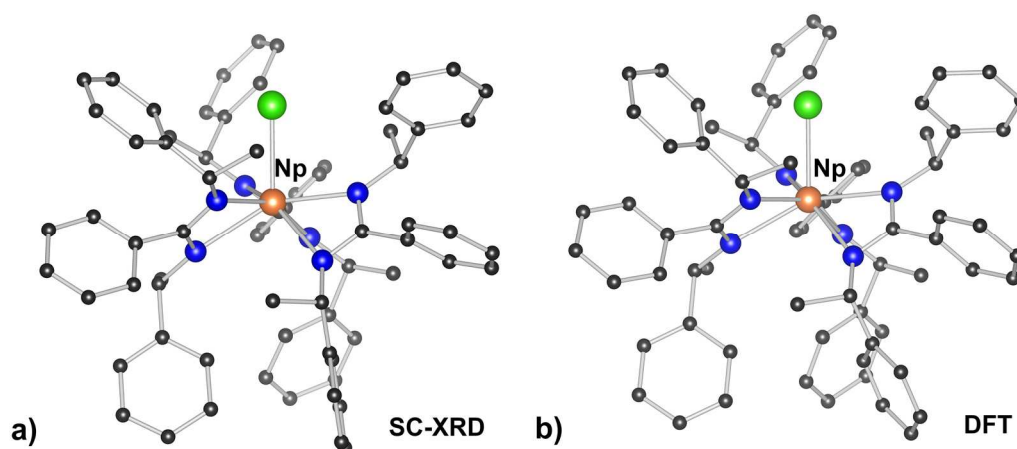

Figure 121. Comparison of crystallographically determined structure of [NpCl(*S*)-PEBA)$_3$] (**11**) (a, left) with geometry optimized structure (b, right). Hydrogen atoms are omitted for clarity Color code: neptunium (Np^{IV}, orange red), carbon (C, dark grey), nitrogen (N, blue), and chlorine (Cl, green).

Similar to the experimentally determined structures of complexes **9**-**11** and **16**, the distances to the nitrogen atoms have been averaged for all nitrogens opposite to the chlorine (i.e. N1, N3, N5) to N_{long} and for the others (i.e. N2, N4, N6) to N_{short}. The intramolecular distances of the SC-XRD and the geometry optimized structures are compared in Table 54. In general, the calculated M–Cl and M–N_{short} bonds are slightly longer (~1-6 pm) than the experimental values whereas the M–N_{long} bonds are shorter for the actinide compounds and similar for the cerium compound. This difference potentially reflects the influence of the crystal packing on the intramolecular distances which is also visible in the increased difference between M–N_{long} and M–N_{short} in the single-crystal structures (Δ(M–$N_{long/short}$) exp.: $\approx$13 pm *vs.* calc.: $\approx$9 pm). Thus, the complex molecules adapt to the crystallographic packing by moving the ligands further away from the metal center.

Table 54. Averaged bond lengths (experimental in black and calculated in grey) in reported tris(amidinate) compounds [MCl(L)₃] (L = (*S*)-PEBA) **9**-**11**, **16**.

	[ThCl(L)₃] (**9**)		[UCl(L)₃] (**10**)		[NpCl(L)₃] (**11**)		[CeCl(L)₃] (**16**)	
M–Cl	2.701	2.726	2.641	2.673	2.630	2.664	2.644	2.705
M–N_{long}	2.560	2.547	2.499	2.488	2.497	2.479	2.512	2.513
M–N_{short}	2.439	2.449	2.379	2.394	2.368	2.390	2.365	2.420

Table 55. Averaged bond lengths in geometry optimized tris(amidinate) compounds [AnCl((*S*)-PEBA)₃] (An = Pa, Pu).

	[PaCl((*S*)-PEBA)₃]	[PuCl((*S*)-PEBA)₃]
M–Cl	2.696	2.705
M–N_{long}	2.496	2.428
M–N_{short}	2.416	2.426

Table 56. Delocalization indices of M–Cl and M–N bonds in tetravalent chloro tris(amidinate) compounds [MCl((*S*)-PEBA)₃] (M = Ce, Th, Pa, U, Np, Pu)

	DI (M–N_{long})	DI (M–N_{short})	DI (M–Cl)
[CeCl(L)₃]	0.40	0.48	0.54
[ThCl(L)₃]	0.36	0.43	0.52
[PaCl(L)₃]	0.40	0.46	0.55
[UCl(L)₃]	0.41	0.49	0.57
[NpCl(L)₃]	0.41	0.49	0.58
[PuCl(L)₃]	0.46	0.46	0.52

Table 57. Summary of values obtained from natural population analysis of tetravalent chloro tris(amidinate) compounds [MCl(L)₃] (M = Ce, Th, Pa, U, Np, Pu; L = (*S*)-PEBA) and trivalent tris(amidinate) complexes [M(L)₃] (M = Ce, Sm, U, Np; L = (*S*)-PEBA).

	population
[CeCl(L)₃]	$6s^{0.18}\,5d^{1.20}\,6d^{0.04}\,4f^{0.81}\,5f^{0.02}$
[ThCl(L)₃]	$7s^{0.19}\,6d^{1.09}\,7d^{0.05}\,5f^{0.81}\,6f^{0.10}$
[PaCl(L)₃]	$7s^{0.22}\,6d^{1.11}\,7d^{0.05}\,5f^{1.73}\,6f^{0.28}$
[UCl(L)₃]	$7s^{0.22}\,6d^{1.16}\,7d^{0.05}\,5f^{2.81}\,6f^{0.22}$
[NpCl(L)₃]	$7s^{0.22}\,6d^{1.13}\,7d^{0.06}\,5f^{3.87}\,6f^{0.15}$
[PuCl(L)₃]	$7s^{0.22}\,6d^{1.05}\,7d^{0.06}\,5f^{4.92}\,6f^{0.06}$
[Ce(L)₃]	$6s^{0.11}\,5d^{0.70}\,6d^{0.02}\,4f^{1.15}\,5f^{0.04}$
[Sm(L)₃]	$6s^{0.12}\,5d^{0.72}\,6d^{0.02}\,4f^{5.12}\,5f^{0.01}$
[U(L)₃]	$7s^{0.14}\,6d^{0.68}\,7d^{0.03}\,5f^{3.28}\,6f^{0.05}$
[Np(L)₃]	$7s^{0.13}\,6d^{0.66}\,7d^{0.03}\,5f^{4.33}\,6f^{0.05}$

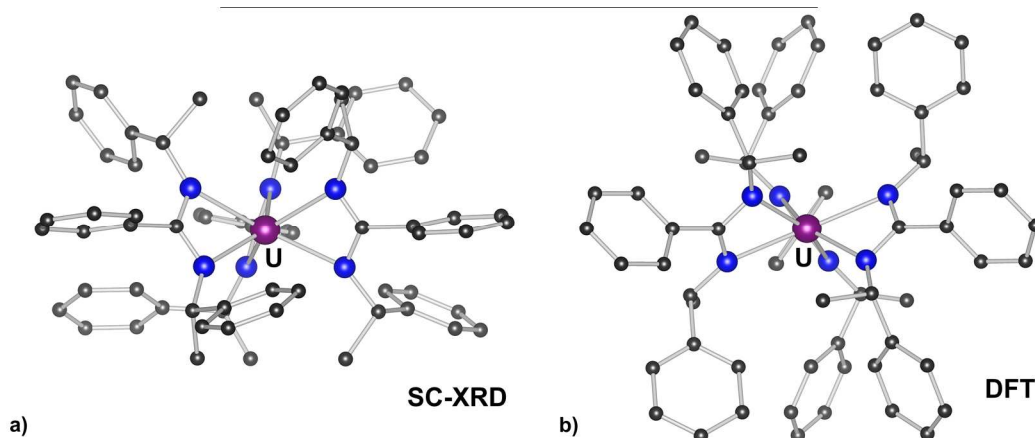**Figure 122.** Molecular structure of [U((*S*)-PEBA)₃] (**26**) from SC-XRD (a, left) and from geometry optimization (b, right). Hydrogen atoms are omitted for clarity Color code: uranium (U^III, purple), carbon (C, dark grey), and nitrogen (N, blue).
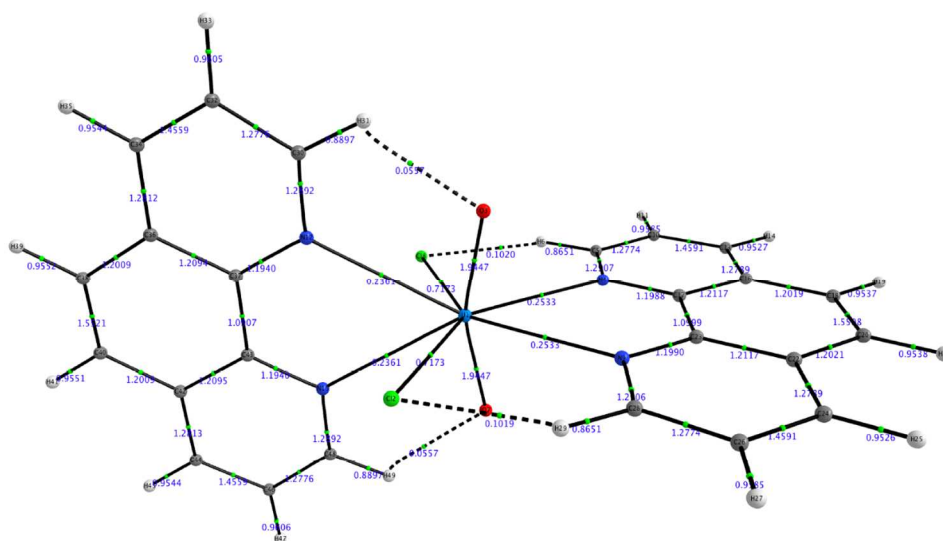

Figure 123. Geometry optimized structure of [UO₂Cl₂(phen)₂] (**30**) with delocalization indices for intramolecular bonds. Reprinted with permission from Wiley-VCH.[82]

EIDESSTATTLICHE VERSICHERUNG

Hiermit versichere ich, dass ich die vorliegende Arbeit ohne unzulässige Hilfe Dritter und ohne Benutzung anderer als der angegebenen Hilfsmittel angefertigt habe; die aus fremden Quellen direkt oder indirekt übernommenen Gedanken sind als solche kenntlich gemacht. Die Arbeit wurde bisher weder im Inland noch im Ausland in gleicher oder ähnlicher Form einer anderen Prüfungsbehörde vorgelegt.

Die vorliegende Arbeit wurde im Zeitraum von November 2016 bis April 2020 am Institut für Ressourcenökologie des Helmholtz-Zentrums Dresden-Rossendorf unter der Betreuung von Herrn Prof. Dr. Thorsten Stumpf und der wissenschaftlichen Leitung von Frau Dr. Juliane März angefertigt.

Dresden, den 23.06.2020   Sebastian Fichter